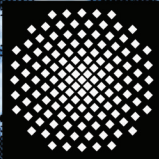


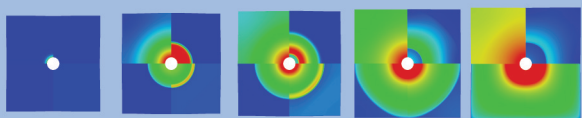
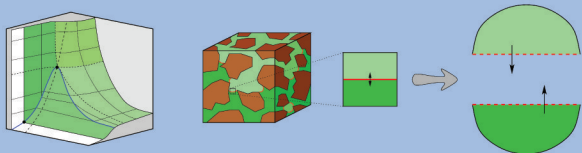
**Universität Stuttgart**  
Germany

**Institut für Mechanik (Bauwesen)**  
Lehrstuhl II, Prof. Dr.-Ing. Dr. h. c. W. Ehlers



# Fluid-Phase Transitions in a Multiphasic Model of CO<sub>2</sub> Sequestration into Deep Aquifers: A Fully Coupled Analysis of Transport Phenomena and Solid Deformations

Kai Häberle



Report No.: II-34 (2017)



**Fluid-Phase Transitions in a Multiphasic Model of  
CO<sub>2</sub> Sequestration into Deep Aquifers:  
A Fully Coupled Analysis of  
Transport Phenomena and Solid Deformation**

Von der Fakultät Bau- und Umweltingenieurwissenschaften  
der Universität Stuttgart zur Erlangung der Würde  
eines Doktor-Ingenieurs (Dr.-Ing.)  
genehmigte Abhandlung

vorgelegt von

Dipl.-Ing. Kai Klaus Häberle

aus

Langenau

Hauptberichter: Prof. Dr.-Ing. Dr. h. c. Wolfgang Ehlers

Mitberichter: Prof. Dr.-Ing. Rainer Helmig

Prof. Dr.-Ing. Tim Ricken

Tag der mündlichen Prüfung: 26. Juli 2017

Institut für Mechanik (Bauwesen) der Universität Stuttgart

Lehrstuhl für Kontinuumsmechanik

Prof. Dr.-Ing. W. Ehlers

2017

Report No. II-34  
Institut für Mechanik (Bauwesen)  
Lehrstuhl für Kontinuumsmechanik  
Universität Stuttgart, Germany, 2017

**Editor:**

Prof. Dr.-Ing. Dr. h. c. W. Ehlers

© Kai Häberle  
Institut für Mechanik (Bauwesen)  
Lehrstuhl für Kontinuumsmechanik  
Universität Stuttgart  
Pfaffenwaldring 7  
70569 Stuttgart, Germany

All rights reserved. No part of this publication may be reproduced, stored in a retrieval system, or transmitted, in any form or by any means, electronic, mechanical, photocopying, recording, scanning or otherwise, without the permission in writing of the author.

ISBN 978-3-937399-34-8  
(D 93 – Dissertation, Universität Stuttgart)

## Acknowledgements

The content of this doctoral thesis was developed during the years 2010 and 2017 when I was working as a research assistant at the Institute of Applied Mechanics (Civil Engineering), Chair of Continuum Mechanics, at the University of Stuttgart. This work would not have been possible without the help and wisdom of a multitude of people, whom I would like to express my deepest gratitude.

First of all, I would like to sincerely thank Professor Wolfgang Ehlers for giving me the opportunity to conduct the work presented here. I really appreciate that he believed in me to find a solution for the given task, although I encountered a few dead ends along the way. His rigorous method and broad expertise were a corner stone in preparing this dissertation. I also have to thank Professor Rainer Helmig, not only for evaluating my thesis, but also for introducing me to the world of numerical simulations and porous media. Furthermore, I thank my third supervisor Professor Tim Ricken for his time reading this work and for the valuable discussions at various conferences.

Very special thanks go to Dr.-Ing. Michael Sprenger, since he dragged me to this institute and, thus, initialised my research career. He is not only a great friend and travel partner, but also contributed to this work by posing critical questions. I will always remember the great and friendly atmosphere at the institute. I believe that the helpful cooperation and various activities outside of the institute were something special. In particular, I would like to thank Dr.-Ing. Maik Schenke for enduring my IT and programming related questions and for the skiing trips, Dr.-Ing. Arndt Wagner for knowing everything about regulatory things and mechanics, Dr.-Ing. David Koch for discussing thermodynamics, Dr.-Ing. Said Jamei for his help with the COMMAS course, my office-mates Dr.-Ing. Irina Komarova, Dr.-Ing. Joffrey Mabuma and Patrick Schröder. Furthermore, I want to thank Sami Bidier, Chenyi Luo, Davina Fink, Christian Bleiler, Lukas Eurich, Professor Oliver Röhrle, Dr.-Ing. Thomas Heidlauf, Ekin Altan, Mylena Mordhorst, Andreas Hessenthaler, Dr.-Ing. Okan Avci, Arzu Avci, Dr.-Ing. Uwe Rempler, Dr.-Ing. Nils Karajan, Dr.-Ing. Yousef Heider, Professor Bernd Markert as the supervisor of my diploma thesis, and all the others from the institute. I owe special thanks to Nicole Karich for her unwavering helpfulness. I am also grateful to the people of the graduate school NUPUS, for the financial support and as a source of profound knowledge regarding porous media topics. For proofreading I appreciate the time that was sacrificed by Dr.-Ing. Arndt Wagner, Dr.-Ing. Maik Schenke and Dr.-Ing. Said Jamei.

This leads me to my clever brother Dr. rer. nat. Thomas Häberle who proofread the whole thesis, as well as the presentation, and always gave wise and constructive remarks. I will not forget that he used so much of his precious time for me despite finishing his own thesis. I deeply thank my parents for their never ending support in all regards and their believe in me. Finally, I would like to express my heartfelt gratitude to my beloved wife Cornelia who had to endure most shortcomings during this long time, but nonetheless always encouraged me. The upcoming birth of our lovely daughter Carlotta in 2016 was a great incentive to conclude the work and now she is the centre of our lives.

Stuttgart, August 2017

Kai Häberle

*In jeder Schwierigkeit  
lebt die Möglichkeit.*

Albert Einstein (1879–1955)

# Contents

<b>Deutschsprachige Zusammenfassung</b>	<b>I</b>
Motivation . . . . .	I
Stand der Forschung, Zielsetzung . . . . .	II
Gliederung der Arbeit . . . . .	V
<b>Nomenclature</b>	<b>IX</b>
Conventions . . . . .	IX
Symbols . . . . .	X
Selected acronyms . . . . .	XVI
<b>1 Introduction</b>	<b>1</b>
1.1 Motivation . . . . .	1
1.2 Scope, aims and state of the art . . . . .	2
1.3 Outline of this thesis . . . . .	5
<b>2 Carbon-dioxide capture and storage</b>	<b>7</b>
2.1 Properties of CO <sub>2</sub> . . . . .	7
2.2 What is CCS? . . . . .	10
2.2.1 Geological storage options . . . . .	11
2.2.2 Storage costs . . . . .	13
2.2.3 Storage mechanisms . . . . .	14
2.2.4 Storage safety . . . . .	15
2.3 Numerical simulation of CO <sub>2</sub> storage . . . . .	17
2.3.1 State of the art . . . . .	17
2.3.2 Tasks and difficulties . . . . .	18
<b>3 Theoretical fundamentals of multiphasic and multicomponent modelling</b>	<b>21</b>
3.1 Theory of Porous Media . . . . .	21
3.2 Kinematical relations . . . . .	23
3.2.1 Motion functions . . . . .	23

3.2.2	Deformation and strain measures . . . . .	25
3.2.3	Deformation rates and velocity gradient . . . . .	27
3.2.4	Stress measures . . . . .	27
3.3	Balance relations . . . . .	29
3.3.1	Specific balance equations . . . . .	32
3.4	Singular surfaces . . . . .	34
3.4.1	Kinematics of a body with a singular surface . . . . .	35
3.4.2	Balance relations for a body with a singular surface . . . . .	35
<b>4</b>	<b>Thermodynamic theory of fluids</b>	<b>39</b>
4.1	Phase behaviour of a single substance . . . . .	40
4.1.1	Chemical potential and first-order phase transitions . . . . .	49
4.1.2	<i>Clausius-Clapeyron</i> equation . . . . .	51
4.2	Vaporisation enthalpy . . . . .	52
4.3	Specific heat capacity . . . . .	52
4.4	Shear viscosity and thermal conductivity . . . . .	54
4.4.1	Effective shear viscosity . . . . .	54
4.4.2	Thermal conductivity . . . . .	55
<b>5</b>	<b>Constitutive settings</b>	<b>57</b>
5.1	A priori assumptions . . . . .	57
5.2	Adaptation of balance relations . . . . .	58
5.2.1	Definition of a thermoelastic solid . . . . .	59
5.2.2	Mass balances of the fluid phases . . . . .	61
5.2.3	Momentum balance of the overall aggregate . . . . .	62
5.2.4	Energy balance of the overall aggregate . . . . .	63
5.2.5	Adaptation of the entropy inequality . . . . .	64
5.3	Determination of constitutive relations . . . . .	67
5.3.1	The basic thermodynamical principles . . . . .	67
5.3.2	Exploitation of the entropy inequality . . . . .	68
5.3.3	Constitutive relations of the solid constituent . . . . .	74
5.3.4	Constitutive relations of the fluid constituents . . . . .	75
5.3.5	Constitutive relations of the overall aggregate . . . . .	85



5.4	Phase transition between the gaseous and liquid phases of a single substance	86
5.4.1	State of the art	86
5.4.2	Development of the constitutive relation for the mass-production term	89
5.4.3	Switching criterion for the mass transition	95
5.5	Governing balance relations in the strong form	96
<b>6</b>	<b>Numerical treatment</b>	<b>99</b>
6.1	Finite-element method	100
6.1.1	Weak formulations of the governing equations	102
6.2	Discretisation procedures	104
6.2.1	Spatial discretisation	104
6.2.2	Temporal discretisation	108
<b>7</b>	<b>Numerical examples</b>	<b>111</b>
7.1	CO <sub>2</sub> sequestration into a deep aquifer	111
7.1.1	Injection into a reservoir with an inclined cap-rock layer	112
7.2	Phase transition and mass transfer during evaporation and condensation	115
7.2.1	Evaporation around a hot pipe	115
7.2.2	Condensation	118
<b>8</b>	<b>Summary and Outlook</b>	<b>123</b>
8.1	Summary	123
8.2	Outlook	124
<b>A</b>	<b>Selected relations of tensor calculus</b>	<b>127</b>
A.1	Tensor algebra	127
A.2	Tensor analysis	129
<b>B</b>	<b>Thermodynamical supplements and specific evaluations</b>	<b>131</b>
B.1	Thermodynamic potentials and <i>Legendre</i> transformation	131
B.2	<i>Maxwell</i> relations and fundamental relations	132
B.3	Derivation of the <i>Maxwell</i> criterion	132
B.4	Derivation of overall mass balance	133

---

B.5	Weak forms of the effective fluid mass-balance relations . . . . .	134
B.6	Treatment of the stress terms of the overall energy balance . . . . .	134
B.7	Simplification of the direct momentum and mass production terms in the energy balance of the overall aggregate . . . . .	135
B.8	Calculation of different versions of the liquid momentum production . . . .	136
B.9	Justifying the assumption of an overall temperature for all constituents . .	136
B.10	Real solutions of a cubic equation in case of the <i>van-der-Waals</i> EOS . . . .	138
<b>Bibliography</b>		<b>141</b>
<b>Curriculum Vitae</b>		<b>155</b>

# Deutschsprachige Zusammenfassung

## Motivation

Es ist allgemein akzeptiert, dass anthropogen emittierte Treibhausgase zur globalen Erderwärmung beitragen. Die Folge davon sind steigende Meeresspiegel, welche tief liegende Wohngebiete bedrohen, häufigere und heftigere Unwetter (z. B. Wirbelstürme, Hochwasser), Dürren und viele weitere negative Erscheinungen. Deshalb ist es nötig, die globale Erderwärmung zu stoppen oder wenigstens zu mindern, indem die Emissionen von Treibhausgasen herabgesetzt werden. Von den verschiedenen Treibhausgasen ist Kohlendioxid,  $\text{CO}_2$ , das Wichtigste, da es in großen Mengen durch menschliche Aktivitäten, zum Beispiel in der Energieproduktion aus fossilen Brennstoffen, freigesetzt wird. In diesem Zusammenhang bietet die Technik des *Carbon-Dioxide Capture and Storage* (CCS) (frei übersetzt: Kohlendioxid-Abfangung und -Speicherung) eine Möglichkeit, die  $\text{CO}_2$ -Emissionen in die Atmosphäre zu reduzieren. Ende des zwanzigsten Jahrhunderts galt CCS daher als die herausragende Technik, um die globale Erwärmung aufzuhalten, und es entstand ein neues Wissenschaftsfeld, in dem sich Wissenschaftler und Ingenieure aus verschiedensten Fachrichtungen um die Lösung offener Fragen kümmerten. Heutzutage hat CCS einiges an Popularität eingebüßt, was zum einen am öffentlichen Widerstand liegt, der sich aus der Angst vor  $\text{CO}_2$ -Leckagen begründet, und zum anderen am fehlenden ökonomischen Anreiz. Ursprünglich sollte dieser durch die sogenannten  $\text{CO}_2$ -Zertifikate erzeugt werden. Diese Maßnahme verfehlt im Moment jedoch ihre Wirkung, weil sich zu viele und zu günstige Zertifikate im Umlauf befinden. Wenn man sich aber bei der Wahl von möglichen Speichern auf Offshore-Lagerstätten oder auf unbesiedelte Regionen beschränkt und das Konzept der  $\text{CO}_2$ -Zertifikate justiert, kann CCS als eine wichtige Brückentechnologie für den Übergang von fossilen zu erneuerbaren Energien angesehen werden.

Die  $\text{CO}_2$ -Emissionen werden hauptsächlich bei der Verbrennung von fossilen Brennstoffen in der Energieproduktion, im Verkehrswesen und in der Industrie erzeugt. Hiervon eignen sich vor allem Punktquellen, wie zum Beispiel Kraftwerke, zur effektiven Abtrennung des  $\text{CO}_2$  aus dem Abgasstrom. Das abgetrennte  $\text{CO}_2$  kann anschließend zum Beispiel in tief liegenden Reservoirs im Untergrund verpresst werden. Geeignete geologische Formationen für die Speicherung bilden existierende und entleerte Erdöl- oder Erdgaslagerstätten, für eine wirtschaftliche Gewinnung zu tief liegende Kohleflötze und Salzwasseraquifere. Diese verschiedenen Speicherstätten haben alle ihre Vor- und Nachteile in Bezug auf die  $\text{CO}_2$ -Speicherung, als da wären: die verbesserte Öl- und Gasförderung durch eingepresstes  $\text{CO}_2$  in aktive Erdöl- oder Erdgaslagerstätten, die bereits existierende logistische Anschließung der Erdöl- oder Erdgaslagerstätten, das Speichervolumen, welches bei Salzwasseraquifere am größten ist, und die Sicherheit der Speicherstätte, d. h. der langzeitige Verbleib des  $\text{CO}_2$  im Untergrund. Der letzte Punkt ist nur dann gewährleistet, wenn eine Leckage des  $\text{CO}_2$  ausgeschlossen werden kann. Dies wird vor allem durch eine geeignete Deckschicht aus undurchlässigem Gestein garantiert, welche die aufwärtsgerichtete Ausbreitung des  $\text{CO}_2$  verhindert. Es kann jedoch durch den hohen Einpressdruck oder durch seismische

Aktivitäten zur Rissbildung in der Deckschicht und daraufhin zur Leckage kommen.

Um solche Ereignisse vorhersagen zu können, bieten numerische Simulationen die Möglichkeit, ein Modell des Injektionsprozesses zu erstellen, das die thermodynamischen Änderungen des CO<sub>2</sub> und die Verformungen der Reservoirsteine berücksichtigt. Dies stellt das angestrebte Ziel der vorliegenden Arbeit dar. Die physikalischen, chemischen und thermodynamischen Prozesse, die bei der CO<sub>2</sub>-Speicherung auftreten, sind jedoch hoch komplex und deshalb immer noch Gegenstand aktueller Forschung. Da es im Moment nicht möglich ist, das komplette Spektrum dieser Prozesse in einem einzigen numerischen Modell realitätsgetreu wiedergeben zu können, wird im Rahmen dieser Arbeit speziell auf das mechanische Verhalten der Geologie und die Phasentransformation des eingepressten CO<sub>2</sub> eingegangen.

## Stand der Forschung, Zielsetzung

Der komplette Prozess des CCS beinhaltet eine Vielzahl verschiedenster Techniken, die sich grob in drei Teile aufspalten lassen: die chemische Abtrennung des CO<sub>2</sub> vom Abluftstrom, die Verflüssigung und den Transports zum Speicherort, sowie die Sequestrierung selbst. Hier soll im Weiteren nur der letzte Teil näher betrachtet werden. Neben Tiefseespeicherung, mineraler Karbonisierung und industriellem Gebrauch des CO<sub>2</sub> wird die geologische Speicherung in tief liegenden, unterirdischen Reservoirs als effektivste Speichermethode angesehen, wie in dem Special Report on CCS des Intergovernmental Panel on Climate Change, Metz *et al.* [119], dargestellt wird.

Die Machbarkeit der Untergrundspeicherung in industriellem Maßstab konnte bereits in verschiedenen Projekten bestätigt werden, z. B. bei der Sequestrierung von CO<sub>2</sub> im Sleipner Gasfeld in der Nordsee und bei den Projekten in Weyburn, Kanada, und In Salah, Algerien. Jedoch wird bei den meisten CCS-Projekten das eingepresste CO<sub>2</sub> zur Verbesserung der Erdöl- oder Erdgasgewinnung (EOR für „enhanced oil recovery“) eingesetzt. Dies senkt zwar die Kosten für die CO<sub>2</sub>-Speicherung, aber die zusätzlich gewonnenen Kohlenwasserstoffe werden wiederum hauptsächlich zur Energieerzeugung eingesetzt und mindern so den Nutzen der Verpressung. Darum kann nur die Speicherung in leeren Lagerstätten oder in Salzwasseraquiferen als ökologisch sinnvoll betrachtet werden. Letztere sind weltweit zu finden und bieten genügend Speichervolumen, um die angestrebte Menge an CO<sub>2</sub> aufzunehmen, damit die globale Erderwärmung aufgehalten werden kann, vergleiche Metz *et al.* [119]. Aus diesem Grund wird im Folgenden nur diese Speicherart weiter betrachtet.

Als Voraussetzung zur Bestimmung der Speicherkapazität und der Beurteilung der Sicherheit ist es essentiell das Verhalten des CO<sub>2</sub> im Reservoir während und nach Beendigung des Einpressens zu kennen. Die hierfür existierenden Überwachungstechniken, wie zum Beispiel Bohrlochmessung und seismische Untersuchung, sind jedoch nur begrenzt in der Lage, genügend Informationen über die komplexen Mechanismen, die zwischen dem CO<sub>2</sub> und dem Gestein ablaufen, zu liefern. Deshalb sind numerische Studien von höchster Bedeutung, um ein Verständnis für die physikalischen Prozesse bei der CO<sub>2</sub>-Speicherung gewinnen zu können. In der Literatur finden sich hierzu eine Vielzahl an Veröffentlichun-

gen. Die frühesten Werke zur CO<sub>2</sub>-Speicherung, welche sich zunächst aus der Simulation der Kohlenwasserstoffgewinnung entwickelt haben, stammen von der Gruppe um *Pruess & García* [46, 141, 144] und weitere Arbeiten werden in *Bielinski* [15] genannt. Verschiedene Techniken zur effizienten Simulation in Form analytischer oder semi-analytischer Modelle wurden von *Kang et al.* [93], *Nordbotten et al.* [129], *Celia et al.* [34] entwickelt. Hierzu zählen auch die vertikal-reduzierten Modelle von *Court et al.* [40] und *Gasda et al.* [70]. *Nordbotten* und *Celia* [34, 127, 128, 143] veröffentlichten mehrere Publikationen über großskalige Simulationen, inklusive einer Abschätzung des Ausmaßes von eventuellen Leckagen als Anhaltspunkt für Entscheidungsträger. Weiterhin wurden die Speicherkapazitäten verschiedener Reservoirs von *Bradshaw et al.* [28] und *Kopp et al.* [99] beurteilt. Auf spezielle Fragestellungen zu verschiedenen physikalischen Parametern, z. B. relative Permeabilität, temperaturabhängiger Kapillardruck, Mineralisierung, verbesserte Einschlusstechniken oder geomechanische Parameter, wurde von *Juanes et al.* [91], *Plug & Bruining* [136], *Kumar et al.* [103], *Ebigbo* [47] und *Rutqvist* [154–156] eingegangen. Benchmark-Studien und Vergleiche verschiedener Simulationssoftware können etwa in *Pruess et al.* [142] und *Class et al.* [37] gefunden werden. An diesem Punkt muss erwähnt werden, dass die Phasentransformation des CO<sub>2</sub> in den genannten Publikationen nur wenig berücksichtigt wurde. Falls doch, so geschieht dies mit Hilfe von tabellarischen Stoffwerten. Dadurch wird jedoch eine explizite Beschreibung des Massentransfers zwischen den Fluidphasen beim Phasenübergang nicht gewährleistet.

Phasentransformationen zwischen den Aggregatzuständen Gas, Flüssigkeit und Feststoff sind ubiquitär vorkommende physikalische Prozesse, die zum Beispiel bei der Trocknung oder dem Gefrieren auftreten. Diese Transformationen treten nicht nur in gut erforschten, sogenannten „offenen Systemen“ auf, sondern auch innerhalb poröser Materialien, etwa im Sandstein von CO<sub>2</sub>-Reservoirs. Der Mechanismus der Phasentransformation in porösen Materialien wurde bisher jedoch nur spärlich untersucht. Außer bei der CO<sub>2</sub>-Speicherung spielen Phasentransformationen auch bei anderen geologischen Aktivitäten (Dampfinjektion für EOR, Erdsanierung, Geothermie), in der Nahrungsmittelindustrie (Trocknungs- und Backprozesse) und in vielen weiteren Bereichen eine wichtige Rolle. Die vorgestellte Arbeit beschränkt sich auf die Betrachtung von Phasentransformationen erster Ordnung (Gas-zu-Flüssigkeit oder Flüssigkeit-zu-Gas) einer einzelnen Substanz, z. B. CO<sub>2</sub>. Diese Art der Phasentransformation muss klar von Übergängen zwischen Mischungen, wie zum Beispiel der Verdampfung von Wasser in die Umgebungsluft, unterschieden werden. Des Weiteren soll in der vorliegenden Arbeit auch der Übergang zwischen den superkritischen und gasförmigen Zuständen berücksichtigt werden. Im Gegensatz zur Beschreibung von Phasentransformationen zwischen Gas und Flüssigkeit, wobei für jede Phase eine eigene Massenbilanz eingeführt wird, genügt hier die Verwendung einer einzelnen beschreibenden Massenbilanz für beide Phasen zusammen, da der Übergang zwischen superkritischem Zustand und Gas (und auch zwischen superkritischem Zustand und Flüssigkeit) kontinuierlich verläuft.

Nach Kenntnis des Autors geht die erste Publikation über Simulationen von Phasentransformationen in porösen Medien auf *Lykov* [112] im Jahr 1974 zurück. Nachfolgend wurden weitere Arbeiten von der Gruppe um *Bénet* [35, 108, 109, 153], von *Hassanizadeh* und *Gray* [75, 81, 125, 126] und von *Bedeaux* [14] zu diesem Thema erstellt. Als Beispiele

zur Anwendung dieser Modelle auf reelle Probleme lassen sich im Hinblick auf Trocknung *Kowalski* [101] und zum Brotbackprozess *Huang et al.* [87] nennen.

Die bereits erwähnten Artikel über Phasentransformationen in porösen Medien betrachten in der Regel die Feststoffmatrix als starr. Sollen die Deformationen des Feststoffs berücksichtigt werden, so bietet es sich an, auf das bewährte Konzept der Theorie Poröser Medien (TPM) zurückzugreifen. Dieser Ansatz stellt eine ideale Grundstruktur zur Beschreibung von Mehrphasen- und Mehrkomponentenkontinua dar. Dies beinhaltet auch die mögliche Einbeziehung verschiedenen Deformationsverhaltens (elastisch, viskoelastisch, elastisch-plastisch) und veränderbarer Poreninhalte von misch- oder nichtmischbaren Fluiden. Die Grundlagen zur TPM werden ausführlich in den Publikationen von *de Boer* [20], *de Boer & Ehlers* [22], *Bowen* [26, 27], der Arbeitsgruppe um *Ehlers* [50, 54–56, 59, 60, 180] oder *Schrefler et al.* [160, 161] dargelegt. Die Zweckmäßigkeit der TPM konnte bereits in vielen Anwendungen aus verschiedensten Bereichen gezeigt werden. So haben *Markert* [115], *Avci* [8] und *Ehlers et al.* [57] die Theorien der Elasto-Plastizität und der Elasto-Viskoplastizität auf Fragestellungen der Materialwissenschaften und der Geomechanik angewendet. Zur Behandlung von Problemen der Biomechanik wurden von *Karajan et al.* [95], *Ricken* und seinen Mitarbeitern [147, 150], sowie *Wagner* [176] den existierenden Modellen chemische, elektrische und biologische Eigenschaften hinzugefügt. Die numerische Simulation biologischer Phasentransformationen in Mülldeponien wurde von der Forschungsgruppe um *Ricken* [151, 152] durchgeführt.

Die Entwicklung einer thermodynamisch konsistenten Beschreibung von Phasentransformationen im Rahmen der TPM beginnt mit den Arbeiten von *de Boer* und Mitarbeitern [19, 21, 23] und setzt sich fort mit den Beiträgen von, z. B. *Kowalski* [101] und *Ghadiani* [71], sowie einem Artikel von *Ehlers & Graf* [59]. Gefrier- und Schmelzprozesse wurden ausführlich, unter anderem, von *Kruschwitz* und *Bluhm* [102] und der Gruppe um *Ricken* und *Bluhm* [17, 148, 149] untersucht. In all diesen Arbeiten wurde die benötigte konstituierende Beziehung für die Beschreibung des Massentransfers zwischen den Fluidphasen durch Auswertung der Entropieungleichung bestimmt. Außerdem handelt es sich bei den betrachteten Phasentransformationen immer um Übergänge zwischen Mischungen, d. h. dass die einzelnen Phasen nicht nur aus einer reinen Fluidsubstanz bestehen, sondern ein Gemisch verschiedener Stoffe, z. B. Wasserdampf und Luft in der Gasphase, darstellen.

Im Rahmen dieser Arbeit soll nun ein Model entwickelt werden, das die Phasentransformation zwischen den reinen Phasen einer einzigen Fluidsubstanz beschreibt. In diesem Zusammenhang stellte sich heraus, dass die Massentransferbeziehung hergeleitet aus der Entropieungleichung für diesen Fall nicht zielführend ist. Darum wird hier nun eine massefreie, glatte singuläre Fläche zur Beschreibung der Phasengrenzfläche zwischen den flüssigen und gasförmigen Phasen eingeführt. Dadurch treten zusätzlich Sprungterme für einzelne Funktionen in den Bilanzgleichungen auf. Durch Auswertung dieser Sprungbedingungen kann dann eine neue konstituierende Bedingung für den Massentransfer gefunden werden. Dieser Ansatz wurde bereits von *Jamet* [89], *Juric & Tryggvason* [92], *Morland et al.* [120, 121], *Tanguy et al.* [170] und *Wang & Oberlack* [177] verfolgt.

Diese Vorgehensweise wird daraufhin in die TPM eingebettet, vgl. *Ehlers and Häberle* [61]. Die resultierende Beziehung für den Massentransfer steht in Abhängigkeit des Verhältnisses der verfügbaren Energie zur latenten Verdampfungswärme. Da die singuläre Fläche auf

der Mikroskala eingeführt wurde, ist auch der Massentransfer auf dieser Skala definiert. Für die Hochskalierung auf die makroskopische Kontinuumsskala wird an dieser Stelle die sogenannte Grenzschichtfläche als spezifische Dichte der Grenzfläche bezüglich des betrachteten Volumens eingeführt. Die Bestimmung der Grenzschichtfläche als Funktion der Sättigung basiert auf den Ergebnissen von *Hassanizadeh* und seinen Mitarbeitern [81, 90, 124, 125], sowie der Dissertation von *Graf* [74]. Die in dieser Arbeit verwendete Anwendung der Grenzschichtfläche besitzt Ähnlichkeiten mit der Veröffentlichung von *Nuske et al.* [130]. Das Prinzip der Grenzschichtfläche wurde auch in den Publikationen von *Miller et al.* [41, 76], der Gruppe um *Celia* [83, 145], sowie von *Gladkikh & Bryant* [72] und *Oostrom et al.* [132] diskutiert.

Um das thermodynamische Verhalten des CO<sub>2</sub> möglichst realistisch modellieren zu können, müssen weitere bestimmende Beziehungen gefunden werden. Zunächst wird das kompressible Verhalten, das heißt die Abhängigkeit zwischen Druck, Temperatur und Dichte, durch eine geeignete Zustandsgleichung beschrieben. Dafür werden die Vor- und Nachteile der Ansätze von *van der Waals*, *Peng* und *Robinson*, sowie *Soave*, *Redlich* und *Kwong* im Hinblick auf ihre Exaktheit und ihre thermodynamische Konsistenz diskutiert. Einen Überblick über verschiedene Zustandsgleichungen verschaffen die Bücher von *Ott* und *Boerio-Goates* [134] sowie von *Poling et al.* [137].

Weitere Konstitutivgleichungen bezeichnen die spezifische Wärme, die Verdampfungsenthalpie, die Scherviskosität und die thermische Leitfähigkeit. Diese Formulierungen sind größtenteils der sehr ergiebigen Literatur zu diesem Thema entnommen, wobei an dieser Stelle nur die hier verwendeten Quellen genannt werden sollen: *Lemmon et al.* [104], *Potter* und *Somerton* [139], *Lewis & Randall* [105], *Pitzer et al.* [135], *Fenghour et al.* [66] und *Vesovic et al.* [175].

Mit den vorliegenden thermodynamischen Eigenschaften ist es dann möglich, ein dreiphasiges Model (Feststoff, Wasser und CO<sub>2</sub>, oder Feststoff, flüssiges CO<sub>2</sub> und gasförmiges CO<sub>2</sub>) zur Beschreibung der CO<sub>2</sub>-Verpressung in tiefe Reservoirs zu erstellen. Wie bereits erwähnt, geschieht dies basierend auf dem kontinuummechanischen Rahmenwerk der TPM. Durch Auswertung der Entropieungleichung werden die restlichen Konstitutivbedingungen bestimmt, nämlich die *Darcy*-Sickerungsgeschwindigkeit, die Kapillardruck-Sättigungsbeziehung und die thermoelastische Beschreibung des Feststoffdeformationsverhaltens der verschiedenen Gesteinsschichten. Dadurch lässt sich letztendlich die CO<sub>2</sub>-Sequestrierung unter Berücksichtigung von Phasentransformation, kompressiblen Fluidphasen und thermisch-elastisch verformbarer Feststoffmatrix in einem vollgekoppelten Verfahren simulieren. Numerische Studien basierend auf diesem Model sollten es ermöglichen, bereits während der Planungsphase die Machbarkeit einer CO<sub>2</sub>-Speicherung abzuwägen und etwaige Sicherheitsrisiken ausschließen zu können.

## Gliederung der Arbeit

Zur Einleitung werden in **Kapitel 1** die Motivation, der Stand der Forschung und die Ziele dieser Arbeit aufgeführt. Daraufhin folgt in **Kapitel 2** eine kurze Zusammenfassung über die Technik des „Carbon-Dioxid Capture and Storage“ (CCS). Es werden die technischen,

ökologischen, ökonomischen und sicherheitsrelevanten Aspekte diskutiert, wobei im Speziellen auf die CO<sub>2</sub>-Speicherung in tief liegenden Aquiferen eingegangen wird. Außerdem wird dargelegt, wie numerische Simulationen helfen können, die während der Speicherung auftretenden Prozesse verstehen und vorhersagen zu können.

Anschließend werden in **Kapitel 3** die theoretischen Grundlagen, die für die Beschreibung eines dreiphasigen porösen Mediums benötigt werden, im Rahmen der Theorie Poröser Medien (TPM) eingeführt. Dies beinhaltet die Kinematik der überlagerten Konstituierenden, die Spannungs- und Dehnungsmaße sowie die Bilanzrelationen, welche sowohl für die einzelnen Konstituierenden als auch für den Gesamtkörper formuliert werden. Zusätzlich wird hier das Prinzip der singulären Flächen vorgestellt, inklusive der daraus entstehenden Änderungen in den Bilanzrelationen. Diese singulären Flächen werden später in der Herleitung der Massentransferrelation für die Phasentransformation wieder benötigt.

Eine detaillierte Erörterung der Thermodynamik von Fluiden folgt in **Kapitel 4**. Dies betrifft vor allem die Beschreibung des Phasenverhaltens. Hierbei werden die Vor- und Nachteile verschiedener Zustandsgleichungen miteinander verglichen, wobei das Augenmerk speziell auf den Bereich der Transformation zwischen den flüssigen und gasförmigen Phasen gerichtet ist. In diesem Kapitel werden außerdem die thermodynamischen Relationen für die spezifische Wärme, die Verdampfungsenthalpie, die Scherviskosität und die thermische Leitfähigkeit präsentiert. Soweit möglich, wird hierbei eine stoffunabhängige Formulierung der einzelnen Funktionen angestrebt.

**Kapitel 5** beinhaltet die Identifikation der benötigten Konstitutivbeziehungen, wobei die jeweiligen Bilanzrelationen an das gegebene Problem angepasst werden. Dazu gehört auch die ausführliche Auswertung der Entropiegleichung als Voraussetzung für eine thermodynamisch konsistente Formulierung der Konstitutivrelationen. Im Weiteren wird hier auch die Beziehung für den Massentransfer hergeleitet, basierend auf der Einführung der singulären Fläche für die Phasengrenzschicht und der Auswertung der daraus resultierenden Sprungbedingungen. In diesem Teil wird zusätzlich die sogenannte Grenzschichtfläche vorgestellt, welche als Abbildungsoperator zwischen der Mikro- und Makroskala fungiert. Das Kapitel endet mit der Aufstellung der maßgeblichen Bilanzrelationen in ihrer starken Form.

Die numerische Realisierung wird in **Kapitel 6** erklärt. Zur näherungsweise Lösung mechanisch dominierter Anfangsrandwertprobleme bietet sich die Finite-Elemente-Methode (FEM) an. Dafür müssen die schwachen Formen der Bilanzrelationen räumlich und zeitlich diskretisiert werden. Als geeigneter numerischer Finite-Elemente-Löser wird das hausinterne Programm PANDAS verwendet, wobei eine monolithische Berechnungsstrategie zum Einsatz kommt.

Mit Hilfe der numerischen Beispiele in **Kapitel 7** sollen die Einsatzmöglichkeiten des entwickelten Modells präsentiert werden. Zunächst wird die CO<sub>2</sub>-Injektion in ein wassergefülltes Reservoir, welches eine geneigte Deckschicht besitzt, simuliert. Hierdurch sollen die Ausbreitung des CO<sub>2</sub> in Folge des Injektionsdrucks und der Auftriebskräfte sowie die Phasenumwandlung von der superkritischen in die gasförmige Phase dargestellt werden. Außerdem werden die Feststoffverformungen auf Grund des Einpressdrucks analysiert. In den beiden anderen numerischen Beispielen wird die Verdampfung und Kondensation von CO<sub>2</sub> ausführlicher betrachtet. Dabei wird vor allem auf das Verhalten des Massentrans-



fers zwischen der flüssigen und der gasförmigen Phase Wert gelegt. Auch hier werden die Feststoffverformungen berücksichtigt.

Schlussendlich wird die Arbeit in **Kapitel 8** zusammengefasst und mögliche Verbesserungen des Modells, sowie weitere interessante Aspekte in einem Ausblick aufgelistet.

Als Ergänzung werden die in dieser Arbeit benötigten mathematischen Relationen der Tensorrechnung im **Anhang A** zusammengefasst. Zusätzliche thermodynamische Gesetzmäßigkeiten und längliche Herleitungen verschiedener Beziehungen werden im **Anhang B** aufgeführt.



# Nomenclature

The notation in this article follows the conventions that are commonly used in modern tensor calculus, such as in the text books of *Ehlers* [51], or *de Boer* [18]. The symbols used in the context of porous-media theories adhere to the established nomenclature given by, e. g., *de Boer* [20] and *Ehlers* [54, 56].

## Conventions

### *Kernel conventions*

---

$(\cdot)$	place holder for arbitrary quantities
$s, t, \dots$ or $\sigma, \tau, \dots$	scalars (0 <sup>th</sup> -order tensors)
$\mathbf{s}, \mathbf{t}, \dots$ or $\boldsymbol{\sigma}, \boldsymbol{\tau}, \dots$	vectors (1 <sup>st</sup> -order tensors)
$\mathbf{S}, \mathbf{T}, \dots$ or $\boldsymbol{\Psi}, \boldsymbol{\Phi}, \dots$	2 <sup>nd</sup> -order tensors

### *Index and suffix conventions*

---

$i, j, m, n, \dots$	indices as super- or subscripts range from 1 to $N$ , where $N = 3$ in the usual 3-d space of our physical experience
$(\cdot)_\alpha$	subscripts indicate kinematical quantities of a constituent within porous-media or mixture theories
$(\cdot)^\alpha$	superscripts indicate the belonging of non-kinematical quantities to a constituent within mixture theories
$(\cdot)^{\beta R}$	effective non-kinematical quantity belonging to a fluid constituent
$\dot{(\cdot)} = d(\cdot)/dt$	material time derivative following the motion of a constituent $\alpha$ with the solid and fluid constituents $\alpha = \{S, L, G\}$
$(\cdot)'_\alpha = d_\alpha(\cdot)/dt$	material time derivative following the motion of a constituent $\alpha$ with the solid and fluid constituents $\alpha = \{S, L, G\}$
$d(\cdot)$	differential operator
$\partial(\cdot)$	partial derivative operator
$(\cdot)_0$	initial value of a non-kinematical quantity
$(\cdot)_{0\alpha}^\alpha$	initial value of a non-kinematical quantity with respect to the referential configuration of a constituent
$(\cdot)^F, (\cdot)_F$	quantities of the fluid constituents
$(\cdot)^T, (\cdot)^{-1}$	transposed and inverse forms of a tensor
$(\cdot)^{\text{sym}}, (\cdot)^{\text{skew}}$	symmetric and skew-symmetric parts of a tensor
$(\cdot)^\Gamma, (\cdot)_\Gamma$	quantities of the interface $\Gamma$

$(\cdot)^+, (\cdot)^-$	quantity belonging to the pore gas ( $\mathcal{B}^+ = \mathcal{B}^G$ ) or pore liquid ( $\mathcal{B}^- = \mathcal{B}^L$ )
$\llbracket (\cdot) \rrbracket$	jump related value of the discontinuity surface $\Gamma$
$(\cdot)_{\text{crit}}$	values at the critical point
$(\cdot)_r$	reduced values, usually with respect to critical values
$(\cdot)^{FM}, (\cdot)_{FM}$	quantities of the fluid matter under consideration
$(\cdot)_m, (\cdot)_\theta$	purely mechanical and purely thermal parts of a quantity associated with thermoelastic solid kinematics
$(\cdot)_E^\alpha$	extra (effective) quantities of a constituent $\varphi^\alpha$
$(\cdot)_{E \text{ dis.}}^\alpha, (\cdot)_{E \text{ mech.}}^\alpha$	dissipative and purely mechanical parts of extra quantities
$(\cdot)$	prescribed quantities (boundary conditions)
$\delta(\cdot)$	test functions of the respective degrees of freedom
$(\cdot)^h$	spatially discretised quantities
$(\cdot)_n, (\cdot)_{n+1}$	discretised quantities in time

## Symbols

### Greek letters

Symbol	Unit	Description
$\alpha$		constituent identifier in super- and subscript, i.e., $\alpha = \{S, L, G\}$
$\alpha^S$	[1/K]	coefficient of thermal expansion of $\varphi^S$
$\beta$		fluid constituent identifier (here: $\beta = \{L, G\}$ )
$\beta'$		fluid constituent identifier complementary to $\beta$ (e.g., $\beta = L$ and $\beta' = G$ )
$\Gamma$		interface between the fluid phases
$\delta_i^j$		<i>Kronecker</i> symbol or <i>Kronecker</i> delta
$\varepsilon, \varepsilon^\alpha$	[J/kg]	mass specific internal energy of $\varphi$ and $\varphi^\alpha$
$\hat{\varepsilon}^\alpha$	[J/m <sup>3</sup> s]	volume specific direct energy production of $\varphi^\alpha$
$\epsilon_{\text{tol}}$	[-]	predefined tolerance used in the <i>Newton</i> solver
$\zeta^\alpha$	[J/kg]	mass specific enthalpy ( <i>Gibbs</i> energy) of $\varphi^\alpha$
$\hat{\zeta}^\alpha$	[J/K m <sup>3</sup> s]	volume specific direct entropy production of $\varphi^\alpha$
$\Delta\zeta_{\text{vap}}$	[J/kg]	mass specific latent heat or enthalpy of evaporation
$\eta, \eta^\alpha$	[J/K kg]	mass specific entropy of $\varphi$ and $\varphi^\alpha$
$\hat{\eta}, \hat{\eta}^\alpha$	[J/K m <sup>3</sup> s]	volume specific total entropy production of $\varphi$ and $\varphi^\alpha$
$\theta, \theta^\alpha$	[K]	absolute temperature of $\varphi$ and $\varphi^\alpha$
$\theta_{\text{eq}}$	[K]	equilibrium temperature

$\theta^{\beta*}$	[K]	reduced temperature in the derivation of the shear viscosity
$\Delta\theta$	[K]	temperature variation
$\Delta\theta_{SF}$	[K]	temperature difference between $\varphi^S$ and $\varphi^F$
$\Delta_g\theta$	[K/km]	geothermal temperature gradient
$\vartheta$	[°]	contact angle of the fluid interface with the solid
$\kappa$	[-]	exponent governing the deformation dependency of $K^S$
$\varkappa, \varkappa^\beta$		overall and partial mass-transfer coefficients of $\varphi^\beta$
$\lambda$	[-]	pore-size distribution index for <i>Brooks &amp; Corey</i> law
$\lambda^S$	[N/m <sup>2</sup> ]	2 <sup>nd</sup> <i>Lamé</i> constant of $\varphi^S$
$\mu^\beta, \Delta\mu^\beta$	[J/mol]	chemical potential of $\varphi^\beta$ and difference in chemical potentials
$\mu^{\beta R}$	[Ns/m <sup>2</sup> ]	effective dynamic fluid viscosity of $\varphi^\beta$
$\mu_0^{\beta R}, \Delta\mu^{\beta R}, \mu_c^{\beta R}$	[Ns/m <sup>2</sup> ]	ideal, excess and critical parts of the effective fluid viscosity of $\varphi^\beta$
$\mu^S$	[N/m <sup>2</sup> ]	1 <sup>st</sup> <i>Lamé</i> constant of $\varphi^S$
$\xi^\beta$	[J/kg]	mass-specific <i>Gibbs</i> free energy (free enthalpy) of $\varphi^\beta$
$\xi_i$		local coordinates of a reference element
$\pi$	[-]	circle constant
$\rho$	[kg/m <sup>3</sup> ]	density of the overall aggregate $\varphi$
$\rho^\alpha, \rho^{\alpha R}$	[kg/m <sup>3</sup> ]	partial and effective (realistic) density of $\varphi^\alpha$
$\rho_F^\beta$	[kg/m <sup>3</sup> ]	partial pore density of the fluid phases $\varphi^\beta$
$\hat{\rho}^\alpha$	[kg/m <sup>3</sup> s]	volume-specific mass production of $\varphi^\alpha$
$\hat{\rho}_\Gamma^\beta$	[kg/m <sup>2</sup> s]	area-specific interfacial mass transfer of $\varphi^\beta$
$\sigma, \sigma^\alpha$		scalar-valued supply terms of mechanical quantities
$\sigma^*$		auxiliary term in the derivation of the shear viscosity
$\sigma_\eta, \sigma_\eta^\alpha$	[J/K m <sup>3</sup> s]	volume specific external entropy supply of $\varphi$ and $\varphi^\alpha$
$\sigma_s$	[N/m]	surface tension of the fluid-fluid interface
$\tau^*$		auxiliary term in the derivation of the thermal conductivity
$\Upsilon$		arbitrary field function (steady and steady differentiable)
$\varphi, \varphi^\alpha$		entire aggregate model and particular constituent $\alpha$
$\phi_u^j$		global basis function of a degree of freedom
$\psi, \psi^\alpha$	[J/kg]	mass-specific <i>Helmholtz</i> free energy of $\varphi^\alpha$
$\Psi, \Psi^\alpha$	[·/m <sup>3</sup> ]	volume-specific densities of scalar mechanical quantities
$\hat{\Psi}, \hat{\Psi}^\alpha$	[·/m <sup>3</sup> ]	volume-specific productions of scalar mechanical quantities
$\omega^\beta$	[-]	acentric factor
$\Omega, \partial\Omega$		spatial domain and boundary of the aggregate body $\mathcal{B}$
$\partial\Omega_B, \partial\Omega_u$		domain boundary and domain boundary of a primary variable
$\partial\Omega_D^u$		<i>Dirichlet</i> boundary with essential boundary conditions for $\mathbf{u}$
$\partial\Omega_N^{(\cdot)}$		<i>Neumann</i> boundary with natural boundary conditions

$\Omega_e, \Omega^h$		a finite element and the discretised finite element domain
$\Omega_e^\xi$		reference finite element described in local coordinates
$\xi$		local coordinates of a reference element
$\sigma, \sigma^\alpha$		vector-valued supply terms of mechanical quantities
$\Upsilon$		arbitrary field function (steady and steady differentiable)
$\phi, \phi^\alpha$		general vector-valued mechanical quantities
$\phi_\eta, \phi_\eta^\alpha$	[J/K m <sup>3</sup> s]	entropy efflux vector of $\varphi$ and $\varphi^\alpha$
$\phi_u^j$		global basis function of a degree of freedom
$\chi_\alpha, \chi_\alpha^{-1}$		motion and inverse motion function of the constituents $\varphi^\alpha$
$\Psi, \Psi^\alpha$	[./m <sup>3</sup> ]	volume-specific densities of vectorial mechanical quantities
$\hat{\Psi}, \hat{\Psi}^\alpha$	[./m <sup>3</sup> ]	volume-specific productions of vectorial mechanical quantities
$\varepsilon_S$	[-]	linearised contravariant <i>Green-Lagrangean</i> solid strain tensor
$\sigma^S$	[N/m <sup>2</sup> ]	linearised 2 <sup>nd</sup> <i>Piola-Kirchhoff</i> stress tensor of $\varphi^S$
$\tau^\alpha$	[N/m <sup>2</sup> ]	<i>Kirchhoff</i> stress tensor of $\varphi^\alpha$
$\Phi, \Phi^\alpha$		general tensor-valued mechanical quantities

## Latin letters

Symbol	Unit	Description
$a$	[m <sup>5</sup> /kg s <sup>2</sup> ]	cohesion pressure, coefficient in the cubic EOS
$a_\Gamma$	[1/m]	interfacial area, surface density of the interface
$a_{SF}$	[1/m]	interfacial area between the solid and the fluid in a two-phasic medium
$a_{\Delta\zeta}, b_{\Delta\zeta},$ $c_{\Delta\zeta}, d_{\Delta\zeta}$		fitting parameters for the vaporisation enthalpy
$a_i, b_i, c_i, d_i,$ $d_{ij}$		coefficients for the calculation of the shear viscosity and thermal conductivity
$da$	[m <sup>2</sup> ]	current area element
$da_{\Gamma REV}$	[m <sup>2</sup> ]	current area element of the interface $\Gamma$ specific in the REV
$A_c, B_c, C_c,$ $D_c, Q_c, R_c,$ $S_c, T_c$		auxiliary terms for the solution of a cubic equation
$A_A, B_A, C_A$		empirical parameters of the <i>Antoine</i> equation
$A^{GL}, A_\Gamma$	[m <sup>2</sup> ]	gas-liquid contact area in the volume-equivalent sphere, where $A^{GL} = A_\Gamma$
$A^{SG}, A^{SL}$	[m <sup>2</sup> ]	solid-gas and solid-liquid contact areas of the volume-equivalent sphere
$A^\varepsilon, B^\varepsilon$		auxiliary terms in the evaluation of the temperature assimilation

$dA_\alpha$	[m <sup>2</sup> ]	reference area element of $\varphi^\alpha$
$b$	[m <sup>3</sup> /kg]	co-volume, coefficient in the cubic EOS
$B_v, C_v, D_v$		virial coefficients of the virial EOS explicit in specific volume
$B_p, C_p, D_p$		virial coefficients of the virial EOS explicit in pressure
$c$	[-]	temperature-dependent correction factor in the cubic EOS
$c_V^{\alpha R}$	[J/kg K]	specific heat capacities for constant volume of $\varphi^\alpha$
$c_{\text{int}}$	[-]	auxiliary term in the derivation of the thermal conductivity
$d$		spatial dimension of the physical problem
$d_{10}, d_{50}$	[m]	diameter of granular soil represented by 10% of the mass and medial grain diameter
$D_{\text{mass}}$	[kg/m s]	local mass-transfer coefficient of $\varphi$
$D_{\text{mass}}^\beta$	[kg/m s]	local mass-transfer coefficient of $\varphi^\beta$
$e$	[-]	<i>Euler's</i> number, mathematical constant
$\hat{e}^\alpha$	[J/m <sup>3</sup> s]	volume specific total energy production of $\varphi^\alpha$
$E$		number of non-overlapping finite elements $\Omega_e$
$E^*$		finite elements attached to a respective node $P^j$
$f$		function identifier or integration constant
$g$	[m/s <sup>2</sup> ]	scalar value of the gravitational force vector
$g, h$		integration constants
$h_d$	[m]	macroscopic entry-pressure head
$h^\beta$	[m]	filling height of volume-equivalent sphere of $\varphi^\beta$
$H^{\alpha R}$	[W/K m]	effective isotropic thermal conductivity of $\varphi^\alpha$
$H_0^{\beta R}, H_c^{\beta R}, \Delta H^{\beta R}$	[W/K m]	ideal, critical and excess parts of the effective thermal conductivity of $\varphi^\beta$
$J_\alpha, \bar{J}$	[-]	<i>Jacobian</i> determinant of $\varphi^\alpha$ and of a reference element $\Omega_e^\xi$
$k^S$	[N/m <sup>2</sup> ]	solid compression modulus
$k_r^\beta$	[-]	relative permeability factor of $\varphi^\beta$
$k_{SF}^\varepsilon$	[W/m <sup>2</sup> K]	surface-specific heat-exchange coefficient
$K_G$		integration points for the <i>Gaußian</i> quadrature scheme
$K^S$	[m <sup>2</sup> ]	isotropic (deformation-dependent) permeability of $\varphi^S$
$m^\alpha$	[kg]	mass of $\varphi^\alpha$
$m_\theta^S$	[N/K m <sup>2</sup> ]	stress-temperature modulus
$dm^\alpha$	[kg]	local mass element of $\varphi^\alpha$
$M^\beta$	[kg/mol]	molar mass of $\varphi^\beta$
$n^\alpha$	[-]	volume fraction of $\varphi^\alpha$
$n^F$	[-]	porosity, total fluid volume fraction
$n_m^\beta$	[-]	number of moles of $\varphi^\beta$
$N, N_e$		number of nodal points for $\Omega^h$ and $\Omega_e$

$p^{\beta R}, p_{\text{vap}}^R$	[N/m <sub>2</sub> ]	effective pore pressure of $\varphi^\beta$ and vapour pressure
$p^c, p_d, p^{FR}$	[N/m <sub>2</sub> ]	capillary pressure, bubbling or entry pressure and overall pore pressure
$p_0$	[N/m <sub>2</sub> ]	standard atmospheric pressure
$P^j$		nodal point in a finite element $\Omega_e$ of the set $\mathcal{N}$
$\bar{q}$	[J/m <sup>2</sup> s]	heat efflux over the boundary
$r, r^\alpha$	[J/kg s]	mass-specific external heat supply of $\varphi$ and $\varphi^\alpha$
$\tilde{r}$	[m]	radius of an idealised pore
$\tilde{r}^F$	[m]	radius of the volume-equivalent sphere representing a pore
$\tilde{r}^S$	[m]	radius of a characteristic spherical solid particle
$r_H$	[-]	coefficient in the derivation of the thermal conductivity
$R$	[J/mol K]	universal gas constant
$R^\alpha$	[J/kg K]	specific gas constant of $\varphi^\alpha$
$R^2$	[-]	error measure
$s^\beta, s_{\text{res}}^\beta$	[-]	saturation and residual saturation of $\varphi^\beta$
$s_{\text{eff}}^L$	[-]	effective liquid saturation
$t$	[s]	time
$u$		adjustment parameter for vdW-EOS
$u_{S2}$	[m]	vertical part of the displacement vector
$\bar{v}^F, \bar{v}^L$	[kg/m <sup>2</sup> ]	volumetric effluxes for $\varphi^F$ and for $\varphi^L$ over the boundary
$v^{\beta R}$	[m <sup>3</sup> /kg]	specific volume of $\varphi^\beta$
$\Delta v$	[m <sup>3</sup> /kg]	difference of specific volumes
$dv, dv^\alpha$	[m <sup>3</sup> ]	current volume element of $\varphi$ and $\varphi^\alpha$
$dv_\xi$	[m <sup>3</sup> ]	current volume element of the reference element $\Omega_e^\xi$
$V, V^\alpha$	[m <sup>3</sup> ]	overall volume of $\mathcal{B}$ and partial volume of $\mathcal{B}^\alpha$
$V^{\beta R}$	[m <sup>3</sup> ]	effective volume of $\varphi^\beta$
$dV_\alpha$	[m <sup>3</sup> ]	reference volume element of $\varphi^\alpha$
$w$		adjustment parameter for vdW-EOS
$w_k$	[-]	weight for the <i>Gaußian</i> quadrature scheme
$x_i$		global coordinates
$\Delta x^\beta$	[m]	film thickness
$y$		constant part of a differential equation
$Z, Z^\beta$	[-]	general compressibility factor and compressibility factor of $\varphi^\beta$
$da$	[m <sup>2</sup> ]	oriented current area element
$dA_\alpha$	[m <sup>2</sup> ]	oriented reference area element of $\varphi^\alpha$
$\mathbf{b}, \mathbf{b}^\alpha$	[m/s <sup>2</sup> ]	mass specific body force vector
$\mathbf{d}_\alpha$	[m/s]	diffusion velocity vector of $\varphi^\alpha$
$\mathbf{f}^\alpha$	[N]	volume force vector acting on $\mathcal{B}$ from a distance



$\mathbf{g}$	[m/s <sup>2</sup> ]	constant gravitation vector with $ \mathbf{g}  = g = 9.81 \text{ m/s}^2$
$\hat{\mathbf{h}}^\alpha$	[N/m <sup>2</sup> ]	volume-specific total angular momentum production of $\varphi^\alpha$
$\mathbf{j}, \mathbf{j}^\beta, \mathbf{j}^{\beta'}$	[kg/m <sup>2</sup> s]	total mass flux and local mass fluxes due to phase transition
$\mathbf{k}^\alpha, \mathbf{k}_{\mathcal{F}}^\alpha, \mathbf{k}_{\mathcal{N}}^\alpha$	[N]	total, external and contact force elements of $\varphi^\alpha$
$\mathbf{m}$	[-]	reference outward-oriented unit-surface normal vector
$\hat{\mathbf{m}}^\alpha$	[N/m <sup>2</sup> ]	volume-specific direct angular momentum production of $\varphi^\alpha$
$\mathbf{n}$	[-]	current outward-oriented unit-surface normal vector
$\hat{\mathbf{p}}^\alpha$	[N/m <sup>3</sup> ]	volume-specific direct momentum production of $\varphi^\alpha$
$\mathbf{q}, \mathbf{q}^\alpha$	[J/m <sup>2</sup> s]	total heat influx vector and heat influx vector of $\varphi^\alpha$
$\hat{\mathbf{s}}^\alpha$	[N/m <sup>3</sup> ]	volume-specific total momentum production of $\varphi^\alpha$
$\bar{\mathbf{t}}$	[N/m <sup>2</sup> ]	external load vector acting on the boundary
$\mathbf{t}^\alpha$	[N/m <sup>2</sup> ]	contact force vector per surface acting on $\mathcal{S}$
$\mathbf{u}_S$	[m]	solid displacement vector
$\mathbf{v}_\alpha$	[m/s]	velocity vector of $\varphi^\alpha$ , $\mathbf{v}_\alpha = \dot{\mathbf{x}}_\alpha$
$\mathbf{w}_\beta$	[m/s]	fluid seepage velocity vector of $\varphi^\beta$
$\mathbf{w}_{\beta\Gamma}$	[m/s]	relative velocity vector of the fluid phases $\varphi^\beta$ with respect to $\Gamma$
$\mathbf{x}$	[m]	current position vector of $\varphi$
$\dot{\mathbf{x}}, \dot{\mathbf{x}}_\alpha$	[m/s]	velocity vector of the aggregate $\varphi$ and the constituent $\varphi^\alpha$
$\ddot{\mathbf{x}}, \ddot{\mathbf{x}}_\alpha$	[m/s <sup>2</sup> ]	acceleration vector of the aggregate $\varphi$ and the constituent $\varphi^\alpha$
$d\mathbf{x}$	[m]	current line element
$\mathbf{X}_\alpha$	[m]	reference position vector at time $t_0$
$d\mathbf{X}_S$	[m]	reference line element of the solid
$\mathbf{A}_\alpha$	[-]	contravariant <i>Almansi</i> strain tensor of $\varphi^\alpha$
$\mathbf{B}_\alpha$	[-]	covariant left <i>Cauchy-Green</i> deformation tensor of $\varphi^\alpha$
$\mathbf{C}_\alpha$	[-]	contravariant right <i>Cauchy-Green</i> deformation tensor of $\varphi^\alpha$
$\mathbf{D}_\alpha$	[·/s]	symmetric deformation velocity tensor of $\varphi^\alpha$
$\mathbf{E}_\alpha$	[-]	contravariant <i>Green-Lagrangean</i> strain tensor of $\varphi^\alpha$
$\mathbf{F}_\alpha$	[-]	material deformation gradient of $\varphi^\alpha$
$\mathbf{H}^\alpha, \mathbf{H}^{\alpha R}$	[W/K m]	partial and effective heat-conduction tensors of $\varphi^\alpha$
$\mathbf{H}_S$	[-]	solid displacement gradient
$\mathbf{I}$	[-]	identity tensor (2 <sup>nd</sup> -order fundamental tensor)
$\mathbf{K}^\beta$	[m/s]	tensor of hydraulic conductivity of $\varphi^\beta$
$\mathbf{K}_r^\beta$	[m/s]	tensor of relative permeability of $\varphi^\beta$
$\mathbf{K}^S$	[m <sup>2</sup> ]	intrinsic (deformation-dependent) permeability tensor of $\varphi^S$
$\mathbf{L}_\alpha$	[·/s]	spatial velocity gradients of $\varphi^\alpha$

$\mathbf{P}^\alpha$	$[\text{N}/\text{m}^2]$	1 <sup>st</sup> <i>Piola-Kirchhoff</i> stress tensor of $\varphi^\alpha$
$\mathbf{S}^\alpha$	$[\text{N}/\text{m}^2]$	2 <sup>nd</sup> <i>Piola-Kirchhoff</i> stress tensor of $\varphi^\alpha$
$\mathbf{S}_f^\beta$	$[\text{N s}/\text{m}^4]$	second-order friction tensor of $\varphi^\beta$
$\mathbf{T}, \mathbf{T}^\alpha$	$[\text{N}/\text{m}^2]$	overall and partial <i>Cauchy</i> (true) stress tensors of $\varphi$ and $\varphi^\alpha$
$\mathbf{W}_\alpha$	$[\cdot/\text{s}]$	skew-symmetric spin tensor of $\varphi^\alpha$

### Calligraphic letters

Symbol	Unit	Description
$\mathcal{A}^u$		ansatz (trial) functions of the primary variables
$\mathcal{B}, \mathcal{B}^\alpha$		aggregate body and partial constituent body
$\mathcal{C}$		critical point in the phase-diagram
$\mathcal{D}$		dissipative part in the entropy inequality
$\mathcal{G}_u$		weak formulation of a governing equation related to a DOF
$\mathcal{H}^1(\Omega)$		<i>Sobolev</i> space
$\mathcal{N}$		set of all nodes for the FE discretisation
$\mathcal{O}$		origin of a coordinate system
$\mathcal{P}$	$[\text{N}/\text{m}_2]$	<i>Lagrangean</i> multiplier
$\mathcal{P}, \mathcal{P}^\alpha$		material points of $\varphi$ and $\varphi^\alpha$
$\mathcal{R}$		set of response functions
$\mathcal{S}, \mathcal{S}^\alpha$		surface of the aggregate and constituent body
$\mathcal{T}$		triple point in the phase-diagram
$\mathcal{T}^u$		test (weighting) functions of the primary variables
$\mathcal{V}$		set of independent process variables
$\mathcal{V}^1$		subset of independent process variables
$\mathbf{f}$		generalised vector of external forces
$\mathcal{F}$		vector containing the global and local system of equations
$\text{D}\mathcal{F}_{n+1}^k$		global residual tangent
$\mathcal{G}_u$		abstract vector containing the weak formulations
$\mathbf{k}$		generalised stiffness vector
$\mathbf{M}$		generalised mass matrix
$\mathbf{u}, \mathbf{u}_1, \mathbf{u}_2$		abstract vectors containing the set of the primary variables
$\mathbf{y}$		abstract vector containing all nodal DOF

### Selected acronyms

Symbol	Description
--------	-------------

---

2-d	two-dimensional
3-d	three-dimensional
BC	boundary condition
$\text{Ca}^{2+}$	calcium ion
$\text{CaCO}_3$	calcium carbonate
CCS	carbon-dioxide capture and storage
$\text{CH}_4$	methane
$\text{CO}_2$	carbon dioxide
$\text{CO}_3^{2-}$	carbonate
CSP	corresponding state principle
DOF	degree of freedom
EOR	enhanced oil recovery
EOS	equation of state
FDM	finite-difference method
FEM	finite-element method
FVM	finite-volume method
GG	greenhouse gases
$\text{HCO}_3^-$	hydrogen carbonate
$\text{H}_2\text{O}$	water
$\text{H}_3\text{O}^+$	hydronium, aqueous cation
IBVP	initial boundary value problem
IPCC	Intergovernmental Panel on Climate Change
LG	coexisting liquid-gas region
NIST	National Institute of Standards and Technology
$\text{N}_2\text{O}$	nitrous oxide
$\text{O}_3$	ozone
PANDAS	porous media adaptive nonlinear finite element solver based on differential algebraic systems
PDE	partial differential equation
PR-EOS	<i>Peng-Robinson</i> equation of state
REV	representative elementary volume
SC	supercritical region
SG	coexisting solid-gas region
SRK-EOS	<i>Soave-Redlich-Kwong</i> equation of state
TPM	Theory of Porous Media
vdW-EOS	<i>van-der-Waals</i> equation of state
XFEM	extended finite-element method



# Chapter 1: Introduction

## 1.1 Motivation

It is a widely accepted fact that anthropogenically emitted *greenhouse gases* (GG) contribute to the global warming. In turn, this might cause rising sea-levels that threaten low lying residential areas, and initiate more severe weather conditions (e. g., hurricanes, floods, tornadoes), droughts and other issues. For these reasons, it is necessary to stop or reduce the global warming by cutting the emissions of GG. In this context, carbon dioxide,  $\text{CO}_2$ , is one of the most important GG since it is emitted in high amounts by human activities, e. g., in energy production by fossil-fuel power plants. As a countermeasure, *carbon-dioxide capture and storage* (CCS) was invented to reduce  $\text{CO}_2$  emissions into the atmosphere. At the end of the 20<sup>th</sup> century, the latter was deemed to help mitigate the problem of global warming and, thus, entailed the initiation of a new field of research, where scientists and engineers from various fields collaborated in solving open questions of CCS. Nowadays, the promising character of CCS has somewhat reduced, which is, on the one hand, due to public resistance caused by the fear of leakage of  $\text{CO}_2$  and, on the other hand, due to the missing economical pressure caused by the ineffectiveness of the  $\text{CO}_2$  certificates that should put a price on  $\text{CO}_2$  emissions, but are too cheap and too numerous. However, by concentrating CCS to offshore projects and uninhabited onshore regions, by improving the communication with the public and by adjusting the concept of the  $\text{CO}_2$  certificates, CCS can still be regarded as a promising technique that bridges the gap until alternative renewable sources can fully replace fossil fuels by reducing the exhaust of greenhouse gases.

The  $\text{CO}_2$  emissions are mainly caused by the combustion of fossil fuels for energy production, for transportation and in industrial processes. Thereof, especially point-like sources such as power plants are suitable for the segregation of the emitted  $\text{CO}_2$  from the exhaust air. This  $\text{CO}_2$  can then be stored, for example, in deep underground reservoirs. Suitable geological formations for this purpose are depleted oil or gas fields, coal beds or deep saline aquifers. All of these storage methods have advantages and disadvantages concerning different factors, for instance, enhanced recovery of oil or gas, accessibility of the storage site, storage volume, and the safety of the reservoir. The latter is only guaranteed if leakage of  $\text{CO}_2$  can be excluded. This is considered fulfilled, if the reservoir is sealed by an almost impermeable cap-rock layer, to prevent the  $\text{CO}_2$  from upwards migration. However, due to the increasing pressure in the reservoir during injection or due to seismic movements, it could still be possible that crack development in the cap-rock layer is initiated and leakage occurs. In order to predict such events beforehand, numerical simulations can provide means to model the injection process including the accompanying thermodynamical changes of the  $\text{CO}_2$  and the deformations of surrounding rock matrix. Hence, this poses the objective of this monograph. The physical, chemical and thermodynamical processes during  $\text{CO}_2$  injection are highly complex and, therefore, in the scope of ongoing research. Since it is not possible at the moment to reproduce the whole set of

processes in a realistic manner in one single numerical model, the investigations in this monograph will be concentrated on the mechanical behaviour of the geological formation and the phase transition of the injected CO<sub>2</sub>.

## 1.2 Scope, aims and state of the art

The whole process of CCS incorporates a great variety of technically challenging steps, which can be separated into the chemical segregation of the CO<sub>2</sub> from the exhaust air, the liquefaction and transport to the storage site and the sequestration of the CO<sub>2</sub>. Here, only the last part is discussed further. In this context, the geological storage of the CO<sub>2</sub> in underground reservoirs is regarded as the most effective storage method apart from deep ocean storage, mineral carbonation, or industrial usage, cf. Special Report on CCS by the Intergovernmental Panel on Climate Change, *Metz et al.* [119].

Existing geological CO<sub>2</sub> storage projects that can confirm the feasibility of underground storage on an industrial scale, i. e., at least 1 MtCO<sub>2</sub>/a, are, for example, the sequestration at the Sleipner gas field in the North Sea, the Weyburn project in Canada and the In Salah project in Algeria. However, as for the first CO<sub>2</sub>-injection process in the early 1970s, also in present CCS projects the CO<sub>2</sub> is mainly used for enhanced oil recovery (EOR). In this regard, the usage of the CO<sub>2</sub> lessens of course the costs for CCS, but does not really improve the greenhouse-gas problem, since the additionally produced oil or gas will also be used mainly for energy production. Thus, only the injection into depleted oil or gas fields and into saline aquifers can be considered as ecologically worthwhile, whereas in this contribution, the latter technique shall be examined further. Deep saline aquifers are distributed world-wide and supposed to provide enough storage space for the aspired amount of CO<sub>2</sub> to reduce global warming, cf. *Metz et al.* [119].

The knowledge of the movement and behaviour of the CO<sub>2</sub> during and after injection is essential for the storage-capacity estimation and to assess safety issues. Since in situ monitoring techniques, e. g. borehole measurements and seismic surveys, do not provide sufficient information of the complex mechanisms acting between the injected CO<sub>2</sub> and the solid matrix, numerical studies are of paramount importance for a detailed understanding of the involved physical processes. The literature contains a vast amount of contributions on the numerical simulation of underground CO<sub>2</sub> storage. This science has been developed from the knowledge in predicting and simulating hydrocarbon production and early works can be found by *Pruess & García* and co-workers [46, 141, 144], as well as *Bielinski* [15] and references therein. Different aspects for an efficient simulation have been investigated, for example, concerning analytical or semi-analytical models by *Kang et al.* [93], *Nordbotten et al.* [129], *Celia et al.* [34], or regarding vertical-equilibrium models by cf. *Court et al.* [40] and *Gasda et al.* [70]. *Nordbotten* and *Celia* [34, 127, 128, 143] have provided several publications on large-scale simulations, including predictions of potential leakage amounts for policy makers. Moreover, *Bradshaw et al.* [28] and *Kopp et al.* [99] estimated the storage capacities of various possible reservoirs. Specific physical questions concerning, e. g., relative permeability, temperature-dependent capillary pressure, mineralisation, enhanced trapping mechanism, or geomechanics, have been studied by *Juanes*

*et al.* [91], *Plug & Bruining* [136], *Kumar et al.* [103], *Ebigbo* [47], and *Rutqvist* [154–156]. Benchmark studies and code comparisons can be found, for instance, by *Pruess et al.* [142] and *Class et al.* [37]. However, the phase transition of the CO<sub>2</sub> has not gained much of interest in these contributions. When the phase transition was considered in these models, usually look-up tables were utilised for the thermodynamics properties. The drawback of these tables is the negligence of an explicit description of the mass transfer between the fluid phases.

Transitions between gas, liquid and solid phases are important physical processes that appear everywhere in the environment. These processes, as for example drying or freezing, do not only occur in well investigated “open systems”, but also in porous media, such as CO<sub>2</sub> reservoirs. However, the mechanism of phase transitions in porous media has been only scarcely investigated so far. Apart from CO<sub>2</sub> sequestration, this kind of processes are also important in other geological activities (e.g., steam injection for enhanced oil recovery, soil remediation, geothermal-energy production), in food industries (drying and baking processes), and in many more. In this work, the consideration is restricted to first-order phase transitions, i.e., “gas-into-liquid” or “liquid-into-gas”, of a single substance, e.g., CO<sub>2</sub>. These specific phase transitions must be clearly distinguished from phase transitions between mixtures of various substances, such as water evaporating into air, since the thermodynamics are rather different. A detailed explanation of these differences will be provided in this work. Furthermore, the phase change between the supercritical and the gaseous state is regarded. This phase change is modelled using a single mass-balance relation for both fluid phases, which is in contrast to gas-liquid phase transitions, where for each phase a distinct mass balance is applied. This is possible, since the transition between supercritical and gas (and also supercritical and liquid) is continuous.

To the authors’ knowledge, the earliest work on the treatment of phase transitions in a porous aggregate goes back to *Lykov* [112] in 1974. Further articles in this direction have been presented by the group around *Bénet* [35, 108, 109, 153], by *Hassanizadeh* and *Gray* [75, 81, 125, 126] or by *Bedeaux* [14]. Examples of applying these models to actual physical problems are the simulation of drying processes by *Kowalski* [101] or the numerical investigation of bread-baking by *Huang et al.* [87].

The previously mentioned articles consider phase-transition processes in porous media, where the solid matrix is usually idealised as a rigid body. If solid deformations shall be included into the model, it is helpful to proceed from the well-founded concept of the Theory of Porous Media (TPM). This approach provides an ideal framework for the modelling of multiphase and multicomponent continua including arbitrary solid deformations based on elasticity, viscoelasticity or elasto-plasticity, as well as an arbitrary pore content of either miscible or immiscible fluids. The reader who is interested in the basics of the TPM is referred to, e.g., the publications of *de Boer* [20], *de Boer & Ehlers* [22], *Bowen* [26, 27], *Ehlers* and coworkers [50, 54–56, 59, 60, 180] or *Schrefler et al.* [160, 161]. The TPM has proven its usefulness in various applications of different fields. With focus on the exact description of the solid deformations, the theories of elasto-plasticity or elasto-viscoplasticity have been applied to topics of material sciences or of geomechanics, e.g., *Markert* [115], *Avci* [8], *Ehlers et al.* [57]. Concerning biomechanical questions, chemical, electrical and biological properties were added to the portfolio by *Karajan et al.*

[95], *Ricken* and coworkers [147, 150] and *Wagner* [176], to name a few. The problem of biological phase transitions within landfills has also been tackled by the research group among *Ricken* [151, 152].

The development of a thermodynamically consistent description of phase-transition processes in porous media based on the TPM starts with contributions by *de Boer* and coworkers [19, 21, 23] and continues with the works of, e. g., *Kowalski* [101] and *Ghadiani* [71], and an article by *Ehlers & Graf* [59]. Extensive investigations of freezing and melting processes have been conducted, for instance, by *Kruschwitz* and *Bluhm* [102] and the group around *Bluhm* and *Ricken* [17, 148, 149]. In all of these works, the constitutive relation for the mass transfer between the two fluid phases was derived from the exploitation of the entropy inequality. Moreover, the phase transition takes place between mixtures of different fluid matters.

Here, it is intended to model the phase transition between pure phases of the same fluid substance. It appears that the constitutive mass-transfer relation derived from the entropy inequality for the phase transition between mixtures is not valid in this case. Instead, an immaterial, smooth singular surface is introduced at the interface that separates the liquid phase from the gas phase. The introduction of this singular surface in turn involves the definition of jump conditions for the respective functions and balance relations. By exploitation of these jump conditions, it is possible to find a constitutive relation for the mass transfer. This approach has been already applied by different groups, for example, *Jamet* [89], *Juric & Tryggvason* [92], *Morland et al.* [120, 121], *Tanguy et al.* [170] and *Wang & Oberlack* [177].

In this monograph, the jump conditions evolving at the interface between the two fluid phases are evaluated within the framework of the TPM, cf. *Ehlers* and *Häberle* [61]. The resulting relation defines the mass transfer as a function of the ration between the energy provided for the phase transition and the latent heat of evaporation. Since the singular surface and therewith also the mass transfer are formulated on the microscale, it is necessary to find a suitable upscaling relation that relates the mass transfer on the microscale to the mass production on the continuum macroscale. In this regard, the interfacial area, i. e., the specific density of the internal phase-transition surface with respect to the considered volume, is introduced as a mapping function. The derivation of this interfacial area is based on the achievements by *Hassanizadeh* and coworkers [81, 90, 124, 125], as well as on the dissertation of *Graf* [74] and bears similarity in its usage with the work of *Nuske et al.* [130]. The principle of interfacial areas is also subject of the contributions by *Miller* and coworkers [41, 76], *Celia* and coworkers [83, 145], *Gladkikh & Bryant* [72] and *Oostrom et al.* [132], amongst others.

For a preferably realistic representation of the thermodynamic behaviour of the CO<sub>2</sub> further constitutive relations must be added to the model. Hereby, the compressibility of the CO<sub>2</sub> is governed by a suitable equation of state (EOS) that represents the relationship between pressure, temperature and density. In this context, different relations from *van der Waals*, from *Peng* and *Robinson*, as well as from *Soave*, *Redlich* and *Kwong* are discussed with regard to their accuracy in describing the phase behaviour and with respect to the thermodynamical consistency for implementation into the TPM framework. An extensive survey of the various EOS is provided, for instance, in the books of *Ott* and



*Boerio-Goates* [134] and *Poling et al.* [137].

Furthermore, constitutive relations for the specific heat, the vaporisation enthalpy, the shear viscosity and the thermal conductivity are defined, which resort to different contributions, wherein the determination of the respective relations are based on collected data and various extents of empiricism. Due to the large number of publications in this field of research only these that have been used in this monograph shall be mentioned here: *Lemmon et al.* [104], *Potter and Somerton* [139], *Lewis & Randall* [105], *Pitzer et al.* [135], *Fenghour et al.* [66] and *Vesovic et al.* [175].

With these thermodynamical properties at hand, a triphasic model (solid, water and CO<sub>2</sub>, or solid, liquid CO<sub>2</sub> and gaseous CO<sub>2</sub>) for the description of CO<sub>2</sub> injection into a deep reservoir is formulated in the continuum-mechanical framework of the TPM. In this regard, further constitutive relations apart from the thermodynamical ones must be obtained from the evaluation of the entropy inequality. In particular, these are a *Darcy*-like relation for the seepage velocity linked to the creeping flow, the capillary-pressure-saturation relation for the interaction between the constituents due to frictional forces, and the thermoelastic formulation for the deformation behaviour of the porous reservoir rock and the impermeable cap rock. Thus, the model is able to simulate CO<sub>2</sub> injection into a deep reservoir, while considering in detail the phase-transition process, the compressibility of the involved fluid phases and the thermoelasticity of the solid rock matrix in a fully coupled way. Consequently, a tool is provided that allows to conduct numerical studies of CO<sub>2</sub> storage in advance of the actual injection in order to provide decision support in view of the safety issues and feasibility of a contemplated reservoir.

### 1.3 Outline of this thesis

The introductory **Chapter 1** is followed by a brief overview of the specifics of carbon-dioxide capture and storage (CCS) in **Chapter 2**. Therein, the technical, environmental, economical and safety aspects are discussed, where special attention is turned on the storage of CO<sub>2</sub> in deep underground aquifers. Furthermore, it is pointed out how numerical simulations can help in understanding the processes in the reservoir.

Subsequently, in **Chapter 3**, the theoretical fundamentals needed for the description of a triphasic porous medium within the Theory of Porous Media (TPM) are explained. This includes the kinematics of superimposed constituents, the strain and stress measures, as well as the balance relations, both for the particular constituents and the overall aggregate. Additionally, singular surfaces are introduced here together with the changes imposed on the balance relations. These singular surfaces are a precondition for the later description of the phase-transition process, which occurs across the gas-liquid interface.

A detailed discussion of the thermodynamics of fluids follows in **Chapter 4**. This concerns especially the description of the phase behaviour, where the advantages and disadvantages of different equations of state (EOS) are pondered. In this context, the specifics of the phase-transition process between the liquid and gaseous phases are of most interest. Moreover, the thermodynamics and the thereon based descriptive relations for the specific heat, the vaporisation enthalpy, the shear viscosity and the thermal conductivity

are presented in this chapter. As far as possible, a general formulation is sought that is independent of the specific fluid substance.

In **Chapter 5**, the required constitutive setting is identified from adapting the respective balance relations, i. e., the mass, momentum and energy balances for the solid material, for the fluid phases and for the overall aggregate, to the problem at hand. In this regard, a sophisticated evaluation of the entropy inequality is conducted to derive the constitutive relations in a thermodynamically consistent manner. Additionally, this chapter comprehends the thorough derivation of the mass-transfer term, which is developed by introducing a separating interface between the two fluid phases gas and liquid and by evaluating the jump conditions at this singularity. This latter part also involves the introduction of the so-called interfacial area as a mapping operator between the micro- and continuum-scale. Furthermore, a switching criterion for the mass transition is formulated. The chapter ends with the presentation of the final strong forms of the governing balance relations.

The numerical realisation is explained in **Chapter 6**. It is customary to solve mechanical dominated initial boundary value problems (IBVP) approximately with the finite-element method (FEM). In this connection, the weak formulations of the governing balance relations are spatially and temporally discretised. As a suitable finite-element tool, the in-house code PANDAS<sup>1</sup> is chosen, wherein an monolithic solution strategy is embedded.

By the numerical examples in **Chapter 7**, the capabilities of the derived model are illustrated. At first, the model is applied to simulate the injection of CO<sub>2</sub> into a water-filled reservoir with an inclined cap-rock layer. Hereby, it is intended to show the migration of the CO<sub>2</sub> due to the injection pressure and buoyancy forces and the phase change from the supercritical phase to the gaseous phase. Furthermore, the solid displacement in consequence of the injection pressure is observed. In the other two examples, the evaporation and condensation processes between liquid and gaseous CO<sub>2</sub> are regarded, while concentrating especially on the mass transfer between the two fluid phases. Here, also the solid displacement is accounted for.

Finally, conclusions are given in **Chapter 8** and possible enhancements of the presented model as well as further interesting aspects are collected in the outlook.

Mathematical relations used throughout this work, specifically on tensor calculus, are added in **Appendix A**. Additional thermodynamic supplements and lengthy derivations of certain relations are stored in **Appendix B**.

---

<sup>1</sup>Porous Media Adaptive Nonlinear Finite Element Solver based on Differential Algebraic Systems

# Chapter 2: Carbon-dioxide capture and storage

It is common sense that greenhouse gases (GG) are the cause for the global warming problem. These gases absorb and emit infrared radiation coming from the earth's surface (caused by solar irradiation) back to earth, and thus, hindering the radiation from emitting into space. This leads to a net increase in energy in the earth's atmosphere and on the surface.

The main GG are water ( $\text{H}_2\text{O}$ ), carbon dioxide ( $\text{CO}_2$ ), methane ( $\text{CH}_4$ ), nitrous oxide ( $\text{N}_2\text{O}$ ) and ozone ( $\text{O}_3$ ). From this group, water is the most important GG, being responsible for about 60 % of the global warming effect. However, it is related to the so-called “natural” GG, since the water in the atmosphere corresponds to the natural water cycle.  $\text{CO}_2$  is regarded as the most important “artificial” GG, because the anthropogenically emitted amount of  $\text{CO}_2$  is much higher compared to the emissions of the other gases.

In this chapter, the specifics of  $\text{CO}_2$  storage in underground reservoirs and the accompanying difficulties are explained. For a better understanding of the process of  $\text{CO}_2$  sequestration and its requirements, first the properties of  $\text{CO}_2$  are provided, then the method of CCS is explained, followed by an overview of different storage options and their advantages and disadvantages. Last, the tasks that arise from open questions concerning the storage size and the safety of the reservoir are collected. These tasks are then further classified into the ones that are possible to solve by numerical simulations of CCS. This serves as the motivation for the development a continuum-mechanical model of  $\text{CO}_2$  injection.

## 2.1 Properties of $\text{CO}_2$

Carbon dioxide is a vital molecule for the life on earth, since it is essential for the respiratory process of most to all organisms<sup>1</sup>. Photosynthetic organisms, such as plants, algae and cyanobacteria, consume  $\text{CO}_2$  together with water and light energy to synthesize carbohydrates, which are then build into their bodies. As a byproduct of the photosynthesis, oxygen is generated that can be respired in the metabolism of aerobic organisms, e. g., in the gills of fish, in the trachea of insects or in the lungs of mammals, reptiles and birds. During the respiratory process, which represents the opposite process of the photosynthesis,  $\text{CO}_2$  is produced again and the  $\text{CO}_2$  cycle is closed.

Other sources of  $\text{CO}_2$  are the metabolism of microorganisms, e. g., the fermentation of sugars during wine or beer production, and the combustion of materials composed of carbohydrates, e. g., wood and fossil fuels, such as coal, peat, oil or natural gas. Furthermore,  $\text{CO}_2$  is discharged at volcanic-active sites, e. g., volcanoes, hot springs or geysers. Another

---

<sup>1</sup>Apart from exotic organisms such as sulfur-based organisms that live around black smokers in the deep sea.

natural source of  $\text{CO}_2$  represents the dissolution of carbonate rocks into water.

$\text{CO}_2$  is widely used in technical applications, for example, as a shielding gas for welding and fire extinguishers or as a pressurised gas for air guns. In the petroleum industry, it is injected for enhanced oil recovery (EOR), it is used as a refrigerant, for example, in automobile air-conditioning systems and also in its solid form, the so-called dry-ice,  $\text{CO}_2$  is applied for cooling applications or as an abrasive in dry-ice blasting. Furthermore,  $\text{CO}_2$  finds usage in the food and beverage industry for the carbonation of drinking water, beer or sparkling wine. Here, also the supercritical state of  $\text{CO}_2$  finds benefit in the so-called supercritical drying process, where it acts as a non-toxic solvent for lipophilic organic materials, e. g., in the decaffeination of coffee, cf. *McHugh & Krukonis* [118].

At atmospheric conditions ( $p_0 = 0.1 \text{ MPa}$ ),  $\text{CO}_2$  in its gaseous state is as a trace gas of the ambient air, with a concentration of about 0.04 % per volume (400 ppm, measured in the year 2015<sup>2</sup>), cf. Figure 2.1.  $\text{CO}_2$  is not classified as a toxic gas, but acts as an asphyxiant gas, where the effects on humans can be already felt at concentrations of 1000 ppm. At concentrations of 7 % to 10 % (70 000 ppm to 100 000 ppm), life threatening conditions are reached. This asphyxiant effect is also applied in butcheries to stun animals.

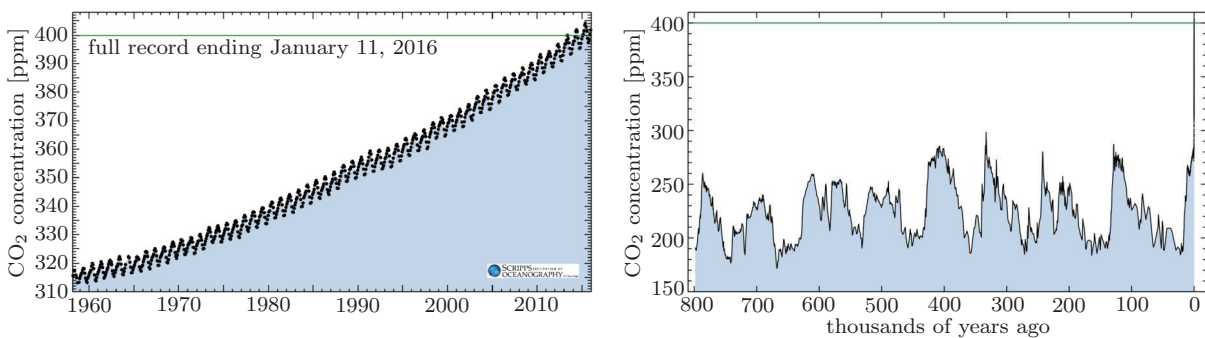


Figure 2.1: (left):  $\text{CO}_2$  concentration measured from 1958 to January 2016 at Mauna Loa Observatory (USA). This curve is also known as the *Keeling curve* [96]. The yearly oscillations originate from the increase of vegetation in spring and summer (decrease in  $\text{CO}_2$  concentration) and decrease of vegetation in autumn and winter (increase of  $\text{CO}_2$  concentration) in the northern hemisphere, since most of the landmass is located there.

(right):  $\text{CO}_2$  concentrations from 800 000 years ago until today. Measurements of the  $\text{CO}_2$  concentrations are taken from ice-cores. It clearly shows that today's  $\text{CO}_2$  concentration has not been encountered for a really long time. (Source: <http://keelingcurve.ucsd.edu/>).

Figure 2.1 shows that today's  $\text{CO}_2$  concentration has not been encountered for almost 800 000 years. *Keeling* [96] also states that the increase in  $\text{CO}_2$  concentration matches the amount of combusted fossil fuels starting with the industrial age. Consequently, these curves indicate that this strong increase in  $\text{CO}_2$  concentration over the last fifty years has an anthropogenic background. Besides its gaseous occurrence in air,  $\text{CO}_2$  is soluble in water and, thus, is pervasive in all natural water distributions, both liquid and ice.

<sup>2</sup>Parts per million (ppm) is a volumetric concentration measure for highly diluted materials, which denotes one part per 1 000 000 parts.

## Physical characteristics of CO<sub>2</sub>

The required conditions and features of an eligible reservoir for a safe storage of CO<sub>2</sub>, explained in the next Section 2.2, are dictated by the physical and thermodynamical properties and characteristics of the CO<sub>2</sub>. As its name implies, carbon-dioxide consists of one carbon and two oxygen atoms, which form a linear molecule without an electrical dipole<sup>3</sup>. A couple of physical and thermodynamical properties are listed in Table 2.1. Considering the sequestration process, it is obvious that a high density and low viscosity

Table 2.1: Selected physical and thermodynamical properties of CO<sub>2</sub>.

molar mass:	44.01 g/mol
critical pressure:	7.374 MPa
critical temperature:	304.12 K
critical density:	468.19 kg/m <sup>3</sup>

of the CO<sub>2</sub> are favourable in order to store as much CO<sub>2</sub> as possible in a given reservoir and, thus, lower the costs of storage. Since the temperature within a reservoir changes only slightly over depth, usually  $\Delta\theta \approx 25.0$  K/km, cf. *Rutqvist* [155], the density of the CO<sub>2</sub> in the reservoir depends mainly on the increasing pressure with depth. In Figure 2.2, the relation between the density of CO<sub>2</sub> and the injection-depth is illustrated. It shows

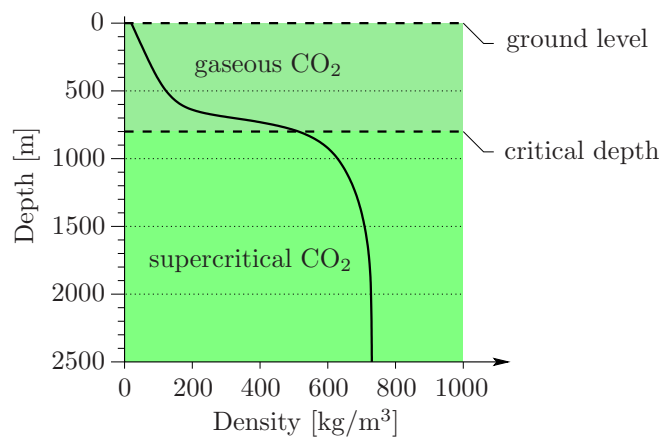


Figure 2.2: Sketch of the depth of a reservoir versus the density of CO<sub>2</sub> illustrating the different phase behaviours.

that below a certain critical depth, at around 800 m, the density increases dramatically from somewhere below 200 kg/m<sup>3</sup> to over 700 kg/m<sup>3</sup>, which indicates the phase change from gaseous to supercritical CO<sub>2</sub>. Thus, injection should be conducted below this critical depth in order to provide that a larger amount of CO<sub>2</sub> can be stored per unit available

<sup>3</sup>The water, H<sub>2</sub>O, molecule on the other hand, which also consists of three atoms, two hydrogen and one oxygen, exhibits an angle of 104.45° and has a strong electrical dipole. This is the reason for several special properties of water, such as the density anomaly (i. e., the solid phase is lighter than the liquid phase and the highest density of water exists at around 4 °C), highest specific heat capacity, highest surface tension and highest latent heat of all fluids.

pore volume, cf., e. g., *Bachu* [10]. Furthermore, supercritical CO<sub>2</sub> has a lower viscosity than liquid CO<sub>2</sub>, which presents another advantage for the injection and storage of CO<sub>2</sub> in subsurface reservoirs, also mentioned by *Celia et al.* [34].

In natural systems, however, it is not guaranteed that the pressure and temperature conditions within the reservoir remain constant over time. In case of changing conditions, the thermodynamical state of CO<sub>2</sub> can alter from the supercritical or the liquid to the gaseous state. Due to the previously mentioned density behaviour, such a phase change is undesirable. Also, a transition to a lower density leads to an increase in pressure, implying a greater stress on the sealing cap-rock layer and causing deformations in the solid skeleton. In the worst case, fractures could be induced leading to leakage of the injected CO<sub>2</sub>. Therefore, it is important to know when and why phase transitions occur. In this regard, in situ experiments are not feasible to find concluding answers and are also too expensive. Hence, the numerical simulation provides a potent, cheap and more feasible tool to understand the phase change and other processes in CO<sub>2</sub> storage.

Besides the position of the reservoir in depths lower than 800 m, several other requirements have to be fulfilled to guarantee a safe storage of the CO<sub>2</sub>. These are discussed in the following Section 2.2.

## 2.2 What is CCS?

The following description of term *carbon-dioxide capture and storage* (CCS) is a brief roundup of the extensive discussion presented in the report of the *Intergovernmental Panel on Climate Change* (IPCC) [119]. CCS incorporates all means necessary to reduce the amount of CO<sub>2</sub> in the atmosphere, which is supposed to be one of the major GG causing global warming. Besides the already discussed CO<sub>2</sub>, there are several other GG with even greater global warming potential<sup>4</sup>, e. g., methane, CH<sub>4</sub>, or nitrous oxide, N<sub>2</sub>O. However, the anthropogenic emitted amount of CO<sub>2</sub> is much higher compared to the other gases and, thus, still has the greatest effect on global warming, which is measured by the so-called radiative forcing<sup>5</sup>, cf. Table 2.2. The sources of CO<sub>2</sub> emissions have been illustrated before. A hint that these emissions really are the cause for the increasing CO<sub>2</sub> concentration in the atmosphere is given by the *Keeling* curve in Figure 2.1. The best method to reduce these emissions is of course to use alternative energy sources, which in case of electricity production could be solar-, wind-, or hydro-power, different means of vehicle propulsion, or the enhancement of biological sinks. If not possible, increasing

---

<sup>4</sup>Measured relative to the same mass of CO<sub>2</sub>, with the global warming potential of CO<sub>2</sub> being equal to 1.

<sup>5</sup>*Radiative forcing* is a measure for the change in energy of the earth-atmosphere system caused by climate-affecting species. Because these species change the balance between incoming solar radiation and outgoing infrared radiation within the earth's atmosphere that controls the earth's surface temperature, the term *radiative* is applied here. Radiative forcing is usually given in W/m<sup>2</sup> and expresses the "rate of energy change per unit area of the globe, measured at the top of the atmosphere", cf. *Myhre et al.* [123]. Positive radiative forcing leads to an increase in the energy of the earth-atmosphere system, i. e., to a warming of the system. In contrast, a negative radiative forcing decreases the energy and leads to a cooling of the system.

Table 2.2: Comparison of global warming potential for a 100-year time horizon in relation to CO<sub>2</sub>, changes in atmospheric concentrations from 2005 until 2011 and radiative forcing in 2011 of CO<sub>2</sub>, CH<sub>4</sub> and N<sub>2</sub>O, taken from *Myhre et al.* [123].

species	global warming potential 100-year horizon	concentration change 2005 - 2011	radiative forcing in 2011
CO <sub>2</sub>	1	+12 ppm	1.82
CH <sub>4</sub>	34	+29 ppb	0.48
N <sub>2</sub> O	298	+5 ppb	0.17

the efficiency of already existing technology should be the second step to reduce CO<sub>2</sub> emissions. Finally, the last possibility to mitigate climate change is CCS, which could be an important strategy to bridge the gap until conventional, fossil-energy production can be replaced by alternative, renewable resources. In the report of the IPCC [119] it is stated that many scenarios show a domination of primary energy production by fossil fuels until the middle of the 20<sup>th</sup> century. Therefore, CCS could be one part of the portfolio to at least stabilise the amount of CO<sub>2</sub> in the atmosphere. A relatively new approach, to even achieve a net removal of atmospheric CO<sub>2</sub>, is the combination of bio-energy power plants with CCS.

The method of CCS comprises the capture of CO<sub>2</sub> at point-like sources (i. e., fossil-fuel power-plants, CO<sub>2</sub>-emitting industries, oil and gas processing, refineries, cement plants and steel mills), compression of the separated CO<sub>2</sub> to its supercritical state, transportation by pipeline or ship to the storage side and a set of different monitoring and verification technologies to control the safety, efficacy and spreading of the injected CO<sub>2</sub> in the reservoir, cf. e. g., *Herzog* [85]. Possible storage methods are: injection into underground reservoirs, deep seafloor ocean storage and industrial fixation of CO<sub>2</sub> into inorganic carbonates. Since this thesis is only concerned about the geological storage process, the other storage methods and the capture and transportation will not be explained any further and the interested reader is referred to the *IPCC Special Report on Carbon Dioxide Capture and Storage* [119].

To get an impression on how many CCS projects have been accomplished so far and how much CO<sub>2</sub> is sequestered, it is resorted to a report by the Global CCS Institute [73]. It states that 75 large-scale geological CO<sub>2</sub> storage projects existed in the year 2012, that captured at least 800 000 tonnes of CO<sub>2</sub> annually per power plant and 400 000 tonnes of CO<sub>2</sub> annually per industrial facility.

### 2.2.1 Geological storage options

Promising geological formations for the underground storage of CO<sub>2</sub> are depleted oil or gas reservoirs, deep saline aquifers and unmineable coal beds, cf. Figure 2.3. These formations can both be onshore and offshore, whereas recent cancellations of onshore projects due to public resistance (e. g., in 2011 Vattenfall discontinues the pilot power-plant in Jämschwalde, Germany) propose less feasibility. A common characteristic of geological

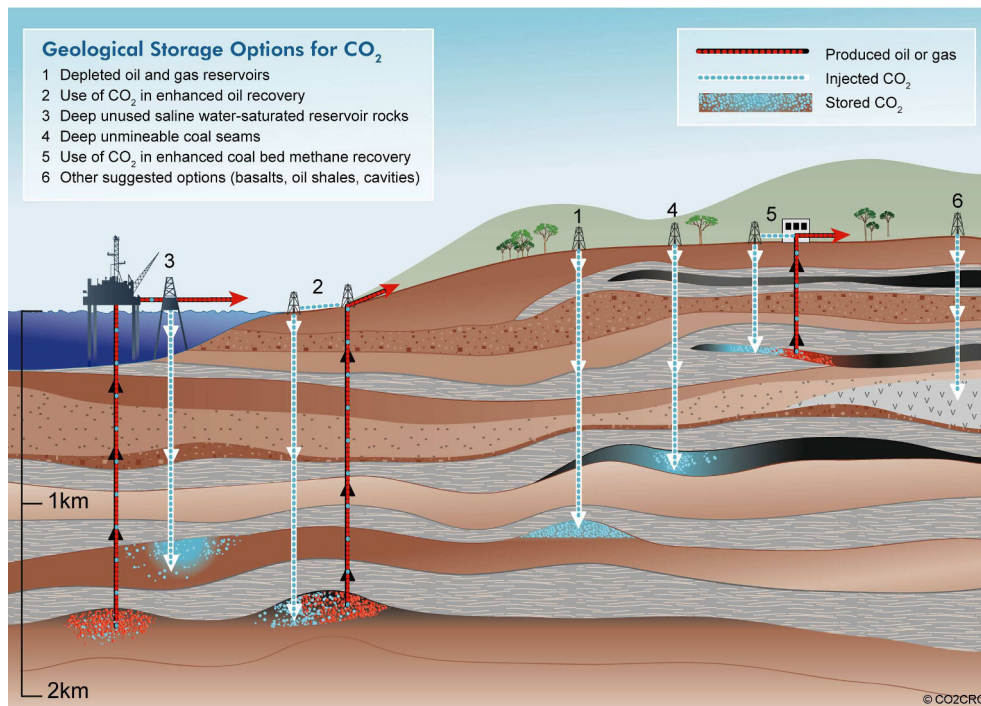


Figure 2.3: Overview of geological storage options for CO<sub>2</sub>, IPCC report [119].

reservoirs is a sealing of the permeable storage layer by an almost impermeable cap-rock layer to prevent the CO<sub>2</sub> from upwards migration. The various geological storage options have different advantages or disadvantages concerning their storage volume, accessibility and safety, which are discussed more thoroughly in the following.

The most obvious candidates for CO<sub>2</sub> storage are *depleted oil and gas reservoirs*, since they already demonstrated their ability to trap fluids lighter than water over a long time. Usually, an extensive amount of data about the geological structure, physical properties of the rock and the storage volume is available from the previous gas or oil production. Furthermore, computer models have been developed to predict the hydrocarbon movement, improve the enhanced oil/gas recovery and to estimate the recovery factor<sup>6</sup> of a reservoir, which can be directly applied to the CO<sub>2</sub> storage.

Table 2.3: Storage capacities of oil and gas fields and deep saline formations [119].

reservoir type	lower estimate of storage capacity (GtCO <sub>2</sub> )	upper estimate of storage capacity (GtCO <sub>2</sub> )
oil and gas fields	675	900
deep saline formations	1000	uncertain, $\sim 10^4$

In case of non-depleted fields with a decreasing production rates, the CO<sub>2</sub> injection can

<sup>6</sup>The *recovery factor* refers to the ratio between the amount of oil that can be produced from a reservoir and the amount of oil initially in place.



be combined with the enhancement of oil recovery. By flooding the oil reservoir with CO<sub>2</sub>, the recovery factor can be risen to an average of 13.2%, furthermore reducing the cost of CO<sub>2</sub> storage by the produced hydrocarbons. However, about half of the injected CO<sub>2</sub> returns with the oil and must be separated and re-injected. Moreover, the physical conditions of the reservoir and the oil must meet certain criteria to allow for an efficient CO<sub>2</sub>-driven oil recovery. For example, very thick, homogeneous reservoir layers are not suitable for EOR, since the lower density of the CO<sub>2</sub> with respect to the reservoir oil leads to a movement of the CO<sub>2</sub> along the top of the reservoir layer without pushing the oil towards the production well.

Another drawback of these developed reservoirs is the high number of wells that are often not thoroughly documented. If these wells are not properly sealed, they pose a risk of leakage by jeopardising the integrity of the cap-rock and its confining character.

The second kind of storage formations with an even greater supposed storage capacity, cf. Table 2.3, are *deep saline aquifers*. These consist of sedimentary rocks containing brine with a high salt concentration and, therefore, are unsuitable for drinking-water production. The only imaginable usage of this salt water is for health spas and geothermal energy. A prominent example for CO<sub>2</sub> storage in a saline formation is the Sleipner Project in the North Sea, cf. IPCC report [123], where CO<sub>2</sub> is removed from the produced natural gas and injected back underground.

The unknown geological properties and a missing infrastructure are disadvantages of saline aquifers compared to the depleted hydrocarbon reservoirs. A further problem, which has now gained more interest is the displacement of the saline water due to the increase in reservoir pressure during the injection of CO<sub>2</sub>, e. g., *Ott et al.* [133]. The question hereby is, if this displaced brine could contaminate neighbouring drinking water reservoirs.

The other storage options pictured in Figure 2.3, i. e., unmineable coal seams, enhanced methane recovery from coal beds and storage in basalts, oil shales or cavities, are of minor importance and will not be discussed at this point. More information to these storage options is provided in the IPCC report [119].

## 2.2.2 Storage costs

It is obvious that CCS requires additional energy for the capture, transportation and storage processes. Thus, the costs of the produced electricity increase, since the efficiency of the energy production is reduced. The largest part of these additional costs stems from the capture process that is technically the most complicated part of the three partial processes. An overview of the range of total costs, the mitigated CO<sub>2</sub> amount, and the increased fuel requirement, is depicted in Table 2.4, both for a coal power plant and a natural gas power plant. Therein, the avoided amount of CO<sub>2</sub> is calculated by comparing the emissions of a regular plant without CCS with the emissions of a plant with capture and storage, which means that the energy requirements for capture and storage are already included in the avoided emissions. The mitigation costs in Table 2.4 show that CCS systems can only become economically feasible, if the prices for carbon emissions reach about 25 – 30 US\$/tCO<sub>2</sub>, cf. [119], if regulatory mandates are established

Table 2.4: Total costs for electricity for a power plant with capture and geological storage in case of a coal and a natural gas power plant. Data taken from the IPCC report [119].

	pulverised coal power plant	natural gas power plant
increased fuel requirement [%]	24 – 40	11 – 22
CO <sub>2</sub> avoided [%]	81 – 88	83 – 88
electricity cost increase [%]	43 – 91	37 – 85
mitigation cost [US\$/tCO <sub>2</sub> avoided]	30 – 71	38 – 91

for the use of CCS, e. g., on new facilities, or if direct or indirect financial support is provided by the policy makers. Otherwise, CCS is not competitive with CO<sub>2</sub>-free energy technologies, such as nuclear power or renewable energy sources. The former of these two, at least in the opinion of the author, does not pose a reasonable solution to the global warming problem, but initiates further difficulties, e. g., the storage of the nuclear waste.

### 2.2.3 Storage mechanisms

Prior to the discussion of risks and security of CO<sub>2</sub> storage, the mechanisms of CO<sub>2</sub> storage must be understood. The migration of the CO<sub>2</sub> is affected by the pressure difference between the injection pressure and the reservoir pressure, the differences in density and viscosity between the CO<sub>2</sub> and the in situ fluids, and the formation heterogeneities. The pressure difference depends on the rate of injection, the permeability and the geological geometry of the reservoir.

In this context, different trapping mechanisms can be distinguished, cf. Figure 2.4, and are introduced in the following. When injecting CO<sub>2</sub> into the reservoir, it displaces the in-situ formation fluids in the reservoir, such as saline water, and collects under the impermeable cap-rock layer due to barycentric forces. This is usually identified as *structural & stratigraphical trapping*. The second trapping mechanism is called *residual trapping* and refers the CO<sub>2</sub> that is trapped in the pore space by capillary forces, cf. *Class* [36]. The mobility<sup>7</sup> contrast between the CO<sub>2</sub> and water or oil can cause viscous fingering (natural convection), intensively investigated by *Homsy* [86]. This is a positive effect, since it enhances the diffusion and dissolution processes of the CO<sub>2</sub> in the formation fluids and, thus, is defined as the third trapping mechanism, namely the *solubility trapping*. The CO<sub>2</sub> will not only interact with the fluids in place, but also with the porous rock. Adsorption and finally mineralisation can guarantee a longterm fixation of the CO<sub>2</sub> in the subsurface. In particular, during the dissolution process in water, the CO<sub>2</sub> forms acidic ions (hydrogen carbonate, HCO<sub>3</sub><sup>-</sup>, and carbonate CO<sub>3</sub><sup>2-</sup>), which react in the next step with the calcium, magnesium, clays or feldspars of the surrounding rock matrix, forming stable carbonate or

<sup>7</sup>The *mobility* is usually defined as the ratio between the relative permeability and the shear viscosity of a constituent.

silicate minerals<sup>8</sup>. This so-called *mineral trapping* is the last and most stable mechanism. All these trapping mechanisms are acting on different time scales, i. e., from the start of the injection, the mainly active trapping mechanism changes, cf. Figure 2.4. This wide

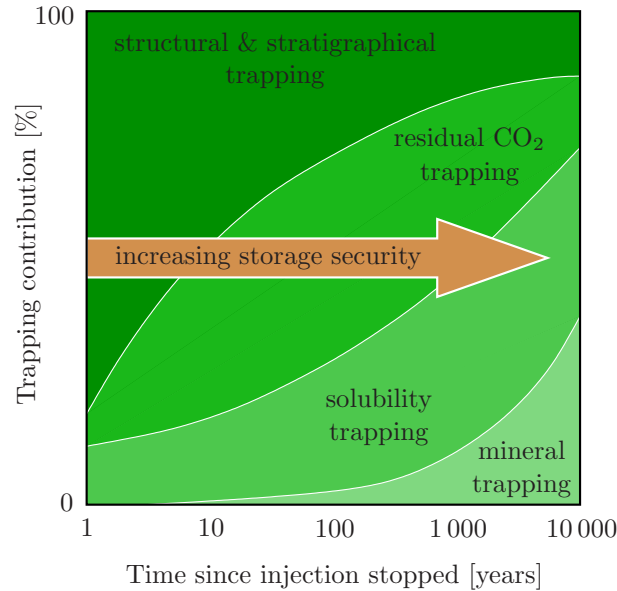


Figure 2.4: Time dependence of different trapping mechanisms in CO<sub>2</sub> storage, cf. IPCC report [119]. The four distinguishable mechanisms replace each other over time, whereas the trapping security increases as well.

range of important time scales severely increases the complexity of the system and, thus, makes the understanding and modelling of all the involved processes, needed for a realistic simulation of CO<sub>2</sub> injection and storage, a task that is not easily achieved. Therefore, numerical simulations usually concentrate only on specific times of the storage process, i. e., either on the early times around the injection itself, or on the longterm behaviour of the CO<sub>2</sub> in the reservoir after the injection has ended. Here in this work, the focus is restricted to the early times around injection, which are the most interesting in terms of high pressures and temperature differences.

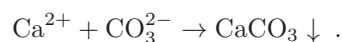
### 2.2.4 Storage safety

Safety issues are an important aspect in CCS. Risks arising from CO<sub>2</sub> storage can be classified into three groups:

<sup>8</sup>The specific dissolution processes of CO<sub>2</sub> in water are:



and the mineralisation with, e. g., calcium ions Ca<sup>2+</sup>, reads:



1. Elevated gas phase concentrations in the shallow subsurface and near-surface environment.
2. Dissolved CO<sub>2</sub> in the groundwater.
3. Displacement of fluids by the injected CO<sub>2</sub>.

The first kind of risks evolves when CO<sub>2</sub> still exists as a separate phase, i. e., it is not yet dissolved into the brine and is hindered from upwards migration by the cap-rock layer. In this early stage, the storage safety is not very high, since the CO<sub>2</sub> can migrate through faults, fractures, or poorly sealed wells towards the surface. In this regard, the crack development in the cap-rock layer can be caused by seismic movements, or due to the increasing pressure in the reservoir during the injection itself. In cases where the leaking CO<sub>2</sub> reaches the atmosphere, the risk of asphyxiation of humans and animals exists for sudden and large amounts of CO<sub>2</sub> releases or at conditions, where the surface topography enables the accumulation of CO<sub>2</sub> in shallow depressions due to its higher density than air. However, this latter risk is rather small, since surface winds will dilute the leaking CO<sub>2</sub> quickly. Figure 2.4 indicates how the continuous change in trapping mechanisms increases the storage security over time. The residual trapping already improves the storage safety by locking a part of the CO<sub>2</sub> in capillary traps. When the CO<sub>2</sub> dissolves into the brine, the solution becomes heavier than the surrounding brine and sinks to the bottom of the reservoir layer, away from the cap-rock layer. Subsequently, in this stage the CO<sub>2</sub> is less affected by potential damages of the cap-rock layer. The safest stage is reached when most of the CO<sub>2</sub> is minerally bound. However, it is supposed to take several thousands of years until this last process is finished.

The second risk of CO<sub>2</sub> dissolving into drinking water was already briefly mentioned before. It describes the contamination of valuable drinking water by contaminants, either brought into the subsurface together with the injected CO<sub>2</sub> or by altering the groundwater chemistry, i. e., the formation of carbonic acids when the CO<sub>2</sub> dissolves into the drinking water. This carbonated water might react with the rock matrix and mobilise possible hazardous contaminants. Furthermore, concerning offshore storage sites, leaking CO<sub>2</sub> might dissolve into the sea water, creating possible harmful environments for marine life. Similar concerns regard the last group of risks. Hereby, the injected CO<sub>2</sub> displaces the saline water, which could then again migrate or leak into more shallow formations and contaminate valuable drinking-water reservoirs.

Possible treatments or assessments of these risks imply the active reservoir management, for example, by withdrawing of formation water to lower the pressure in the reservoir, and of course detailed measurement, monitoring, and verification of injection data, in order to quickly detect any leakage out of the reservoir layer.

Obviously, the prediction of these risks and the probability estimations are an important part of the planning process of CCS. Besides the information from the few already existing storage sites and geological measurements, numerical simulations can contribute a major part to gain data for the risk assessment.

## 2.3 Numerical simulation of CO<sub>2</sub> storage

In order to predict the storage capacity, to estimate a suitable injection pressure, and to classify the safety of a storage site, numerical simulations of the CO<sub>2</sub> injection are of great importance. Their advantage lies in the low costs and comparatively minor effort in relation to expensive on-site tests. However, numerics are at the moment not able to handle the full complexity of the storage process, e. g., regarding the wide span in time and space scales, the multitude in physical and chemical effects and the heterogeneity of the subsurface. Hence, reasonable assumptions and simplifications have to be made to allow for meaningful simulation results within adequate simulation times.

### 2.3.1 State of the art

The numerical simulation of CO<sub>2</sub> storage is relatively new, starting around the beginning of the 21<sup>st</sup> century. Due to the close relation to the petroleum industry, it is only logical that the first sequestration simulations were conducted using existing hydrocarbon production simulators, mainly for the understanding of enhanced oil or gas recovery, cf. *Bielinski* [15] and the references therein. Further early works originate from, e. g., *Pruess & García* and co-workers [46, 141, 144], including the development of the well-known FEM-simulator TOUGH2, or the group around *Ennis-King* [65], looking, for example, at convective mixing in the long-term of the injection process.

Benchmark studies and code comparisons were initiated and executed by *Pruess et al.* [142] and *Class et al.* [37]. These showed that most of the discrepancies in the results between the numerical simulations conducted with different codes, originate from uncertainties in material parameters, diverse definitions of the boundary conditions and errors or various behaviour induced by the gridding.

Analytical or semi-analytical models were derived by, *Kang et al.* [93], *Nordbotten et al.* [129], *Celia et al.* [34]. The latter two include these models in a quantitative estimation of CO<sub>2</sub> leakage from geological storage at leaky wells.

Since the vertical extent of a subsurface reservoir is usually much smaller than the lateral extent, also the horizontal movement of CO<sub>2</sub> is in many scenarios more important. Therefore, so-called vertical-equilibrium models are developed to reduce numerical costs and to allow for the simulation of models with a larger horizontal dimensions, cf. *Court et al.* [40] and *Gasda et al.* [70].

The group around *Nordbotten* and *Celia* established a number of models to efficiently simulate CO<sub>2</sub> sequestration with regard to reliable predictions for policy makers. These include the long-term evolution of the CO<sub>2</sub>, the leakage from geological storage sites, and large-scale simulations, cf. e. g., [34, 127, 143]. *Nordbotten et al.* [128] also state that simulations alone cannot give satisfactory answers to CO<sub>2</sub> storage problems, but must be complemented by monitoring and history matching<sup>9</sup> during the injection process. In this

---

<sup>9</sup>The term *history matching* refers to the process of adjusting the parameters and boundary conditions of a model by comparing the measured data with the data gained from numerical simulations for the same time span.

context, one can also mention the works of *Bradshaw et al.* [28] and *Kopp et al.* [99] on storage-capacity estimations.

It was already mentioned in the previous sections that the CO<sub>2</sub> sequestration incorporates many different processes and difficulties. Thus, a multiplicity of researches have been conducted on specific topics to understand these processes. To give an impression of the broadness of this field, a few shall be mentioned here: *Juanes et al.* [91] investigated the impact of relative permeability on CO<sub>2</sub> sequestration, the temperature dependencies of capillary pressure in CCS were modelled by *Plug & Bruining* [136], the long-term storage mechanism of mineralisation was, for example, considered by *Kumar et al.* [103], *Ebigbo* modelled enhanced trapping mechanisms due to biofilm growth [47], and *Rutqvist* [154–156] looked at the geomechanical impact of CO<sub>2</sub> sequestration, especially, at one of the presently three main injection sites at In Salah, Algeria.

This is by no means an exhaustive listing of all the work done in the field of CO<sub>2</sub> sequestration, but shall give a brief overview. For a more extensive collection, the interested reader is referred to, e. g., the IPCC report [119] or the dissertation by *Bielinski* [15].

### 2.3.2 Tasks and difficulties

Although extensive research has been conducted in CCS, open questions still remain. These are related to all parts of the CCS process, e. g., improving the efficiency of the CO<sub>2</sub> capture, which still contributes most to the costs of CCS, cf. *Bruckner et al.* [32]. However, in the framework of this monograph, only questions concerning the storage of CO<sub>2</sub> are discussed. Basically, these are usually related to the operational safety and long-term integrity of a CO<sub>2</sub> storage site:

- the effects of the pressure build-up due to injection, which can cause various unwanted situations:
  - uplift of the overlying rock, e. g., at the injection site In Salah, Algeria [156],
  - leakage of the injected CO<sub>2</sub> through cracks in the sealing cap-rock layer or re-opened faults, induced by the high pressure,
  - initiation of seismic events,
  - far-field pressure effects, i. e., the displacement of the saline formation water, which might lead to a contamination of nearby drinking water reservoirs.
- a sudden pressure increase in the reservoir, which can also be caused by a phase change of the injected CO<sub>2</sub> due to changing reservoir conditions (temperature or pressure), causing the before mentioned situations. In particular, the transition from the high density supercritical or liquid phase to the low density gaseous phase has to be regarded in this context.
- the long-term integrity of wells, where leakage along the well-casing can occur if the carbonic acid, originating from the dissolution of CO<sub>2</sub> in the formation water, harms the cement of the well-casing and makes it porous.

A collection of further open questions is given, e. g., by *Komarova* [98].

These points represent the background for the following derivation of a multiphasic model, which is able to handle phase-transition processes under various thermodynamical conditions together with solid deformations. In this context, numerical models can definitely help to understand the physical processes occurring in the reservoir. In combination with geological and geophysical data, it should then become possible to form a judgment of the suitability of a reservoir for CO<sub>2</sub> sequestration.





# Chapter 3: Theoretical fundamentals of multiphasic and multicomponent modelling

This chapter introduces the theoretical fundamentals for the modelling of multiphasic and multicomponent systems, e. g., CO<sub>2</sub> and water percolating a porous rock. First of all, the *Theory of Porous Media* (TPM) is outlined as the basic concept for the continuum-mechanical description of miscible and immiscible constituents, including the definitions of volume fractions and densities. Subsequently, kinematical relations are defined for the superimposed constituents, passing on to presenting relevant deformation and strain measures. Furthermore, a brief overview of the stress state is given. It follows an elaborate introduction of general balance relations and their adaptation to both, the overall aggregate and the specific constituents. Finally, the concept of singular surfaces is provided, together with corresponding kinematical and balance relations. This last part is a prerequisite for the later description of the phase-transition process at the interface between the two fluid phases. Therewith, a model of a thermo-elastic porous solid percolated by two immiscible, compressible and interacting fluid phases is established later in Chapter 5.

## 3.1 Theory of Porous Media

For a detailed and realistic model of a CO<sub>2</sub> injection and storage process, the multiphasic and multicomponent structure of the reservoir and the percolating fluids have to be mathematically acknowledged. In this regard, a macroscopic approach embedded in a continuum theory has proven to be a suitable model for such a complex and heterogeneous medium as subsurface rock. This was shown, for example, by the petroleum industry and their simulations of oil and gas recovery, e. g., *Coats et al.* [38]. Moreover, due to the scarce knowledge of the exact underground conditions, where only statistical information can be obtained by geophysical measurements (e. g., seismic surveys, ground-radar, core samples), such a homogenised macroscopic model provides a more reasonable approach than microscopic models or singlephase material models. A comparison of the macroscopic approach, i. e., the TPM, with the classical continuum-mechanical approach of singlephasic materials is presented in *Ehlers* [56]. Furthermore, the TPM provides a profound basement not only for the description of soil formations, but also for other natural systems and materials, such as biological systems, cf. *Ehlers* [55].

In combining the classical *Theory of Mixtures* (e. g., *Truesdell & Toupin* [173] and *Bowen* [25]) with the *concept of volume fractions* (cf. *Biot* [16], *Bowen* [26, 27] and *Ehlers* [56]), the modelling of miscible constituents in a macroscopic model is enhanced with the microscopic information of the inner composition of the system. Thus, since the structure of the pores is usually not known, a statistical homogenisation over a representative volume element provides a basis for a continuum-mechanical description, cf. Figure 3.1. Formulating the basic idea of the TPM, a multiphasic aggregate  $\varphi$  consisting of constituents  $\varphi^\alpha$  is statistically distributed over the representative elementary volume (REV), leading to a

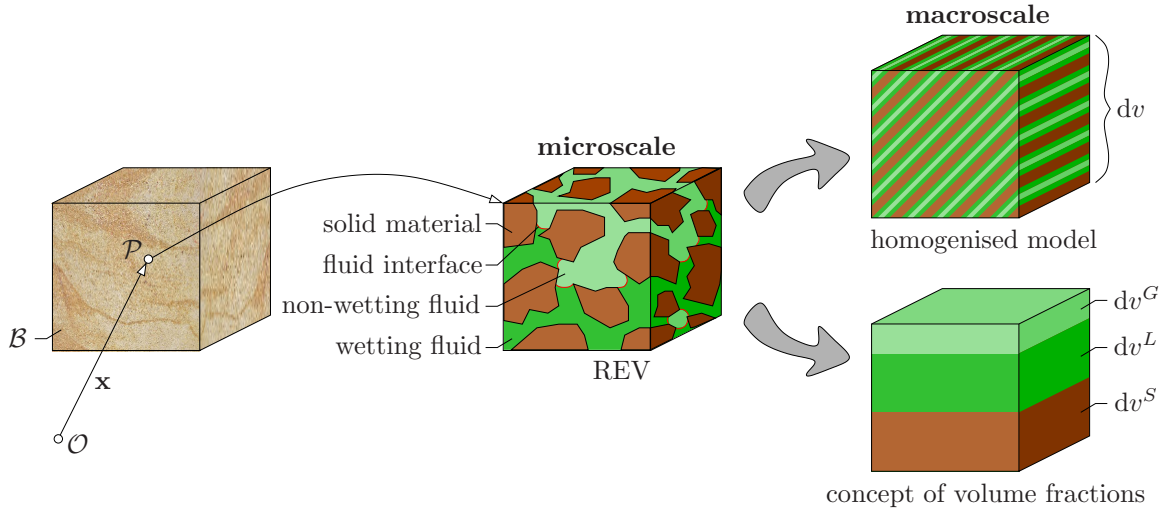


Figure 3.1: The point  $\mathcal{P}$  of a porous sandstone, filled with two fluid phases  $\varphi^L$  and  $\varphi^G$ , is located in the current configuration at position  $\mathbf{x}$ . From the idealistic model of an REV on the microscale the development of a macroscopic, multiphasic modelling approach follows, consisting of the homogenised model and the concept of volume fractions.

model of superimposed and interacting continua

$$\varphi = \bigcup_{\alpha} \varphi^{\alpha} = \varphi^S \cup \varphi^F, \quad \alpha \in \{S, L, G\}, \quad \text{and} \quad \varphi^F = \bigcup_{\beta} \varphi^{\beta}, \quad \beta \in \{L, G\}. \quad (3.1)$$

Hereby, the porous solid constituent is indicated by  $S$  and is percolated by the fluid phases  $F$ , which again can be subdivided into the liquid phase  $L$  and the gaseous phase  $G$ . The constituents  $\varphi^{\alpha}$  are usually identified as the differentiable parts which build the multiphasic aggregate. It is not essential that these constituents just represent the different phases, they can also be distinguished as the constituents of a solution. However, in this monograph diffusion processes are neglected and, thus, it suffices to deal with a classification of the constituents as phases.

The summation over the partial volumes of the immiscible phases  $V^{\alpha}$  provides the total volume  $V$  of the overall aggregate  $\mathcal{B}$  at its current configuration:

$$V = \int_{\mathcal{B}} dv = \sum_{\alpha} V^{\alpha}. \quad (3.2)$$

Herein, the partial volumes can be further split via

$$V^{\alpha} = \int_{\mathcal{B}} n^{\alpha}(\mathbf{x}) dv =: \int_{\mathcal{B}} dv^{\alpha} \quad \rightarrow \quad n^{\alpha} = \frac{dv^{\alpha}}{dv}, \quad \text{with} \quad \sum_{\alpha} n^{\alpha} = 1, \quad (3.3)$$

where  $n^{\alpha}$  is the volume fraction at a certain position  $\mathbf{x}$ , defined as the ratio between the volume element  $dv^{\alpha}$  of a constituent and the volume element  $dv$  of the overall aggregate. Furthermore, it is assumed that the regarded system contains no vacant spaces, which is guaranteed by the closure condition (3.3)<sub>3</sub>.

When considering multiphasic aggregates, where two fluids have different wetting behaviours, it is practical to introduce the saturation  $s^\beta$ , which is defined as the volume fraction of the pore fluids  $\varphi^\beta$  with respect to the pore space:

$$s^\beta = \frac{n^\beta}{n^F}, \quad \text{where } n^F = \sum_{\beta} n^\beta \quad \text{and} \quad \sum_{\beta} s^\beta = 1. \quad (3.4)$$

Herein, the volume fraction of the pore space  $n^F$  is also known as the so-called porosity. Assuming that the individual phases are immiscible and occupy separate volumes within the overall medium, two different densities can be defined:

$$\rho^{\alpha R} = \frac{dm^\alpha}{dv^\alpha}, \quad \rho^\alpha = \frac{dm^\alpha}{dv} \quad \text{and} \quad \rho^\alpha = n^\alpha \rho^{\alpha R}. \quad (3.5)$$

Therein, the effective (or realistic) density  $\rho^{\alpha R}$  represents the real material density of  $\varphi^\alpha$  at a local point, the partial density  $\rho^\alpha$  relates the local mass to the bulk volume of the overall porous medium and  $dm^\alpha$  is the local mass.

The relation between the two density definitions (3.5)<sub>3</sub> implies the two possible reasons for a change in the partial density  $\rho^\alpha$ :

1. The volume fraction  $n^\alpha$  can change due to, e. g., deformations of the solid matrix, explained later in the evaluation of the solid mass balance in Section 5.2.1.
2. The material can be mechanically compressible, i. e.,  $\rho^{\alpha R} = \rho^{\alpha R}(p^{\beta R}, \theta^\alpha)$ , whereas  $p^{\beta R}$  is the specific pressure and  $\theta^\alpha$  is the absolute temperature of the constituent  $\varphi^\alpha$ .

## 3.2 Kinematical relations

The formulation of motion functions for a superimposed continuum are based on classical continuum mechanics of singlephasic materials, e. g., *Altenbach* [4] or *Haupt* [82]. A complete overview of these for multiphasic materials is presented, e. g., by *Ehlers* [54, 56]. Here, only the required kinematical relations for a triphasic mixture of a thermo-elastic solid material and two immiscible fluid phases are provided. For more complex kinematical formulations of material deformations, e. g., visco-plasticity and miscible components, the interested reader is referred to, e. g., *Avci* [8] or *Wagner* [176].

### 3.2.1 Motion functions

Subsequently, a body  $\mathcal{B}$  with its surface  $\mathcal{S}$  is regarded that is composed of a multiphasic mixture consisting of the three constituents  $\varphi^S$ ,  $\varphi^L$  and  $\varphi^G$ , as illustrated in Figure 3.2. Following the basic concept of the TPM, each constituent  $\varphi^\alpha$  is represented by its own motion function

$$\mathbf{x} = \boldsymbol{\chi}_\alpha(\mathbf{X}_\alpha, t), \quad (3.6)$$

due to the superposition of the interacting continua over the REV. This implies that each spatial point  $\mathbf{x}$  is simultaneously occupied by material points  $\mathcal{P}^\alpha$  of all constituents  $\varphi^\alpha$ , cf. Figure 3.2. Assuming a unique motion function  $\chi_\alpha$ , each material point  $\mathcal{P}^\alpha$  in the current

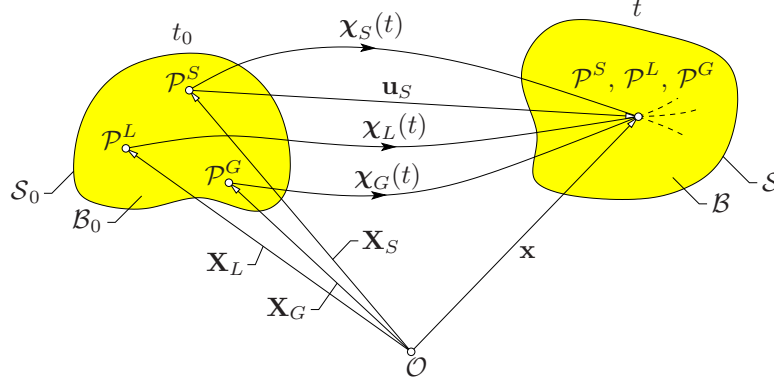


Figure 3.2: Motion of a multiphasic body  $\mathcal{B}$  with surface  $\mathcal{S}$  between the reference configuration (time  $t_0$ ) and the current configuration (time  $t$ ). Motion functions  $\chi_\alpha$  connect the reference positions  $\mathbf{X}_\alpha$  of a point  $\varphi^\alpha$  to the current position  $\mathbf{x}$ .

configuration at time  $t$  must have a unique reference position  $\mathbf{X}_\alpha$  at time  $t_0$ . Because of the requested uniqueness of these motion functions at all times  $t$ , Equation (3.6) can be inverted to identify the reference position  $\mathbf{X}_\alpha$  at time  $t_0$ :

$$\mathbf{X}_\alpha = \chi_\alpha^{-1}(\mathbf{x}, t), \quad \text{if } J_\alpha := \det \frac{\partial \chi_\alpha(\mathbf{X}_\alpha, t)}{\partial \mathbf{X}_\alpha} \neq 0. \quad (3.7)$$

The uniqueness of the inverse motion function requires the non-singularity of the *Jacobian determinant*  $J_\alpha$ , cf. (3.7)<sub>2</sub>. From (3.6) and (3.7) it can be concluded that each constituent has its own velocity and acceleration fields, which are given in the *Lagrangian* description as:

$$\dot{\mathbf{x}}_\alpha = \frac{\partial \chi_\alpha(\mathbf{X}_\alpha, t)}{\partial t}, \quad \ddot{\mathbf{x}}_\alpha = \frac{\partial^2 \chi_\alpha(\mathbf{X}_\alpha, t)}{\partial t^2}. \quad (3.8)$$

In Equation (3.8), the material time derivative  $(\cdot)'_\alpha$  was used<sup>1</sup>, which follows the motion of the constituent  $\varphi^\alpha$ . Thus, due to the conventions made in the TPM, the total material time derivative of an arbitrary, steady and sufficiently differentiable scalar function  $\Upsilon$  or vector function  $\mathbf{\Upsilon}$  depends on the motion of the overall aggregate  $\varphi$

$$\begin{aligned} \dot{\Upsilon} &= \frac{d}{dt} \Upsilon(\mathbf{x}, t) = \frac{\partial \Upsilon}{\partial t} + \text{grad } \Upsilon \cdot \dot{\mathbf{x}}, \\ \dot{\mathbf{\Upsilon}} &= \frac{d}{dt} \mathbf{\Upsilon}(\mathbf{x}, t) = \frac{\partial \mathbf{\Upsilon}}{\partial t} + (\text{grad } \mathbf{\Upsilon}) \dot{\mathbf{x}}, \end{aligned} \quad (3.9)$$

or on the motion of the constituent  $\varphi^\alpha$

$$\begin{aligned} (\Upsilon)'_\alpha &= \frac{d_\alpha}{dt} \Upsilon(\mathbf{x}, t) = \frac{\partial \Upsilon}{\partial t} + \text{grad } \Upsilon \cdot \dot{\mathbf{x}}_\alpha, \\ (\mathbf{\Upsilon})'_\alpha &= \frac{d_\alpha}{dt} \mathbf{\Upsilon}(\mathbf{x}, t) = \frac{\partial \mathbf{\Upsilon}}{\partial t} + (\text{grad } \mathbf{\Upsilon}) \dot{\mathbf{x}}_\alpha. \end{aligned} \quad (3.10)$$

<sup>1</sup>Throughout this monograph,  $(\cdot)$  is used as a placeholder for either arbitrary scalar or vectorial quantities, depending on the context of its use.

In the latter four equations, the differential operator  $\text{grad}(\cdot)$  denotes the gradient with respect to the current position  $\mathbf{x}$ . This is in contrast to the partial derivative with respect to the reference position  $\mathbf{X}_\alpha$  of the constituent  $\varphi^\alpha$ , which is written as  $\text{Grad}_\alpha(\cdot)$ . Finally, the velocity of the overall medium can be derived from a mass average over all constituents leading to the local barycentric velocity:

$$\dot{\mathbf{x}} = \frac{1}{\rho} \sum_{\alpha} \rho^{\alpha} \dot{\mathbf{x}}_{\alpha}, \quad (3.11)$$

wherein,  $(\dot{\cdot})$  is the material time derivative with respect to the overall aggregate  $\varphi$ . Due to the fact that the constituents  $\varphi^\alpha$  can move independently from the overall aggregate  $\varphi$ , a diffusion velocity<sup>2</sup> is introduced via

$$\mathbf{d}_\alpha := \dot{\mathbf{x}}_\alpha - \dot{\mathbf{x}}, \quad \text{with} \quad \sum_{\alpha} \rho^{\alpha} \mathbf{d}_\alpha = \sum_{\alpha} \rho^{\alpha} \dot{\mathbf{x}}_\alpha - \dot{\mathbf{x}} \sum_{\alpha} \rho^{\alpha} = \mathbf{0}. \quad (3.12)$$

In continuum mechanics, the solid phase  $\varphi^S$  is usually described by a *Lagrangean* setting, which leads to the introduction of the displacement vector  $\mathbf{u}_S$  as follows:

$$\mathbf{u}_S = \mathbf{x} - \mathbf{X}_S. \quad (3.13)$$

In contrast to the solid phase, it is more practical to use a modified *Eulerian* setting for the pore fluids  $\varphi^\beta$ . Therefore, the seepage velocity  $\mathbf{w}_\beta$  is defined as

$$\mathbf{w}_\beta := \dot{\mathbf{x}}_\beta - \dot{\mathbf{x}}_S, \quad (3.14)$$

describing the fluid motions with respect to the deforming solid matrix.

Due to the *Lagrangean* formulation of the continuum-mechanical model with respect to the solid deformation vector  $\mathbf{u}_S$ , it is of great help to transform the material time derivatives  $(\cdot)'_\beta$ , to the motion of the solid constituent. The required transformation operator is derived by subtracting (3.10)<sub>1</sub> of the considered constituent from that of the solid constituent and by further using (3.14), viz.:

$$(\cdot)'_\beta = (\cdot)'_S + \text{grad}(\cdot) \cdot \mathbf{w}_\beta. \quad (3.15)$$

### 3.2.2 Deformation and strain measures

The material deformation gradient  $\mathbf{F}_\alpha$  is introduced as the basic deformation measure, which is essential in continuum mechanics to describe motion changes of the constituents  $\varphi^\alpha$ .  $\mathbf{F}_\alpha$  and its inverse form are given by

$$\begin{aligned} \mathbf{F}_\alpha &= \frac{\partial \chi_\alpha(\mathbf{X}_\alpha, t)}{\partial \mathbf{X}_\alpha} = \frac{\partial \mathbf{x}}{\partial \mathbf{X}_\alpha} = \text{Grad}_\alpha \mathbf{x}, \\ \mathbf{F}_\alpha^{-1} &= \frac{\partial \chi_\alpha^{-1}(\mathbf{x}, t)}{\partial \mathbf{x}} = \frac{\partial \mathbf{X}_\alpha}{\partial \mathbf{x}} = \text{grad} \mathbf{X}_\alpha. \end{aligned} \quad (3.16)$$

---

<sup>2</sup>This *diffusion velocity* must not be confused with the pore-diffusion velocity, which describes the relative motion of a miscible component to the motion of the fluid mixture.

The requirement of uniqueness of the motion function  $\chi_\alpha$  was already mentioned in (3.7), and it follows that the *Jacobian* is restricted to positive values, viz.:

$$J_\alpha = \det \mathbf{F}_\alpha > 0 \quad \text{if} \quad \det \mathbf{F}_\alpha(t_0) = 1, \quad \text{for} \quad \mathbf{F}_\alpha(t_0) = \frac{\partial \mathbf{X}_\alpha}{\partial \mathbf{X}_\alpha} = \text{Grad}_\alpha \mathbf{X}_\alpha = \mathbf{I}, \quad (3.17)$$

wherein  $\mathbf{I}$  is the second order identity tensor, and the definition of the determinant  $\det \mathbf{F}_\alpha$  is provided in Appendix A. With this at hand, the mapping characteristic of the material deformation gradient can be applied to do a push-forward transformation of a local line element from the reference configuration into the current configuration via

$$d\mathbf{x} = \mathbf{F}_\alpha d\mathbf{X}_\alpha \quad \leftrightarrow \quad d\mathbf{X}_\alpha = \mathbf{F}_\alpha^{-1} d\mathbf{x}, \quad (3.18)$$

where also the pull-back transformation, i. e., from the current to the reference configuration, is presented and requires the existence of the inverse deformation gradient (3.16)<sub>2</sub>. In an analogue way, the mapping can also be adopted to area and volume elements

$$d\mathbf{a} = (\text{cof } \mathbf{F}_\alpha) d\mathbf{A}_\alpha \quad \text{and} \quad dv = (\det \mathbf{F}_\alpha) dV_\alpha, \quad (3.19)$$

where the referential configuration quantities  $d\mathbf{A}_\alpha$  and  $dV_\alpha$  of the area and volume elements are mapped to the current configuration quantities  $d\mathbf{a}$  and  $dv$ , respectively. The vectorial form of the area elements originates from a definite surface orientation, indicated in the following by the normal vector  $\mathbf{n}$  for the current configuration and the normal vector  $\mathbf{m}$  for the referential configuration. Thus, the vectorial area elements can be written as  $d\mathbf{a} = \mathbf{n} da$  and  $d\mathbf{A}_\alpha = \mathbf{m}_\alpha dA_\alpha$ . The calculation of the cofactor  $\text{cof } \mathbf{F}_\alpha$ , appearing in (3.19), is given in Appendix A.

So far, the formulation of the deformation gradient is valid for all kinds of constituents, such as solid, liquid or gas. However, since the fluid motion is described relative to the deforming solid matrix (i. e., motions of the pore fluids  $\varphi^\beta$  are given in a modified *Eulerian* setting), the fluid deformation gradients  $\mathbf{F}_\beta$  are not needed in the following, but are indirectly included by the seepage velocity  $\mathbf{w}_\beta$  (3.14). Hence, the following discussions of the finite kinematical relations are presented only for the solid constituent. By taking the solid displacement vector  $\mathbf{u}_S$  as the primary variable for the solid constituent, it is customary to write the solid deformation tensor as

$$\mathbf{F}_S = \frac{\partial(\mathbf{X}_S + \mathbf{u}_S)}{\partial \mathbf{X}_S} = \mathbf{I} + \text{Grad}_S \mathbf{u}_S, \quad (3.20)$$

where (3.6) and (3.13) were applied. The inverse of the solid material deformation gradient then reads

$$\mathbf{F}_S^{-1} = \frac{\partial \mathbf{X}_S}{\partial \mathbf{x}} = \text{grad } \mathbf{X}_S = \mathbf{I} - \text{grad } \mathbf{u}_S. \quad (3.21)$$

Next, deformation measures are derived from the square of the line elements (3.18) in both, referential and current configurations:

$$\begin{aligned} d\mathbf{x} \cdot d\mathbf{x} &= d\mathbf{X}_S \cdot (\mathbf{F}_S^T \mathbf{F}_S) d\mathbf{X}_S =: d\mathbf{X}_S \cdot \mathbf{C}_S d\mathbf{X}_S \quad \rightarrow \quad \mathbf{C}_S = \mathbf{F}_S^T \mathbf{F}_S, \\ d\mathbf{X}_S \cdot d\mathbf{X}_S &= d\mathbf{x} \cdot \underbrace{(\mathbf{F}_S^{T-1} \mathbf{F}_S^{-1})}_{(\mathbf{F}_S \mathbf{F}_S^T)^{-1}} d\mathbf{x} =: d\mathbf{x} \cdot \mathbf{B}_S d\mathbf{x} \quad \rightarrow \quad \mathbf{B}_S = \mathbf{F}_S \mathbf{F}_S^T. \end{aligned} \quad (3.22)$$

Therein, the right,  $\mathbf{C}_S$ , and the left,  $\mathbf{B}_S$ , *Cauchy-Green* deformation tensor of the solid matrix were introduced. Furthermore, strain measures are found by subtracting the squares of the current and referential line elements:

$$\begin{aligned} \mathrm{d}\mathbf{x} \cdot \mathrm{d}\mathbf{x} - \mathrm{d}\mathbf{X}_S \cdot \mathrm{d}\mathbf{X}_S &= \mathrm{d}\mathbf{X}_S \cdot \mathbf{C}_S \mathrm{d}\mathbf{X}_S - \mathrm{d}\mathbf{X}_S \cdot \mathrm{d}\mathbf{X}_S = \\ &= \mathrm{d}\mathbf{X}_S \cdot (\mathbf{C}_S - \mathbf{I}) \mathrm{d}\mathbf{X}_S && \rightarrow \mathbf{E}_S = \frac{1}{2} (\mathbf{C}_S - \mathbf{I}) , \\ \mathrm{d}\mathbf{x} \cdot \mathrm{d}\mathbf{x} - \mathrm{d}\mathbf{X}_S \cdot \mathrm{d}\mathbf{X}_S &= \mathrm{d}\mathbf{x} \cdot \mathrm{d}\mathbf{x} - \mathrm{d}\mathbf{x} \cdot \mathbf{B}_S^{-1} \mathrm{d}\mathbf{x} = \\ &= \mathrm{d}\mathbf{x} \cdot (\mathbf{I} - \mathbf{B}_S^{-1}) \mathrm{d}\mathbf{x} && \rightarrow \mathbf{A}_S = \frac{1}{2} (\mathbf{I} - \mathbf{B}_S^{-1}) \end{aligned} \quad (3.23)$$

with the *Green-Lagrangean* strain tensor  $\mathbf{E}_S$  and the *Almansi* strain tensor  $\mathbf{A}_S$ . The factor  $\frac{1}{2}$  dates back to the common convention that the strain tensor should be reducible to the one-dimensional *Hookean* elasticity law in case of linearisation. The *Green-Lagrangean* and the *Almansi* strain tensor can be converted into each other by  $\mathbf{A}_S = \mathbf{F}_S^{T-1} \mathbf{E}_S \mathbf{F}_S^{-1}$ . Further existing strain measures are not important in the context of this monograph, but can be found in, e. g., *Truesdell & Noll* [172], or *Ogden* [131], also cf. *Ehlers* [50].

### 3.2.3 Deformation rates and velocity gradient

To describe the temporal change of the previously established deformation and strain measures, the material velocity gradient  $(\mathbf{F}_\alpha)'_\alpha$  is introduced as the deformation rate relating to the reference state via

$$(\mathbf{F}_\alpha)'_\alpha = \frac{\mathrm{d}_\alpha}{\mathrm{d}t} \mathbf{F}_\alpha = \frac{\partial \dot{\mathbf{x}}_\alpha(\mathbf{X}_\alpha, t)}{\partial \mathbf{X}_\alpha} = \mathrm{Grad}_S \dot{\mathbf{x}}_\alpha \quad (3.24)$$

and the spatial velocity gradient  $\mathbf{L}_\alpha$  of the current state:

$$\mathbf{L}_\alpha = (\mathbf{F}_\alpha)'_\alpha \mathbf{F}_\alpha^{-1} = \mathrm{grad} \dot{\mathbf{x}}_\alpha \quad \text{and} \quad \mathbf{L}_\alpha \cdot \mathbf{I} = \mathrm{div} \dot{\mathbf{x}}_\alpha . \quad (3.25)$$

The spatial velocity gradient can be additively decomposed into its symmetric part  $\mathbf{D}_\alpha$  and its skew-symmetric part  $\mathbf{W}_\alpha$ , as shown in the following:

$$\mathbf{L}_\alpha = \frac{1}{2} (\mathbf{L}_\alpha + \mathbf{L}_\alpha^T) + \frac{1}{2} (\mathbf{L}_\alpha - \mathbf{L}_\alpha^T) = \mathbf{L}_\alpha^{\mathrm{sym}} + \mathbf{L}_\alpha^{\mathrm{skw}} =: \mathbf{D}_\alpha + \mathbf{W}_\alpha . \quad (3.26)$$

### 3.2.4 Stress measures

The deformations and strains discussed before are caused by forces  $\mathbf{k}$  acting on the body  $\mathcal{B}$ . These total forces can also be given separately for each constituent  $\varphi^\alpha$  via  $\mathbf{k}^\alpha$  and split into external forces  $\mathbf{k}_f^\alpha$  acting from a distance onto the volume of the body  $\mathcal{B}$  and into contact forces  $\mathbf{k}_N^\alpha$  acting at the near vicinity on the surface of the body  $\mathcal{S}$ :

$$\mathbf{k}^\alpha = \mathbf{k}_f^\alpha + \mathbf{k}_N^\alpha = \int_{\mathcal{B}} \mathbf{f}^\alpha \mathrm{d}v + \int_{\mathcal{S}} \mathbf{t}^\alpha \mathrm{d}a . \quad (3.27)$$

Hereby,  $\mathbf{f}^\alpha$  is the constituent- and volume-specific force acting from a distance and  $\mathbf{t}^\alpha$  is the contact force per surface area acting on the constituent  $\varphi^\alpha$ . With the a priori assumption that the external body force  $\mathbf{f}^\alpha$  is proportional to the partial density  $\rho^\alpha$  for all constituents  $\varphi^\alpha$  and with the usual interpretation of the body force as the gravitation<sup>3</sup>  $\mathbf{g}$ , it follows

$$\mathbf{f}^\alpha =: \rho^\alpha \mathbf{b}^\alpha = \rho^\alpha \mathbf{g} , \quad (3.28)$$

wherein,  $\mathbf{b}^\alpha$  is the external volume force per mass unit.

The contact force per surface area  $\mathbf{t}^\alpha = \mathbf{t}^\alpha(\mathbf{x}, t, \mathbf{n})$  is also called the traction and is a function of the current position  $\mathbf{x}$ , the time  $t$  and of the outward-oriented, normal surface vector  $\mathbf{n}$ , which was already introduced in (3.19). In order to find a stress measure that is independent of this surface normal vector, *Cauchy's* theorem is applied and yields

$$\mathbf{t}^\alpha(\mathbf{x}, t, \mathbf{n}) = [\mathbf{T}^\alpha(\mathbf{x}, t)] \mathbf{n} . \quad (3.29)$$

The stress measure  $\mathbf{T}^\alpha$  is the partial *Cauchy* stress tensor of the constituent  $\varphi^\alpha$ , also known as the true stress tensor. Proceeding from there, the surface force element  $d\mathbf{k}_\mathcal{N}^\alpha$  can be written as

$$d\mathbf{k}_\mathcal{N}^\alpha = \mathbf{t}^\alpha da = \mathbf{T}^\alpha \mathbf{n} da = \mathbf{T}^\alpha d\mathbf{a} . \quad (3.30)$$

Up to this point, the stress measures were completely formulated in the current configuration. Naturally, different alternative stress measures can be found by transporting both, the stress tensor itself and the area element back into the referential configuration. The sequential pull-back transport of the contact force then leads to the following expressions:

$$\begin{aligned} \mathbf{T}^\alpha d\mathbf{a} &= (\det \mathbf{F}_\alpha) \mathbf{T}^\alpha (\det \mathbf{F}_\alpha)^{-1} d\mathbf{a} && =: \boldsymbol{\tau}^\alpha d\bar{\mathbf{a}}_\alpha = \\ &= (\det \mathbf{F}_\alpha) \mathbf{T}^\alpha \mathbf{F}_\alpha^{T-1} (\text{cof } \mathbf{F}_\alpha)^{-1} d\mathbf{a} && =: \mathbf{P}^\alpha d\mathbf{A}_\alpha = \\ &= (\det \mathbf{F}_\alpha) \mathbf{F}_\alpha^{-1} \mathbf{T}^\alpha \mathbf{F}_\alpha^{T-1} (\text{cof } \mathbf{F}_\alpha)^{-1} d\mathbf{a} && =: \mathbf{S}^\alpha d\mathbf{A}_\alpha . \end{aligned} \quad (3.31)$$

The *Kirchhoff* stress tensor  $\boldsymbol{\tau}^\alpha = (\det \mathbf{F}_\alpha) \mathbf{T}^\alpha$  is derived by applying (3.19)<sub>2</sub> in order to weight the area element  $d\mathbf{a}$  in the current configuration with the volumetric change, via  $d\bar{\mathbf{a}}_\alpha = \frac{dV_\alpha}{dv} d\mathbf{a}$ . The pull-back transformation of the area element  $d\mathbf{a}$  to the referential configuration by  $d\mathbf{A}_\alpha = (\text{cof } \mathbf{F}_\alpha)^{-1} d\mathbf{a}$  leads to the first *Piola-Kirchhoff* stress tensor  $\mathbf{P}^\alpha = (\det \mathbf{F}_\alpha) \mathbf{T}^\alpha \mathbf{F}_\alpha^{T-1}$ . This two-field tensor relates forces specified in the current configuration to geometrical quantities given in the referential configuration. A further pull-back transport of the first *Piola-Kirchhoff* stress tensor finally results in the second *Piola-Kirchhoff* stress tensor  $\mathbf{S}^\alpha = \mathbf{F}_\alpha^{-1} \mathbf{P}^\alpha$ , which completely lives in the referential configuration. For completeness, the relations between the *Kirchhoff* and both *Piola-Kirchhoff* stress tensors are deduced from (3.31) and read:

$$\begin{aligned} \mathbf{P}^\alpha &= \boldsymbol{\tau}^\alpha \mathbf{F}_\alpha^{T-1} && \text{and } \boldsymbol{\tau}^\alpha = \mathbf{P}^\alpha \mathbf{F}_\alpha^T , \\ \mathbf{S}^\alpha &= \mathbf{F}_\alpha^{-1} \boldsymbol{\tau}^\alpha \mathbf{F}_\alpha^{T-1} && \text{and } \boldsymbol{\tau}^\alpha = \mathbf{F}_\alpha \mathbf{S}^\alpha \mathbf{F}_\alpha^T . \end{aligned} \quad (3.32)$$

---

<sup>3</sup>Other external forces are, for example magnetism.



Throughout the present work, the assumption of small deformations is made. Thus, a geometrically linear theory is exerted with  $\mathbf{F}_\alpha \approx \mathbf{I}$ , for both, push-forward and pull-back operations. Hence, the above developed relations between the stress tensors show that in the linear case, the current and the referential configurations of the stress tensors are approximately equal and are given by the linear stress tensor  $\boldsymbol{\sigma}^\alpha$ , viz.:

$$\mathbf{T}^\alpha \approx \boldsymbol{\tau}^\alpha \approx \mathbf{P}^\alpha \approx \mathbf{S}^\alpha \approx: \boldsymbol{\sigma}^\alpha . \quad (3.33)$$

### 3.3 Balance relations

Balance relations are the basic instrument to describe the change of a physical quantity over time. In this fundamental principle, the temporal change of the physical quantity in a body  $\mathcal{B}$  is balanced with the flow (influx or efflux) over the body's surface  $\mathcal{S}$ , the external source (supply) and the production of the physical quantity inside the body  $\mathcal{B}$ , cf. Figure 3.2. It is possible to integrate all balance relations into a master balance formulation, from which the particular balance relations can be axiomatically determined by inserting the respective quantities. Since this procedure has already been discussed in a number of contributions, e. g., *Ehlers* [54, 55] and citations therein, only a brief summary is given here.

In case of multi-phasic continua, which are the subject of this monograph, the formulation of the balance relations follows the works on the classical Theory of Mixtures, e. g., by *Bowen* [24, 25], *Kelly* [97], *Truesdell & Toupin* [173], and is especially based on the three well-known *metaphysical principles*, introduced by *Truesdell* [171]:

1. All properties of the mixture must be mathematical consequences of properties of the constituents.
2. So as to describe the motion of a constituent, we may in imagination isolate it from the rest of the mixture, provided we allow properly for the actions of the other constituents upon it.
3. The motion of the mixture is governed by the same equations as is a single body.

These three arguments state that the balance relations of the mixture result from the summation of the balance relations of the constituents. Thus, firstly, the global master balance relations for the constituents shall be presented here, according to *Ehlers* [52], both for scalar  $\Psi^\alpha$  and vectorial quantities  $\boldsymbol{\Psi}^\alpha$ , respectively:

$$\begin{aligned} \frac{d_\alpha}{dt} \int_{\mathcal{B}} \Psi^\alpha \, dv &= \int_{\mathcal{S}} \boldsymbol{\phi}^\alpha \cdot \mathbf{n} \, da + \int_{\mathcal{B}} \sigma^\alpha \, dv + \int_{\mathcal{B}} \hat{\Psi}^\alpha \, dv , \\ \frac{d_\alpha}{dt} \int_{\mathcal{B}} \boldsymbol{\Psi}^\alpha \, dv &= \int_{\mathcal{S}} \boldsymbol{\Phi}^\alpha \mathbf{n} \, da + \int_{\mathcal{B}} \boldsymbol{\sigma}^\alpha \, dv + \int_{\mathcal{B}} \hat{\boldsymbol{\Psi}}^\alpha \, dv . \end{aligned} \quad (3.34)$$

The physical quantities in (3.34) are itemised in the following:  $\Psi^\alpha$  and  $\mathbf{\Psi}^\alpha$  are the volume-specific densities of the physical quantity to be balanced,  $\sigma^\alpha$ ,  $\boldsymbol{\sigma}^\alpha$  are the volume densities of the supply acting on the body (external source) and  $\hat{\Psi}^\alpha$ ,  $\hat{\mathbf{\Psi}}^\alpha$  represent the total production due to interactions between the constituents  $\varphi^\alpha$  (intrinsic supply). Furthermore,  $\phi^\alpha$ ,  $\Phi^\alpha$  are the surface densities, describing the efflux of the physical quantity at the outer surface  $\mathcal{S}$  of  $\mathcal{B}$ . All these quantities are identified for the respective balance relations according to Table 3.1. The coefficients in Table 3.1 that have not been explained yet are: the *Cauchy*

Table 3.1: Specific physical quantities of the modified constituent master balances.

Balance	$\Psi^\alpha, \mathbf{\Psi}^\alpha$	$\phi^\alpha, \Phi^\alpha$	$\sigma^\alpha, \boldsymbol{\sigma}^\alpha$	$\hat{\Psi}^\alpha, \hat{\mathbf{\Psi}}^\alpha$
mass	$\rho^\alpha$	$\mathbf{0}$	0	$\hat{\rho}^\alpha$
momentum	$\rho^\alpha \dot{\mathbf{x}}_\alpha$	$\mathbf{T}^\alpha$	$\rho^\alpha \mathbf{b}^\alpha$	$\hat{\mathbf{s}}^\alpha$
m.o.m.	$\mathbf{x} \times (\rho^\alpha \dot{\mathbf{x}}_\alpha)$	$\mathbf{x} \times \mathbf{T}^\alpha$	$\mathbf{x} \times (\rho^\alpha \mathbf{b}^\alpha)$	$\hat{\mathbf{h}}^\alpha$
energy	$\rho^\alpha (\varepsilon^\alpha + \frac{1}{2} \dot{\mathbf{x}}_\alpha \cdot \dot{\mathbf{x}}_\alpha)$	$(\mathbf{T}^\alpha)^T \dot{\mathbf{x}}_\alpha - \mathbf{q}^\alpha$	$\rho^\alpha (\dot{\mathbf{x}}_\alpha \cdot \mathbf{b}^\alpha + r^\alpha)$	$\hat{e}^\alpha$
entropy	$\rho^\alpha \eta^\alpha$	$\phi_\eta^\alpha$	$\sigma_\eta^\alpha$	$\hat{\eta}^\alpha$

stress tensor  $\mathbf{T}^\alpha$ , the body force  $\mathbf{b}^\alpha$ , the internal energy  $\varepsilon^\alpha$ , the heat influx  $\mathbf{q}^\alpha$ , the external heat supply  $r^\alpha$ , the entropy  $\eta^\alpha$ , the entropy efflux  $\phi^\alpha$ , the external entropy supply  $\sigma_\eta^\alpha$  and the total production terms for mass  $\hat{\rho}^\alpha$ , momentum  $\hat{\mathbf{s}}^\alpha$ , moment of momentum  $\hat{\mathbf{h}}^\alpha$ , energy  $\hat{e}^\alpha$  and entropy  $\hat{\eta}^\alpha$ . Hereby, the total production terms follow the restrictions:

$$\sum_\alpha \hat{\rho}^\alpha = 0, \quad \sum_\alpha \hat{\mathbf{s}}^\alpha = \mathbf{0}, \quad \sum_\alpha \hat{\mathbf{h}}^\alpha = \mathbf{0}, \quad \sum_\alpha \hat{e}^\alpha = 0, \quad \sum_\alpha \hat{\eta}^\alpha \geq 0. \quad (3.35)$$

Therewith, it is guaranteed that the summation over all respective constituent balances results in the relations of the overall aggregate. The mass production  $\hat{\rho}^\alpha$  can be understood as the mass that is transferred from one constituent to the other, either due to chemical reactions, or due to phase-transition processes, whereas this work is only interested in the latter one. In mixture theories, it is customary to split the total production terms into direct parts and parts including productions terms from the lower balance relations, viz.:

$$\begin{aligned} \hat{\mathbf{s}}^\alpha &= \hat{\mathbf{p}}^\alpha + \hat{\rho}^\alpha \dot{\mathbf{x}}_\alpha, \\ \hat{\mathbf{h}}^\alpha &= \hat{\mathbf{m}}^\alpha + \mathbf{x} \times \hat{\mathbf{s}}^\alpha, \\ \hat{e}^\alpha &= \hat{\varepsilon}^\alpha + \hat{\mathbf{p}}^\alpha \cdot \dot{\mathbf{x}}_\alpha + \hat{\rho}^\alpha (\varepsilon^\alpha + \frac{1}{2} \dot{\mathbf{x}}_\alpha \cdot \dot{\mathbf{x}}_\alpha), \\ \hat{\eta}^\alpha &= \hat{\zeta}^\alpha + \hat{\rho}^\alpha \eta^\alpha. \end{aligned} \quad (3.36)$$

Herein,  $\hat{\mathbf{p}}^\alpha$  denotes the direct momentum production,  $\hat{\mathbf{m}}^\alpha$  corresponds to the direct moment of momentum production,  $\hat{\varepsilon}^\alpha$  is the direct part of the energy production and  $\hat{\zeta}^\alpha$  is the direct entropy production.

The global representation of the master balances in (3.34) can be transferred into the

local form by presuming the steadiness and the steady differentiability of (3.34):

$$\begin{aligned} (\Psi^\alpha)'_\alpha + \Psi^\alpha \operatorname{div} \dot{\mathbf{x}}_\alpha &= \operatorname{div} \phi^\alpha + \sigma^\alpha + \hat{\Psi}^\alpha, \\ (\Psi^\alpha)'_\alpha + \Psi^\alpha \operatorname{div} \dot{\mathbf{x}}_\alpha &= \operatorname{div} \Phi^\alpha + \sigma^\alpha + \hat{\Psi}^\alpha. \end{aligned} \quad (3.37)$$

Note in passing that (3.37) is valid at each material point  $\mathcal{P}^\alpha$  of the body  $\mathcal{B}$ .

Following the first and third metaphysical principles posted by *Truesdell*, the summation of the constituent balance relations leads to the mixture balance relations, where the global form reads:

$$\begin{aligned} \frac{d}{dt} \int_{\mathcal{B}} \Psi \, dv &= \int_{\mathcal{S}} \phi \cdot \mathbf{n} \, da + \int_{\mathcal{B}} \sigma \, dv + \int_{\mathcal{B}} \hat{\Psi} \, dv, \\ \frac{d}{dt} \int_{\mathcal{B}} \Psi \, dv &= \int_{\mathcal{S}} \Phi \mathbf{n} \, da + \int_{\mathcal{B}} \sigma \, dv + \int_{\mathcal{B}} \hat{\Psi} \, dv. \end{aligned} \quad (3.38)$$

The physical quantities in (3.38) have the same meaning as in the constituent balance relations, cf. Table 3.2. However, production terms cannot be encountered in the mixture

Table 3.2: Specific physical quantities of the modified mixture master balances.

Balance	$\Psi, \Psi$	$\phi, \Phi$	$\sigma, \sigma$	$\hat{\Psi}, \hat{\Psi}$
mass	$\rho$	$\mathbf{0}$	0	0
momentum	$\rho \dot{\mathbf{x}}$	$\mathbf{T}$	$\rho \dot{\mathbf{x}}$	$\mathbf{0}$
m.o.m.	$\mathbf{x} \times (\rho \dot{\mathbf{x}})$	$\mathbf{x} \times \mathbf{T}$	$\mathbf{x} \times (\rho \mathbf{b})$	$\mathbf{0}$
energy	$\rho (\varepsilon + \frac{1}{2} \dot{\mathbf{x}} \cdot \dot{\mathbf{x}})$	$(\mathbf{T})^T \dot{\mathbf{x}} - \mathbf{q}$	$\rho (\dot{\mathbf{x}} \cdot \mathbf{b} + r)$	0
entropy	$\rho \eta$	$\phi_\eta$	$\sigma_\eta$	$\hat{\eta} \geq 0$

balance relations for the fact of (3.35), except for the total entropy production  $\hat{\eta}$ .

In analogy to the local form of the constituent balance relation (3.37), the local mixture balance relation follows as

$$\begin{aligned} \dot{\Psi} + \Psi \operatorname{div} \dot{\mathbf{x}} &= \operatorname{div} \phi + \sigma + \hat{\Psi}, \\ \dot{\Psi} + \Psi \operatorname{div} \dot{\mathbf{x}} &= \operatorname{div} \Phi + \sigma + \hat{\Psi}, \end{aligned} \quad (3.39)$$

wherein  $(\dot{\cdot})$  represents the material time derivative  $d/dt$  of the respective quantity. By comparison of the constituent formulations with the mixture formulations, the result of *Truesdell's* first principle becomes apparent in each field of the balance relations:

$$\begin{aligned} \Psi &= \sum_{\alpha} \Psi^\alpha, \quad \phi \cdot \mathbf{n} = \sum_{\alpha} (\phi^\alpha - \Psi^\alpha \mathbf{d}_\alpha) \cdot \mathbf{n}, \quad \sigma = \sum_{\alpha} \sigma^\alpha, \quad \hat{\Psi} = \sum_{\alpha} \hat{\Psi}^\alpha, \\ \Psi &= \sum_{\alpha} \Psi^\alpha, \quad \Phi \mathbf{n} = \sum_{\alpha} (\Phi^\alpha - \Psi^\alpha \otimes \mathbf{d}_\alpha) \mathbf{n}, \quad \sigma = \sum_{\alpha} \sigma^\alpha, \quad \hat{\Psi} = \sum_{\alpha} \hat{\Psi}^\alpha. \end{aligned} \quad (3.40)$$

### 3.3.1 Specific balance equations

The specific balance equations for both, the mixture  $\varphi$  and the constituents  $\varphi^\alpha$ , are found by inserting the physical quantities of the Tables 3.1 and 3.2 into the respective master balance equations (3.37) and (3.39), in this case in the local form. Since the balance equations fashion a hierarchical structure, where “higher” equations build upon the “lower” ones, the lowest relation should be mentioned first.

#### Mass balance

The mass balance states that in a closed system the mass of the overall aggregate  $\varphi$  or of a constituent  $\varphi^\alpha$  must always remain constant:

$$\begin{aligned} \text{mixture :} \quad \dot{\rho} + \rho \operatorname{div} \dot{\mathbf{x}} &= 0, \\ \text{constituent :} \quad (\rho^\alpha)'_\alpha + \rho^\alpha \operatorname{div} \dot{\mathbf{x}}_\alpha &= \hat{\rho}^\alpha. \end{aligned} \tag{3.41}$$

The summation of (3.41)<sub>2</sub> over all constituents  $\varphi^\alpha$ , while using relations (3.9), (3.11) and (3.35)<sub>1</sub>, yields (3.41)<sub>1</sub>, which verifies *Truesdell's* first principle.

#### Momentum balance

The mixture and constituent formulations of the momentum balance follow next in the sequence of balance relations:

$$\begin{aligned} \text{mixture :} \quad \rho \ddot{\mathbf{x}} &= \operatorname{div} \mathbf{T} + \rho \mathbf{b}, \\ \text{constituent :} \quad \rho^\alpha \ddot{\mathbf{x}}_\alpha &= \operatorname{div} \mathbf{T}^\alpha + \rho^\alpha \mathbf{b}^\alpha + \hat{\mathbf{p}}^\alpha. \end{aligned} \tag{3.42}$$

The momentum balance is essential to describe the motions of the mixture or constituents, respectively.

#### Moment of momentum balance

The balance of moment of momentum is given as

$$\begin{aligned} \text{mixture :} \quad \mathbf{0} &= \mathbf{I} \times \mathbf{T}, \\ \text{constituent :} \quad \mathbf{0} &= \mathbf{I} \times \mathbf{T}^\alpha + \hat{\mathbf{m}}^\alpha. \end{aligned} \tag{3.43}$$

Thereof, the relation for the overall aggregate (3.43)<sub>1</sub> can be rewritten into  $\mathbf{T} = \mathbf{T}^T$ , which represents the symmetry of the overall *Cauchy* stress tensor. In case of non-polar materials (*Cauchy* or *Boltzmann* continua) that exhibit symmetric stresses on the microscale, the symmetry can be shown for the macroscopic stresses as well, cf. *Ehlers* [54] and *Hassanizadeh & Gray* [79]. Thus, the moment of momentum balance of a constituent (3.43)<sub>2</sub> becomes for non-polar materials

$$\mathbf{T}^\alpha = (\mathbf{T}^\alpha)^T \rightarrow \hat{\mathbf{m}}^\alpha \equiv \mathbf{0}. \tag{3.44}$$

Since this monograph deals only with non-polar materials, it shall only be mentioned here that the polar theory is applied for so-called *Cosserat* continua and more information on this topic can be found in, e. g., *Scholz* [159], *Diebels* [44, 45] and *Ehlers* [54].

### Energy balance

The next balance relation is the energy balance, also known as the *first law of thermodynamics*. The energy balance plays a major role in governing heat-transport processes and relating the different storage forms of energy, i. e., the internal energy, the kinetic energy, the external mechanical power and the non-mechanical power. Therefore, it is of special interest in this monograph, concerning the main topic of fluid-phase transition. The formulations of the energy balances for the mixture and the specific constituents read:

$$\begin{aligned} \text{mixture :} \quad \rho \dot{\varepsilon} &= \mathbf{T} \cdot \mathbf{L} - \operatorname{div} \mathbf{q} + \rho r, \\ \text{constituent :} \quad \rho^\alpha (\varepsilon^\alpha)'_\alpha &= \mathbf{T}^\alpha \cdot \mathbf{L}^\alpha - \operatorname{div} \mathbf{q}^\alpha + \rho^\alpha r^\alpha + \hat{\varepsilon}^\alpha. \end{aligned} \quad (3.45)$$

### Entropy balance

Finally, the entropy balance is given as

$$\begin{aligned} \text{mixture :} \quad \rho \dot{\eta} &= -\operatorname{div} \left( \frac{\mathbf{q}}{\theta} \right) + \frac{\rho r}{\theta} + \hat{\eta}, \\ \text{constituent :} \quad \rho^\alpha (\eta^\alpha)'_\alpha &= -\operatorname{div} \left( \frac{\mathbf{q}^\alpha}{\theta^\alpha} \right) + \frac{\rho^\alpha r^\alpha}{\theta^\alpha} + \hat{\zeta}^\alpha, \end{aligned} \quad (3.46)$$

wherein, the entropy efflux  $\phi_\eta$  and the entropy supply  $\sigma_\eta$  were replaced based on a priori constitutive assumptions, which can be found in *Ehlers* [52–56] and citations therein, and are formulated as

$$\phi_\eta = -\frac{\mathbf{q}}{\theta} \quad \text{and} \quad \sigma_\eta = \frac{\rho r}{\theta}, \quad \text{or} \quad \phi_\eta^\alpha = -\frac{\mathbf{q}^\alpha}{\theta^\alpha} \quad \text{and} \quad \sigma_\eta^\alpha = \frac{\rho^\alpha r^\alpha}{\theta^\alpha} \quad (3.47)$$

with  $\theta$  and  $\theta^\alpha$  being the mixture and constituent temperatures, respectively. The summation of (3.46)<sub>2</sub> over all constituents  $\varphi^\alpha$  together with the restriction of the entropy production (3.35)<sub>5</sub>, demonstrates that the total entropy production  $\hat{\eta}$  is never negative, cf. Table 3.2:

$$\hat{\eta} = \sum_\alpha \hat{\eta}^\alpha = \sum_\alpha \left[ \rho^\alpha (\eta^\alpha)'_\alpha + \hat{\rho}^\alpha \eta^\alpha + \operatorname{div} \left( \frac{\mathbf{q}^\alpha}{\theta^\alpha} \right) - \frac{\rho^\alpha r^\alpha}{\theta^\alpha} \right] \geq 0. \quad (3.48)$$

This means that the entropy of a closed system can only increase, but never decrease, which is mathematically captured in the famous *second law of thermodynamics*. Since the entropy is a physical quantity which is hardly determinable, a better applicable relation can be derived by incorporating both the energy balance (3.45)<sub>2</sub> and the definition of the *Helmholtz* free energy by the *Legendre* transformation (B.5),

$$\psi^\alpha := \varepsilon^\alpha - \theta^\alpha \eta^\alpha, \quad (3.49)$$

into (3.48), yielding the so-called inequality

$$\begin{aligned} \sum_{\alpha} \frac{1}{\theta^{\alpha}} \left\{ \mathbf{T}^{\alpha} \cdot \mathbf{L}^{\alpha} - \rho^{\alpha} [(\psi^{\alpha})'_{\alpha} + (\theta^{\alpha})'_{\alpha} \eta^{\alpha}] - \hat{\mathbf{p}}^{\alpha} \cdot \dot{\mathbf{x}}_{\alpha} - \right. \\ \left. - \hat{\rho}^{\alpha} (\psi^{\alpha} + \frac{1}{2} \dot{\mathbf{x}}_{\alpha} \cdot \dot{\mathbf{x}}_{\alpha}) - \frac{\mathbf{q}^{\alpha}}{\theta^{\alpha}} \cdot \text{grad } \theta^{\alpha} + \hat{e}^{\alpha} \right\} \geq 0. \end{aligned} \quad (3.50)$$

The formulations of constitutive relations for the mechanical and thermodynamical behaviour of multiphasic materials, which will be presented in Chapter 5, starts from evaluating this *Clausius-Duhem* entropy inequality to ensure the thermodynamical consistency of the formulation.

The balance relations in (3.41), (3.42), (3.43), (3.45) and (3.46) have been presented both for the overall aggregate  $\varphi$  and for the individual constituents  $\varphi^{\alpha}$ . The two formulations are linked together by the sum over all constituents with respect to the barycentric motion of the overall aggregate, shown already in general in (3.40) and which dictates the usage of (3.11) and (3.12). The resulting restrictions between the mixture and constituent formulations are:

$$\begin{aligned} \rho &= \sum_{\alpha} \rho^{\alpha}, & \rho \mathbf{b} &= \sum_{\alpha} \rho^{\alpha} \mathbf{b}^{\alpha}, \\ \rho \dot{\mathbf{x}} &= \sum_{\alpha} \rho^{\alpha} \dot{\mathbf{x}}_{\alpha}, & \rho \ddot{\mathbf{x}} &= \sum_{\alpha} [\rho^{\alpha} \ddot{\mathbf{x}}_{\alpha} - \text{div}(\rho^{\alpha} \mathbf{d}_{\alpha} \otimes \mathbf{d}_{\alpha}) + \hat{\rho}^{\alpha} \dot{\mathbf{x}}_{\alpha}], \\ \mathbf{T} &= \sum_{\alpha} (\mathbf{T}^{\alpha} - \rho^{\alpha} \mathbf{d}_{\alpha} \otimes \mathbf{d}_{\alpha}), & \mathbf{q} &= \sum_{\alpha} [\mathbf{q}^{\alpha} - (\mathbf{T}^{\alpha})^T \mathbf{d}_{\alpha} + \rho^{\alpha} \varepsilon^{\alpha} \mathbf{d}_{\alpha} + \frac{1}{2} (\mathbf{d}_{\alpha} \cdot \mathbf{d}_{\alpha}) \mathbf{d}_{\alpha}], \\ \rho r &= \sum_{\alpha} \rho^{\alpha} (r^{\alpha} + \mathbf{b}^{\alpha} \cdot \mathbf{d}_{\alpha}), & \rho \varepsilon &= \sum_{\alpha} \rho^{\alpha} (\varepsilon^{\alpha} + \frac{1}{2} \mathbf{d}_{\alpha} \cdot \mathbf{d}_{\alpha}). \end{aligned} \quad (3.51)$$

### 3.4 Singular surfaces

In Section 5.4.2 a constitutive relation for the mass production term  $\hat{\rho}^{\alpha}$  is developed based on the microscopic behaviour at the interface between the liquid and gaseous phases. This interface is mathematically described by a singular surface  $\Gamma$ , where discontinuities or jumps exist in the physical quantities. For this purpose, the balance relations introduced in Section 3.3 have to be adapted to include possible discontinuities. These are formulated here in a general form according to the work of *Mahnkopf* [113], who applied singular surfaces for the description of shear-band localisation within the TPM and derives the required compatibility conditions based on *Hadamard's* Lemma [78]. To avoid too much repetition of the work done by *Mahnkopf*, only a brief summary of the additional changes in the kinematics and balance relations is presented here.

### 3.4.1 Kinematics of a body with a singular surface

The derivation of the kinematical relations for a singular surface is oriented at the works of *Truesdell & Toupin* [173] and *Kosinski* [100], and described here within the TPM for multiphase continua, based on, e. g., *Markert et al.* [117] and *Ehlers & Haberle* [61]. Consider a triphasic aggregate  $\mathcal{B} = \bigcup_{\alpha} \mathcal{B}^{\alpha}$  with boundary surface  $\mathcal{S}$ , where  $\alpha = \{S, L, G\}$ . By introducing a separating and immaterial smooth and local surface indicating the interface  $\Gamma$ , the body  $\mathcal{B}$  is locally separated into two parts given by  $\mathcal{B}^+$  and  $\mathcal{B}^-$ , cf. Figure 3.3. The

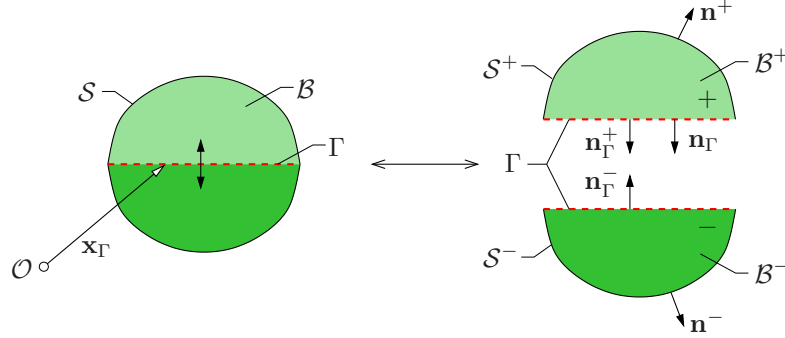


Figure 3.3: Local microstructural interface  $\Gamma$  dividing the body  $\mathcal{B}$  into the partitions  $\mathcal{B}^+$  and  $\mathcal{B}^-$ .

local body itself and its total surface are then given by  $\mathcal{B} = \mathcal{B}^+ \cup \mathcal{B}^-$  and  $\mathcal{S} = \mathcal{S}^+ \cup \mathcal{S}^-$ , whereas  $\mathcal{S}^{\pm} \cup \Gamma$  yields the entire surface of the body parts  $\mathcal{B}^{\pm}$ .

In this regard, a scalar-valued function  $\Psi(\mathbf{x}, t)$ , which is continuous in  $\mathcal{B}^+$  and  $\mathcal{B}^-$ , and which experiences a jump of  $\Psi$  over the interface  $\Gamma$ , is defined as the difference between its values in  $\mathcal{B}^+$  and  $\mathcal{B}^-$ , viz.:

$$\llbracket \Psi \rrbracket := \Psi^+ - \Psi^-, \quad (3.52)$$

wherein the jump operator  $\llbracket \cdot \rrbracket$  is introduced. The orientation of  $\Gamma$  at  $\mathcal{B}^+$  and  $\mathcal{B}^-$  is given by the outward-oriented surface normals  $\mathbf{n}_{\Gamma}^+$  and  $\mathbf{n}_{\Gamma}^-$  yielding

$$\mathbf{n}_{\Gamma}^+ = -\mathbf{n}_{\Gamma}^-, \quad \text{where} \quad \mathbf{n}_{\Gamma}^+ =: \mathbf{n}_{\Gamma}, \quad \mathbf{n}_{\Gamma}^- = -\mathbf{n}_{\Gamma}. \quad (3.53)$$

Regarding the kinematics of the singular surface shown in Figure 3.3, the inner surface  $\Gamma$  with the unit normal vector  $\mathbf{n}_{\Gamma}$  pointing from  $\mathcal{B}^+$  to  $\mathcal{B}^-$ , is allowed to propagate through  $\mathcal{B}$  and its velocity, as well as the relative velocity of a constituent  $\varphi^{\alpha}$  with respect to the moving interface  $\Gamma$ , are defined as

$$\dot{\mathbf{x}}_{\Gamma} = \mathbf{v}_{\Gamma}, \quad \mathbf{w}_{\alpha\Gamma} = \dot{\mathbf{x}}_{\alpha} - \dot{\mathbf{x}}_{\Gamma}. \quad (3.54)$$

### 3.4.2 Balance relations for a body with a singular surface

In case that  $\mathcal{B}$  is intersected by a singular surface  $\Gamma$ , one has to derive balance equations for the partitions  $\mathcal{B}^+$  and  $\mathcal{B}^-$  with the respective external surfaces  $\mathcal{S}(\mathcal{B}^+) = \mathcal{S}^+ \cup \Gamma$  and  $\mathcal{S}(\mathcal{B}^-) = \mathcal{S}^- \cup \Gamma$ . The derivation starts from the global master balance relations (3.34), which are still valid for the partitions  $\mathcal{B}^+$  and  $\mathcal{B}^-$ , if the partitions do not contain any

further discontinuous surfaces themselves. Thus, the respective master balances for the two partitions read, cf. right picture in Figure 3.3:

$$\begin{aligned} \text{in } \mathcal{B}^- : \quad \frac{d_\alpha}{dt} \int_{\mathcal{B}^-} \Psi^\alpha \, dv &= \int_{\mathcal{S}^-} \boldsymbol{\phi}^\alpha \cdot \mathbf{n}^- \, da + \int_{\Gamma} (\boldsymbol{\phi}^\alpha)^- \cdot \mathbf{n}_\Gamma^- \, da + \int_{\mathcal{B}^-} (\sigma^\alpha + \hat{\Psi}^\alpha) \, dv , \\ \text{in } \mathcal{B}^+ : \quad \frac{d_\alpha}{dt} \int_{\mathcal{B}^+} \Psi^\alpha \, dv &= \int_{\mathcal{S}^+} \boldsymbol{\phi}^\alpha \cdot \mathbf{n}^+ \, da + \int_{\Gamma} (\boldsymbol{\phi}^\alpha)^+ \cdot \mathbf{n}_\Gamma^+ \, da + \int_{\mathcal{B}^+} (\sigma^\alpha + \hat{\Psi}^\alpha) \, dv , \end{aligned} \quad (3.55)$$

provided that the field functions  $\Psi^\alpha$ ,  $\boldsymbol{\phi}^\alpha$  and  $\sigma^\alpha$  are continuous in  $\mathcal{B}^-$  and  $\mathcal{B}^+$ , as well as on the surface  $\Gamma$ . Please notice in passing that in (3.55) the surface integral for the flux  $\boldsymbol{\phi}^\alpha \cdot \mathbf{n}$  has been split into a part for the outer boundary of the partition ( $\mathcal{S}^-$  and  $\mathcal{S}^+$ ) and a part for the interface  $\Gamma$ . The summation of the balances of the two partitions (3.55)<sub>1,2</sub> yields the global balance relation for a body containing a singular surface  $\Gamma$ :

$$\frac{d_\alpha}{dt} \int_{\mathcal{B}} \Psi^\alpha \, dv = \int_{\mathcal{B} \setminus \Gamma} (\sigma^\alpha + \hat{\Psi}^\alpha) \, dv + \int_{\mathcal{S}} \boldsymbol{\phi}^\alpha \cdot \mathbf{n} \, da + \int_{\Gamma} [[\boldsymbol{\phi}^\alpha]] \cdot \mathbf{n}_\Gamma \, da . \quad (3.56)$$

In an analogous way, this form can be derived for vectorial physical quantities  $\boldsymbol{\Psi}^\alpha$ ,  $\boldsymbol{\Phi}^\alpha$  and  $\boldsymbol{\sigma}^\alpha$ :

$$\frac{d_\alpha}{dt} \int_{\mathcal{B}} \boldsymbol{\Psi}^\alpha \, dv = \int_{\mathcal{B} \setminus \Gamma} (\boldsymbol{\sigma}^\alpha + \hat{\boldsymbol{\Psi}}^\alpha) \, dv + \int_{\mathcal{S}} \boldsymbol{\Phi}^\alpha \cdot \mathbf{n} \, da + \int_{\Gamma} [[\boldsymbol{\Phi}^\alpha]] \cdot \mathbf{n}_\Gamma \, da . \quad (3.57)$$

Proceeding to the local form of the balance relations, in a first step, the modified *Reynolds* transport theorem has to be deduced, following *Mahnkopf* [113]:

$$\begin{aligned} \frac{d_\alpha}{dt} \int_{\mathcal{B}} \Psi^\alpha \, dv &= \int_{\mathcal{B} \setminus \Gamma} \frac{\partial \Psi^\alpha}{\partial t} \, dv + \int_{\mathcal{S}} \Psi^\alpha \dot{\mathbf{x}}_\alpha \cdot \mathbf{n} \, da + \int_{\Gamma} [[\Psi^\alpha (\dot{\mathbf{x}}_\alpha - \dot{\mathbf{x}}_\Gamma)]] \cdot \mathbf{n}_\Gamma \, da , \\ \frac{d_\alpha}{dt} \int_{\mathcal{B}} \boldsymbol{\Psi}^\alpha \, dv &= \int_{\mathcal{B} \setminus \Gamma} \frac{\partial \boldsymbol{\Psi}^\alpha}{\partial t} \, dv + \int_{\mathcal{S}} (\boldsymbol{\Psi}^\alpha \otimes \dot{\mathbf{x}}_\alpha) \cdot \mathbf{n} \, da + \int_{\Gamma} [[\boldsymbol{\Psi}^\alpha \otimes (\dot{\mathbf{x}}_\alpha - \dot{\mathbf{x}}_\Gamma)]] \cdot \mathbf{n}_\Gamma \, da . \end{aligned} \quad (3.58)$$

Herein, the left side stands for the material change of the field function  $\Psi^\alpha$  in relation to a material and timely variable volume element  $dv$ . This equals on the right side the local change of  $\Psi^\alpha$  based on a fixed (in time and space) volume element  $dv$ , the flux of  $\Psi^\alpha$  over the constant surface element  $da$  and the inner flux of  $\Psi^\alpha$  over the interface  $\Gamma$  for  $\dot{\mathbf{x}}_\alpha \neq \dot{\mathbf{x}}_\Gamma$ . Furthermore, the formulation for a vectorial physical quantity  $\boldsymbol{\Psi}^\alpha$  is provided in (3.58)<sub>2</sub>. Next, the insertion of the modified *Reynolds* transport theorem (3.58)<sub>1</sub> into the global



balance relations (3.56) and (3.57) yields:

$$\begin{aligned}
& \int_{\mathcal{B} \setminus \Gamma} \frac{\partial \Psi^\alpha}{\partial t} dv + \int_{\mathcal{S}} \Psi^\alpha \dot{\mathbf{x}}_\alpha \cdot \mathbf{n} da + \int_{\Gamma} \left[ \left[ \Psi^\alpha (\dot{\mathbf{x}}_\alpha - \dot{\mathbf{x}}_\Gamma) \right] \right] \cdot \mathbf{n}_\Gamma da = \\
& = \int_{\mathcal{B} \setminus \Gamma} (\sigma^\alpha + \hat{\Psi}^\alpha) dv + \int_{\mathcal{S}} \phi^\alpha \cdot \mathbf{n} da + \int_{\Gamma} \left[ \left[ \phi^\alpha \right] \right] \cdot \mathbf{n}_\Gamma da , \\
& \int_{\mathcal{B} \setminus \Gamma} \frac{\partial \Psi^\alpha}{\partial t} dv + \int_{\mathcal{S}} (\Psi^\alpha \otimes \dot{\mathbf{x}}_\alpha) \mathbf{n} da + \int_{\Gamma} \left[ \left[ \Psi^\alpha \otimes (\dot{\mathbf{x}}_\alpha - \dot{\mathbf{x}}_\Gamma) \right] \right] \mathbf{n}_\Gamma da = \\
& = \int_{\mathcal{B} \setminus \Gamma} (\boldsymbol{\sigma}^\alpha + \hat{\boldsymbol{\Psi}}^\alpha) dv + \int_{\mathcal{S}} \boldsymbol{\Phi}^\alpha \mathbf{n} da + \int_{\Gamma} \left[ \left[ \boldsymbol{\Phi}^\alpha \right] \right] \mathbf{n}_\Gamma da .
\end{aligned} \tag{3.59}$$

Applying the *Gaußian* integral theorem to the integrals over the outer surface  $\mathcal{S}$ , and using the relations for the total material time derivative (3.10) and for the relative interface velocity  $\mathbf{w}_{\alpha\Gamma}$  (3.54)<sub>2</sub>, it follows from (3.59), also compare, e. g., *Alts* and *Hutter* [5]:

$$\begin{aligned}
& \int_{\mathcal{B} \setminus \Gamma} [(\Psi^\alpha)'_\alpha + \Psi^\alpha \operatorname{div} \dot{\mathbf{x}}_\alpha] dv + \int_{\Gamma} \left[ \left[ \Psi^\alpha \mathbf{w}_{\alpha\Gamma} \right] \right] \cdot \mathbf{n}_\Gamma da = \int_{\mathcal{B} \setminus \Gamma} (\operatorname{div} \phi^\alpha + \sigma^\alpha + \hat{\Psi}^\alpha) dv + \\
& \quad + \int_{\Gamma} \left[ \left[ \phi^\alpha \right] \right] \cdot \mathbf{n}_\Gamma da , \\
& \int_{\mathcal{B} \setminus \Gamma} [(\boldsymbol{\Psi}^\alpha)'_\alpha + \boldsymbol{\Psi}^\alpha \operatorname{div} \dot{\mathbf{x}}_\alpha] dv + \int_{\Gamma} \left[ \left[ \boldsymbol{\Psi}^\alpha \otimes \mathbf{w}_{\alpha\Gamma} \right] \right] \mathbf{n}_\Gamma da = \int_{\mathcal{B} \setminus \Gamma} (\operatorname{div} \boldsymbol{\Phi}^\alpha + \boldsymbol{\sigma}^\alpha + \hat{\boldsymbol{\Psi}}^\alpha) dv + \\
& \quad + \int_{\Gamma} \left[ \left[ \boldsymbol{\Phi}^\alpha \right] \right] \mathbf{n}_\Gamma da .
\end{aligned} \tag{3.60}$$

Since these equations have to hold at the same time as (3.34), one obtains after sorting the integral terms for the body  $\mathcal{B}$  and the singular surface  $\Gamma$ :

$$\left. \begin{aligned}
& (\Psi^\alpha)'_\alpha + \Psi^\alpha \operatorname{div} \dot{\mathbf{x}}_\alpha = \operatorname{div} \phi^\alpha + \sigma^\alpha + \hat{\Psi}^\alpha , \\
& (\boldsymbol{\Psi}^\alpha)'_\alpha + \boldsymbol{\Psi}^\alpha \operatorname{div} \dot{\mathbf{x}}_\alpha = \operatorname{div} \boldsymbol{\Phi}^\alpha + \boldsymbol{\sigma}^\alpha + \hat{\boldsymbol{\Psi}}^\alpha
\end{aligned} \right\} \quad \forall \mathbf{x} \in \mathcal{B} \setminus \Gamma , \tag{3.61}$$

and

$$\left. \begin{aligned}
& \left[ \left[ \Psi^\alpha \mathbf{w}_{\alpha\Gamma} - \phi^\alpha \right] \right] \cdot \mathbf{n}_\Gamma = 0 , \\
& \left[ \left[ \boldsymbol{\Psi}^\alpha \otimes \mathbf{w}_{\alpha\Gamma} - \boldsymbol{\Phi}^\alpha \right] \right] \mathbf{n}_\Gamma = \mathbf{0}
\end{aligned} \right\} \quad \forall \mathbf{x} = \mathbf{x}_\Gamma \in \Gamma \tag{3.62}$$

substituting (3.37). Note that the local balances (3.61) are unchanged in comparison with (3.37), but are accompanied by jump conditions (3.62), describing the jump of the physical quantities across  $\Gamma$ .

Combining (3.61) and (3.62) with the specific physical quantities of Table 3.1, one obtains the local balance equations and jump conditions for mass, momentum and energy:

- mass:

$$\begin{aligned} (\rho^\alpha)'_\alpha + \rho^\alpha \operatorname{div} \dot{\mathbf{x}}_\alpha &= \hat{\rho}^\alpha \quad \forall \mathbf{x} \in \mathcal{B} \setminus \Gamma, \\ \llbracket \rho^\alpha \mathbf{w}_{\alpha\Gamma} \rrbracket \cdot \mathbf{n}_\Gamma &= 0 \quad \forall \mathbf{x} = \mathbf{x}_\Gamma \in \Gamma, \end{aligned} \quad (3.63)$$

- momentum:

$$\begin{aligned} \rho^\alpha \ddot{\mathbf{x}}_\alpha &= \operatorname{div} \mathbf{T}^\alpha + \rho^\alpha \mathbf{b} + \hat{\mathbf{p}}^\alpha \quad \forall \mathbf{x} \in \mathcal{B} \setminus \Gamma, \\ \llbracket \rho^\alpha \dot{\mathbf{x}}_\alpha \otimes \mathbf{w}_{\alpha\Gamma} - \mathbf{T}^\alpha \rrbracket \cdot \mathbf{n}_\Gamma &= \mathbf{0} \quad \forall \mathbf{x} = \mathbf{x}_\Gamma \in \Gamma, \end{aligned} \quad (3.64)$$

- energy:

$$\begin{aligned} \rho^\alpha (\varepsilon^\alpha)'_\alpha &= \mathbf{T}^\alpha \cdot \mathbf{L}_\alpha - \operatorname{div} \mathbf{q}^\alpha + \rho^\alpha r^\alpha + \hat{\varepsilon}^\alpha \quad \forall \mathbf{x} \in \mathcal{B} \setminus \Gamma, \\ \llbracket \rho^\alpha (\varepsilon^\alpha + \frac{1}{2} \dot{\mathbf{x}}_\alpha \cdot \dot{\mathbf{x}}_\alpha) \mathbf{w}_{\alpha\Gamma} - (\mathbf{T}^\alpha)^T \dot{\mathbf{x}}_\alpha + \mathbf{q}^\alpha \rrbracket \cdot \mathbf{n}_\Gamma &= 0 \quad \forall \mathbf{x} = \mathbf{x}_\Gamma \in \Gamma. \end{aligned} \quad (3.65)$$

These are the final local forms of the balance equations, which will be evaluated later in Chapter 5 to derive constitutive relations, e. g., for the mass production term  $\hat{\rho}^\alpha$ , and to formulate the governing balance relations.

Therewith, the theoretical fundamentals are completed and one can proceed to the next Chapter 4, where the thermodynamics of fluids are examined more closely.

## Chapter 4: Thermodynamic theory of fluids

Obviously, the main focus of this work, i. e., the phase transition of fluids, can only be handled by understanding the thermodynamic theory of fluids. The physical properties of gases and liquids are dependent on the physical interactions between the molecules of a substance. Since the direct modelling of this molecular behaviour is difficult and too expensive for an engineering approach in large systems, the thermodynamic properties shall be derived here by correlations and semi-empirical functions, i. e., the so-called *equations of state* (EOS).

In this context, the probably most well-known correlation is based on *Avogadro's hypothesis* [9]:

Equal volumes of all gases, at the same temperature and pressure, have the same number of molecules.

This correlation between the three physical properties effective fluid pressure  $p^{\beta R}$ , effective fluid volume  $V^{\beta R}$ , and temperature  $\theta^\beta$ , is mathematically formulated in the *ideal-gas law*:

$$p^{\beta R} V^{\beta R} = n_m^\beta R \theta^\beta, \quad (4.1)$$

where  $n_m^\beta$  is the number of moles and  $R = 8.314 \text{ J/molK}$  is the universal gas constant. Hence, the  $p^{\beta R}$ - $V^{\beta R}$ - $\theta^\beta$ -relation defines the thermodynamical conditions. As the name of the ideal gas law already suggests, it is only valid for ideal gases. An ideal gas is distinguished by randomly moving, point-like molecules, which only interact with each other by elastic collisions. To describe real gases and also liquids, this equation has to be extended, which will be presented in Section 4.1 together with a detailed discussion of the phase-transition process from the thermodynamical point of view.

In the subsequent sections, the relations for further thermodynamic properties are introduced. In particular, these are the vaporisation enthalpy, the specific heat capacity, the shear viscosity and the thermal conductivity. These properties are required for a realistic model of non-isothermal fluid flow through porous media.

Although the main topic of this monograph is the  $\text{CO}_2$  sequestration and the thermodynamical behaviour of this material under changing reservoir conditions, it is intended in the following, to formulate the model and the thermodynamic theory not specifically for  $\text{CO}_2$ , but in general for arbitrary substances. Hence, the goal is to develop a model that is capable of describing different substances by only changing the respective parameters for the fluid in question, e. g.,  $\text{CO}_2$ , or water, and so on.

## 4.1 Phase behaviour of a single substance

Each substance can inherit different physical states, i. e. solid, liquid, gas or supercritical<sup>1</sup>. These states are defined by the pressure  $p^{\beta R}$ , the temperature  $\theta^\beta$  and the specific volume  $v^{\beta R}$  (or the density  $\rho^{\beta R}$  as the inverse form). The relationship between these variables and how they define the different states or phases of a substance are visualised in the phase-diagram in Figure 4.1. The regions denoted by  $S$ ,  $L$  and  $G$  represent the solid, liquid and

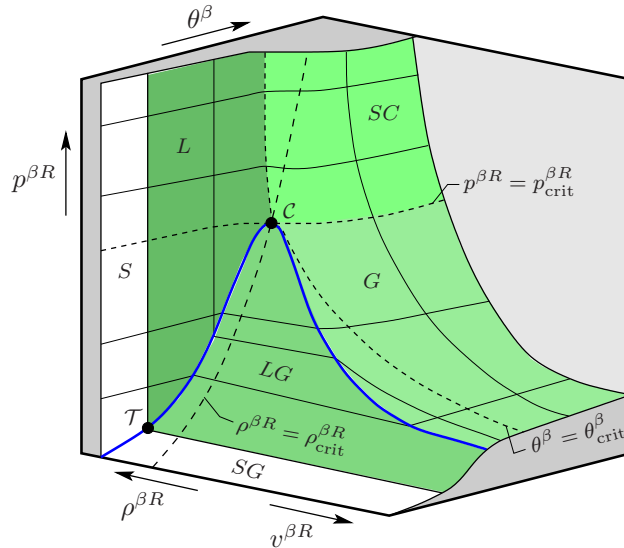


Figure 4.1: 3-d phase diagram of the  $p^{\beta R}$ - $\theta^\beta$ - $\rho^{\beta R}$  (or  $-v^{\beta R}$ ) relationship. The dashed lines indicate the lines of constant critical values of the three variables. The character abbreviations stand for the regions with specific phase behaviour:  $S$ : solid,  $L$ : liquid,  $G$ : gas,  $SG$ : solid-gas,  $LG$ : liquid-gas,  $SC$ : supercritical,  $\mathcal{C}$ : critical point and  $\mathcal{T}$ : triple point.

gaseous phases, respectively. Below the blue line, which is called the vaporisation curve, are the two-phase regions  $LG$  and  $SG$ , where two phases, liquid and gas or solid and gas, coexist. The vapour-pressure curve comprises also the critical point  $\mathcal{C}$ , which marks the end of the two-phase region for increasing pressures, as well as the triple point  $\mathcal{T}$ , that is the point of three coexisting phases solid, liquid and gas. The supercritical region  $SC$  is reached for pressures and temperatures above the critical values of the respective material. In Figure 4.1, the thin black lines and the dashed lines mark lines of constant variables, whereas the latter stand for critical values of pressure  $p_{\text{crit}}^{\beta R}$ , temperature  $\theta_{\text{crit}}^\beta$  and density  $\rho_{\text{crit}}^{\beta R}$ . Please note in passing that the critical isotherm  $\theta_{\text{crit}}^\beta$  exhibits a saddle point at the critical point  $\mathcal{C}$ .

A projection of the 3-d phase diagram into the pressure-temperature plane reveals the 2-d phase diagram in Figure 4.2(a), showing the vaporisation curve (blue). During the phase transition from liquid to gas, under isothermal conditions and driven by a decreasing pressure, the actual phase transition appears in the  $p^{\beta R}$ - $\theta^\beta$ -diagram, Figure 4.2(a), as a

<sup>1</sup>Sometimes, also plasma is regarded as a separate physical state. Plasma is generated by heating gas or applying a strong electromagnetic field to gas. It is characterised by its charged ions, making it electrically conductive.

single point on the vaporisation curve, whereas in the  $p^{\beta R}$ - $v^{\beta R}$ -diagram, Figure 4.2(b), an isobar connects the points of the liquid and gaseous phases on the vaporisation curve. These two points indicate the liquid specific volume  $v^{LR}$  and the gaseous specific volume  $v^{GR}$ , which are in equilibrium during phase transition. It is also possible to change between the gas and liquid phases without crossing the two-phase region. This can be accomplished by making a detour around the critical point through the supercritical region. In this regard, it is important to point out that changes between liquid and supercritical, as well as between gas and supercritical are continuous, i. e., without jumps in the density, unlike the phase transition through the two-phase region. This feature is adopted, e. g., in extraction processes, called supercritical fluid extraction, such as the decaffeination of coffee. For further information on this topic, the interested reader is referred to *Brunner & Budich* [33] and citations therein.

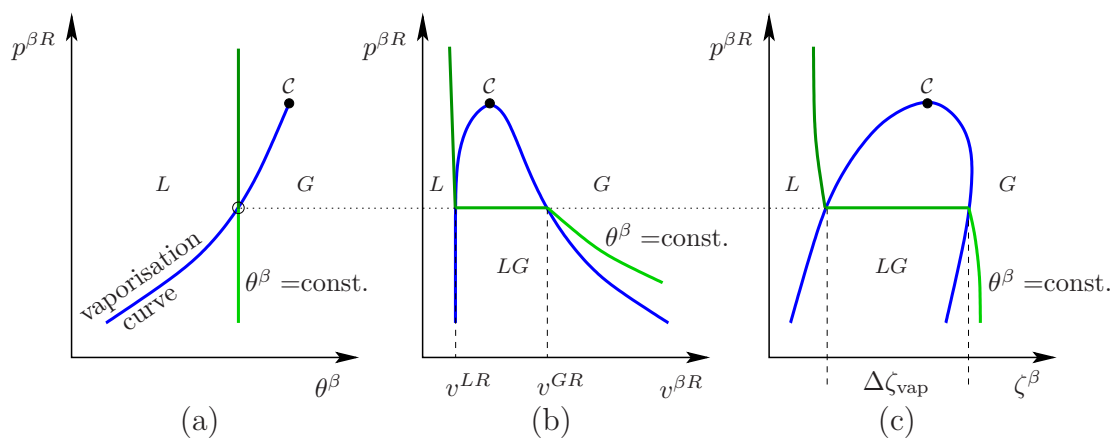


Figure 4.2: 2-d phase diagrams, where in all of them the same isotherm is highlighted (dark green: liquid, green: two-phase region, light green: gas). (a)  $p^{\beta R}$ - $\theta^{\beta}$ -diagram with the vaporisation curve (blue), (b)  $p^{\beta R}$ - $v^{\beta R}$ -diagram with the two-phase region  $LG$ , (c)  $p^{\beta R}$ - $\zeta^{\beta}$ -diagram with the vaporisation enthalpy  $\Delta\zeta_{\text{vap}}$ . The dotted line connects the point or lines of phase transition in all three diagrams.

Furthermore, the rightmost diagram, Figure 4.2(c), shows the relation between the effective pressure  $p^{\beta R}$  and the enthalpy  $\zeta^{\beta}$ . The difference between the liquid and gas enthalpies,  $\Delta\zeta_{\text{vap}} = \zeta^G - \zeta^L$ , expresses the vaporisation enthalpy. This enthalpy difference will be discussed in more detail later in Section 4.1.2.

### Ideal gas law

The first attempt to describe the relationship between pressure, temperature and volume builds upon findings by *Boyle* and *Mariotte*:

The pressure is inversely proportional to the volume for isothermal processes.

by *Gay-Lussac* and *Charles*:

The volume is proportional to the temperature for isobaric processes.

and *Avogadro*:

The gas constant is identical for all ideal gases.

These statements condense into the so-called ideal-gas law, as already mentioned in (4.1) in the introduction to this chapter, cf., e. g., *Lewis & Randall* [105]:

$$p^{\beta R} v^{\beta R} = R^{\beta} \theta^{\beta} , \quad (4.2)$$

which takes into account the linear relationship between pressure, temperature and specific volume and where  $R^{\beta}$  is the specific gas constant related to the considered substance by dividing the universal gas constant  $R$  with the respective molar mass  $M^{\beta}$ ,  $R^{\beta} = R/M^{\beta}$ . Furthermore, (4.1) and (4.2) are connected by the definition of the specific volume  $v^{\beta R} = V^{\beta R}/m^{\beta}$  and the relation between the mass  $m^{\beta}$  and the number of moles  $n_m^{\beta}$ ,  $m^{\beta} = n_m^{\beta} M^{\beta}$ . Ideal-gas behaviour can only be assumed for a gas at very low pressure and/or high temperature, where the interactions between the molecules of the gas can be neglected. To account for the deviations from ideal-gas behaviour, the dimensionless compressibility factor  $Z^{\beta}$  has been introduced via

$$Z^{\beta} \equiv \frac{p^{\beta R} v^{\beta R}}{R^{\beta} \theta^{\beta}} . \quad (4.3)$$

The compressibility factor is equal to one for an ideal gas, little less for real gases and much less for liquids. In case of very high temperatures and pressures, it can be slightly larger than one. Due to the dimensionless formulation of the compressibility factor, it is usually given as a function of reduced temperature and pressure or volume, e. g., *Poling et al.* [137]:

$$Z^{\beta} = f_{p_r^{\beta R}}(p_r^{\beta R}, \theta_r^{\beta}) = f_{v_r^{\beta R}}(v_r^{\beta R}, \theta_r^{\beta}) . \quad (4.4)$$

The dimensionless or reduced variables are derived by relating the actual quantities to characteristic properties, where usually the critical properties ( $p_{\text{crit}}^{\beta R}$ ,  $\theta_{\text{crit}}^{\beta}$ ,  $\rho_{\text{crit}}^{\beta R}$ ) of a substance are taken:

$$p_r^{\beta R} = \frac{p^{\beta R}}{p_{\text{crit}}^{\beta R}} , \quad \theta_r^{\beta} = \frac{\theta^{\beta}}{\theta_{\text{crit}}^{\beta}} , \quad v_r^{\beta R} = \frac{v^{\beta R}}{v_{\text{crit}}^{\beta R}} . \quad (4.5)$$

This allows for a substance-independent description of the  $p^{\beta R}$ - $v^{\beta R}$ - $\theta^{\beta}$ -relation, also called the *corresponding states principle* (CSP). This principle was proposed by *van der Waals* on the assumption that intermolecular forces dictate equilibrium properties, such as the critical properties. These forces are universal for many fluids, except for molecules with strong polarisations or subjected to hydrogen-bonds. In other words, most substances obey the same form of EOS, which results in a general compressibility factor

$$Z = \frac{p_r^{\beta R} v_r^{\beta R}}{R^{\beta} \theta_r^{\beta}} , \quad (4.6)$$

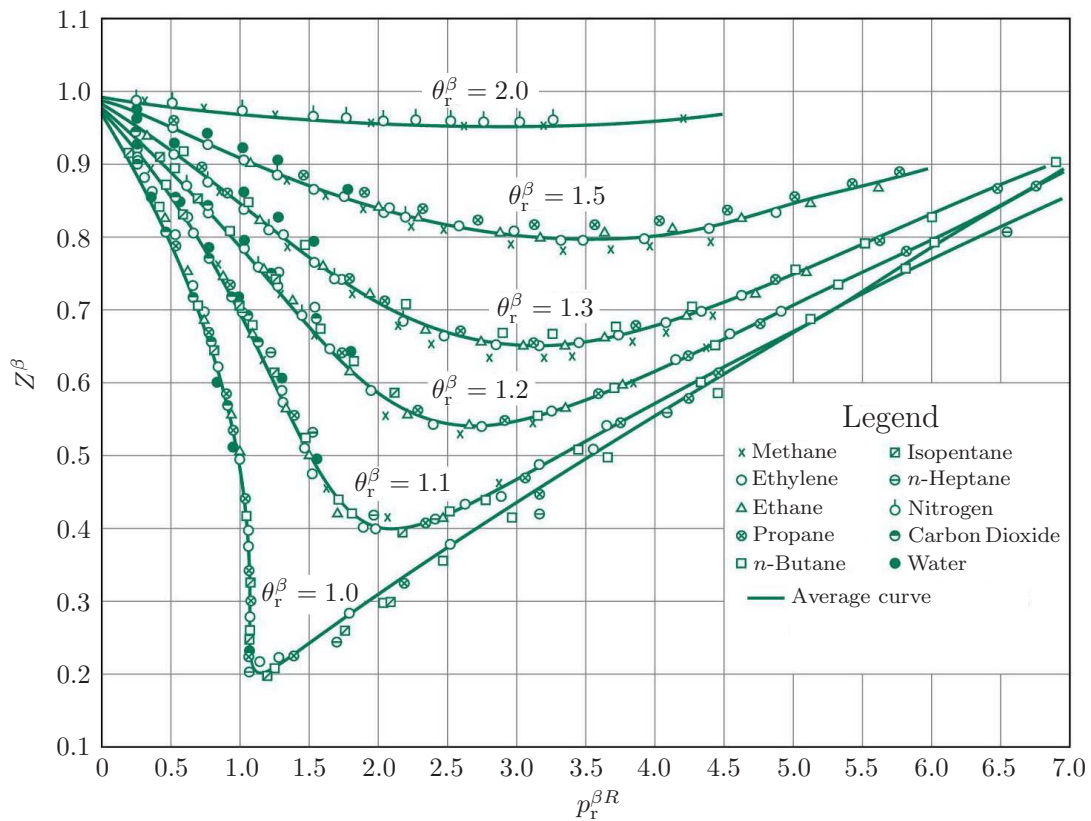


Figure 4.3: Graph of the compressibility factor  $Z^\beta$  versus the reduced pressure  $p_r^{\beta R}$  at different reduced temperatures  $\theta_r^\beta$  for several gases. Additionally, an average curve derived from data of hydrocarbons is given. It shows that in terms of reduced variables, all gases obey the same EOS. Figure was taken from *Su* [169].

when using reduced variables as illustrated in Figure 4.3. Therefore, CSP is often the basis for the development of correlations between different substances, not only for the determination of the EOS, but also for other thermodynamic properties, e. g., viscosity. For further information on the topic of the application of CSP, the interested reader is referred to *Lewis & Randall* [105], or *Ott & Boerio-Goates* [134].

### Virial equation of state

The ideal gas law is the lowest level CSP and works only for simple fluids, such as inert gases. For other substances, the EOS must be expanded. This can be accomplished based on the *kinetic theory of gases*, which takes into account the non-zero size of the molecules and describes them as hard spheres. In this regard, semi-empirical functions are defined for the mutual attractive and repulsive behaviour between these hard spheres. One approach to describe real gases on this basis is the so-called *virial equation of state*, which uses a power series in either  $1/v^{\beta R}$ , such that:

$$p^{\beta R} v^{\beta R} = R^\beta \theta^\beta \left[ 1 + \frac{B_v(\theta^\beta)}{v^{\beta R}} + \frac{C_v(\theta^\beta)}{(v^{\beta R})^2} + \frac{D_v(\theta^\beta)}{(v^{\beta R})^3} + \dots \right], \quad (4.7)$$

or in  $p^{\beta R}$

$$p^{\beta R} v^{\beta R} = R^{\beta} \theta^{\beta} + B_p(\theta^{\beta}) p^{\beta R} + C_p(\theta^{\beta}) (p^{\beta R})^2 + D_p(\theta^{\beta}) (p^{\beta R})^3 + \dots \quad (4.8)$$

Therein,  $B_v, C_v, D_v$  are the virial coefficients of the virial EOS explicit in specific volume, and  $B_p, C_p, D_p$  are the virial coefficients of the virial EOS explicit in pressure. These coefficients are only functions of the temperature. In case of (4.7), they roughly represent the interaction potential between the molecules, i. e., pair-wise interaction in  $B_v$ , interaction between three molecules in  $C_v$  and so on. However, these calculations become difficult and inaccurate for higher order terms and must be usually derived experimentally. The first two coefficients of (4.7) and (4.8) are related via

$$B_p = B_v, \quad \text{and} \quad C_p = \frac{C_v - B_v^2}{R^{\beta} \theta^{\beta}}. \quad (4.9)$$

In case of low pressures, equation (4.8) is truncated after the second term and solved explicitly for the volume:

$$v^{\beta R} = \frac{R^{\beta} \theta^{\beta}}{p^{\beta R}} + B_p. \quad (4.10)$$

### Cubic equation of state

The next type of EOS, which shall be discussed here, is the *cubic equation of state*. These equations are able to represent the pressure as a function of temperature and volume or density for both, gas and liquid phases at the same time. To achieve this with only one set of parameters, the equation requires at least a cubic formulation in the volume / density. The simplest formulation of this kind was proposed by *van der Waals* (vdW-EOS), who derived an extension of the ideal gas law (4.2), e. g., *Abbott & van Ness* [1]:

$$p^{\beta R} = \frac{R^{\beta} \theta^{\beta}}{v^{\beta R} - b} - \frac{a}{(v^{\beta R})^2}. \quad (4.11)$$

Herein, the constant  $a$  is a measure for the attractive forces, also called the cohesion pressure, and the constant  $b$  refers to the non-zero volume of the molecules and is sometimes denoted as the co-volume. To achieve better representation of the real phase behaviour, the parameters  $a$  and  $b$  in (4.11) can be calculated from the compressibility factor (4.6), which yields a representation depending on the critical temperatures  $\theta_{\text{crit}}^{\beta}$  and the critical pressures  $p_{\text{crit}}^{\beta R}$ :

$$a = \frac{27 (R^{\beta} \theta_{\text{crit}}^{\beta})^2}{64 p_{\text{crit}}^{\beta R}}, \quad b = \frac{R^{\beta} \theta_{\text{crit}}^{\beta}}{8 p_{\text{crit}}^{\beta R}}. \quad (4.12)$$

This semi-empirical equation gives reasonable results for conditions which are not too close to the critical point and not at too high temperatures and pressures. In other words, the vdW-EOS is not very accurate for the liquid phase, cf. *Ott & Boerio-Goates* [134].

Since in this work,  $\text{CO}_2$  is the mainly investigated substance, the two most prominent cubic EOS for the description of this substance shall be mentioned here. These are the *Peng-Robinson* equation (PR-EOS) and the *Soave-Redlich-Kwong* equation (SRK-EOS).



The PR-EOS is given here with respect to the density, but can easily be written in the form of the specific volume:

$$p^{\beta R} = \frac{R^\beta \theta^\beta \rho^{\beta R}}{1 - b \rho^{\beta R}} - \frac{a c (\rho^{\beta R})^2}{1 + 2b \rho^{\beta R} - (\rho^{\beta R})^2}. \quad (4.13)$$

The coefficients  $a$ ,  $b$  and  $c$  are calculated as follows:

$$\begin{aligned} a &= 0.45724 \frac{(R^\beta \theta_{\text{crit}}^\beta)^2}{p_{\text{crit}}^{\beta R}}, \\ b &= 0.0778 \frac{R^\beta \theta_{\text{crit}}^\beta}{p_{\text{crit}}^{\beta R}}, \\ c &= \left[ 1 + (0.37464 + 1.54226 \omega^\beta - 0.26992 (\omega^\beta)^2) \left(1 - \sqrt{\frac{\theta^\beta}{\theta_{\text{crit}}^\beta}}\right) \right]^2. \end{aligned} \quad (4.14)$$

Therein,  $\omega^\beta$  is the acentric factor, which is a CSP parameter for phase characterisation, based on the polarisation of the substance in question. The estimation for the acentric factor proposed by *Lewis and Randall* [105],

$$\omega^\beta \equiv -\log_{10} \left( \frac{p_{\text{vap}}^R}{p_{\text{crit}}^{\beta R}} \right) - 1.0, \quad \text{at } \theta_r^\beta = 0.7, \quad (4.15)$$

is calculated for a vapour pressure  $p_{\text{vap}}^R$  at  $\theta_r^\beta = \theta^\beta / \theta_{\text{crit}}^\beta = 0.7$ . The latter can be determined, for example, with the *Antoine* equation, cf. (4.19). In case of  $\text{CO}_2$ , the acentric factor is found as  $\omega^{\text{CO}_2} = 0.225$ .

An EOS with a similarly good descriptive behaviour as the PR-EOS is the *Soave-Redlich-Kwong* equation SRK-EOS, *Soave* [166]:

$$p^{\beta R} = \frac{R^\beta \theta^\beta \rho^{\beta R}}{1 - b \rho^{\beta R}} - \frac{a c (\rho^{\beta R})^2}{1 + b \rho^{\beta R}}, \quad (4.16)$$

where the coefficients  $a$ ,  $b$  and  $c$  are given as

$$\begin{aligned} a &= 0.42747 \frac{(R^\beta \theta_{\text{crit}}^\beta)^2}{p_{\text{crit}}^{\beta R}}, \\ b &= 0.08664 \frac{R^\beta \theta_{\text{crit}}^\beta}{p_{\text{crit}}^{\beta R}}, \\ c &= \left[ 1 + (0.48 + 1.574 \omega^\beta - 0.176 (\omega^\beta)^2) \left(1 - \sqrt{\frac{\theta^\beta}{\theta_{\text{crit}}^\beta}}\right) \right]^2. \end{aligned} \quad (4.17)$$

Beside these three presented cubic EOS, a long list of slightly different definitions of cubic EOS exist, which will not all be mentioned here. A good overview of them is presented,

e. g., in *Poling et al.* [137]. The different EOS are compared in their prediction of  $p^{\beta R}$ - $\theta^\beta$ - $\rho^{\beta R}$ -properties using the CSP in the work of *Ott & Boerio-Goates* [134].

In this monograph, it is intended to implement a holistic calculation of the thermodynamical properties, i. e., the *Helmholtz* free energy, the internal energy and the entropy, in the numerical model, that are needed, for example, in the energy balance. These calculations build upon the relation between the *Helmholtz* free energy with the quantities  $p^{\beta R}$ ,  $\theta^\beta$ , and  $\rho^{\beta R}$ , which are again dependent on the EOS. Therefore, it is necessary that the EOS is good-natured, since it is applied in building the derivatives or integrals with respect to temperature and pressure during the determination of the *Helmholtz* free energies. More precisely, it became obvious that the second terms in the PR-EOS (4.13) and in the SRK-EOS (4.16) jeopardise the calculations, because of the square-root in the temperature, appearing in the coefficient  $c$ . Thus, it would not be possible to find a closed formulation for the *Helmholtz* free energies. This is due to the fact that EOS are usually only phenomenologically motivated, without caring for their thermodynamic consistency, which was already acknowledged by *Lewis and Randall* [105]. Thus, many EOS are not suitable for a closed formulation. Consequently, it was decided to chose the vdW-EOS as the governing EOS in the development of the model, since (4.11) does not contain the coefficient  $c$ . The principle of deriving the *Helmholtz* free energies based on the cubic EOS is discussed in Section 5.3.4.

The drawback in the choice of the vdW-EOS is the poor accuracy in the description of the liquid phase, as was already explained before. In order to illustrate this discrepancy, water is selected as a fluid with well-known phase behaviour. Figure 4.4 depicts several isotherms in a pressure-density diagram for water. Therein, the dashed lines were calculated from the

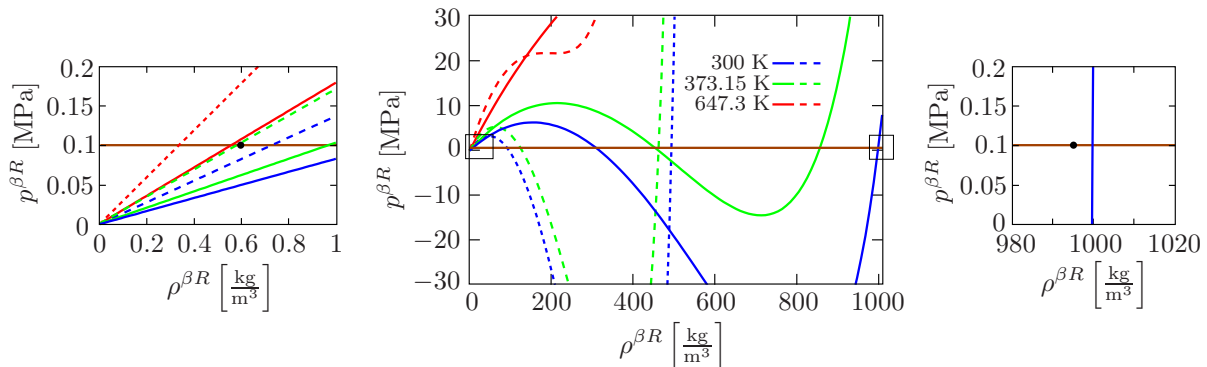


Figure 4.4: Middle: Pressure-density diagram of water calculated for ambient (300 K), boiling (373.15 K) and critical (647.3 K) temperatures from the original vdW-EOS (4.11) (dashed lines) and from the modified vdW-EOS (4.18) (solid lines). For water, the parameters of the modified vdW-EOS were found as  $u = 1.34$  and  $w = 2.23$ , by adjusting to two points: first, at boiling temperature, the *Maxwell* criterion must provide a density of  $0.598 \text{ kg/m}^3$  for the gaseous phase at ambient pressure (0.1013 MPa), cf. black dot in the left picture, and second, the blue isotherm should yield a density of  $996.56 \text{ kg/m}^3$  at ambient pressure (0.1013 MPa), cf. black dot depicted in the right picture. The positions of the black dots were taken from the NIST Chemistry WebBook *Lemmon et al.* [104]. The brown line marks the standard atmospheric pressure at  $p^{\beta R} = 0.1013 \text{ MPa}$ .

original vdW-EOS. It clearly shows that the density at standard conditions ( $\theta^\beta = 300 \text{ K}$

and  $p^{LR} = 1.0 \cdot 10^5$  Pa) is not around the expected  $1000 \text{ kg/m}^3$ , but much smaller at ca.  $500 \text{ kg/m}^3$ . By adding two parameters  $u$  and  $w$  to (4.11) for adjustment and replacing  $v^{\beta R}$  by  $1/\rho^{\beta R}$  via

$$p^{\beta R} = u \frac{R^\beta \theta^\beta \left(\frac{\rho^{\beta R}}{w}\right)}{1 - b \left(\frac{\rho^{\beta R}}{w}\right)} - a \left(\frac{\rho^{\beta R}}{w}\right)^2, \quad (4.18)$$

this discrepancy can be removed. The results of this modified vdW-EOS are shown in Figure 4.4 by the solid isotherms, where in the right picture the zoom of the 300 K isotherm at ambient pressure  $p^{\beta R} = 0.1$  MPa reveals the improved reproduction of the real behaviour of the water. However, these parameters cause the vdW-EOS to be incorrect at other conditions, for example, the critical isotherm (for water at 647.3 K) is no longer marked by a saddle point at the critical pressure (for water at 22.09 MPa), cf. red solid isotherm in Figure 4.4. Even so, these adjustment parameters will be used in the following, since the temperature changes are limited to  $\Delta\theta_{\max.} = 120$  K and the considered conditions stay away from the critical temperature<sup>2</sup>. Thus, it is possible to determine realistic densities, also in the case of phase change, which can be seen in the left picture in Figure 4.4, where the green curves compare the boiling temperature of water calculated with the original and the modified vdW-EOS. Applying the *Maxwell* criterion (introduced in the next section) to the boiling temperature isotherm (for water 373,15 K) shows that the dashed green line does not yield a vapour density close to one at ambient pressure, whereas for the solid green line, calculated with the adjustment parameters, the *Maxwell* criterion calculates the correct vapour density.

When dealing with  $\text{CO}_2$ , one also has to mention another kind of EOS, which is often applied. This is the *Span* and *Wagner* formulation, cf. [167], a non-analytic EOS derived by an optimization strategy based rigorously on vast amounts of experimental data. This model consists of about forty different terms and coefficients, depending on the considered substance. Due to this complicated formulation, the *Span* and *Wagner* EOS turns out to be too expensive to handle the problems discussed in this monograph. Furthermore, this model cannot be differentiated or integrated for the determination of other thermodynamic functions, which jeopardises the self-imposed restrictions in this monograph of deriving a consistent thermodynamical model.

### ***Maxwell* criterion**

Calculating the pressures using the vdW-EOS (4.11) for a given set of temperatures and densities yields the phase-diagram presented in Figure 4.5. Therein, the red line depicts the isotherm at the critical temperature of  $\text{CO}_2$ ,  $\theta_{\text{crit}}^{\text{CO}_2} = 304.21$  K with zero gradient at the critical point (black dot in Figure 4.5). One can see that for higher temperatures and pressures above the critical values, there is a unique dependence between the pressure and the density, whereas for lower temperatures, i. e., in the two-phase region, one pressure is connected to three density values. However, the latter cannot be observed in reality.

---

<sup>2</sup>This problem constellation is the reason for the vast amount of existing EOS, which try to solve these issues by adding additional terms and parameters to the vdW-EOS. However, in many cases there is no thermodynamical motivation for these additional terms.

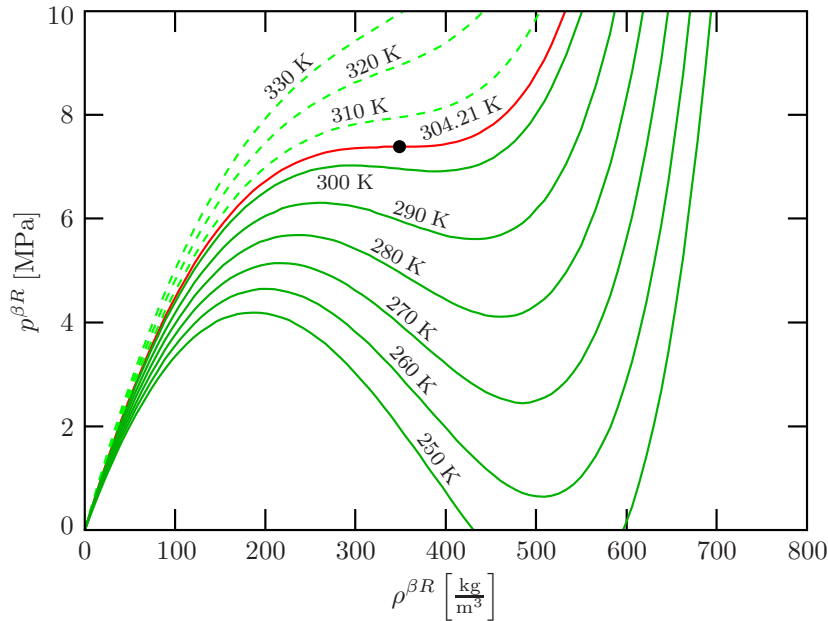


Figure 4.5: Pressure versus density for  $\text{CO}_2$  calculated for different temperatures from the vdW-EOS (4.11). The red line represents the isotherm at the critical temperature  $\theta_{\text{crit}}^{\text{CO}_2} = 304.21 \text{ K}$  and the black dot indicates the critical point.

Experiments reveal that the temperature and the pressure are constant during evaporation or condensation. Thus, the isotherm crossing the two-phase region must be replaced by a straight line according to the so-called *Maxwell criterion*, e.g., *Ott & Boerio-Goates* [134]. To execute this criterion, the isotherm must be cut by an isobar such that the emerging regions (grey) between the isotherm and the isobar have equal areas, illustrated exemplary in Figure 4.6. This specific isobar is also sometimes named the *tie-line*, since it connects the coexisting gaseous and liquid densities in the pressure-density diagram. The

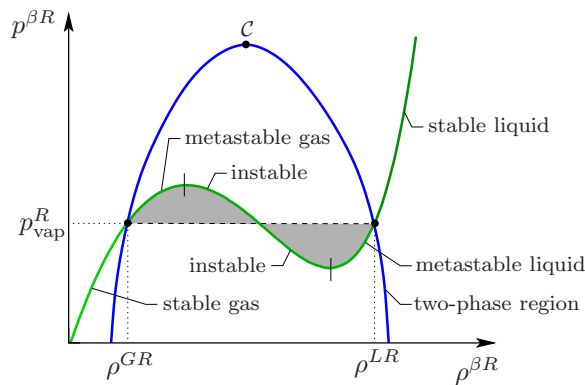


Figure 4.6: Identification of the gas-liquid equilibrium exemplary for one isotherm using the *Maxwell criterion*, which states that the grey indicated regions must have equal areas. Furthermore, the border of the two-phase region (blue) is sketched that connects all saturation densities for all  $\theta^\beta < \theta_{\text{crit}}^\beta$ . The maximum of the two-phase region is given by the critical point  $C$ .

constant pressure value of the tie-line is called the vapour pressure  $p_{\text{vap}}^R$ . The derivation of the *Maxwell criterion* from an equilibrium observation is given in Appendix B.3.

### Antoine equation

The *Antoine* equation provides a phenomenological description of the relation between  $p_{\text{vap}}^R$  and  $\theta^\beta$  during vapour-liquid equilibrium, e. g., *Antoine* [7] or *Abbott & van Ness* [1]

$$\log_{10}(p_{\text{vap}}^R) = A_A - \frac{B_A}{(\theta^\beta - 273.15 + C_A)}, \quad (4.19)$$

where  $A_A$ ,  $B_A$  and  $C_A$  are material parameters and 273.15 has to be subtracted, since the original equation was formulated for temperatures in °C. More information to the correlation and extrapolation of vapour pressures, as well as tabulated values of the parameters  $A_A$ ,  $B_A$  and  $C_A$  for various materials, can be found in *Poling et al.* [137].

By collecting the liquid and gaseous densities of all isotherms that satisfy the *Maxwell* criterion, the border of the two-phase region (blue) in Figure 4.6 is found. This border is also called the saturated-liquid line on the liquid side and saturated-vapour line on the gaseous side.

Additionally, one can identify states of varying stability on the isotherm in Figure 4.6. The stable states lie outside of the two-phase region and indicate gas or liquid in their single phase. The metastable states, between the intersection points of the isotherm with the border of the two-phase region and the local maximum/minimum of the isotherm, are called superheated and subcooled conditions, referring to the metastable liquid and metastable gas, respectively. These states can be observed in experiments only in undisturbed conditions<sup>3</sup>. What cannot be experienced in reality are the instable states, i. e., the remaining section of the isotherm.

#### 4.1.1 Chemical potential and first-order phase transitions

Regarding equilibrium assumptions, e. g., during the gas-liquid phase transition, three transient processes can be observed before equilibrium is reached: first, heat is transferred until the whole systems has the same temperature, second, dilatations and compressions occur to reach equal pressures (except for mechanical constraints), and third, mass is transported to achieve chemical equilibrium. Mathematically, this can be described by the total differential of the *Gibbs* free enthalpy  $\xi^\beta$ ,

$$d\xi^\beta = \underbrace{\left(\frac{\partial \xi^\beta}{\partial \theta^\beta}\right)_{p^{\beta R}, n_m^\beta}}_{\text{thermal}} d\theta^\beta + \underbrace{\left(\frac{\partial \xi^\beta}{\partial p^{\beta R}}\right)_{\theta^\beta, n_m^\beta}}_{\text{mechanical}} dp^{\beta R} + \underbrace{\sum_i \left(\frac{\partial \xi^\beta}{\partial n_m^i}\right)_{\theta^\beta, p^{\beta R}, n_m^{j \neq i}}}_{\text{chemical}} dn_m^i \stackrel{!}{=} 0, \quad (4.20)$$

where  $n_m^\beta$  are the moles of material  $\varphi^\beta$  and use was made of the equilibrium criterion for the total derivative of the *Gibbs* free enthalpy,  $d\xi^\beta = 0$ , cf. *Poling et al.* [137]. For thermal and mechanical equilibrium, i. e., equal temperatures and pressures, respectively,

<sup>3</sup>Subcooled vapours are used, for example, in the cloud chamber, also known as the *Wilson* chamber, as a particle detector for ionizing radiation. If an ion crosses the chamber, it acts as a condensation nucleus, which initiates phase change from the subcooled vapour to liquid, making the ion-crossing visible, cf. *Das Gupta & Ghosh* [43].

the first and second terms in (4.20) vanish. Consequently, the third term must refer to the chemical equilibrium. At this point, the chemical potential  $\mu^\beta$  is introduced as the change in *Gibbs* free enthalpy  $\xi^\beta$  per change of moles  $n_m^\beta$  at constant temperature and pressure via

$$\mu^\beta = \left( \frac{\partial \xi^\beta}{\partial n_m^\beta} \right)_{\theta^\beta, p^{\beta R}}. \quad (4.21)$$

In case of a system that consists of a single pure material, where two phases  $\varphi^L$  and  $\varphi^G$  coexist, the total free-enthalpy change at constant temperature and pressure yields

$$d\xi_{\theta^\beta, p}^\beta = d\xi^L + d\xi^G = \mu^L dn_m^L + \mu^G dn_m^G = 0. \quad (4.22)$$

Assuming that the system is closed, i. e., no mass is added from the outside,  $dn_m^L = -dn_m^G$ , it follows

$$(\mu^L - \mu^G) dn_m^G = 0 \quad \text{and} \quad dn_m^G > 0. \quad (4.23)$$

Finally, it can be concluded that at equilibrium, the chemical potentials of the two involved phases must be equal, viz.:

$$\mu^L = \mu^G. \quad (4.24)$$

Of course, this directly implies the non-equilibrium conditions, when the chemical potentials are not equal, i. e.,  $\mu^L \leq \mu^G$ . These latter conditions lead to spontaneous transitions from the phase with high chemical potential to the phase with low chemical potential, until equilibrium is reached again. Figure 4.7 illustrates this relationship between the phase transition and the chemical potential in dependence of the temperature.

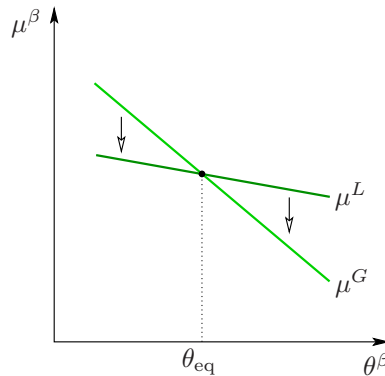


Figure 4.7: Illustration of the chemical potential  $\mu^\beta$  versus the temperature  $\theta^\beta$ . At the equilibrium temperature  $\theta_{\text{eq}}$ , equilibrium exists, i. e.,  $\mu^L = \mu^G$ . For higher temperatures  $\theta^\beta > \theta_{\text{eq}}$  and  $\mu^L > \mu^G$  phase  $\varphi^L$  changes to phase  $\varphi^G$ , whereas for lower temperatures  $\theta^\beta < \theta_{\text{eq}}$  and  $\mu^G > \mu^L$  phase  $\varphi^G$  changes to phase  $\varphi^L$ . In imitation of *Ott & Boerio-Goates* [134].

Phase transitions can be grouped into *first-order phase transitions* and *second-order phase transitions*. The former correspond to transitions, where, although the difference of the chemical potentials at the equilibrium temperature  $\theta_{\text{eq}}$  is zero  $\Delta\mu = \mu^L - \mu^G = 0$ , cf. Figure 4.7, the *Gibbs* free enthalpy changes its slope there. This means that the first derivative of the chemical potential with respect to an intensive parameter (e. g.,  $p^{\beta R}$ ),

which represents the corresponding extensive parameter (e. g.,  $v^{\beta R}$ ), is not continuous:

$$\left(\frac{\partial \xi^\beta}{\partial p^{\beta R}}\right)_{\theta_{\text{eq}}} = v^{\beta R} \neq 0. \quad (4.25)$$

From this jump in the first derivative of the free enthalpy, the name “first-order phase transitions” is deduced.

Second-order phase transitions denote continuous phase transitions, e. g., liquid to gas at the critical point, where also the first derivatives become equal to zero and only the second derivative of the potential has a jump at the point of phase transition. This second group is important for the treatment of superfluid helium and transitions from paramagnetic to ferromagnetic conditions, which are not discussed in this monograph, since here the focus is restricted to first-order phase transitions.

### 4.1.2 Clausius-Clapeyron equation

In Figure 4.2(a) the circle indicates the coexistence point of the gaseous and liquid phase on the vaporisation curve. As mentioned before, temperature and pressure are constant during phase change and equal for both phases:  $\theta^L = \theta^G = \theta_{\text{eq}}$  and  $p^{LR} = p^{GR} = p_{\text{vap}}^R$ . From the definition (4.24) of the chemical equilibrium derived in the previous Section 4.1.1, it was found for the chemical potentials  $\mu^L$  and  $\mu^G$  at equilibrium:

$$\mu^L(p^{LR}, \theta^\beta) = \mu^G(p^{GR}, \theta^\beta). \quad (4.26)$$

Taking the derivative of (4.26) with respect to  $p_{\text{vap}}^R$  and  $\theta^\beta$ , leads to

$$\left(\frac{\partial \mu^L}{\partial \theta^\beta}\right)_{p_{\text{vap}}^R} d\theta^\beta + \left(\frac{\partial \mu^L}{\partial p_{\text{vap}}^R}\right)_{\theta^\beta} dp_{\text{vap}}^R = \left(\frac{\partial \mu^G}{\partial \theta^\beta}\right)_{p_{\text{vap}}^R} d\theta^\beta + \left(\frac{\partial \mu^G}{\partial p_{\text{vap}}^R}\right)_{\theta^\beta} dp_{\text{vap}}^R. \quad (4.27)$$

From the fundamental relations of the chemical potential, cf. Appendix B.2, it follows for its partial derivatives

$$\left(\frac{\partial \mu^\beta}{\partial \theta^\beta}\right)_{p_{\text{vap}}^R} = -\eta^\beta, \quad \text{and} \quad \left(\frac{\partial \mu^\beta}{\partial p_{\text{vap}}^R}\right)_{\theta^\beta} = v^{\beta R}, \quad (4.28)$$

where  $\eta^\beta$  is the entropy of  $\varphi^\beta$ . Applying these relations to (4.27), yields

$$-\eta^L d\theta^\beta + v^{LR} dp_{\text{vap}}^R = -\eta^G d\theta^\beta + v^{GR} dp_{\text{vap}}^R. \quad (4.29)$$

Subsequently, a separation of variables leads to

$$(\eta^G - \eta^L) d\theta^\beta = (v^{GR} - v^{LR}) dp_{\text{vap}}^R \quad (4.30)$$

and by application of  $d\eta^\beta = d\zeta^\beta/\theta^\beta$ , cf. Appendix B.2, one gets

$$\frac{dp_{\text{vap}}^R}{d\theta^\beta} = \frac{\eta^G - \eta^L}{v^{GR} - v^{LR}} = \frac{\zeta^G - \zeta^L}{\theta^\beta (v^{GR} - v^{LR})}. \quad (4.31)$$

Furthermore, with the definition of the vaporisation enthalpy or latent heat  $\Delta\zeta_{\text{vap}} := \zeta^G - \zeta^L$  and the difference of specific volume  $\Delta v = v^{GR} - v^{LR}$ , the most-known form of the *Clausius-Clapeyron* equation is derived:

$$\frac{dp_{\text{vap}}^R}{d\theta^\beta} = \frac{\Delta\zeta_{\text{vap}}}{\theta^\beta \Delta v}. \quad (4.32)$$

This is a relation for the vaporisation curve in Figure 4.2(a), while the specific-volume difference and the vaporisation enthalpy are indicated in Figures 4.2(b) and 4.2(c), respectively. The *Clausius-Clapeyron* equation is therefore also the basis for the formulation of the *Antoine* equation (4.19), where a detailed discussion is given, for example, by *Graf* [74].

## 4.2 Vaporisation enthalpy

The *enthalpy of vaporisation*,  $\Delta\zeta_{\text{vap}}$ , is the difference between the enthalpies of the saturated gas and liquid phases at the same temperature and pressure. In case of vaporisation, it delineates the energy required to destroy the intermolecular bonds within the liquid phase. In the other direction, i. e., condensation, the same amount of energy is released when these bonds are restored. A frequently used synonym for the vaporisation enthalpy is *latent heat of vaporisation*. To estimate the vaporisation enthalpy, one can resort to the CSP, which was mentioned earlier. *Pitzer et al.* [135] developed from the *Clausius-Clapeyron* equation (4.32) an expression depending on the critical temperature  $\theta_{\text{crit}}^\beta$ , the acentric factor  $\omega^\beta$  and the molar mass  $M^\beta$  of the respective substance:

$$\Delta\zeta_{\text{vap}} = 7.08 R M^\beta \left[ \theta_{\text{crit}}^\beta (1 - \theta_r^\beta)^{0.354} + 10.95 \omega^\beta (1 - \theta_r^\beta)^{0.456} \right]. \quad (4.33)$$

This equation is valid for reduced temperatures between  $0.6 < \theta_r^\beta < 1.0$ .

The vaporisation enthalpy or latent heat  $\Delta\zeta_{\text{vap}}$  is calculated in this work by fitting an exponential function to the  $\text{CO}_2$  vaporisation data taken from *Potter & Somerton* [139] and displayed in Figure 4.8:

$$\Delta\zeta_{\text{vap}} = \frac{1000.0 a_{\Delta\zeta}}{[c_{\Delta\zeta} (\theta^\beta - 273.15) + d_{\Delta\zeta}] b_{\Delta\zeta}} \quad (4.34)$$

with the fitting parameters  $a_{\Delta\zeta}$ ,  $b_{\Delta\zeta}$ ,  $c_{\Delta\zeta}$  and  $d_{\Delta\zeta}$ .

## 4.3 Specific heat capacity

The heat capacity is a measure for the amount of heat needed to change the temperature of a substance by 1 K and which is an extensive quantity with the unit J/K. However, it is convenient to use the mass-specific formulation in J/(kg K) as an intensive property. In classical thermodynamics, it is common to look at a heating process under various circumstances, i. e., either at constant density (respectively volume) or at constant pressure,



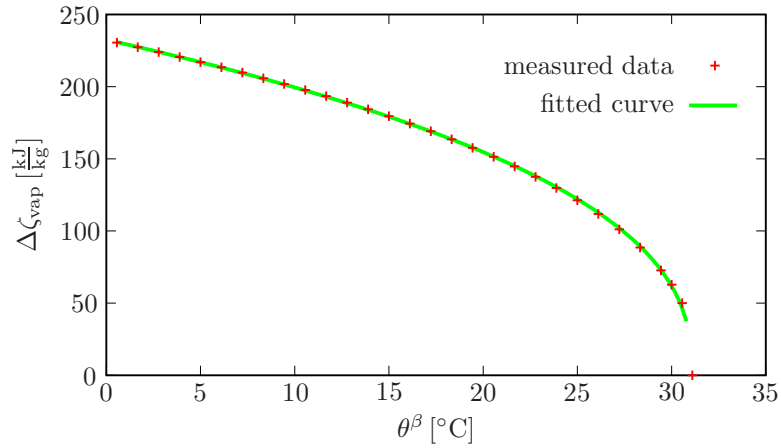


Figure 4.8: Vaporisation enthalpy of  $\text{CO}_2$ . Data are taken from *Potter & Somerton* [139], and the parameters for the fitted curve (4.34) are:  $a_{\Delta\zeta} = 239.90$ ,  $b_{\Delta\zeta} = -0.40$ ,  $c_{\Delta\zeta} = -0.030$  and  $d_{\Delta\zeta} = 0.92$ .

cf. *Lewis & Randall* [105]. In this work, only the first formulation is needed:

$$c_V^{\beta R} = \left. \frac{\partial \varepsilon^\beta}{\partial \theta^\beta} \right|_{\rho^{\beta R} = \text{const.}}. \quad (4.35)$$

The specific internal energy  $\varepsilon^\beta$ , found in (4.35), is a function of the extensive state variables entropy  $\eta^\beta$  and strain  $\mathbf{E}_\beta$ , namely  $\varepsilon^\beta = \varepsilon^\beta(\eta^\beta, \mathbf{E}_\beta)$ . In case of non-viscous fluids, the original dependency of the specific internal energy on the strain changes to a dependency on the volume, respectively the density, via  $\varepsilon^\beta = \varepsilon^\beta(\eta^\beta, \rho^{\beta R})$ . With the conjugated intensive quantity  $\theta^\beta$  for the entropy, it follows

$$\left. \frac{\partial \varepsilon^\beta}{\partial \eta^\beta} \right|_{\mathbf{E}_\beta \text{ or } \rho^{\beta R}} = \theta^\beta. \quad (4.36)$$

Hence, if (4.36) is used in (4.35), one finds for the specific heat capacity at constant volume

$$c_V^{\beta R} = \frac{\partial \varepsilon^\beta}{\partial \eta^\beta} \frac{\partial \eta^\beta}{\partial \theta^\beta} = \theta^\beta \frac{\partial \eta^\beta}{\partial \theta^\beta}. \quad (4.37)$$

*Potter and Somerton* [139] state in their work that the specific heat capacity of gases increases slowly with increasing temperature and, thus, can be taken as constant. However, Figure 4.9, which shows the specific heat capacity for  $\text{CO}_2$ , indicates that this is only true for higher temperatures ( $\theta^\beta > 320$  K). Close to the temperature, where phase transition occurs (in this case at  $p^{\beta R} = 4.5 \cdot 10^6$  Pa and  $\theta^\beta = 283.13$  K), the change in the specific heat capacity cannot be neglected. For a continuous approximation of the whole curve, i. e., both, liquid and gas, a hyperbolic tangent function is fitted to the data obtained from the NIST Chemistry WebBook *Lemmon et al.* [104], cf. Figure 4.9. The resulting function reads

$$c_V^{\beta R} = -75.351 \tanh [1.695 (\theta^\beta - 289.985)] + 871.396 \quad \text{with} \quad [c_V^{\beta R}] = \frac{\text{J}}{\text{kg K}} \quad (4.38)$$

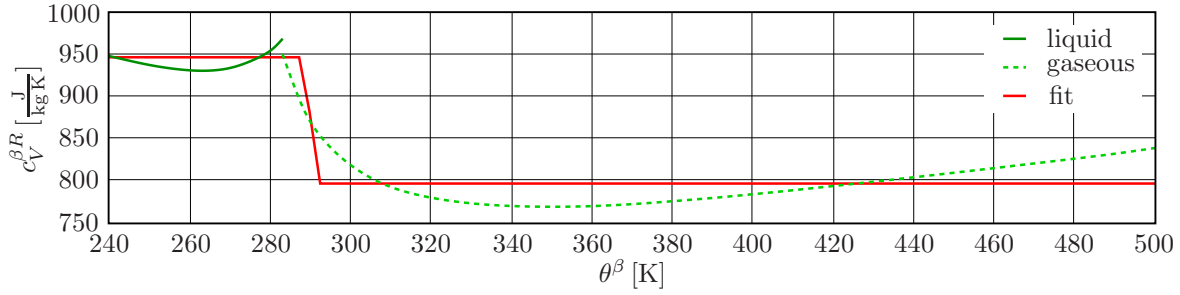


Figure 4.9: Specific heat capacity of CO<sub>2</sub> for constant density and at a pressure of  $p^{\beta R} = 4.5 \cdot 10^6$  Pa. The jump at  $\theta^{\beta} = 283.13$  K coincides with the phase transition between liquid and gaseous CO<sub>2</sub>. The green lines, both for liquid and gas, were derived with the NIST Chemistry WebBook by *Lemmon et al.* [104]. The red line shows a continuous fit using a hyperbolic tangent function (4.38) with an error of  $R^2 = 0.915$ .

and has an error of  $R^2 = 0.915$ . Since the heat capacity is only weakly dependent on the pressure, it can be argued to choose a single reference pressure, cf. *Poling et al.* [137]. Please note in passing that in the derivation of the *Helmholtz* free energies of the fluid constituents in Section 5.3.4, the liquid and gaseous specific heat capacities are taken as constant for the integration procedures.

## 4.4 Shear viscosity and thermal conductivity

The empirical relations for the calculations of the effective shear (dynamic) viscosity  $\mu^{\beta R}$  and the effective thermal conductivity  $H^{\beta R}$  for the fluid phases are gathered from the works of *Fenghour et al.* [66] and *Vesovic et al.* [175], which were developed solely for CO<sub>2</sub>. For both parameters, the formulations are composed of a part for the zero-density limit (i. e., ideal-gas behaviour), an excess part (added for non-ideal temperature-pressure conditions) and a third enhancement part for the critical region (accounting for the strong divergence of parameters close to the critical point). Hence, the structure of the universal formulation for both, the viscosity and conductivity, looks like this:

$$(\cdot) = \underbrace{(\cdot)_0}_{\text{id. gas}} + \underbrace{\Delta(\cdot)}_{\text{excess}} + \underbrace{\Delta(\cdot)_c}_{\text{crit.}} \quad (4.39)$$

Formulations and empirical relations that are valid for other substances besides CO<sub>2</sub> are presented and compared, e. g., in *Poling et al.* [137].

### 4.4.1 Effective shear viscosity

As mentioned before, the shear viscosity is decomposed into three parts:

$$\mu^{\beta R}(\rho^{\beta R}, \theta^{\beta}) = [\mu_0^{\beta R}(\theta^{\beta}) + \Delta\mu^{\beta R}(\rho^{\beta R}, \theta^{\beta}) + \Delta\mu_c^{\beta R}(\rho^{\beta R}, \theta^{\beta})] \cdot 10^{-6}, \quad [\mu^{\beta R}] = \text{Pa s}, \quad (4.40)$$

where  $\mu_0^{\beta R}(\theta^{\beta})$  is the effective shear viscosity for a density close to zero, i. e., ideal gas, the excess viscosity  $\Delta\mu^{\beta R}(\rho^{\beta R}, \theta^{\beta})$  stands for the increase in viscosity for higher densities

and the critical enhancement  $\Delta\mu_c^{\beta R}(\rho^{\beta R}, \theta^\beta)$  accounts for the divergence of the viscosity around the critical point. In contrast to the original publication, (4.40) has been multiplied by  $10^{-6}$ . This is due to the fact that *Fenghour et al.* [66] have based their shear-viscosity formulation on  $\mu\text{Pas}$  instead of  $\text{Pas}$ , what is required in this work.

According to *Fenghour et al.* [66], the zero-density viscosity is given as:

$$\mu_0^{\beta R}(\theta^\beta) = \frac{1.00697 \sqrt{\theta^\beta}}{e^{\sigma^*(\theta^\beta)}} \quad \text{with} \quad \sigma^*(\theta^\beta) = \sum_{i=1}^m a_i \left( \ln \frac{\theta^\beta}{251.196 \text{ K}} \right)^i \quad \text{and} \quad [\mu_0^{\beta R}] = \mu\text{Pas}. \quad (4.41)$$

The coefficients  $a_i$  are listed in Table 4.1 on the left with  $m = 4$ .

Table 4.1: The coefficients  $a_i$  for the formulation of the zero-density viscosity (left) and the coefficients  $d_{ij}$  for the formulation of the excess viscosity (right), both only valid for  $\text{CO}_2$ , *Fenghour et al.* [66].

$i$	$a_i$	$ij$	$d_{ij}$
0	0.235156	11	$0.4071119 \cdot 10^{-2}$
1	-0.491566	21	$0.7198037 \cdot 10^{-4}$
2	$5.211155 \cdot 10^{-2}$	64	$0.2411697 \cdot 10^{-16}$
3	$5.347906 \cdot 10^{-2}$	81	$0.2971072 \cdot 10^{-22}$
4	$-1.537105 \cdot 10^{-2}$	82	$-0.1627888 \cdot 10^{-22}$

The excess viscosity  $\Delta\mu^{\beta R}(\rho^{\beta R}, \theta^\beta)$  is the real-gas/fluid correction factor at higher densities. Due to the lack of a sufficient theory for the determination of this factor, an empirical equation in the form of a power-series expansion of the density provides adequate accuracy:

$$\Delta\mu^{\beta R}(\rho^{\beta R}, \theta^\beta) = d_{11} \rho^{\beta R} + d_{21} (\rho^{\beta R})^2 + \frac{d_{64} (\rho^{\beta R})^6}{(\theta^{\beta*})^3} + d_{81} (\rho^{\beta R})^8 + \frac{d_{82} (\rho^{\beta R})^8}{\theta^{\beta*}}, \quad (4.42)$$

where  $\theta^{\beta*} = \theta^\beta / 251.196 \text{ K}$  and the constants  $d_{ij}$  are depicted in the right-hand side of Table 4.1. The excess viscosity in (4.42) is formulated in  $[\Delta\mu^{\beta R}] = \mu\text{Pas}$ .

Finally, it remains to define the critical enhancement  $\Delta\mu_c^{\beta R}(\rho^{\beta R}, \theta^\beta)$ . *Fenghour et al.* [66] state in their work that the deviation of the shear viscosity in narrow vicinity to the critical point is rather small. Since in this monograph conditions close to the critical point are avoided, this term is omitted in the following. For a detailed discussion on the critical enhancement, the interested reader is referred to *Vesovic et al.* [175].

#### 4.4.2 Thermal conductivity

Analogous to the kinematic viscosity, the partitioning function (4.39) is applied for the thermal conductivity, viz.:

$$H^{\beta R}(\rho^{\beta R}, \theta^\beta) = [H_0^{\beta R}(\theta^\beta) + \Delta H^{\beta R}(\rho^{\beta R}, \theta^\beta) + \Delta H_c^{\beta R}(\rho^{\beta R}, \theta^\beta)] \cdot 10^{-3}, \quad [H^{\beta R}] = \frac{\text{W}}{\text{m K}}, \quad (4.43)$$

where the original formulation has been multiplied by  $10^{-3}$ , since *Vesovic et al.* [175] have calculated the thermal conductivity in mW/mK, whereas here W/mK is needed. In (4.43), the zero-density part of the thermal conductivity is given via

$$H_0^{\beta R}(\theta^\beta) = \frac{0.475598 \sqrt{\theta^\beta} (1 + (r_H)^2)}{\tau^*(\theta^\beta)} \quad \text{with} \quad \tau^*(\theta^\beta) = \sum_{i=0}^7 \frac{b_i}{(\theta^{\beta*})^i} \quad \text{and} \quad [H_0^{\beta R}] = \frac{\text{mW}}{\text{m K}}. \quad (4.44)$$

The coefficient  $r_H$  in (4.44) is expressed as

$$r_H = \sqrt{\frac{2}{5} c_{\text{int}}} \quad \text{and} \quad c_{\text{int}} = 1.0 + e^{\frac{-183.5}{\theta^\beta}} \sum_{i=1}^5 c_i \left(\frac{\theta^\beta}{100}\right)^{2-i}. \quad (4.45)$$

Furthermore, the coefficients  $b_i$  and  $c_i$  in (4.44) and (4.45)<sub>2</sub> are taken from Table 4.2.

Table 4.2: The coefficients  $b_i$  and  $c_i$  for the formulation of the zero-density thermal viscosity and the coefficients  $d_i$  for the formulation of the excess thermal conductivity for CO<sub>2</sub>, cf. *Vesovic et al.* [175].

$i$	$b_i$	$c_i$	$d_i$
0	0.4226159		
1	0.6280115	$2.387869 \cdot 10^{-2}$	$2.447164 \cdot 10^{-2}$
2	-0.5387661	4.350794	$8.705605 \cdot 10^{-5}$
3	0.6735941	-10.33404	$-6.547950 \cdot 10^{-8}$
4	0.0	7.981590	$6.594919 \cdot 10^{-11}$
5	0.0	-1.940558	
6	-0.4362677		
7	0.2255388		

The excess thermal conductivity  $\Delta H^{\beta R}(\rho^{\beta R})$ , as the correction factor for higher densities, is again determined from a polynomial in the density:

$$\Delta H^{\beta R}(\rho^{\beta R}) = \sum_{i=1}^4 d_i (\rho^{\beta R})^i \quad \text{and} \quad [\Delta H^{\beta R}] = \frac{\text{mW}}{\text{m K}}, \quad (4.46)$$

where the coefficients  $d_i$  are listed in Table 4.2.

Opposite to the kinematic viscosity, the change in thermal conductivity around the critical point is significant and cannot be neglected. However, since this region will not be touched in the simulations presented in this monograph, it is decided to omit the critical enhancement part in the calculation of the kinematic viscosity as well. The formulation of this critical factor can be found in *Vesovic et al.* [175].

# Chapter 5: Constitutive settings

In Chapter 3, the general framework for the description of a multiphasic model was presented without any specification to a particular system. In the present chapter, this framework shall be adapted to the problem of CO<sub>2</sub> sequestration. It was illustrated in Chapter 2 that the modelling of CO<sub>2</sub> sequestration into a deep aquifer is a numerically challenging task due to the considered range in time and length scales, the multiphasic composition, and the process complexity with respect to thermodynamics and chemistry. As the early time span of the injection process is most critical in terms of high pressures, including the unwanted consequences of uplift, crack formation, induced seismicity and displacement of saline formation-water, which was elucidated in Section 2.3.2, this stage is of particular interest for policy makers regarding the storage safety, cf. *Celia et al.* [34]. Hence, the customised model should be able to describe the solid deformations and the phase transitions between the fluid phases, which are induced either by the rising pore pressures during the injection stage or by changing temperature conditions. However, it is not intended to include dissolution or mineralisation, since these effects only appear over a greater time span and can therefore be treated separately.

At first, in Section 5.1, a priori assumptions are made for the simplification of the problem at hand, which is of course accomplished without losing the important characteristics that distinguish the CO<sub>2</sub> storage problem. In Section 5.2, the basic balance equations derived in Chapter 3 are adopted to these assumptions. This section also incorporates a comparison between the number of governing equations and the number of unknowns that are needed for an exhaustive description of the motion and temperature states. The comparison displays a superior number of unknowns, which is distinguished as the so-called closure problem. The surplus unknowns have to be defined by additional constitutive equations that are derived in Section 5.3 for the involved constituents by evaluating the entropy inequality in order to ensure the thermodynamic consistent modelling procedure. These constitutive equations solve the closure problem by adding the required number of equations to the set of governing equations and, thus, even out the superior number of unknowns. Furthermore, the particular thermodynamical and physical behaviours of the involved constituents in the process of CO<sub>2</sub> storage in the subsurface are represented by the constitutive equations. Since the phase transition process is of paramount importance in this work, the derivation of the corresponding constitutive equations is regarded in detail in Section 5.4. The final Section 5.5 contains the collection of the strong forms of the governing balance relations, while applying the results of the previous evaluations. These strong forms build the basis for the numerical simulations.

## 5.1 A priori assumptions

The triphasic model consists of an inert ( $\hat{\rho}^S \equiv 0$ ), thermoelastic solid phase  $\varphi^S$  and two immiscible and compressible pore-fluid phases  $\varphi^L$  and  $\varphi^G$ . The following derivations will

be done for the case, where one single matter can adopt two different phases. More specifically, the two fluid phases belong to one single substance, e. g.,  $\text{CO}_2$ . Hence, the two fluid phases are  $\varphi^L$  (liquid  $\text{CO}_2$ ) and  $\varphi^G$  (gaseous  $\text{CO}_2$ ). However, as in Chapter 7 a numerical example of  $\text{CO}_2$  being injected into a water-filled reservoir is presented, two different fluid matters are considered, i. e., water ( $\varphi^L$ ) and  $\text{CO}_2$  ( $\varphi^G$ ). The minor but necessary changes in the formulations of the model for the second case will be explained in detail in the introduction to the particular numerical example.

The flow and heat transport processes in  $\text{CO}_2$  reservoirs are supposed to be slow, which justifies the assumption of quasi-static conditions and, thus, the acceleration terms of the respective constituents can be neglected:

$$\ddot{\mathbf{x}}_\alpha \equiv \mathbf{0} . \quad (5.1)$$

In connection to the assumption of slow processes (quasi-static), which also excludes chemical reactions originating from sudden temperature variations, it is postulated that a local thermodynamical equilibrium exists. Consequently, a common temperature for all constituents can be assumed:

$$\theta^\alpha = \theta . \quad (5.2)$$

The single temperature formulation requires only the consideration of the mixture energy balance of the overall aggregate in the set of the governing balance equations, instead of three separate energy balances for the individual constituents. This is further justified by an evaluation of the temperature equalisation between a fluid and a solid constituent, see Appendix B.9. In this context, it is important to point out that the assumption of local thermal equilibrium between the constituents ( $\theta^\alpha = \theta$ ) is rather strong, but does not imply global thermal equilibrium, meaning the temperature can change spatially. Still, non-thermal equilibrium conditions trigger the mass transfer during phase transition through, for instance, a heat flux  $\sum_\alpha \mathbf{q}^\alpha$ .

Finally, the body forces are assumed to be governed by constant and homogeneous gravitational forces for all constituents, i. e.,  $\mathbf{b}^\alpha = \mathbf{g}$ .

## 5.2 Adaptation of balance relations

The balance relations introduced by (3.63)<sub>1</sub>, (3.64)<sub>1</sub> and (3.65)<sub>1</sub> are altered with the previously introduced a priori assumptions. In particular, the adapted mass, momentum and energy balances comprise the set of the governing balance relations:

$$\begin{aligned} (\rho^S)'_S + \rho^S \operatorname{div} \dot{\mathbf{x}}_S &= 0 , \\ (\rho^\beta)'_\beta + \rho^\beta \operatorname{div} \dot{\mathbf{x}}_\beta &= \hat{\rho}^\beta , & \beta &= \{L, G\} , \\ \mathbf{0} &= \operatorname{div} \mathbf{T}^\alpha + \rho^\alpha \mathbf{g} + \hat{\mathbf{p}}^\alpha , & \alpha &= \{S, L, G\} , \\ \rho^\alpha (\varepsilon^\alpha)'_\alpha &= \mathbf{T}^\alpha \cdot \mathbf{L}_\alpha - \operatorname{div} \mathbf{q}^\alpha + \rho^\alpha r^\alpha + \hat{\varepsilon}^\alpha , & \alpha &= \{S, L, G\} . \end{aligned} \quad (5.3)$$

Note in passing that the solid mass balance (5.3)<sub>1</sub> reduces to a volume balance, i. e.,  $(n^S)'_S + n^S \operatorname{div} \dot{\mathbf{x}}_S = 0$ , for  $\rho^{SR} = \text{const}$ . However, this only holds for materially incompressible solid constituents under isothermal conditions, which is not the case in this monograph.

The other balance relations are the two fluid mass balances (5.3)<sub>2</sub>, the momentum balances (5.3)<sub>3</sub> and the energy balances (5.3)<sub>4</sub>. Comparing this set of balance relations with the relations introduced in Section 3.3.1, the attentive reader recognises the missing entropy inequality, since the entropy inequality does not serve as a governing equation. Instead, it reveals constraints to be imposed on the constitutive relations for the sake of a thermodynamically consistent modelling procedure. These constitutive relations are needed to solve the closure problem.

The closure problem arises as the system of governing equations in (5.3) incorporates more unknowns than equations. In numbers, the three constituents lead to three mass balance equations, nine momentum balance equations (or three vector-valued equations) and three energy balance equations summing up to 15 equations. These stand adversely to the set of unknowns:  $\rho^\alpha$  (1·3),  $\dot{\mathbf{x}}_\alpha$  (3·3),  $\hat{\rho}^\beta$  (1·2),  $\mathbf{T}^\alpha$  (6·3),  $\mathbf{g}$  (3·1),  $\hat{\mathbf{p}}^\alpha$  (3·3),  $\varepsilon^\alpha$  (1·3),  $\mathbf{L}_\alpha$  (6·3),  $\mathbf{q}^\alpha$  (3·3),  $r^\alpha$  (1·3) and  $\hat{\varepsilon}^\alpha$  (1·3), which makes a total of 80 unknowns<sup>1</sup>. It is now easy to conclude that besides the equations in (5.3), further constitutive relations are required to determine the 65 open fields, consisting of the densities, velocities, stress tensors, internal energies, heat fluxes and production terms.

The procedure of generating sound constitutive equations for a multiphasic, multicomponent model, which in this case concerns the CO<sub>2</sub> storage, follows the line of action of *Ehlers* [54, 55]. It can be subdivided into several successive steps. At first, the governing balance relations (5.3) are adapted. Next, the application of the basic thermodynamic principles retrieves the dependencies of the *Helmholtz* free energies  $\psi^\alpha$ , which are then used to, finally, gain the missing constitutive relations exploiting the entropy inequality.

### 5.2.1 Definition of a thermoelastic solid

In this monograph, an inert, thermoelastic, porous solid material is regarded following the line of *Ehlers* and *Häberle* [61]. Its describing mass balance was already presented in (5.3)<sub>1</sub>. Due to the thermoelastic behaviour, it is not enough to just use this mass balance for the computation of the solid volume fraction  $n^S$ , as it was done, e. g., by *Wagner* [176]. Here, besides the solid volume fraction, also the solid partial and material densities,  $\rho^S$  and  $\rho^{SR}$ , are determined from the solid mass balance. To do this, at first, the thermomechanical behaviour of the solid constituent must be discussed, which basically depends on a multiplicative split of the total solid deformation gradient  $\mathbf{F}_S$  into a purely mechanical and a purely thermal part:

$$\mathbf{F}_S = \mathbf{F}_{Sm} \mathbf{F}_{S\theta} . \quad (5.4)$$

While  $\mathbf{F}_S$  only depends on the solid displacement  $\mathbf{u}_S$  through the displacement gradient  $\mathbf{H}_S = \operatorname{Grad}_S \mathbf{u}_S$ , the thermal part  $\mathbf{F}_{S\theta}$  is described by a constitutive assumption following

<sup>1</sup>Herein, the first number in the bracket refers to a scalar (1), a vectorial (3), or a tensorial quantity (6) (for symmetric tensors) and the second number to the involved constituents.

Lu & Pister [110], viz.:

$$\begin{aligned}\mathbf{F}_S &= \mathbf{I} + \text{Grad}_S \mathbf{u}_S = \mathbf{I} + \mathbf{H}_S, \\ \mathbf{F}_{S\theta} &= (\det \mathbf{F}_{S\theta})^{1/3} \mathbf{I} \quad \text{with} \quad \det \mathbf{F}_{S\theta} = \exp(3 \alpha^S \Delta\theta), \\ \mathbf{F}_{Sm} &= \mathbf{F}_S \mathbf{F}_{S\theta}^{-1}.\end{aligned}\tag{5.5}$$

Therein,  $\alpha^S$  is the coefficient of thermal expansion, and  $\Delta\theta = \theta - \theta_0$  is the temperature variation with respect to the initial temperature  $\theta_0$ . Furthermore, (5.4) is reorganised for the purely mechanical part  $\mathbf{F}_{Sm}$ .

The multiplicative decomposition of the deformation gradient is associated with the existence of an intermediate configuration and an additive split of the strain tensors in the solid reference, intermediate and current configuration, similar to elasto-plasticity, cf., for example, Ehlers [50]. One obtains, for instance, the following decomposition of the *Green-Lagrangean* strain in the solid reference configuration:

$$\begin{aligned}\mathbf{E}_S &= \frac{1}{2}(\mathbf{F}_S^T \mathbf{F}_S - \mathbf{I}) = \mathbf{E}_{Sm} + \mathbf{E}_{S\theta}, \\ \mathbf{E}_{S\theta} &= \frac{1}{2}(\mathbf{F}_{S\theta}^T \mathbf{F}_{S\theta} - \mathbf{I}), \\ \mathbf{E}_{Sm} &= \mathbf{E}_S - \mathbf{E}_{S\theta}.\end{aligned}\tag{5.6}$$

Hence, it is possible to describe a stress-free strain condition at the reference state, where the initial strain state is governed by the initial temperature  $\theta_0$ .

Proceeding from the small-strain assumption, a formal linearisation of the above strain measures around the reference state is suitable and yields for the linearised *Green-Lagrangean* solid strains

$$\begin{aligned}\boldsymbol{\varepsilon}_S &:= \text{lin } \mathbf{E}_S = \frac{1}{2}(\mathbf{F}_S + \mathbf{F}_S^T) - \mathbf{I} = \frac{1}{2}(\mathbf{H}_S + \mathbf{H}_S^T), \\ \boldsymbol{\varepsilon}_{S\theta} &:= \text{lin } \mathbf{E}_{S\theta} = \frac{1}{2}(\mathbf{F}_{S\theta} + \mathbf{F}_{S\theta}^T) - \mathbf{I}, \\ \boldsymbol{\varepsilon}_{Sm} &= \boldsymbol{\varepsilon}_S - \boldsymbol{\varepsilon}_{S\theta}.\end{aligned}\tag{5.7}$$

Furthermore, if the temperature variation is such that  $\det \mathbf{F}_{S\theta}$  is approximately equal to  $\text{lin}(\det \mathbf{F}_{S\theta})$ , a formal linearisation of  $(\det \mathbf{F}_{S\theta})^{1/3}$  around  $\Delta\theta = 0$  provides

$$\text{lin}(\det \mathbf{F}_{S\theta})^{1/3} = 1 + \alpha^S \Delta\theta.\tag{5.8}$$

Given this result, the thermal part of the deformation gradient (5.5)<sub>2</sub> and the thermal strain (5.7)<sub>2</sub> read

$$\begin{aligned}\text{lin}(\mathbf{F}_{S\theta}) &= (1 + \alpha^S \Delta\theta) \mathbf{I}, \\ \boldsymbol{\varepsilon}_{S\theta} &= \alpha^S \Delta\theta \mathbf{I}.\end{aligned}\tag{5.9}$$

By integration of the solid mass balance (5.3)<sub>1</sub> over time  $t$ , one obtains

$$\rho^S = \rho_{0S}^S (\det \mathbf{F}_S)^{-1},\tag{5.10}$$



where  $\rho_{0S}^S$  is the partial solid density in the solid reference configuration at  $t = t_0$ . Splitting the partial density into the effective density and the volume fraction yields by use of (5.4)

$$n^S \rho^{SR} = n_{0S}^S \rho_{0S}^{SR} (\det \mathbf{F}_{Sm})^{-1} (\det \mathbf{F}_{S\theta})^{-1} \quad (5.11)$$

with  $n_{0S}^S$  and  $\rho_{0S}^{SR}$  being the solid volume fraction and the effective density at  $t = t_0$ , respectively.

As explained before,  $\rho^{SR} = \rho_{0S}^{SR}$  is constant at constant temperatures for materially incompressible solids. Consequently, variations in  $\rho^{SR}$  can only be initiated by temperature variations. Thus, it is obvious that (5.11) can be split as follows, see *Ghadiani* [71],

$$\begin{aligned} \rho^{SR} &= \rho_{0S}^{SR} (\det \mathbf{F}_{S\theta})^{-1} = \rho_{0S}^S \exp(-3 \alpha^S \Delta\theta), \\ n^S &= n_{0S}^S (\det \mathbf{F}_{Sm})^{-1} = n_{0S}^S (\det \mathbf{F}_S)^{-1} \exp(3 \alpha^S \Delta\theta), \end{aligned} \quad (5.12)$$

where (5.5)<sub>3</sub> has been used. Linearising  $(\det \mathbf{F}_S)^{-1}$ ,  $(\det \mathbf{F}_{S\theta})^{-1}$  and  $(\det \mathbf{F}_{Sm})^{-1}$  via

$$\begin{aligned} \text{lin}(\det \mathbf{F}_S)^{-1} &= 1 - \text{Div}_S \mathbf{u}_S, \\ \text{lin}(\det \mathbf{F}_{Sm})^{-1} &= 1 - \text{Div}_S \mathbf{u}_S + 3 \alpha^S \Delta\theta, \\ \text{lin}(\det \mathbf{F}_{S\theta})^{-1} &= 1 - 3 \alpha^S \Delta\theta, \end{aligned} \quad (5.13)$$

wherein  $\text{Div}_S(\cdot)$  is the divergence operator corresponding to  $\text{Grad}_S(\cdot)$ , the following relations for the solid densities and the volume fractions are obtained:

$$\begin{aligned} \rho^S &= \rho_{0S}^S (1 - \text{Div}_S \mathbf{u}_S), \\ n^S &= n_{0S}^S (1 - \text{Div}_S \mathbf{u}_S + 3 \alpha^S \Delta\theta), \\ \rho^{SR} &= \rho_{0S}^{SR} (1 - 3 \alpha^S \Delta\theta). \end{aligned} \quad (5.14)$$

Summarising the results of the present section, the evaluation of the solid volume balance towards a thermoelastic material behaviour by applying a multiplicative split of the solid deformation gradient, led to comprehensive formulations for the solid density relations and the solid volume fraction. This is also justified by the fact that in solid mechanics,  $\rho^S$  is given solely by  $\rho_{0S}^S$  and  $\mathbf{F}_S$ , as far as  $\hat{\rho}^S = 0$ . The latter is a consequence of the integration of (5.3)<sub>1</sub>. Because of this procedure, the solid volume balance is already inherently added and is therefore removed from the set of governing equations.

## 5.2.2 Mass balances of the fluid phases

The mass balance of the fluid phase  $\varphi^\beta$  was displayed in (5.3)<sub>2</sub>, where  $\beta = \{L, G\}$ . Therein, the partial density  $\rho^\beta$  is replaced by its relation to the material density  $\rho^{\beta R}$  (3.5)<sub>3</sub>, viz.:

$$n^\beta (\rho^{\beta R})'_\beta + (n^\beta)'_\beta \rho^{\beta R} + n^\beta \rho^{\beta R} \text{div}' \mathbf{x}_\beta = \hat{\rho}^\beta. \quad (5.15)$$

For a formulation of the material time derivatives solely with respect to the solid motion  $(\cdot)'_S$ , the time derivative  $(\cdot)'_\beta$  in (5.15) must be transcribed by the help of (3.15), which yields

$$(n^\beta \rho^{\beta R})'_S + \operatorname{div} (n^\beta \rho^{\beta R} \mathbf{w}_\beta) + n^\beta \rho^{\beta R} \operatorname{div} (\mathbf{u}_S)'_S = \hat{\rho}^\beta . \quad (5.16)$$

Hereby, the definitions of the seepage velocity (3.14), the solid displacement (3.13) and the divergence theorem (cf. Appendix A) were used.

In this context, the coupling between the two fluid mass balances should be addressed. This coupling is ensured by the mass-production terms  $\hat{\rho}^\beta$ . From the sum over all constituents of the mass-production term (3.35)<sub>1</sub> and the preliminary assumption of an inert solid material, i. e.,  $\hat{\rho}^S \equiv 0$ , it follows:

$$\hat{\rho}^L = -\hat{\rho}^G . \quad (5.17)$$

In the case, where the fluid phases are composed of water ( $\varphi^L$ ) and CO<sub>2</sub> ( $\varphi^G$ ), no mass exchange between the two fluid phases is considered and, hence, the mass-production term on the right-hand side of (5.16) vanishes,  $\hat{\rho}^\beta = 0$ . Additionally, it is assumed in this case that the water phase is incompressible for  $\theta^L = \text{const.}$ , hence,  $\rho^{LR} = \text{const.}$ , and, thus, the water mass balance becomes the water volume balance after dividing (5.16) by  $\rho^{LR}$ :

$$(n^L)'_S + \operatorname{div} (n^L \mathbf{w}_L) + n^L \operatorname{div} (\mathbf{u}_S)'_S = 0 . \quad (5.18)$$

### 5.2.3 Momentum balance of the overall aggregate

The summation of the constituent momentum balances (5.3)<sub>3</sub> over all constituents  $\varphi^\alpha$  yields the mixture or overall momentum balance in its quasi-static formulation

$$\mathbf{0} = \sum_{\alpha} [\operatorname{div} \mathbf{T}^\alpha + \rho^\alpha \mathbf{g} + \hat{\mathbf{p}}^\alpha] . \quad (5.19)$$

Prior to this, one has to go back to the restrictions between the overall aggregate and the individual constituent formulations given in (3.51) to derive the particular terms for the mixture formulation of the momentum balance. Specifically, the overall *Cauchy* stress tensor  $\mathbf{T}$  is given by

$$\mathbf{T} = \sum_{\alpha} (\mathbf{T}^\alpha - \rho^\alpha \mathbf{d}_\alpha \otimes \mathbf{d}_\alpha) = \mathbf{T}^S + \mathbf{T}^L + \mathbf{T}^G - \rho^S \mathbf{d}_S \otimes \mathbf{d}_S - \rho^L \mathbf{d}_L \otimes \mathbf{d}_L - \rho^G \mathbf{d}_G \otimes \mathbf{d}_G , \quad (5.20)$$

and the density of the overall aggregate  $\rho$  reads

$$\rho = \sum_{\alpha} \rho^\alpha = n^S \rho^{SR} + n^L \rho^{LR} + n^G \rho^{GR} , \quad (5.21)$$

where the definition of partial densities (3.5) has been exploited. The sum over the momentum productions  $\hat{\mathbf{p}}^\alpha$  is treated by the help of (3.14), (3.35)<sub>1</sub>, (3.35)<sub>2</sub>, (3.36)<sub>1</sub> and the previously found relation  $\hat{\rho}^L = -\hat{\rho}^G$  (5.17) via

$$\sum_{\alpha} \hat{\mathbf{p}}^\alpha = \sum_{\alpha} (\hat{\mathbf{s}}^\alpha - \hat{\rho}^\alpha \mathbf{x}_\alpha) = \hat{\rho}^L (\mathbf{w}_G - \mathbf{w}_L) . \quad (5.22)$$

Although quasi-static problems were assumed, which allows for the negligence of the constituent accelerations  $\overset{\prime\prime}{\mathbf{x}}_\alpha \equiv 0$ , the same cannot be concluded directly for the barycentric acceleration  $\ddot{\mathbf{x}}$ . The reason therefor is found in (3.51)<sub>4</sub>:

$$\ddot{\mathbf{x}} = \frac{1}{\rho} \sum_{\alpha} [\rho^{\alpha} \overset{\prime\prime}{\mathbf{x}}_{\alpha} - \operatorname{div}(\rho^{\alpha} \mathbf{d}_{\alpha} \otimes \mathbf{d}_{\alpha}) + \hat{\rho}^{\beta} \overset{\prime}{\mathbf{x}}_{\beta}]. \quad (5.23)$$

This equation shows that even for vanishing constituent accelerations, the terms including the diffusion velocities  $\mathbf{d}_{\alpha}$  and the mass production  $\hat{\rho}^{\beta}$  do remain. Inserting (5.20), (5.21) and (5.23) into the momentum balance of the overall aggregate (3.42), the divergence of the diffusion velocity terms vanishes and only the *Cauchy* stress tensors remain. The final result of the mixture momentum balance after these manipulation reads:

$$\mathbf{0} = \sum_{\alpha} (\operatorname{div} \mathbf{T}^{\alpha}) + \rho \mathbf{g} + \hat{\rho}^L (\mathbf{w}_G - \mathbf{w}_L), \quad (5.24)$$

where the body force was replaced by the gravitational acceleration and the mass productions  $\hat{\rho}^{\beta}$  were replaced with the help of (3.14).

### 5.2.4 Energy balance of the overall aggregate

In case that all components share the same temperature, as it is assumed in the present consideration, cf. Section 5.1, the energy balances of the constituents have to be summed up towards the total energy balance for the computation of the temperature change. In this case, the direct energy production  $\hat{\varepsilon}^{\alpha}$  has to be substituted by (3.36)<sub>3</sub>, where the sum over all constituents of  $\hat{\varepsilon}^{\alpha}$  vanishes according to (3.35)<sub>3</sub>, viz.:

$$\sum_{\alpha} \rho^{\alpha} (\varepsilon^{\alpha})'_{\alpha} = \sum_{\alpha} [\mathbf{T}^{\alpha} \cdot \mathbf{L}_{\alpha} - \operatorname{div} \mathbf{q}^{\alpha} + \rho^{\alpha} r^{\alpha} - \hat{\mathbf{p}}^{\alpha} \cdot \overset{\prime}{\mathbf{x}}_{\alpha} - \hat{\rho}^{\alpha} (\varepsilon^{\alpha} + \frac{1}{2} \overset{\prime}{\mathbf{x}}_{\alpha} \cdot \overset{\prime}{\mathbf{x}}_{\alpha})]. \quad (5.25)$$

Thus, no constitutive equation is needed for the heat exchange  $\hat{\varepsilon}^{\alpha}$  between the different constituents. For more information to  $\hat{\varepsilon}^{\alpha}$ , please refer to *Ghadiani* [71]. However, frictional effects induced by  $\hat{\mathbf{p}}^{\alpha} \cdot \overset{\prime}{\mathbf{x}}_{\alpha}$  and energetic quantities transported during the phase-transition process through  $\hat{\rho}^{\alpha}$  also lead to mechanical and non-mechanical energy exchanges and heat transfers. Therewith, the energy balance of the overall aggregate (5.25) becomes:

$$\begin{aligned} \rho^S (\varepsilon^S)'_S + \rho^L (\varepsilon^L)'_L + \rho^G (\varepsilon^G)'_G &= \mathbf{T}^S \cdot \mathbf{L}_S + \mathbf{T}^L \cdot \mathbf{L}_L + \mathbf{T}^G \cdot \mathbf{L}_G - \\ &- \sum_{\alpha} \operatorname{div} \mathbf{q}^{\alpha} + \sum_{\alpha} \rho^{\alpha} r^{\alpha} - \hat{\mathbf{p}}^S \cdot \overset{\prime}{\mathbf{x}}_S - \hat{\mathbf{p}}^L \cdot \overset{\prime}{\mathbf{x}}_L - \hat{\mathbf{p}}^G \cdot \overset{\prime}{\mathbf{x}}_G - \\ &- \hat{\rho}^S (\varepsilon^S + \frac{1}{2} \overset{\prime}{\mathbf{x}}_S \cdot \overset{\prime}{\mathbf{x}}_S) - \hat{\rho}^L (\varepsilon^L + \frac{1}{2} \overset{\prime}{\mathbf{x}}_L \cdot \overset{\prime}{\mathbf{x}}_L) - \hat{\rho}^G (\varepsilon^G + \frac{1}{2} \overset{\prime}{\mathbf{x}}_G \cdot \overset{\prime}{\mathbf{x}}_G). \end{aligned} \quad (5.26)$$

An additional simplification of (5.26) can be achieved by combining the direct momentum and mass production terms in a similar manner as in the derivation of (5.22). The detailed

procedure is presented in Appendix B.7. The implementation of these simplifications into (5.26) yields:

$$\begin{aligned} \rho^S (\varepsilon^S)'_S + \rho^L (\varepsilon^L)'_L + \rho^G (\varepsilon^G)'_G &= \mathbf{T}^S \cdot \mathbf{L}_S + \mathbf{T}^L \cdot \mathbf{L}_L + \mathbf{T}^G \cdot \mathbf{L}_G - \sum_{\alpha} \operatorname{div} \mathbf{q}^{\alpha} + \\ &+ \sum_{\alpha} \rho^{\alpha} r^{\alpha} - \hat{\mathbf{p}}^L \cdot \mathbf{w}_L - \hat{\mathbf{p}}^G \cdot \mathbf{w}_G + \hat{\rho}^L [\varepsilon^G - \varepsilon^L + \frac{1}{2} (\mathbf{w}_G \cdot \mathbf{w}_G - \mathbf{w}_L \cdot \mathbf{w}_L)], \end{aligned} \quad (5.27)$$

which is the form of the mixture energy balance used in the following.

### 5.2.5 Adaptation of the entropy inequality

It was mentioned before that the derivation of the required constitutive relations for the constituents  $\varphi^{\alpha}$  is based on the evaluation of the entropy inequality. The latter was introduced in its general form as the *Clausius-Duhem* inequality, see (3.50). Incorporating therein the assumptions of equal constituent temperatures  $\theta^{\alpha} = \theta$ , as well as the sum of the total energy productions (3.35)<sub>4</sub>, (3.50) recasts to:

$$\begin{aligned} \frac{1}{\theta} \left\{ \mathbf{T}^S \cdot \mathbf{L}_S + \mathbf{T}^L \cdot \mathbf{L}_L + \mathbf{T}^G \cdot \mathbf{L}_G - \rho^S [(\psi^S)'_S + (\theta)'_S \eta^S] - \rho^L [(\psi^L)'_L + (\theta)'_L \eta^L] - \right. \\ \left. - \rho^G [(\psi^G)'_G + (\theta)'_G \eta^G] - \hat{\mathbf{p}}^S \cdot \dot{\mathbf{x}}_S - \hat{\mathbf{p}}^L \cdot \dot{\mathbf{x}}_L - \hat{\mathbf{p}}^G \cdot \dot{\mathbf{x}}_G - \hat{\rho}^S (\psi^S + \frac{1}{2} \dot{\mathbf{x}}_S \cdot \dot{\mathbf{x}}_S) - \right. \\ \left. - \hat{\rho}^L (\psi^L + \frac{1}{2} \dot{\mathbf{x}}_L \cdot \dot{\mathbf{x}}_L) - \hat{\rho}^G (\psi^G + \frac{1}{2} \dot{\mathbf{x}}_G \cdot \dot{\mathbf{x}}_G) - \frac{1}{\theta} \sum_{\alpha} \mathbf{q}^{\alpha} \cdot \operatorname{grad} \theta \right\} \geq 0. \end{aligned} \quad (5.28)$$

Next, one can again merge the direct momentum and mass production terms,  $\hat{\mathbf{p}}^{\alpha}$  and  $\hat{\rho}^{\beta}$ , following the procedures presented above for the momentum and energy balances:

$$\begin{aligned} \mathbf{T}^S \cdot \mathbf{L}_S + \mathbf{T}^L \cdot \mathbf{L}_L + \mathbf{T}^G \cdot \mathbf{L}_G - \rho^S [(\psi^S)'_S + (\theta)'_S \eta^S] - \rho^L [(\psi^L)'_L + (\theta)'_L \eta^L] - \\ - \rho^G [(\psi^G)'_G + (\theta)'_G \eta^G] - \hat{\mathbf{p}}^L \cdot \mathbf{w}_L - \hat{\mathbf{p}}^G \cdot \mathbf{w}_G + \\ + \hat{\rho}^L [\psi^G - \psi^L + \frac{1}{2} (\mathbf{w}_G \cdot \mathbf{w}_G - \mathbf{w}_L \cdot \mathbf{w}_L)] - \frac{1}{\theta} \sum_{\alpha} \mathbf{q}^{\alpha} \cdot \operatorname{grad} \theta \geq 0. \end{aligned} \quad (5.29)$$

Herein, in addition, the whole equation was multiplied with the absolute temperature, where  $\theta > 0$  K.

#### Saturation constraint:

By incorporating the saturation constraint (3.3)<sub>2</sub> into the entropy inequality, the mechanical constraint of a constant mass of the overall aggregate is added to the restrictions of the thermodynamical process. However, not the saturation constraint (3.3)<sub>2</sub> itself is applied, but its material time derivative with respect to the solid motion:

$$(n^S)'_S + (n^L)'_S + (n^G)'_S = 0, \quad (5.30)$$

where

$$\begin{aligned}
(n^S)'_S &= \frac{1}{\rho^{SR}} [-n^S (\rho^{SR})'_S - n^S \rho^{SR} \operatorname{div}' \mathbf{x}_S], \\
(n^L)'_S &= \frac{1}{\rho^{LR}} [\hat{\rho}^L - n^L (\rho^{LR})'_L - n^L \rho^{LR} \operatorname{div}' \mathbf{x}_L] - \operatorname{grad} n^L \cdot \mathbf{w}_L, \\
(n^G)'_S &= \frac{1}{\rho^{GR}} [\hat{\rho}^G - n^G (\rho^{GR})'_G - n^G \rho^{GR} \operatorname{div}' \mathbf{x}_G] - \operatorname{grad} n^G \cdot \mathbf{w}_G.
\end{aligned} \tag{5.31}$$

Therein, the material time derivatives of the volume fractions with respect to the solid constituent  $\varphi^S$  were transformed by utilising the mass balance equations of the respective constituents  $\varphi^\alpha$  (5.3)<sub>1,2</sub> and the relation (3.15). The material time derivative of the effective solid density  $\rho^{SR}$  in (5.31)<sub>1</sub> has to be defined according to its material behaviour, cf. (5.14)<sub>3</sub>. In particular, the effective density of the materially incompressible solid material solely depends on the temperature  $\theta$ . Consequently, its material time derivative reads

$$\rho^{SR} = \rho^{SR}(\theta) \quad \rightarrow \quad (\rho^{SR})'_S = \frac{d\rho^{SR}}{d\theta} (\theta)'_S. \tag{5.32}$$

Subsequently, relations (5.31) and (5.32) are inserted into (5.30), where the latter is multiplied with a so-called *Lagrangean multiplier*<sup>2</sup>  $\mathcal{P}$ , cf. *Liu* [107]:

$$\begin{aligned}
\mathcal{P} \left\{ \frac{1}{\rho^{SR}} [n^S \frac{d\rho^{SR}}{d\theta} (\theta)'_S + n^S \rho^{SR} \operatorname{div}' \mathbf{x}_S] + \right. \\
+ \frac{1}{\rho^{LR}} [-\hat{\rho}^L + n^L (\rho^{LR})'_L + n^L \rho^{LR} \operatorname{div}' \mathbf{x}_L] + \operatorname{grad} n^L \cdot \mathbf{w}_L + \\
\left. + \frac{1}{\rho^{GR}} [-\hat{\rho}^G + n^G (\rho^{GR})'_G + n^G \rho^{GR} \operatorname{div}' \mathbf{x}_G] + \operatorname{grad} n^G \cdot \mathbf{w}_G \right\} = 0.
\end{aligned} \tag{5.33}$$

---

<sup>2</sup>For further information on the principle of *Lagrange* multipliers please refer to, e. g., *Zinatbakhsh* [182].

The usage of a *Lagrangean* multiplier allows for an incorporation of the saturation constraint into the entropy inequality (5.29), which then yields the following formulation:

$$\begin{aligned}
& \underbrace{(\mathbf{T}^S + \mathcal{P} n^S \mathbf{I})}_{\mathbf{T}_E^S} \cdot \mathbf{L}_S - \rho^S (\psi^S)'_S - \rho^S \underbrace{\left( \eta^S - \mathcal{P} \frac{1}{(\rho^{SR})^2} \frac{d\rho^{SR}}{d\theta} \right)}_{\eta_E^S} (\theta)'_S + \\
& + \underbrace{(\mathbf{T}^L + \mathcal{P} n^L \mathbf{I})}_{\mathbf{T}_E^L} \cdot \mathbf{L}_L - \rho^L (\psi^L)'_L - \rho^L \eta^L (\theta)'_L + \mathcal{P} \frac{n^L}{\rho^{LR}} (\rho^{LR})'_L + \\
& + \underbrace{(\mathbf{T}^G + \mathcal{P} n^G \mathbf{I})}_{\mathbf{T}_E^G} \cdot \mathbf{L}_G - \rho^G (\psi^G)'_G - \rho^G \eta^G (\theta)'_G + \mathcal{P} \frac{n^G}{\rho^{GR}} (\rho^{GR})'_G - \\
& - \underbrace{(\hat{\mathbf{p}}^L - \mathcal{P} \text{grad } n^L)}_{\hat{\mathbf{p}}_E^L} \cdot \mathbf{w}_L - \underbrace{(\hat{\mathbf{p}}^G - \mathcal{P} \text{grad } n^G)}_{\hat{\mathbf{p}}_E^G} \cdot \mathbf{w}_G - \frac{1}{\theta} \sum_{\alpha} \mathbf{q}^{\alpha} \cdot \text{grad } \theta + \\
& + \hat{\rho}^L \left[ \psi^L - \psi^G + \frac{1}{2} (\mathbf{w}_G \cdot \mathbf{w}_G - \mathbf{w}_L \cdot \mathbf{w}_L) + \mathcal{P} \frac{1}{\rho^{LR}} - \mathcal{P} \frac{1}{\rho^{GR}} \right] \geq 0.
\end{aligned} \tag{5.34}$$

Herein, the relation (3.25) in the form

$$\text{div } \dot{\mathbf{x}}_{\alpha} = \mathbf{I} \cdot \text{grad } \dot{\mathbf{x}}_{\alpha} = \mathbf{I} \cdot \mathbf{L}_{\beta} \tag{5.35}$$

was applied. Furthermore, the so-called extra (or effective) quantities are introduced following the work of *Truesdell & Noll* [172]. Therewith, the partial stresses,  $\mathbf{T}^S$ ,  $\mathbf{T}^L$  and  $\mathbf{T}^G$ , the partial entropy,  $\eta^S$ , and the total momentum productions,  $\hat{\mathbf{p}}^L$  and  $\hat{\mathbf{p}}^G$ , are split into their extra part and a part containing the *Lagrange* multiplier  $\mathcal{P}$ :

$$\begin{aligned}
\mathbf{T}_E^S & := \mathbf{T}^S + \mathcal{P} n^S \mathbf{I}, & \mathbf{T}_E^L & := \mathbf{T}^L + \mathcal{P} n^L \mathbf{I}, & \mathbf{T}_E^G & := \mathbf{T}^G + \mathcal{P} n^G \mathbf{I}, \\
\eta_E^S & := \eta^S - \mathcal{P} \frac{1}{(\rho^{SR})^2} \frac{d\rho^{SR}}{d\theta}, & \hat{\mathbf{p}}_E^L & := \hat{\mathbf{p}}^L - \mathcal{P} \text{grad } n^L, & \hat{\mathbf{p}}_E^G & := \hat{\mathbf{p}}^G - \mathcal{P} \text{grad } n^G.
\end{aligned} \tag{5.36}$$

By including these extra terms into (5.34), one obtains the final form of the entropy inequality, as it will be used in the constitutive modelling procedure:

$$\begin{aligned}
& \mathbf{T}_E^S \cdot \mathbf{L}_S - \rho^S (\psi^S)'_S - \rho^S \eta_E^S (\theta)'_S + \mathbf{T}_E^L \cdot \mathbf{L}_L - \rho^L (\psi^L)'_L - \rho^L \eta^L (\theta)'_L + \mathcal{P} \frac{n^L}{\rho^{LR}} (\rho^{LR})'_L + \\
& + \mathbf{T}_E^G \cdot \mathbf{L}_G - \rho^G (\psi^G)'_G - \rho^G \eta^G (\theta)'_G + \mathcal{P} \frac{n^G}{\rho^{GR}} (\rho^{GR})'_G - \hat{\mathbf{p}}_E^L \cdot \mathbf{w}_L - \hat{\mathbf{p}}_E^G \cdot \mathbf{w}_G + \\
& + \hat{\rho}^L \left[ \psi^L - \psi^G + \frac{1}{2} (\mathbf{w}_G \cdot \mathbf{w}_G - \mathbf{w}_L \cdot \mathbf{w}_L) + \mathcal{P} \frac{1}{\rho^{LR}} - \mathcal{P} \frac{1}{\rho^{GR}} \right] - \frac{1}{\theta} \sum_{\alpha} \mathbf{q}^{\alpha} \cdot \text{grad } \theta \geq 0.
\end{aligned} \tag{5.37}$$

## 5.3 Determination of constitutive relations

The set of governing balance relations for the considered CO<sub>2</sub> sequestration model in (5.3) has to be closed by constitutive relations in order to account for the open fields described in Section 5.2. Reasonable and thermodynamically consistent constitutive relations are hereby found by taking into account the basic thermodynamic principles. These basic principles are the same as in classical continuum mechanics of single-phasic materials, presented for example by *Truesdell* [171], *Truesdell & Noll* [172] and *Truesdell & Toupin* [173]. The particular principles of determinism, equipresence, local action, material frame indifference and dissipation are introduced and discussed in the following. With these principles it is possible to obtain constitutive relations, which describe the physical behaviour of the constituents and the interactions between themselves in the considered CO<sub>2</sub> sequestration model.

### 5.3.1 The basic thermodynamical principles

Following, e. g., *Ehlers* [56], the quantities in the entropy inequality (5.37), which cannot be directly determined from the given motion and temperature fields  $\mathbf{x} = \chi_\alpha(\mathbf{X}_\alpha, t)$  and  $\theta = \theta(\mathbf{x}, t)$ , and from the balance relations, are collected in the set of undetermined response functions  $\mathcal{R}$ , viz.:

$$\mathcal{R} = \{ \psi^\alpha, \mathbf{T}_E^\alpha, \eta_E^S, \eta^\beta, \mathbf{p}_E^\beta, \hat{\rho}^\beta, \mathbf{q}^\alpha \}. \quad (5.38)$$

The *principle of determinism* now states that these response functions must be defined by the constitutive relations. The response functions  $\mathcal{R}(\mathcal{V})$  may depend on the whole set of process or constitutive variables  $\mathcal{V}$ , both at the initial and at the current state of the system (*principle of equipresence*). In the general case of a multiphasic material, this set is given as, cf. *Ehlers* [56]:

$$\mathcal{V} = \{ \theta^\alpha, \text{grad } \theta^\alpha, n^\alpha, \text{grad } n^\alpha, \rho^{\alpha R}, \text{grad } \rho^{\alpha R}, \mathbf{F}_\alpha, \text{grad } \mathbf{F}_\alpha, \dot{\mathbf{x}}_\alpha, \text{grad } \dot{\mathbf{x}}_\alpha, \mathbf{X}_\alpha \}. \quad (5.39)$$

Remembering the preliminary assumptions from Section 5.1, the general set  $\mathcal{V}$  can be reduced to a subset  $\mathcal{V}^1$  of the process variables

$$\mathcal{V}^1 = \{ \theta^\alpha, s^L, \rho^{LR}, \rho^{GR}, \mathbf{F}_S, \mathbf{w}_\beta, \mathbf{D}_\alpha \}, \quad \text{where } \mathcal{V}^1 \subset \mathcal{V}. \quad (5.40)$$

Herein, the volume fractions  $n^\alpha$  were replaced solely by the liquid saturation  $s^L$  by evaluation of the expressions in (3.3)<sub>2</sub>, (3.4) and (5.12)<sub>2</sub>. Furthermore, based on the *principle of frame indifference* that states that the response functions should be independent of the position of the observer, cf., e. g., *Bowen* [26], *de Boer* and *Ehlers* [22], *Ehlers* [56], as well as *Wagner* [176], the velocities  $\dot{\mathbf{x}}_\alpha$  are replaced by the seepage velocities  $\mathbf{w}_\beta$  according to (3.14) and the gradients of the fluid velocities are substituted by the symmetric parts of the velocity gradients  $\mathbf{D}_\beta$ . Moreover, due to the assumption of a homogeneous distribution of all material quantities in the reference configuration, the reference position vector  $\mathbf{X}_\alpha$  can be removed from (5.40). Based on the *principle of local action*, the gradients of

the process variables can be omitted in (5.40), since only the action at and close to the material point  $\mathcal{P}^\alpha$  is of interest, cf. e. g., Ehlers [56], Bowen [26, 27] or Truesdell & Noll [172].

From the *principle of phase separation*, i. e., each constituent  $\varphi^\alpha$  only depends on its own process variables, it follows that the subset of process variables  $\mathcal{V}^1$  can be distinguished into parts corresponding only to the specific constituents  $\varphi^\alpha$ , compare with Ehlers [49]. Therefore, it follows for the dependencies of the *Helmholtz* free energies  $\psi^\alpha$  in case of the given CO<sub>2</sub> sequestration model

$$\begin{aligned}\psi^S &= \psi^S(\mathbf{F}_S, \theta) & \rightarrow & (\psi^S)'_S = \frac{\partial \psi^S}{\partial \mathbf{F}_S} \mathbf{F}_S^T \cdot \mathbf{D}_S + \frac{\partial \psi^S}{\partial \theta} (\theta)'_S, \\ \psi^L &= \psi^L(\rho^{LR}, \theta, s^L) & \rightarrow & (\psi^L)'_L = \frac{\partial \psi^L}{\partial \rho^{LR}} (\rho^{LR})'_L + \frac{\partial \psi^L}{\partial \theta} (\theta)'_L + \frac{\partial \psi^L}{\partial s^L} (s^L)'_L, \\ \psi^G &= \psi^G(\rho^{GR}, \theta) & \rightarrow & (\psi^G)'_G = \frac{\partial \psi^G}{\partial \rho^{GR}} (\rho^{GR})'_G + \frac{\partial \psi^G}{\partial \theta} (\theta)'_G,\end{aligned}\tag{5.41}$$

where the dependency of  $\psi^L$  on both  $\rho^{LR}$  and  $s^L$  takes into account the existence of the two fluid phases and their distribution in the pore space.

The last principle, in particular the *principle of dissipation*, is applied in the following Section 5.3.2, where the entropy inequality is evaluated to finally derive the required constitutive relations.

### 5.3.2 Exploitation of the entropy inequality

To implement the time derivative of the liquid free energy (5.41)<sub>2</sub> into the modified entropy inequality (5.37), the derivative of the liquid saturation  $(s^L)'_L$  has to be modified by using the definition of the saturations (3.4)<sub>1</sub>, viz.:

$$(s^L)'_L = \frac{1}{n^F} [(n^L)'_L - s^L (n^F)'_L],\tag{5.42}$$

where the derivative of the fluid volume fraction can be altered with the transformation relation (3.15) towards

$$(n^F)'_L = (1 - n^S)'_L = -(n^S)'_L = -(n^S)'_S - \text{grad } n^S \cdot \mathbf{w}_L.\tag{5.43}$$

Furthermore,  $(n^L)'_L$  is replaced in (5.42) with the help of the liquid mass balance (5.15)

$$(n^L)'_L = -\frac{n^L}{\rho^{LR}} (\rho^{LR})'_L - n^L \text{div } \dot{\mathbf{x}}_L + \frac{\hat{\rho}^L}{\rho^{LR}}.\tag{5.44}$$

In the same manner,  $(n^S)'_S$  in (5.43) is substituted by the mass balance of the solid constituent (5.3)<sub>1</sub>, where, in addition, the dependence of the effective solid density on the temperature (5.32) is accounted for:

$$(n^S)'_S = -\frac{1}{\rho^{SR}} \left[ n^S (\rho^{SR})'_S + \rho^S \text{div } \dot{\mathbf{x}}_S \right] = -\frac{1}{\rho^{SR}} \left[ n^S \frac{\partial \rho^{SR}}{\partial \theta} (\theta)'_S + \rho^S \mathbf{D}_S \cdot \mathbf{I} \right].\tag{5.45}$$



The combination of (5.42), (5.43), (5.44) and (5.45) yields the time derivative of the liquid saturation:

$$(s^L)'_L = \frac{1}{n^F} \left[ -\frac{n^L}{\rho^{LR}} (\rho^{LR})'_L - n^L \mathbf{D}_L \cdot \mathbf{I} + \frac{\hat{\rho}^L}{\rho^{LR}} - s^L \frac{n^S}{\rho^{SR}} \frac{\partial \rho^{SR}}{\partial \theta} (\theta)'_S - s^L n^S \mathbf{D}_S \cdot \mathbf{I} + s^L \text{grad } n^S \cdot \mathbf{w}_L \right]. \quad (5.46)$$

Herein and in (5.45), the relation  $\text{div } \dot{\mathbf{x}}_\alpha = \mathbf{L}_\alpha \cdot \mathbf{I} = \mathbf{D}_\alpha \cdot \mathbf{I}$  was used.

Inserting the material time derivatives of the *Helmholtz* free energies (5.41) into the modified entropy inequality (5.37), thereby replacing  $(s^L)'_L$  in (5.41)<sub>2</sub> by (5.46) and sorting the terms, yields:

$$\begin{aligned} & \left( \underbrace{\mathbf{T}_E^S + s^L \frac{n^S}{n^F} \rho^L \frac{\partial \psi^L}{\partial s^L} \mathbf{I} - \rho^S \frac{\partial \psi^S}{\partial \mathbf{F}_S} \mathbf{F}_S^T}_{\mathbf{T}_{E \text{ mech.}}^S} \right) \cdot \mathbf{D}_S - \rho^S \left( \underbrace{\eta_E^S - s^L \frac{\rho^{LR}}{(\rho^{SR})^2} \frac{\partial \rho^{SR}}{\partial \theta} \frac{\partial \psi^L}{\partial s^L} + \frac{\partial \psi^S}}_{\eta_{E \text{ mech.}}^S} \right) (\theta)'_S + \\ & + \left( \underbrace{\mathbf{T}_E^L + s^L \rho^L \frac{\partial \psi^L}{\partial s^L} \mathbf{I}}_{\mathbf{T}_{E \text{ dis.}}^L} \right) \cdot \mathbf{D}_L - \rho^L \left( \eta^L + \frac{\partial \psi^L}{\partial \theta} \right) (\theta)'_L + \mathbf{T}_E^G \cdot \mathbf{D}_G - \rho^G \left( \eta^G + \frac{\partial \psi^G}{\partial \theta} \right) (\theta)'_G + \\ & + \left( \mathcal{P} \frac{n^L}{\rho^{LR}} + s^L n^L \frac{\partial \psi^L}{\partial s^L} - \rho^L \frac{\partial \psi^L}{\partial \rho^{LR}} \right) (\rho^{LR})'_L + \left( \mathcal{P} \frac{n^G}{\rho^{GR}} - \rho^G \frac{\partial \psi^G}{\partial \rho^{GR}} \right) (\rho^{GR})'_G + \\ & + \hat{\rho}^L \left[ \psi^G - \psi^L + \mathcal{P} \frac{1}{\rho^{GR}} - \mathcal{P} \frac{1}{\rho^{LR}} + s^L \frac{\partial \psi^L}{\partial s^L} + \frac{1}{2} (\mathbf{w}_G \cdot \mathbf{w}_G - \mathbf{w}_L \cdot \mathbf{w}_L) \right] - \\ & - \left( \underbrace{\hat{\mathbf{p}}_E^L + \frac{s^L}{n^F} \rho^L \frac{\partial \psi^L}{\partial s^L} \text{grad } n^S}_{\hat{\mathbf{p}}_{E \text{ dis.}}^L} \right) \cdot \mathbf{w}_L - \hat{\mathbf{p}}_E^G \cdot \mathbf{w}_G - \frac{1}{\theta} \sum_\alpha \mathbf{q}^\alpha \cdot \text{grad } \theta \geq 0. \end{aligned} \quad (5.47)$$

Following the evaluation procedure of *Coleman & Noll* [39], the resulting factors in (5.47) in front of the process variables  $\mathbf{D}_\alpha$ ,  $(\theta)'_\alpha$ ,  $(\rho^{\beta R})'_\beta$ ,  $\hat{\rho}^L$ ,  $\mathbf{w}_\beta$  and  $\mathbf{q}^\alpha$  must fulfill the entropy inequality on their own, which ensures the satisfaction of (5.47) for an arbitrary choice of the free parameters. *Wagner* [176] argues that the first part in (5.47) can be recognized as a non-dissipative (equilibrium) part in case of an elastic solid behaviour. In this regard, equilibrium is achieved if the expression in parentheses in front of the free parameter  $\mathbf{D}_S$  vanishes. Thus, the solid mechanical extra-stress tensor reads

$$\mathbf{T}_{E \text{ mech.}}^S = \mathbf{T}_E^S + s^L \frac{n^S}{n^F} \rho^L \frac{\partial \psi^L}{\partial s^L} \mathbf{I} = \rho^S \frac{\partial \psi^S}{\partial \mathbf{F}_S} \mathbf{F}_S^T. \quad (5.48)$$

In analogy to the solid mechanical extra-stress tensor, the solid mechanical extra entropy is defined via

$$\eta_{E \text{ mech.}}^S = \eta_E^S - s^L \frac{\rho^{LR}}{(\rho^{SR})^2} \frac{\partial \rho^{SR}}{\partial \theta} \frac{\partial \psi^L}{\partial s^L} = -\frac{\partial \psi^S}{\partial \theta}. \quad (5.49)$$

Further constraints are found from (5.47) in case of equilibrium assumptions for the fluid entropies  $\eta^\beta$  and the *Lagrange* multiplier  $\mathcal{P}$ :

$$\begin{aligned}\eta^L &= -\frac{\partial\psi^L}{\partial\theta}, \\ \eta^G &= -\frac{\partial\psi^G}{\partial\theta}, \\ \mathcal{P} &= (\rho^{LR})^2 \frac{\partial\psi^L}{\partial\rho^{LR}} - s^L \rho^{LR} \frac{\partial\psi^L}{\partial s^L}, \\ \mathcal{P} &= (\rho^{GR})^2 \frac{\partial\psi^G}{\partial\rho^{GR}}.\end{aligned}\tag{5.50}$$

The *Lagrange* multiplier  $\mathcal{P}$  in (5.50)<sub>4</sub> is distinguished as the effective gas pressure  $p^{GR}$ , viz.:

$$\mathcal{P} = (\rho^{GR})^2 \frac{\partial\psi^G}{\partial\rho^{GR}} =: p^{GR}.\tag{5.51}$$

In this context, it is helpful to introduce the capillary pressure  $p^c$  as the difference between the effective fluid pressure of the non-wetting fluid, here  $p^{GR}$ , and the effective fluid pressure of the wetting fluid, in this case  $p^{LR}$ , cf. *Brooks & Corey* [31] or *Graf* [74]:

$$p^c = p^{GR} - p^{LR}.\tag{5.52}$$

Subsequently, the definition (5.51) is inserted into (5.50)<sub>3</sub> and a comparison with (5.52) yields

$$\mathcal{P} = p^{GR} = (\rho^{LR})^2 \frac{\partial\psi^L}{\partial\rho^{LR}} - s^L \rho^{LR} \frac{\partial\psi^L}{\partial s^L} = p^{LR} + p^c.\tag{5.53}$$

Hence, the following relations between the liquid effective pressure  $p^{LR}$  and the capillary pressure  $p^c$  together with the derivatives of the liquid *Helmholtz* free energy  $\psi^L$  are determined:

$$\begin{aligned}p^{LR} &:= (\rho^{LR})^2 \frac{\partial\psi^L}{\partial\rho^{LR}}, \\ p^c &:= -s^L \rho^{LR} \frac{\partial\psi^L}{\partial s^L}.\end{aligned}\tag{5.54}$$

Dividing (5.51) by  $\rho^{GR}$  and dividing (5.50)<sub>3</sub> by  $\rho^{LR}$  after insertion of (5.54)<sub>1</sub> yields

$$\frac{\mathcal{P}}{\rho^{GR}} = \frac{p^{GR}}{\rho^{GR}} \quad \text{and} \quad \frac{\mathcal{P}}{\rho^{LR}} = \frac{p^{LR}}{\rho^{LR}} - s^L \frac{\partial\psi^L}{\partial s^L},\tag{5.55}$$

which will be needed in the following derivations.

Next, the attention is drawn to the dissipative terms of the entropy inequality (5.47), which are greater than zero. For convenience, the following two abbreviations for the liquid extra stress  $\mathbf{T}_{E \text{ dis.}}^L$  and the liquid extra momentum production  $\hat{\mathbf{p}}_{E \text{ dis.}}^L$  are postulated:

$$\begin{aligned}\mathbf{T}_{E \text{ dis.}}^L &= \mathbf{T}_E^L + s^L \rho^L \frac{\partial\psi^L}{\partial s^L} \mathbf{I}, \\ \hat{\mathbf{p}}_{E \text{ dis.}}^L &= \hat{\mathbf{p}}_E^L + \frac{s^L}{n^F} \rho^L \frac{\partial\psi^L}{\partial s^L} \text{grad } n^S.\end{aligned}\tag{5.56}$$

Furthermore, following *Dalton's law*<sup>3</sup> the overall pore pressure  $p^{FR}$  is introduced as the sum of the effective fluid pressures  $p^{\beta R}$ , weighted by the respective saturations  $s^\beta$  via

$$p^{FR} = s^L p^{LR} + s^G p^{GR} . \quad (5.57)$$

With the previously found relations for the *Lagrange* multiplier  $\mathcal{P} = p^{GR}$  and for the capillary pressure  $p^c$ , cf. (5.54)<sub>2</sub>, and with the formulation of the overall pore pressure  $p^{FR}$  (5.57), a second look is taken on the extra terms. Starting with the solid mechanical extra stress  $\mathbf{T}_{E\text{ mech.}}^S$ , the relations (5.36)<sub>1</sub> and (5.48) are combined to retrieve the overall solid *Cauchy* stress tensor:

$$\mathbf{T}^S = \mathbf{T}_{E\text{ mech.}}^S - \mathcal{P} n^S \mathbf{I} - s^L \frac{n^S}{n^F} \rho^L \frac{\partial \psi^L}{\partial s^L} \mathbf{I} . \quad (5.58)$$

Replacing the *Lagrange* multiplier  $\mathcal{P}$  and the term including the derivative of the liquid *Helmholtz* free energy by (5.54)<sub>2</sub> and using the relations for the capillary pressure (5.52), the partial density (3.5)<sub>3</sub>, the saturations (3.4), as well as the overall pore pressure (5.57), yields:

$$\mathbf{T}^S = \mathbf{T}_{E\text{ mech.}}^S - p^{FR} n^S \mathbf{I} . \quad (5.59)$$

This clearly shows that loads imposed on a fluid filled porous body do not stress the solid material alone, but are also absorbed by the fluids inside the pore space.

Continuing with the fluid extra stress tensors from (5.36)<sub>2</sub>, (5.56)<sub>1</sub> and (5.36)<sub>3</sub> the same replacements are used as in the derivation of the overall *Cauchy* stress tensor. Consequently, the fluid stresses are given by

$$\begin{aligned} \mathbf{T}^L &= \mathbf{T}_{E\text{ dis.}}^L - \mathcal{P} n^L \mathbf{I} - s^L \rho^L \frac{\partial \psi^L}{\partial s^L} \mathbf{I} & \rightarrow & \mathbf{T}^L = \mathbf{T}_{E\text{ dis.}}^L - p^{LR} n^L \mathbf{I} , \\ \mathbf{T}^G &= \mathbf{T}_E^G - \mathcal{P} n^L \mathbf{I} & \rightarrow & \mathbf{T}^G = \mathbf{T}_E^G - p^{GR} n^G \mathbf{I} . \end{aligned} \quad (5.60)$$

Next, the solid mechanical extra entropy given in (5.49) and (5.36)<sub>4</sub> is reformulated to obtain the solid entropy. Hereby, (5.55)<sub>2</sub> is used, which relates the *Lagrange* parameter  $\mathcal{P}$ , the liquid pressure  $p^{LR}$  and the liquid saturation  $s^L$  :

$$\begin{aligned} \eta^S &= \eta_{E\text{ mech.}}^S + \mathcal{P} \frac{1}{(\rho^{SR})^2} \frac{d\rho^{SR}}{d\theta} + s^L \frac{\rho^{LR}}{(\rho^{SR})^2} \frac{\partial \rho^{SR}}{\partial \theta} \frac{\partial \psi^L}{\partial s^L} , \\ \rightarrow \eta^S &= \eta_{E\text{ mech.}}^S + \frac{p^{LR}}{(\rho^{SR})^2} \frac{\partial \rho^{SR}}{\partial \theta} . \end{aligned} \quad (5.61)$$

Thereafter, the fluid extra momentum productions are investigated. The relations (5.36)<sub>5</sub>, (5.56)<sub>2</sub> and (5.36)<sub>5</sub> are processed in the same way as the other extra terms before, yielding

---

<sup>3</sup>The original definition of *Dalton's law* was established only for ideal gases, cf., e. g., *Class* [36] or *Lewis & Randall* [105]. However, it is still valid here (also for real gases and liquids), since the formulation of  $p^{FR}$  is based on the TPM, more exactly, on the principle of superimposed, statistically distributed continua, where the interaction between the constituents is controlled by production terms and the porous medium together with its percolating fluid constituents is treated as a mixture. Thus, the effective pressures  $p^{\beta R}$  act similar as in an ideal gas, where it is assumed that the different molecules do not "see" each other.

for the liquid momentum production

$$\begin{aligned}\hat{\mathbf{p}}^L &= \hat{\mathbf{p}}_{E\text{ dis.}}^L + \mathcal{P} \text{grad } n^L - \frac{s^L}{n^F} \rho^L \frac{\partial \psi^L}{\partial s^L} \text{grad } n^S \\ \rightarrow \hat{\mathbf{p}}^L &= \hat{\mathbf{p}}_{E\text{ dis.}}^L + p^{LR} \text{grad } n^L + p^c n^F \text{grad } s^L .\end{aligned}\quad (5.62)$$

The result of (5.62) can be varied by the relations of the volume fractions, saturations and capillary pressure as shown in Appendix B.8. In case of the gaseous constituent, the fluid extra momentum production reads

$$\hat{\mathbf{p}}^G = \hat{\mathbf{p}}_E^G + \mathcal{P} \text{grad } n^G \quad \rightarrow \quad \hat{\mathbf{p}}^G = \hat{\mathbf{p}}_E^G + p^{GR} \text{grad } n^G . \quad (5.63)$$

At this point, the attention is drawn to the discussion of the specific heat capacities  $c_V^{\alpha R}$ . Starting with the fluid constituents, the relations for the entropies  $\eta^\beta$ , found in (5.50)<sub>1</sub> and (5.50)<sub>2</sub>, can be combined with the definition of the specific heat capacities  $c_V^{\beta R}$  of the fluid constituents, see Section 4.3. This yields a formulation for the specific heat capacity with respect to the *Helmholtz* free energy  $\psi^\beta$  for the individual fluid constituents:

$$c_V^{\beta R} = \theta \frac{\partial \eta^\beta}{\partial \theta} = -\theta \frac{\partial^2 \psi^\beta}{\partial \theta^2} . \quad (5.64)$$

A similar relation is obtained for the specific heat capacity of the solid constituent. However, within the derivation, care has to be taken on the solid entropy  $\eta^S$  of (5.61), which includes the derivative of the solid density with respect to the temperature as an additional term. In this context, it is postulated that the solid internal energy depends on the mechanical extra entropy via  $\varepsilon^S = \varepsilon^S(\eta_{E\text{ mech.}}^S, \mathbf{E}_S)$ . Hence, it follows for the solid specific heat capacity:

$$c_V^S = \frac{\partial \varepsilon^S}{\partial \theta} = \frac{\partial \varepsilon^S}{\partial \eta_{E\text{ mech.}}^S} \frac{\partial \eta_{E\text{ mech.}}^S}{\partial \theta} . \quad (5.65)$$

The *Legendre* transformation for the internal energy  $\varepsilon^S(\eta_{E\text{ mech.}}^S, \mathbf{E}_S)$ , cf. Appendix (B.5), yields

$$\varepsilon^S = \psi^S + \theta \eta_{E\text{ mech.}}^S . \quad (5.66)$$

Thus, the derivative of the internal energy with respect to the mechanical extra entropy reads

$$\frac{\partial \varepsilon^S}{\partial \eta_{E\text{ mech.}}^S} = \theta . \quad (5.67)$$

With the usage of (5.49), the specific heat capacity of the solid constituent is then found as

$$c_V^S = \theta \frac{\partial \eta_{E\text{ mech.}}^S}{\partial \theta} = -\theta \frac{\partial}{\partial \theta} \left( \frac{\partial \psi^S}{\partial \theta} \right) = -\theta \frac{\partial^2 \psi^S}{\partial \theta^2} . \quad (5.68)$$

### Dissipation inequality

With the help of the abbreviations of the extra terms (5.36) and the relations found in (5.55), the remaining dissipative parts of the entropy inequality (5.47) can be collected in

the so-called dissipation inequality  $\mathcal{D}$

$$\begin{aligned} \mathcal{D} = & \mathbf{T}_{E \text{ dis.}}^L \cdot \mathbf{L}_L + \mathbf{T}_E^G \cdot \mathbf{L}_G - \hat{\mathbf{p}}_{E \text{ dis.}}^L \cdot \mathbf{w}_L - \hat{\mathbf{p}}_E^G \cdot \mathbf{w}_G - \frac{1}{\theta} \sum_{\alpha} \mathbf{q}^{\alpha} \cdot \text{grad } \theta + \\ & + \hat{\rho}^L \left[ \psi^G - \psi^L + \frac{p^{GR}}{\rho^{GR}} - \frac{p^{LR}}{\rho^{LR}} + \frac{1}{2} (\mathbf{w}_G \cdot \mathbf{w}_G - \mathbf{w}_L \cdot \mathbf{w}_L) \right] \geq 0. \end{aligned} \quad (5.69)$$

According to *Ehlers et al.* [58], who carried out a dimensional analysis, the fluid extra stress tensors  $\mathbf{T}_{E \text{ dis.}}^L$  and  $\mathbf{T}_E^G$ , which describe the frictional stresses, can be neglected in comparison with the fluid extra momentum productions. Thus,

$$\mathbf{T}_{E \text{ dis.}}^L \approx \mathbf{0}, \quad \text{and} \quad \mathbf{T}_E^G \approx \mathbf{0}. \quad (5.70)$$

Consequently, the dissipation inequality reduces to

$$\begin{aligned} \mathcal{D} = & -\hat{\mathbf{p}}_{E \text{ dis.}}^L \cdot \mathbf{w}_L - \hat{\mathbf{p}}_E^G \cdot \mathbf{w}_G - \frac{1}{\theta} \sum_{\alpha} \mathbf{q}^{\alpha} \cdot \text{grad } \theta + \\ & + \underbrace{\hat{\rho}^L \left[ \psi^G - \psi^L + \frac{p^{GR}}{\rho^{GR}} - \frac{p^{LR}}{\rho^{LR}} + \frac{1}{2} (\mathbf{w}_G \cdot \mathbf{w}_G - \mathbf{w}_L \cdot \mathbf{w}_L) \right]}_{\mathcal{D}_{\text{mass transition}}} \geq 0. \end{aligned} \quad (5.71)$$

To ensure the positive definiteness of (5.71), all terms by themselves must be positive. For the given problem, a possible way to guarantee this is to require a proportionality (negative or positive, depending on the sign of the term) between the variables of each term, leading to a quadratic formulation that assures the positiveness. At first, this is performed for the third term in (5.71), where the heat flux and the gradient of the temperature<sup>4</sup> should be proportional to each other, i. e.,  $\mathbf{q}^{\alpha} \propto \text{grad } \theta^5$ . From this, the well-known *Fourier's* law can be developed, which will be shown in Section 5.3.5. In the same way, proportionalities are defined between the extra momentum productions of the fluids and the seepage velocities, namely  $\hat{\mathbf{p}}_{E \text{ dis.}}^L \propto \mathbf{w}_L$  and  $\hat{\mathbf{p}}_E^G \propto \mathbf{w}_G$ . In turn, these relations will result in the well-known *Darcy's* law, which describes the motion of percolating fluids in a porous medium, due to a pressure gradient. The detailed derivation will be presented in Section 5.3.4.

A discussion of the liquid mass production  $\hat{\rho}^L$  in the dissipation inequality (5.71) is addressed in what follows. To begin with, the definition of the chemical potential

$$\mu^{\beta} = \psi^{\beta} + \frac{p^{\beta R}}{\rho^{\beta R}}, \quad (5.72)$$

as it was introduced in Section 4.1.1, will be incorporated in the mass-transition term of the dissipation inequality, i. e.,

$$\mathcal{D}_{\text{mass transition}} = \hat{\rho}^L \left[ \mu^G - \mu^L + \frac{1}{2} (\mathbf{w}_G \cdot \mathbf{w}_G - \mathbf{w}_L \cdot \mathbf{w}_L) \right]. \quad (5.73)$$

<sup>4</sup>The division by  $\theta$  can be omitted in this procedure, since the absolute temperature is always greater than zero, i. e.,  $\theta > 0$  K.

<sup>5</sup>Please keep in mind that this holds for a single common temperature  $\theta = \theta^{\alpha}$ .

Herein, the quadratic seepage-velocity terms  $\mathbf{w}_\beta \cdot \mathbf{w}_\beta$  can be neglected, since kinetic effects are usually smaller than thermal ones, cf. *Morland & Gray* [120]. In consequence, only the difference in the chemical potentials remains. In order to ensure positive definiteness of the dissipation inequality, a proportional relation between the mass production  $\hat{\rho}^L$  and the difference between the chemical potentials is proposed, i. e.,  $\hat{\rho}^L \propto (\mu^G - \mu^L)$ . This relationship will be discussed further in Section 5.4.

### 5.3.3 Constitutive relations of the solid constituent

The effective and partial densities  $\rho^{SR}$  and  $\rho^S$ , as well as the solid volume fraction  $n^S$  were already defined in Section 5.2.1 by evaluating the solid volume balance with respect to a thermoelastic solid material. Therein, the solid deformation gradient  $\mathbf{F}_S$  was multiplicatively split into a purely mechanical and a purely thermal part to account for the dependence of the solid deformation, both on the displacement  $\mathbf{u}_S$  and the temperature  $\theta$ . Furthermore, the *Green-Lagrangian* deformation tensor  $\mathbf{E}_S$  and after linearisation also the total strain tensor  $\boldsymbol{\varepsilon}_S$  were additively decomposed into mechanical and thermal parts, cf. (5.6)<sub>3</sub> and (5.7)<sub>3</sub>, discussed in Section 5.2.1. Consequently, an additively splitting procedure must also be exercised on the solid *Helmholtz* energy  $\psi^S$ , in order to find the conjugated variables. Following *Ehlers* and *Häberle* [61] and proceeding from the small strain assumption, the solid free energy can be given as the sum of a purely mechanical part  $\psi_m^S$  and a purely thermal part  $\psi_\theta^S$  in the geometrically linearised setting

$$\rho_{0S}^S \psi^S(\boldsymbol{\varepsilon}_{Sm}, \theta) = \rho_{0S}^S \psi_m^S(\boldsymbol{\varepsilon}_{Sm}) + \rho_{0S}^S \psi_\theta^S(\theta). \quad (5.74)$$

Subsequently, formulations for the linearised solid extra stress  $\boldsymbol{\sigma}_{E\text{mech}}^S$  and the solid entropy  $\eta^S$  can be obtained from the *Helmholtz* free energy by exploiting the conjugated variable pairs  $\{\boldsymbol{\sigma}_{E\text{mech}}^S, \boldsymbol{\varepsilon}_{Sm}\}$  and  $\{\eta_{E\text{mech}}^S, \theta\}$ .

Assuming an elastic material governed by *Hooke's* law, the mechanical part in (5.74) is given by

$$\rho_{0S}^S \psi_m^S(\boldsymbol{\varepsilon}_{Sm}) = \mu^S \boldsymbol{\varepsilon}_{Sm} \cdot \boldsymbol{\varepsilon}_{Sm} + \frac{1}{2} \lambda^S (\boldsymbol{\varepsilon}_{Sm} \cdot \mathbf{I})^2, \quad (5.75)$$

where  $\mu^S$  and  $\lambda^S$  are the *Lamé* constants. The thermal part is found from the specific heat capacity at constant volume, cf. (5.68),

$$c_V^S = -\theta \frac{\partial^2 \psi_\theta^S}{\partial \theta^2}. \quad (5.76)$$

Substituting  $\boldsymbol{\varepsilon}_{Sm}$  by  $\boldsymbol{\varepsilon}_S - \boldsymbol{\varepsilon}_{S\theta}$  from (5.7)<sub>3</sub> and (5.9)<sub>2</sub> and integrating (5.76) together with the side conditions  $\psi_\theta^S(\theta_0) = 0$  and  $\partial \psi_\theta^S / \partial \theta(\theta_0) = 0$ , one obtains

$$\begin{aligned} \rho_{0S}^S \psi_m^S &= \mu^S (\boldsymbol{\varepsilon}_S \cdot \boldsymbol{\varepsilon}_S) + \frac{1}{2} \lambda^S (\boldsymbol{\varepsilon}_S \cdot \mathbf{I})^2 - 3k^S \alpha^S \Delta\theta (\boldsymbol{\varepsilon}_S \cdot \mathbf{I}) + \frac{1}{2} k^S (3\alpha^S \Delta\theta)^2, \\ \rho_{0S}^S \psi_\theta^S &= -\frac{1}{2} k^S (3\alpha^S \Delta\theta)^2 - \rho_{0S}^S c_V^S (\theta \ln \frac{\theta}{\theta_0} - \Delta\theta), \end{aligned} \quad (5.77)$$

where  $k^S = \frac{2}{3}\mu^S + \lambda^S$  is the compression modulus. A summation of both relations in (5.77) yields the free energy of a linear thermoelastic solid skeleton:

$$\rho_{0S}^S \psi^S = \mu^S (\boldsymbol{\varepsilon}_S \cdot \boldsymbol{\varepsilon}_S) + \frac{1}{2} \lambda^S (\boldsymbol{\varepsilon}_S \cdot \mathbf{I})^2 + m_\theta^S \Delta\theta (\boldsymbol{\varepsilon}_S \cdot \mathbf{I}) - \rho_{0S}^S c_V^S \left( \theta \ln \frac{\theta}{\theta_0} - \Delta\theta \right). \quad (5.78)$$

Therein,  $m_\theta^S = -3k^S \alpha^S$  is introduced as the stress-temperature modulus.

Proceeding from the basic constitutive relations derived in Section 5.3.2, the second *Piola-Kirchhoff* stress  $\mathbf{S}_{E \text{ mech.}}^S$  is given by

$$\mathbf{S}_{E \text{ mech.}}^S = \rho_{0S}^S \frac{\partial \psi^S}{\partial \mathbf{E}_S} = \det \mathbf{F}_S \mathbf{F}_S^{-1} \mathbf{T}_{E \text{ mech.}}^S \mathbf{F}_S^{T-1}. \quad (5.79)$$

Under small-strain conditions, where  $\mathbf{T}_{E \text{ mech.}}^S \approx \mathbf{S}_{E \text{ mech.}}^S \approx \boldsymbol{\sigma}_{E \text{ mech.}}^S$  and  $\mathbf{E}_S \approx \boldsymbol{\varepsilon}_S$ , the first partial derivative of  $\rho_{0S}^S \psi^S$  with respect to  $\boldsymbol{\varepsilon}_S$  yields the solid extra stress  $\boldsymbol{\sigma}_{E \text{ mech.}}^S$ :

$$\boldsymbol{\sigma}_{E \text{ mech.}}^S = 2\mu^S \boldsymbol{\varepsilon}_S + \lambda^S (\boldsymbol{\varepsilon}_S \cdot \mathbf{I}) \mathbf{I} + m_\theta^S \Delta\theta \mathbf{I}. \quad (5.80)$$

Note in passing that (5.80) can also be found directly from (5.75), when (5.75) is differentiated with respect to  $\boldsymbol{\varepsilon}_{Sm}$ , which is then substituted by  $\boldsymbol{\varepsilon}_S - \boldsymbol{\varepsilon}_{S\theta}$ .

Given the above, the solid mechanical extra entropy is obtained on the basis of (5.49) and (5.78), viz.:

$$\eta_{E \text{ mech.}}^S = -\frac{\partial \psi^S}{\partial \theta} = -\frac{1}{\rho_{0S}^S} m_\theta^S (\boldsymbol{\varepsilon}_S \cdot \mathbf{I}) + c_V^S \ln \frac{\theta}{\theta_0}. \quad (5.81)$$

Finally, the internal energy of the solid constituent is found by use of the *Legendre* transformation, cf. (B.5),

$$\varepsilon^\alpha = \psi^\alpha + \theta \eta^\alpha. \quad (5.82)$$

After multiplication with the initial solid density  $\rho_{0S}^S$  and with (5.78) and (5.61) together with (5.81), the solid internal energy<sup>6</sup> reads

$$\rho_{0S}^S \varepsilon^S = \mu^S (\boldsymbol{\varepsilon}_S \cdot \boldsymbol{\varepsilon}_S) + \frac{1}{2} \lambda^S (\boldsymbol{\varepsilon}_S \cdot \mathbf{I})^2 - m_\theta^S \theta_0 (\boldsymbol{\varepsilon}_S \cdot \mathbf{I}) + \rho_{0S}^S c_V^S \Delta\theta + \rho_{0S}^S \theta \frac{p^{LR}}{(\rho^{SR})^2} \frac{\partial \rho^{SR}}{\partial \theta}. \quad (5.83)$$

### 5.3.4 Constitutive relations of the fluid constituents

After having found the required constitutive relations of the solid constituent, the evaluation of the entropy inequality with respect to the fluid constituents follows. Herein, the distribution of the percolating fluid phases in the pore space, their respective motion, the  $p^{\beta R}$ - $\theta$ - $\rho^{\beta R}$  behaviour and the thermodynamical quantities, i. e., the *Helmholtz* free energy and the entropy, are investigated. The parts concerning the porosity, the capillary pressure, the saturation and the seepage velocity are of particular interest in groundwater engineering, e. g., *Helmiğ* [84]. The preliminaries for the part, where the thermodynamical constitutive relations are identified, have already been discussed in Chapter 4.

<sup>6</sup>Please note in passing that the internal energy is actually a function of the entropy, whereas here it is given with respect to its conjugated variable the temperature  $\theta$ . This can be justified with regard to the measurability, which is simple for the temperature, but more or less impossible in case of the entropy.

## Porosity and capillary-pressure-saturation relation

To start with, the volume fraction of the overall pore fluid  $n^F$ , also denoted as the porosity, was introduced in (3.4)<sub>2</sub> and is related to the solid volume fraction  $n^S$  by (3.3)<sub>2</sub>. In addition, an insertion of the relations for the solid volume fraction (5.12)<sub>2</sub> and (5.13)<sub>2</sub> yields

$$n^F = 1 - n^S = 1 - n_{0S}^S (1 - \text{Div}_S \mathbf{u}_S + 3 \alpha^S \Delta \theta). \quad (5.84)$$

Further considerations have to be made for the determination of distributive quantities of the specific fluid constituents, namely  $n^L$  and  $n^G$ , or  $s^L$  and  $s^G$ . Note that both the fluid volume fractions and the saturations  $n^\beta$  and  $s^\beta$ , respectively, are inversely proportional related to each other, cf. (3.4)<sub>1</sub>. The introduction of the saturation is motivated by the fact that the distribution of the two fluid constituents in the pore space is only a function of the pore-fluid pressures  $p^{LR}$  and  $p^{GR}$ . More precisely, the saturations are a function of the difference between these pressures, denoted as the capillary pressure, cf. (5.52),  $p^c = p^{GR} - p^{LR}$ . A prominent formulation of this relationship is provided by the *Brooks* and *Corey* law<sup>7</sup> [31], given by

$$s_{\text{eff}}^L = \left( \frac{p_d}{p^c} \right)^\lambda. \quad (5.85)$$

Therein,  $s_{\text{eff}}^L$  is the effective saturation, and the material parameters  $p_d$  and  $\lambda$  are the entry pressure<sup>8</sup> and the pore-size distribution index, respectively. In this context, it has to be mentioned that capillary-pressure-saturation relations are usually regarded as time-independent, cf. *Morrow* [122]. Equation (5.85) basically accounts in a homogenised sense for the surface tension, where the latter acts on the microscale between the wetting and non-wetting fluids, cf. Figure 5.1. The surface tension  $\sigma_s$  originates from inter-molecular

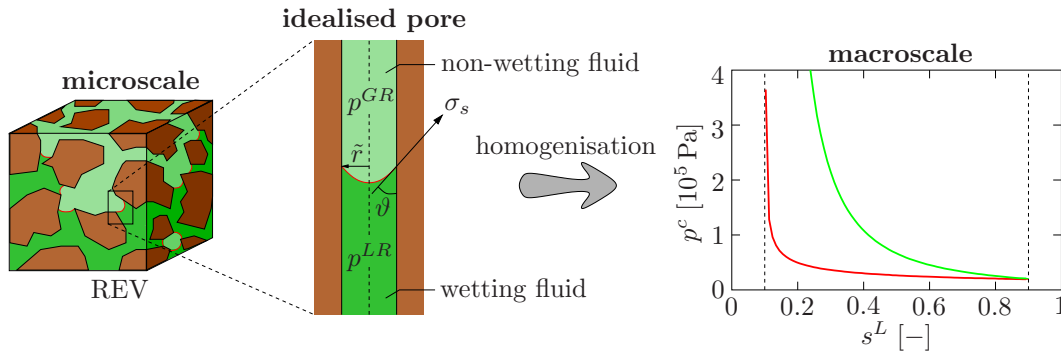


Figure 5.1: Depiction of the surface tension in a capillary tube with the different pressures of the two fluid phases and the macroscopic equivalent approximation by *Brooks & Corey* for an entry pressure of  $p_d = 2.0 \cdot 10^4$  Pa and for two pore-size distribution parameters  $\lambda = 2.3$  (red) and  $\lambda = 0.6$  (green). The residual saturations were chosen to  $s_{\text{res}}^L = s_{\text{res}}^G = 0.1$ .

forces in the involved fluids that tries to minimise the surface area between the two

<sup>7</sup>A further well-known capillary-pressure-saturation relation is the law by *van Genuchten* [174], which in contrast to the *Brooks* and *Corey* law exhibits a continuous behaviour around the entry pressure  $p_d$ . For more information on the *van Genuchten* law and its relation to the *Brooks* and *Corey* law, the interested reader is referred to, e. g., *Class* [36].

<sup>8</sup>Also sometimes called “bubbling pressure” or “threshold pressure”.



fluids and between the fluids and the solid. In consequence, the surface tension causes a discontinuity in the pressure field across the interface, where the pressure difference between the low pressure of the wetting fluid and the high pressure of the non-wetting side depends on the curvature of the interface. The *Laplace* equation formulates the relation between the pressure difference and the surface tension  $\sigma_s$  via

$$p^{GR} - p^{LR} = \frac{2\sigma_s \cos\vartheta}{\tilde{r}} = p^c. \quad (5.86)$$

Herein,  $\tilde{r}$  is the radius of an idealised pore or the meniscus formed by the wetting fluid. Moreover, the surface tension  $\sigma_s$  is the tangential force at the contact line between the fluid interface and the solid material, and the contact angle  $\vartheta$  between the fluid interface and the solid, measured through the wetting fluid, is an indicator for the so-called wettability of a fluid. Hereby, a contact angle of  $0^\circ \leq \vartheta < 90^\circ$  identifies the wetting fluid (here  $\varphi^L$ ), an angle of  $90^\circ < \vartheta \leq 180^\circ$  defines the non-wetting fluid (here  $\varphi^G$ ), and for  $\vartheta = 90^\circ$  no capillary forces exist. For further information on this topic, e. g., the temperature dependence of the surface tension, please refer to *Bear* [13] or *Class* [36]. Equation (5.86) shows that the capillarity effect is more pronounced in small pores, tubes or channels with a small radius  $\tilde{r}$ , as it usually is the case in porous media, cf. Figure 5.1.

At this point, the introduction of the phrases *imbibition* and *drainage* might be helpful. These originate from the fields of groundwater and petroleum engineering and describe the displacement of one fluid phase by the other fluid phase. In particular, the displacement of the non-wetting phase by the wetting phase is named imbibition, whereas the opposite, in particular the displacement of the non-wetting phase by the wetting phase, is called drainage.

It is obvious that a porous medium is not composed of pores with just one single diameter, as in the idealised pore depicted in Figure 5.1 (middle). Rather, a great variety exists, where for the considered soil material, the *Gaußian* distribution of the diameters is a function of the assortment and packing of the solid particles, cf., e. g., *Fredlund et al.* [69]. The plot on the right side in Figure 5.1 shows the capillary-pressure-saturation relation, on the one hand, for a well-sorted soil (red curve) with a high value for the pore-size distribution parameter  $\lambda = 2.3$ , for instance of a sand, and on the other hand, for a poorly sorted soil (green curve) with many different pore sizes resulting in a small value in  $\lambda = 0.6$ , e. g., of a clayey silt. Obviously, the pore-size distribution is directly related to the grain-size distribution. More information on this relationship can be found, for example, in *Folk* [67].

The porous medium can be understood as a bundle of idealised pores with different diameters, where, based on (5.86), large diameters correspond to a low capillary pressure and vice versa. Consequently, for a high wetting-fluid pressure, i. e., low  $p^c$ , almost all pores are liquid-filled implying a high saturation of the wetting fluid. This is also depicted in the diagram in Figure 5.1 (left). The diagram furthermore shows that in the fully liquid- and in the fully gas-saturated cases residual saturations,  $s_{\text{res}}^L$  and  $s_{\text{res}}^G$ , remain. These are fluid portions that are trapped by capillary forces in the system and are, therefore, no longer reachable for pressure-induced saturation changes. Accordingly, only the saturation in between these residual saturations, denoted as the effective saturation  $s_{\text{eff}}^L$ , is free in

the sense of replacement and, thus, is calculated from the *Brooks & Corey* law, see (5.85). A relation for the effective saturation is given for example by *van Genuchten* [174] via

$$s_{\text{eff}}^L = \frac{s^L - s_{\text{res}}^L}{1 - s_{\text{res}}^L - s_{\text{res}}^G}. \quad (5.87)$$

With this relation at hand, the entry pressure  $p_d$  of (5.85) can be explained as follows. Considering a porous medium fully saturated by the wetting fluid ( $s_{\text{eff}}^L = 1.0$ ), the entry pressure equals the minimal pressure needed for the non-wetting fluid to enter the pore space during drainage. Thus, the entry pressure resembles the capillary pressure associated with the largest pore in the system, cf. (5.86).

Please note in passing that in reality hysteresis effects in the capillary-pressure-saturation relation are encountered if successive imbibition and drainage processes occur. This is caused, for example, by the so-called *ink-bottle effect* or *Haines jump*, where the changing pore diameters trigger local instabilities between neighbouring pores, cf. *Morrow* [122]. A second cause is the *raindrop effect*, which describes the different contact angles  $\vartheta$  in case of an advancing or receding wetting phase. For more information on this topic, please refer to, e. g., *Bear* [13]. Furthermore, *Niessner & Hassanizadeh* [125], *Joekar-Niasar et al.* [90] and *Pop et al.* [138] commonly suggested that other factors should be included into the capillary-pressure-saturation relation as well, such as the specific interfacial area. The intention behind this suggestion is that the interfacial-area concept inherently incorporates hysteresis. Since in this monograph no alternating imbibition and drainage processes are considered, the influence of hysteretic effects are omitted. However, in the derivation of the constitutive relation for the mass-production term  $\hat{\rho}^\beta$  in Section 5.4, a similar approach for the specific interfacial area, as suggested by *Niessner & Hassanizadeh* [125], is used.

The required properties for the entry pressure  $p_d$  and the pore-size distribution index  $\lambda$  can be found for water-CO<sub>2</sub> systems, e. g., in *Graf* [74]. To the best knowledge of the author, the capillary-pressure-saturation data for pure CO<sub>2</sub> systems, where only liquid and gaseous CO<sub>2</sub> exist, has not been determined so far. Thus, the properties of  $p_d$  and  $\lambda$  for water-CO<sub>2</sub> systems are also applied to the CO<sub>2</sub>-only system.

## Fluid velocities

In Section 3.2.1 it was explained that the pore-fluid motion is given in an *Eulerian* setting by the seepage velocity  $\mathbf{w}_\beta$ , cf. (3.14). Considering a multiphasic system with two fluids encountering each other in the pore space, the formulation of the seepage velocity must also incorporate constraints that reflect the mutual obstruction between these two percolating fluids. In this regard, it is logical to proceed from the extra momentum production terms in the dissipation inequality (5.71), to find thermodynamically consistent descriptions for  $\mathbf{w}_\beta$ . Following, for instance, *Graf* [74] and *Wagner* [176], the dissipation inequality can be satisfied by requesting a negative proportionality between the extra momentum production and the seepage velocity, i. e.,

$$\hat{\mathbf{p}}_{E \text{ dis.}}^L \propto -\mathbf{w}_L \quad \text{and} \quad \hat{\mathbf{p}}_E^G \propto -\mathbf{w}_G, \quad (5.88)$$

which can be reformulated by introducing the so-called friction tensors  $\mathbf{S}_f^\beta$  of second-order, cf. *Ehlers* [56] and *Wagner* [176], via

$$\hat{\mathbf{p}}_{E \text{ dis.}}^L = -\mathbf{S}_f^L \mathbf{w}_L \quad \text{and} \quad \hat{\mathbf{p}}_E^G = -\mathbf{S}_f^G \mathbf{w}_G, \quad (5.89)$$

respectively. A constitutive relation for the positive-definite friction tensor  $\mathbf{S}_f^\beta$  includes physical meaningful parameters for the description of the fluid-flow processes, see *Ehlers* [55],

$$\mathbf{S}_f^\beta = (n^\beta)^2 \rho^{\beta R} \mathbf{g} (\mathbf{K}_r^\beta)^{-1}, \quad (5.90)$$

where  $\mathbf{K}_r^\beta$  is the second-order tensor of the relative permeability and  $\mathbf{g} = |\mathbf{g}|$  is the scalar value of the gravitational force. Proceeding from the fluid momentum balance (5.3)<sub>3</sub> under the assumption of creeping-flow conditions ( $\mathbf{x}_\beta'' \approx \mathbf{0}$ ), thereby neglecting the fluid extra stresses (5.70) and inserting the derived relations for the liquid momentum production (5.62)<sub>3</sub> and for the gas momentum production (5.63), yields for the liquid constituent

$$\begin{aligned} \mathbf{0} &= \operatorname{div} \mathbf{T}^L + \rho^L \mathbf{g} + \hat{\mathbf{p}}^L = \\ &= \operatorname{div} (-n^L p^{LR} \mathbf{I}) + \rho^L \mathbf{g} + \hat{\mathbf{p}}_{E \text{ dis.}}^L + p^{LR} \operatorname{grad} n^L + p^c n^F \operatorname{grad} s^L = \\ &= -n^L \operatorname{grad} p^{LR} + n^L \rho^{LR} \mathbf{g} + p^c n^F \operatorname{grad} s^L - (n^L)^2 \rho^{LR} \mathbf{g} (\mathbf{K}_r^L)^{-1} \mathbf{w}_L, \quad (5.91) \\ &\rightarrow n^L \mathbf{w}_L = -\frac{\mathbf{K}_r^L}{\rho^{LR} \mathbf{g}} [\operatorname{grad} p^{LR} - \rho^{LR} \mathbf{g} - \frac{p^c}{s^L} \operatorname{grad} s^L], \end{aligned}$$

and for the gaseous constituent

$$\begin{aligned} \mathbf{0} &= \operatorname{div} \mathbf{T}^G + \rho^G \mathbf{g} + \hat{\mathbf{p}}^G = \\ &= \operatorname{div} (-n^G p^{GR} \mathbf{I}) + \rho^G \mathbf{g} + \hat{\mathbf{p}}_{E \text{ dis.}}^G + p^{GR} \operatorname{grad} n^G = \\ &= -n^G \operatorname{grad} p^{GR} + n^G \rho^{GR} \mathbf{g} - (n^G)^2 \rho^{GR} \mathbf{g} (\mathbf{K}_r^G)^{-1} \mathbf{w}_G, \quad (5.92) \\ &\rightarrow n^G \mathbf{w}_G = -\frac{\mathbf{K}_r^G}{\rho^{GR} \mathbf{g}} [\operatorname{grad} p^{GR} - \rho^{GR} \mathbf{g}]. \end{aligned}$$

Consequently, after rigorous exploitation of the dissipation inequality, *Darcy*-like filter velocities  $n^\beta \mathbf{w}_\beta$ , cf. *Darcy* [42], are obtained from the fluid momentum balances. However, the liquid filter velocity (5.91) contains an additional gradient of the liquid saturation in the right-most term, which does not appear in the original *Darcy* filter law. In some works, e. g., *Avci* [8], *Fredlund & Rahardjo* [68], *Graf* [74] and *Wagner* [176], it is discussed that the contribution of this liquid saturation gradient can be omitted, since it has usually negligible effects on  $\mathbf{w}_L$  compared to the other terms in the liquid filter-velocity law. However, in this monograph the term is kept in the following.

The tensor of relative permeability  $\mathbf{K}_r^\beta$  in (5.91) and (5.92) can be related to the tensor of hydraulic conductivity  $\mathbf{K}^\beta$  (also called *Darcy* permeability) and to the intrinsic permeability tensor  $\mathbf{K}^S$  of the deformable solid skeleton through

$$\mathbf{K}_r^\beta = k_r^\beta \mathbf{K}^\beta \quad \text{and} \quad \mathbf{K}^\beta = \frac{\rho^{\beta R} \mathbf{g}}{\mu^{\beta R}} \mathbf{K}^S. \quad (5.93)$$

Therein,  $\mu^{\beta R}$  indicates the effective shear viscosity of the pore fluids, cf. Section 4.4, and  $k_r^\beta$  are the so-called relative permeability factors, which, following *Brooks & Corey* [31], read

$$\begin{aligned} k_r^L &= (s_{\text{eff}}^L)^{\frac{2+3\lambda}{\lambda}}, \\ k_r^G &= (1 - s_{\text{eff}}^L)^2 (1 - (s_{\text{eff}}^L)^{\frac{2+\lambda}{\lambda}}). \end{aligned} \quad (5.94)$$

The relative permeability factors are weighting functions for the hydraulic conductivities and are depicted in Figure 5.2 for two different pore-size distributions, in particular,  $\lambda = 2.3$  and  $\lambda = 0.6$ . Since both fluid phases percolate the same pore space, the two fluids

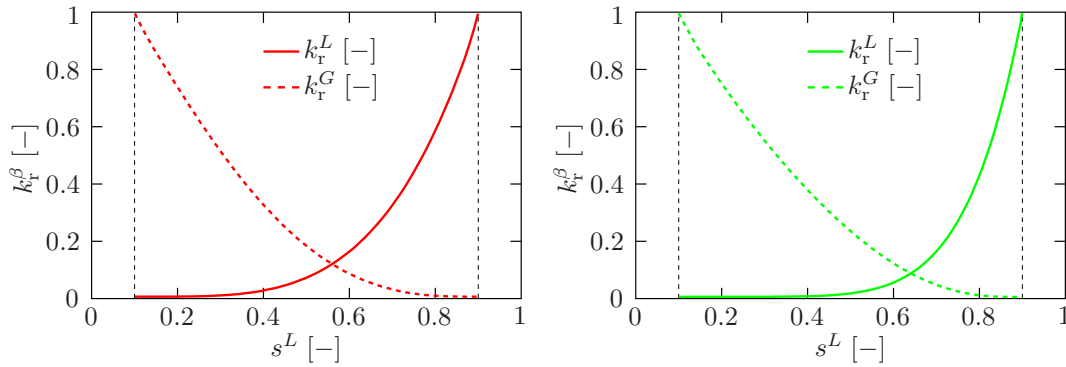


Figure 5.2: Relative permeabilities  $k_r^\beta$  after *Brooks & Corey* for a pore-size distribution index  $\lambda = 2.3$  (left) and  $\lambda = 0.6$  (right), corresponding to the  $p^c$ - $s^L$ -curves in Figure 5.1. The solid line corresponds to the wetting liquid phase and the dashed line to the non-wetting gaseous phase. The residual saturations are set to  $s_{\text{res}}^L = s_{\text{res}}^G = 0.1$ .

affect each other in their flow behaviour, cf. *Helmig* [84]. The equations (5.94) already show that this behaviour is connected to the effective saturation, which can be explained as follows. If the liquid saturation is equal to the residual saturations, i. e.,  $s^L = s_{\text{res}}^L$ , the liquid phase is immobile and, thus, the liquid relative permeability  $k_r^L$  becomes equal to zero. In contrast, the gas phase “owns” almost the whole pore space and is free to move and, consequently, its relative permeability is equal to one. This applies of course for the opposite case as well. Hence, in (5.94) the effective saturation  $s_{\text{eff}}^\beta$  corresponds only to saturations, where both fluids are mobile. Furthermore, Figure 5.2 shows that the grade of sorting of the soil particles (here defined by the pore-size distribution index  $\lambda$ ) has almost no influence on the gaseous phase, whereas the liquid phase exhibits in the case of a poorly sorted soil a reduced mobility for low liquid saturations. This is due to the fact that the wetting fluid enters mainly the small pores, which present a stronger hindrance to flow, cf. *Class* [36]. Please note in passing that the equations in (5.94) are only empirical relations, derived from the capillary-pressure-saturation conditions. More information on the topic of relative permeabilities, for instance the temperature dependency of  $k_r^\beta$ , can be found, e. g., in *Class* [36], or *Bear* [13] and citations therein.

Considering isotropic permeabilities, the permeability tensor  $\mathbf{K}^S$  reduces to the scalar quantity  $K^S$ . According to *Markert* [115], the following relation for the deformation-

dependent isotropic permeability  $K^S$  can be given

$$K^S = \left( \frac{1 - n^S}{1 - n_{0S}^S} \det \mathbf{F}_{Sm} \right)^\kappa K_{0S}^S, \quad (5.95)$$

where  $K_{0S}^S$  is the intrinsic solid permeability in the reference configuration and  $\kappa > 0$  is an additional material parameter governing the deformation dependency. Furthermore, note that  $\det \mathbf{F}_{Sm}$  can be substituted within the given geometrically linear approach by the formula (5.13)<sub>2</sub>, which reads

$$\ln(\det \mathbf{F}_{Sm}) = 1 + \text{Div} \mathbf{u}_S - 3 \alpha^S \Delta \theta. \quad (5.96)$$

It is possible, to estimate the intrinsic solid permeability  $K_{0S}^S$  based on the effective grain diameter<sup>9</sup>  $d_{10}$ , cf. *Bear* [13]. Note that, therein, also other, more or less empirical, relations are presented for  $K_{0S}^S$ . For further insights into the different permeability measures, please refer to, e. g., *Eipper* [63] or *Markert* [115].

Finally, by inserting relations (5.93) into (5.91) and (5.92), while considering isotropic permeabilities, the filter velocities of the fluid phases in their final forms read

$$\begin{aligned} n^L \mathbf{w}_L &= -\frac{k_r^L K^S}{\mu^{LR}} (\text{grad} p^{LR} - \rho^{LR} \mathbf{g} - \frac{p^c}{s^L} \text{grad} s^L), \\ n^G \mathbf{w}_G &= -\frac{k_r^G K^S}{\mu^{GR}} (\text{grad} p^{GR} - \rho^{GR} \mathbf{g}). \end{aligned} \quad (5.97)$$

### Effective fluid densities

Proceeding from the thermodynamical properties of the fluids, the determination of the effective fluid density by means of an equation of state (EOS) is given in what follows. The EOS defines a relation between the effective pressure  $p^{\beta R}$ , the temperature  $\theta$  and the effective density  $\rho^{\beta R}$ , whereas the former two are governed by the mass and the energy balances, respectively. Therefore, the EOS must be solved for the density. Note that the principle of the EOS was elaborately discussed in Chapter 4. For reasons of thermodynamical consistency in the derivation of the *Helmholtz* free energy  $\psi^\beta$ , the *van-der-Waals* EOS (vdW-EOS) is applied, whereas in the following the modification parameters  $u$  and  $w$  that were introduced in (4.18) are omitted here for the sake of clarity. Thus, the substitution of the specific volume  $v^{\beta R}$  in (4.11) by the effective density  $\rho^{\beta R}$  yields

$$p^{\beta R} = R^\beta \theta \frac{\rho^{\beta R}}{1 - b \rho^{\beta R}} - a (\rho^{\beta R})^2. \quad (5.98)$$

Therein,  $R^\beta$  is the specific gas constant of  $\varphi^\beta$  and the material constants for the cohesion pressure  $a$  and the co-volume  $b$  are functions of the critical temperature  $\theta_{\text{crit}}^\beta$  and the critical pressure  $p_{\text{crit}}^{\beta R}$ , proceeding from the CSP:

$$a = \frac{27 (R^\beta \theta_{\text{crit}}^\beta)^2}{64 p_{\text{crit}}^{\beta R}}, \quad b = \frac{R^\beta \theta_{\text{crit}}^\beta}{8 p_{\text{crit}}^{\beta R}}. \quad (5.99)$$

---

<sup>9</sup>The reference diameter  $d_{10}$  implies that 10% per mass of the grains have a smaller diameter than that specific diameter.

In order to retrieve the effective fluid densities from (5.98), one has to solve a cubic equation. The real roots of a cubic equation can be derived by the mathematical procedure presented in the *Numerical Recipes* by *Press et al.* [140] and is demonstrated in detail for the vdW-EOS in Appendix B.10. The resulting three real roots correlate to the intersections of a constant pressure with the respective isotherm, cf. Figure 5.3. After

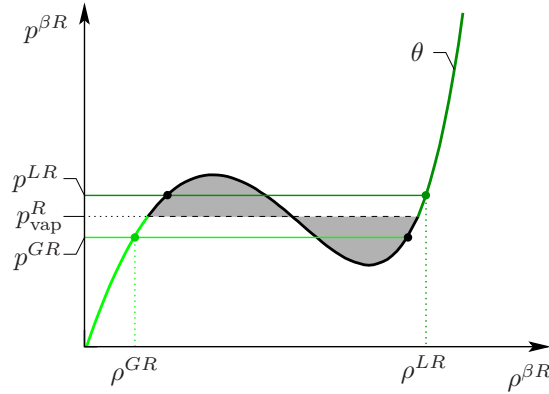


Figure 5.3: Example of the derivation of the density  $\rho^{\beta R}$  for a given pressure  $p^{\beta R}$  and temperature  $\theta$  with the vdW-EOS and the *Antoine* equation, both for liquid conditions (dark green) and for gaseous conditions (light green).

ordering the three roots, or densities, by size, the middle value can be discarded, since it refers to an unnatural state, see Section 4.1. From the remaining two solutions, the smallest value equals the density of the gas phase and the largest value belongs to the liquid phase, as shown in Figure 5.3. To choose the correct density for the given temperature and pressure conditions, the pressure  $p^{\beta R}$  is compared with the vapour pressure  $p_{\text{vap}}^R$  that was calculated for the given temperature  $\theta$  with the *Antoine* equation (4.19). If  $p^{\beta R} > p_{\text{vap}}^R$  (dark green in Figure 5.3), the fluid is in its liquid state, cf. Figure 4.2(a), and the final solution is the liquid density  $\rho^{LR}$ . In the other case, i. e.,  $p^{\beta R} < p_{\text{vap}}^R$  (light green), the gaseous density  $\rho^{GR}$  would be the solution.

### **Helmholtz free energies of the fluid constituents**

Next, the *Helmholtz* free energies  $\psi^\beta$  are derived for the fluid constituents  $\varphi^\beta$ . The derivatives of the final form of the free energies must satisfy the equations (5.64), (5.54)<sub>1</sub> and (5.54)<sub>2</sub> in case of the liquid constituent and the equations (5.64) and (5.51) for the gaseous constituent. In this regard, the procedure proposed by *Ghadiani* [71] and *Graf* [74] is executed. At first, the partial derivatives of the *Helmholtz* free energies are indefinitely integrated. Then, by properly combining these integrated forms, the integration constants can be identified and the final relations for  $\psi^L$  and  $\psi^G$  are obtained. In this connection, it will also be explained, why the simpler vdW-EOS is chosen instead of a more exact EOS like the *Peng-Robinson* or *Soave-Redlich-Kwong* EOS.

Commencing with the liquid constituent  $\varphi^L$ , the derivative of the *Helmholtz* free energy

$\psi^L$  with respect to the liquid saturation  $s^L$  (5.54)<sub>2</sub> reads

$$p^c = -s^L \rho^{LR} \frac{\partial \psi^L}{\partial s^L} \quad \rightarrow \quad \frac{\partial \psi^L}{\partial s^L} = -\frac{p^c}{\rho^{LR}} (s^L)^{-1}. \quad (5.100)$$

By inserting the inverted form of the *Brooks & Corey* law (5.85) to replace the capillary pressure,

$$p^c = p_d (s_{\text{eff}}^L)^{-1/\lambda} = \rho^{LR} g h_d (s_{\text{eff}}^L)^{-1/\lambda}, \quad (5.101)$$

where the entry pressure is substituted by  $p_d = \rho^{LR} g h_d$ ,  $g$  is the norm of the local gravitational force  $\mathbf{g}$  and  $h_d$  is the macroscopic entry-pressure head, one obtains from (5.100)<sub>2</sub>

$$\frac{\partial \psi^L}{\partial s^L} = -g h_d (s^L)^{-\frac{1+\lambda}{\lambda}}. \quad (5.102)$$

Hereby, it was assumed that the difference between the liquid saturation  $s^L$  and the effective liquid saturation  $s_{\text{eff}}^L$  can be neglected in the derivation of  $\psi^L$ . Now, (5.102) is indefinitely integrated

$$\psi^L = g h_d \lambda (s^L)^{-\frac{1}{\lambda}} + f, \quad (5.103)$$

wherein, the integration constant  $f = f(\rho^{LR}, \theta)$  is a function of the remaining dependencies,  $\rho^{LR}$  and  $\theta$ . Proceeding from the derivative of the *Helmholtz* free energy with respect to the effective liquid density (5.54)<sub>1</sub>

$$p^{LR} = (\rho^{LR})^2 \frac{\partial \psi^L}{\partial \rho^{LR}} \quad \rightarrow \quad \frac{\partial \psi^L}{\partial \rho^{LR}} = \frac{p^{LR}}{(\rho^{LR})^2}, \quad (5.104)$$

a comparison with the derivative of (5.103) with respect to the effective liquid density yields

$$\frac{\partial \psi^L}{\partial \rho^{LR}} = \frac{\partial f}{\partial \rho^{LR}} \stackrel{!}{=} \frac{p^{LR}}{(\rho^{LR})^2}. \quad (5.105)$$

Subsequently, the effective pressure  $p^{LR}$  is substituted in (5.105) by the vdW-EOS (5.98),

$$\frac{\partial f}{\partial \rho^{LR}} = \frac{R^L \theta}{\rho^{LR} - b (\rho^{LR})^2} - a. \quad (5.106)$$

Indefinite integration over  $\rho^{LR}$  results in

$$f = R^L \theta \ln \frac{\rho^{LR}}{1 - b \rho^{LR}} - a \rho^{LR} + g, \quad (5.107)$$

where  $g = g(\theta)$  is a temperature dependent integration constant. Inserting  $f$  back into (5.103) and taking the first and second derivatives with respect to the temperature  $\theta$  gives

$$\begin{aligned} \frac{\partial \psi^L}{\partial \theta} &= R^L \frac{\rho^{LR}}{1 - b \rho^{LR}} + \frac{\partial g}{\partial \theta}, \\ \frac{\partial^2 \psi^L}{\partial \theta^2} &= \frac{\partial^2 g}{\partial \theta^2}. \end{aligned} \quad (5.108)$$

**Remark:** At this point, the discrepancy between a more elaborate and exact EOS on the one hand and a thermodynamically consistent derivation of  $\psi^\beta$  on the other hand becomes obvious. The more exact equations of state, e. g., the PR-EOS (4.13), or the SRK-EOS (4.16), exhibit a dependency on the square root of the temperature in the term containing the cohesion pressure  $a$ , cf. (4.14)<sub>3</sub> and (4.17)<sub>3</sub>. Due to the square root, this term would not vanish for the first and second derivatives with respect to the temperature, as it does in case of the vdW-EOS (5.108). Consequently, it is not possible to find a closed form for the *Helmholtz* free energies of the pore fluids with the PR-EOS or SRK-EOS.

Continuing with the formula for the specific heat capacity (5.64) and comparing it with (5.108)<sub>2</sub> yields

$$c_V^{LR} = -\theta \frac{\partial^2 \psi^\alpha}{\partial \theta^2} \quad \rightarrow \quad \frac{\partial^2 \psi^\alpha}{\partial \theta^2} = -\frac{c_V^{LR}}{\theta} \stackrel{!}{=} \frac{\partial^2 g}{\partial \theta^2}. \quad (5.109)$$

Double integration of (5.109)<sub>2</sub> together with the side conditions  $\psi_\theta^\beta(\theta_0) = 0$  and  $\partial \psi_\theta^\beta / \partial \theta(\theta_0) = 0$ , cf. (5.77), determines the integration constant  $g(\theta)$ . It reads

$$\begin{aligned} \frac{\partial g}{\partial \theta} &= -c_V^{LR} \ln \frac{\theta}{\theta_0}, \\ g &= -c_V^{LR} \left( \theta \ln \frac{\theta}{\theta_0} - \Delta \theta \right). \end{aligned} \quad (5.110)$$

Finally, by assembling the derived integration constants  $f$  and  $g$  together with (5.103), the *Helmholtz* free energy of the liquid phase reads

$$\psi^L = g h_d \lambda (s^L)^{-\frac{1}{\lambda}} + R^L \theta \ln \frac{\rho^{LR}}{1 - b \rho^{LR}} - a \rho^{LR} - c_V^{LR} \left( \theta \ln \frac{\theta}{\theta_0} - \Delta \theta \right). \quad (5.111)$$

It can be shown that this relation of  $\psi^L$  yields again the equations (5.64), (5.54)<sub>1</sub> and (5.54)<sub>2</sub> through derivatives with respect to  $\theta$ ,  $\rho^{LR}$  and  $s^L$ .

In the same way, the gaseous *Helmholtz* free energy  $\psi^G$  is derived. However, it lacks the dependency on the saturation, hence, simplifying the calculations. Here, the starting point is the derivative of  $\psi^G$  with respect to the effective gas density, cf. (5.51)

$$p^{GR} = (\rho^{GR})^2 \frac{\partial \psi^G}{\partial \rho^{GR}} \quad \rightarrow \quad \frac{\partial \psi^G}{\partial \rho^{GR}} = \frac{p^{GR}}{(\rho^{GR})^2} = \frac{R^G \theta}{\rho^{GR} - b (\rho^{GR})^2} - a, \quad (5.112)$$

where the vdW-EOS (5.98) was implemented for  $p^{GR}$ . It follows from the indefinite integration of (5.112) over  $\rho^{GR}$

$$\psi^G = R^G \theta \ln \frac{\rho^{GR}}{1 - b \rho^{GR}} - a \rho^{GR} + h \quad (5.113)$$

with the integration constant  $h = h(\theta)$ . Before (5.113) can be combined with the specific heat capacity (5.64), the first and second derivatives with respect to the temperature are computed, yielding

$$\begin{aligned} \frac{\partial \psi^G}{\partial \theta} &= R^G \frac{\rho^{GR}}{1 - b \rho^{GR}} + \frac{\partial h}{\partial \theta}, \\ \frac{\partial^2 \psi^G}{\partial \theta^2} &= \frac{\partial^2 h}{\partial \theta^2}. \end{aligned} \quad (5.114)$$



Double integration, thereby utilising the specific heat capacity  $c_V^{GR}$ , yields the integration constant  $h$

$$h = -c_V^{GR} \left( \theta \ln \frac{\theta}{\theta_0} - \Delta\theta \right), \quad (5.115)$$

which is afterwards substituted into (5.113) to derive the final form of the *Helmholtz* free energy of the gas phase:

$$\psi^G = R^G \theta \ln \frac{\rho^{GR}}{1 - b \rho^{GR}} - a \rho^{GR} - c_V^{GR} \left( \theta \ln \frac{\theta}{\theta_0} - \Delta\theta \right). \quad (5.116)$$

If the two fluid phases  $\varphi^L$  and  $\varphi^G$  belong to the same substance, the constants  $a$  and  $b$  in (5.111) and (5.116) and the specific gas constant  $R^\beta$  are equal for both phases. However, the specific heat capacities  $c_V^{LR}$  and  $c_V^{GR}$  remain different, due to their temperature dependency, cf. Section 4.3 for details.

### Entropies and internal energies

With the fluid *Helmholtz* free energies at hand, cf. (5.111), (5.116), and applying the thermodynamic potentials (5.50)<sub>1,2</sub>, the fluid entropies are obtained:

$$\eta^\beta = -R^\beta \ln \frac{\rho^{\beta R}}{1 - b \rho^{\beta R}} + c_V^{\beta R} \ln \frac{\theta}{\theta_0}. \quad (5.117)$$

The internal energies of the fluid constituents can then be determined by using the *Legendre* transformation (B.5) and they read

$$\begin{aligned} \varepsilon^L &= -a \rho^{LR} + c_V^{LR} \Delta\theta + g h_d \lambda (s^L)^{-\frac{1}{\lambda}}, \\ \varepsilon^G &= -a \rho^{GR} + c_V^{GR} \Delta\theta. \end{aligned} \quad (5.118)$$

### 5.3.5 Constitutive relations of the overall aggregate

Next, the constitutive relations for the mixture terms appearing in the mixture momentum and the mixture energy balances are defined. To begin with, the overall pore pressure  $p^{FR}$  is given by *Dalton's* law, which was already mentioned in (5.57)

$$p^{FR} = s^L p^{LR} + s^G p^{GR}. \quad (5.119)$$

Subsequently, the constituent heat influx vectors  $\mathbf{q}^\alpha$  are regarded. On the basis of the dissipation inequality (5.71)<sub>3</sub>, one easily concludes to the applicability of *Fourier's* law for the heat influx vectors  $\mathbf{q}^\alpha$ . Thus,

$$\mathbf{q}^\alpha = -\mathbf{H}^\alpha \text{grad } \theta, \quad (5.120)$$

where  $\mathbf{H}^\alpha$  is the partial heat-conduction tensor, which is related to the effective heat-conduction tensor  $\mathbf{H}^{\alpha R}$  by

$$\mathbf{H}^\alpha = n^\alpha \mathbf{H}^{\alpha R}. \quad (5.121)$$

Moreover, in case of isotropic heat conduction the effective heat-conduction tensor  $\mathbf{H}^{\alpha R}$  reduces to

$$\mathbf{H}^{\alpha R} = H^{\alpha R} \mathbf{I}. \quad (5.122)$$

Note that the identification of the isotropic thermal conductivity  $H^{\alpha R}$  in terms of its density and temperature dependency was extensively discussed in Section 4.4.

## 5.4 Phase transition between the gaseous and liquid phases of a single substance

A major goal of this monograph is to model the phase-transition process between two different phases of a single substance, e. g.,  $\text{CO}_2$ . The quantities that govern this process are the so-called mass-production terms  $\hat{\rho}^\beta$ , which couple the constituent mass balances of the respective fluid constituents  $\varphi^\beta$  (5.16), but also appear in the mixture momentum balance (5.24) and the mixture energy balance (5.27). The appearance of  $\hat{\rho}^\beta$  in the latter two equations results from the momentum and the heat being transported by the transferred mass between the two phases over the interface  $\Gamma$ . The mass production  $\hat{\rho}^\beta$  is the last remaining variable that has to be defined by a thermodynamically consistent, constitutive relation, which will be accomplished within this chapter.

Before the newly developed derivation of the constitutive relation is presented, a brief overview of the existing works on this topic is given. Also, the difference in describing phase-change processes between mixtures and between phases of one single matter shall be pointed out. Thereafter, the new constitutive law for  $\hat{\rho}^\beta$ , which is based on the introduction of a singular surface for the interface, is discussed thoroughly. Finally, a switching criterion is specified, which controls the phase-transition process within the numerical implementation.

### 5.4.1 State of the art

First articles that investigate phase transitions between percolating pore fluids in non-deformable, porous aggregates date back to *Lykov* [112] and continue with the group around *Bénet* [35, 108, 109, 153] or *Bedeaux* [14]. *Hassanizadeh* and *Gray* together with *Niessner* [75, 81, 125, 126] also looked extensively at heat and mass transfer in porous media, where in their more recent works the focus lies on the interfacial area. *Nuske et al.* [130] also studied the phase-transition process, where the formulation of the interfacial area is based on the work of *Hassanizadeh*, *Niessner* and *Gray*. These latter works bear a certain similarity to the model to be presented in this monograph, but are not based on the TPM and describe the phase-transition process between mixtures and not between the phases of a single material.

In the literature one can also find contributions with closer connection to this monograph, i. e., discussions of the phase-transition process in deformable porous media based on the TPM. The first works in this context are provided by *de Boer* and coworkers [19, 21, 23]. Basically in all of these works, the mass production term  $\hat{\rho}^\beta$  is derived from the dissipative

part of the entropy inequality, where the dissipation due to phase transition is recapped here, cf. (5.73),

$$\mathcal{D}_{\text{mass transition}} = \hat{\rho}^L \left[ \mu^G - \mu^L + \frac{1}{2} (\mathbf{w}_G \cdot \mathbf{w}_G - \mathbf{w}_L \cdot \mathbf{w}_L) \right]. \quad (5.123)$$

To satisfy the inequality constraint, proportionality is demanded between the liquid mass production and the term in brackets containing the differences in the chemical potentials and the kinetic energies, i. e.,

$$\hat{\rho}^L \propto \left[ \mu^G - \mu^L + \frac{1}{2} (\mathbf{w}_G \cdot \mathbf{w}_G - \mathbf{w}_L \cdot \mathbf{w}_L) \right]. \quad (5.124)$$

Furthermore, by introducing the so-called mass-transfer coefficient  $\varkappa$  as a positive response parameter, a constitutive relation for the liquid mass production is found

$$\hat{\rho}^L = \varkappa \left[ \mu^G - \mu^L + \frac{1}{2} (\mathbf{w}_G \cdot \mathbf{w}_G - \mathbf{w}_L \cdot \mathbf{w}_L) \right]. \quad (5.125)$$

If the difference in the squares of the kinetic energies in (5.125) is neglected, the resulting relation equals the one found by *de Boer & Kowalski* [23], viz.:

$$\hat{\rho}^L = \varkappa (\mu^G - \mu^L). \quad (5.126)$$

The discrepancy to the other works by *de Boer* [19, 21] originates from the fact that they did not neglect solid mass production  $\hat{\rho}^S$  and used separate temperatures  $\theta^\alpha$  for all constituents  $\varphi^\alpha$ , which read

$$\hat{\rho}^L = -\varkappa^L \left( \frac{\mu^L}{\theta^L} - \frac{\mu^S}{\theta^S} \right) \quad \text{and} \quad \hat{\rho}^G = -\varkappa^G \left( \frac{\mu^G}{\theta^G} - \frac{\mu^S}{\theta^S} \right), \quad (5.127)$$

where in [19], also the kinetic-energy term from (5.125) appears. More recent works on phase transitions using this approach are provided by *Ricken & Bluhm* and coworkers [17, 102, 148, 149], however, applied to thawing and freezing processes. Therein, the response parameter  $\varkappa$  is derived by evaluating the energy balance and postulating a proportionality of  $\varkappa$  to the divergence of the mixture heat flux  $\sum_\alpha \text{div } \mathbf{q}^\alpha$ .

The literature also provides examples which descend from the same theory as used in the present work, i. e., the evaluation of the dissipation inequality in the framework of the TPM, but are not formulated for phase-transition systems in the thermodynamical sense. In this regard, *Steeb & Diebels* [168] present a continuum-mechanical model for erosion and deposition, growth and atrophy, and remodelling phenomena. The continuum-mechanical model for bacterial-driven methane oxidation in landfill cover-layers by *Ricken et al.* [151, 152] is a further example. This group has also published a work, based on the same continuum-mechanical principles, for the phenomenological description of transversely isotropic, saturated, biological tissues including the phenomena of growth [150]. In this context, the contribution of *Kowalski* [101] on the simulation of drying processes shall be mentioned as an example for the actual application of the phase-change model to real physical problems.

If the works on thermodynamical phase-transition processes are studied thoroughly, it becomes obvious that the main problem in the constitutive relation (5.127) for the mass

production is the definition of the mass-transfer coefficient  $\varkappa$ . So far, the only thermodynamical explanation for  $\varkappa$  exists for the freezing/thawing problem, cf. *Ricken* and *Bluhm* [17, 102, 148, 149]. A comparison of equation (5.127) with the classical thermodynamical description of mass transport during phase transition in a two-fluid phase system, based on the two-film idea of *Lewis & Whitman* [106], shows strong similarities between both approaches.

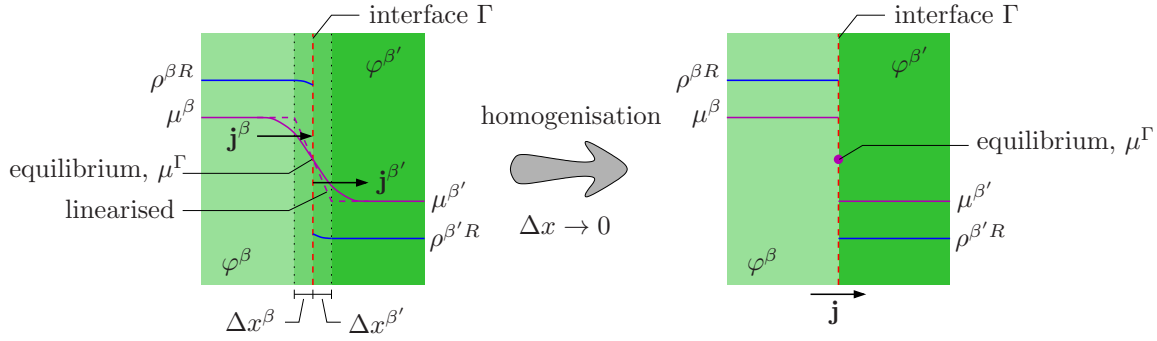


Figure 5.4: Sketch of the two-film principle that describes transition processes between two phases  $\varphi^\beta$  and  $\varphi^{\beta'}$ , following the idea of *Lewis & Whitman* [106].

In the two-film theory, two bulk phases (e. g.,  $\varphi^\beta$  and  $\varphi^{\beta'}$ ) with different chemical potentials,  $\mu^\beta$  and  $\mu^{\beta'}$ , are divided by an interface  $\Gamma$ , cf. Figure 5.4. Due to the difference in the chemical potentials a chemical non-equilibrium exists, which induces mass transfer over the interface. However, locally at the interface equilibrium still remains. Furthermore, it is supposed that the interface is connected on both sides to boundary layers, which indicate the regions, where the motion of convection is small compared to the motion in the bulk phase. In these boundary layers, the phase transition becomes obvious within the changes in density and chemical potential. For simplicity, stationary films with thicknesses  $\Delta x^\beta$  and  $\Delta x^{\beta'}$  are assumed on both sides of the interface and the change in process variables is linearised, cf. purple dashed line in Figure 5.4. The film thickness couples the film-theory to a specific problem at hand, for example, to specific flow characteristics, where the flow velocity parallel to the interface influences the transition. Consequently, the mass fluxes on either side of the interface depend on the film thicknesses  $\Delta x^\beta$  and  $\Delta x^{\beta'}$ , the local mass-transfer coefficients  $D_{\text{mass}}^\beta$  and  $D_{\text{mass}}^{\beta'}$ , and the gradients of the chemical potential  $\Delta\mu^\beta$  and  $\Delta\mu^{\beta'}$ , hence,

$$\mathbf{j}^\beta = -\frac{D_{\text{mass}}^\beta}{R\theta} \frac{\Delta\mu^\beta}{\Delta x^\beta} \stackrel{!}{=} \mathbf{j}^{\beta'} = -\frac{D_{\text{mass}}^{\beta'}}{R\theta} \frac{\Delta\mu^{\beta'}}{\Delta x^{\beta'}}. \quad (5.128)$$

Herein, in addition, it was included that the interface is mass-less and cannot store any mass, thus  $\mathbf{j}^\beta = \mathbf{j}^{\beta'}$ . The change in the chemical potential is given as  $\Delta\mu^\beta = \mu^\beta - \mu^\Gamma$  and, in analogy, as  $\mu^{\beta'} = \mu^\Gamma - \mu^{\beta'}$ .

After a homogenisation by taking the limes of the film thicknesses  $\Delta x^\beta \rightarrow 0$  and  $\Delta x^{\beta'} \rightarrow 0$  and by furthermore assuming that the local mass-transfer coefficients are equal on both sides of the interface, i. e.,  $D_{\text{mass}}^\beta = D_{\text{mass}}^{\beta'} = D_{\text{mass}}$ , it follows for the mass flux

$$\mathbf{j} = -\frac{D_{\text{mass}}}{R\theta} (\mu^\beta - \mu^{\beta'}). \quad (5.129)$$

This relation possesses great similarity to the equation for  $\hat{\rho}^L$  (5.127), which was derived from the dissipation inequality. It seems that the exploitation of the dissipation inequality is a viable procedure for the determination of  $\hat{\rho}^L$ . Consequently, one could comprise the terms standing in front of the difference in chemical potential in (5.127) and (5.129) to find  $\varkappa$ , i. e.,

$$\varkappa \hat{=} \frac{D_{\text{mass}}}{R\theta}. \quad (5.130)$$

At this point, a closer look shall be taken at the local mass-transfer coefficient  $D_{\text{mass}}$  in (5.130).  $D_{\text{mass}}$  is a measure for the resistance that fluid molecules of one phase experience while moving through the boundary layer of the other phase. Hence,  $D_{\text{mass}}$  is the common diffusion coefficient used for the description of diffusion in mixtures, also known as *Fick's law*. However, in this monograph it is intended to find a constitutive relation for the description of mass transfer between phases of the same fluid substance, which means that only pure phases but no mixtures are regarded. This implies in turn that boundary layers on both sides of the interface consist of the same molecules. Thus, no resistance for the movement of the molecules exists and the diffusion coefficient is equal to zero  $D_{\text{mass}} = 0$ . Consequently, the mass flux  $\mathbf{j}$  or the mass production  $\hat{\rho}^L$  would equal zero, which shows that this approach is not applicable for the description of the transition between phases of a single substance. Unfortunately, this issue is not communicated in most of the previously named articles, where (5.127) is used. Therefore, in the next section, a new and different way for the determination of a constitutive relation for the mass-production term in case of single-substance phase transition is presented.

### 5.4.2 Development of the constitutive relation for the mass-production term

In order to find a constitutive relation for the mass-production term appearing in the balance relations as the macroscopic density production  $\hat{\rho}^\alpha$ , cf. (3.63)<sub>1</sub> and (3.36), a closer look is taken at the microstructure of the porous medium, cf. Figure 5.5. The

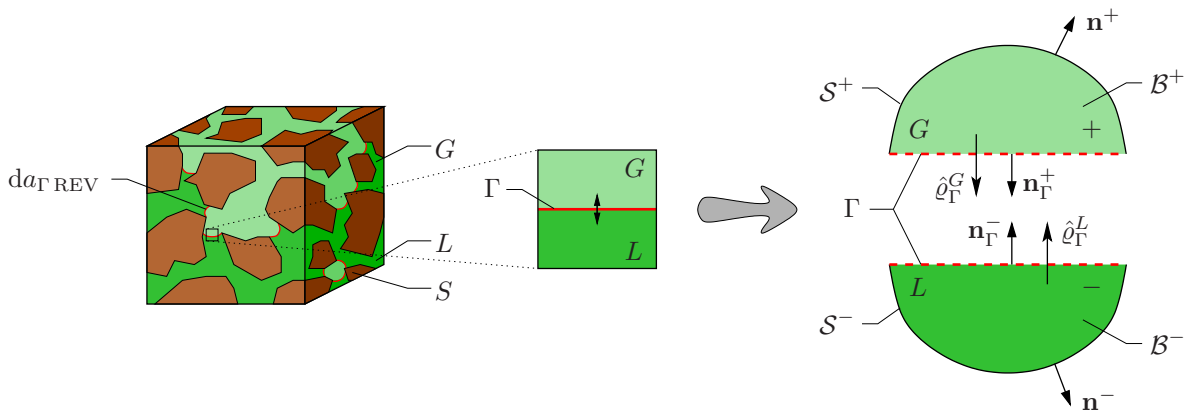


Figure 5.5: Illustrations of the gas-liquid interface  $\Gamma$  in a porous microstructure and the mass transfer  $\hat{q}_\Gamma^\beta$  between the gaseous and liquid phases across the singular surface.

phase-transition process is characterised by a mass transfer over the local interfaces  $\Gamma$ ,

separating the gas from the liquid. The solid phase remains continuous over  $\Gamma$ , since it is not affected by this mass exchange. For the description of this process, a bicomponent, triphasic aggregate of a porous rock and a single fluid matter<sup>10</sup> (component)  $\varphi^{FM}$  is concerned, where the three phases are given by the porous solid  $\varphi^S$  together with the liquid phase  $\varphi^L$  and the gas phase  $\varphi^G$  of component  $\varphi^{FM}$ . Furthermore, the interface is mathematically represented by a singular surface, cf. Section 3.4. Hence, local jumps in physical quantities over the singular surface are described by the discontinuous part of the local mass balance (3.63)<sub>2</sub>. Since the solid phase is not affected by the jump across  $\Gamma$ , only the jump of the fluid matter  $\varphi^{FM}$  has to be observed. Additionally, it is assumed that  $\varphi^{FM}$  exists in  $\mathcal{B}^+$  only in its gaseous phase and in  $\mathcal{B}^-$  only in its liquid phase, cf. right part of Figure 5.5. The following derivations are taken from the contribution by *Ehlers and Häberle* [61] and otherwise.

Applying the mass-jump equation (3.63)<sub>2</sub> to  $\varphi^{FM}$  yields

$$\llbracket \rho^{FM} \mathbf{w}_{FM\Gamma} \rrbracket \cdot \mathbf{n}_\Gamma = (\rho^{FM+} \mathbf{w}_{FM\Gamma}^+ - \rho^{FM-} \mathbf{w}_{FM\Gamma}^-) \cdot \mathbf{n}_\Gamma = 0. \quad (5.131)$$

With  $\rho^{FM+} \mathbf{w}_{FM\Gamma}^+ = \rho^G \mathbf{w}_{G\Gamma}$  and  $\rho^{FM-} \mathbf{w}_{FM\Gamma}^- = \rho^L \mathbf{w}_{L\Gamma}$ , (5.131) becomes

$$(\rho^G \mathbf{w}_{G\Gamma} - \rho^L \mathbf{w}_{L\Gamma}) \cdot \mathbf{n}_\Gamma = 0. \quad (5.132)$$

Following the work of *Whitaker* [178], the interfacial mass-transfer  $\hat{\varrho}_\Gamma^\beta$  of  $\varphi^\beta$  is specified through

$$\hat{\varrho}_\Gamma^\beta := \rho^\beta \mathbf{w}_{\beta\Gamma} \cdot \mathbf{n}_\Gamma^\beta, \quad (5.133)$$

such that

$$\begin{aligned} \hat{\varrho}_\Gamma^G &= \rho^{FM+} \mathbf{w}_{FM\Gamma}^+ \cdot \mathbf{n}_\Gamma^{FM+} = \rho^G \mathbf{w}_{G\Gamma} \cdot \mathbf{n}_\Gamma, \\ \hat{\varrho}_\Gamma^L &= \rho^{FM-} \mathbf{w}_{FM\Gamma}^- \cdot \mathbf{n}_\Gamma^{FM-} = -\rho^L \mathbf{w}_{L\Gamma} \cdot \mathbf{n}_\Gamma \end{aligned} \quad (5.134)$$

$$\text{and } \hat{\varrho}_\Gamma^G + \hat{\varrho}_\Gamma^L = 0,$$

where  $\mathbf{n}_\Gamma^{FM+} = \mathbf{n}_\Gamma$  and  $\mathbf{n}_\Gamma^{FM-} = -\mathbf{n}_\Gamma$  have been used. From (5.134)<sub>3</sub>, it is clearly seen that, for example during evaporation, mass is removed from the liquid phase and added to the gaseous phase through  $\hat{\varrho}_\Gamma^G = -\hat{\varrho}_\Gamma^L$ . Since the interfacial mass production  $\hat{\varrho}_\Gamma^\beta$  and the continuum mass production  $\hat{\rho}^\beta$  have to be equivalent in the sense that  $\hat{\varrho}_\Gamma^G$  leaves  $\mathcal{B}^+$  and generates the density production  $\hat{\rho}^L$  in  $\mathcal{B}^-$  and vice versa,  $\hat{\varrho}_\Gamma^\beta$  and  $\hat{\rho}^\beta$  can be related to each other by

$$\hat{\rho}^G dv \hat{=} \hat{\varrho}_\Gamma^L da_\Gamma \quad \text{and} \quad \hat{\rho}^L dv \hat{=} \hat{\varrho}_\Gamma^G da_\Gamma, \quad (5.135)$$

where  $dv$  is the unit volume of the REV and  $da_\Gamma$  is the unit area of the interface in the REV given by

$$da_\Gamma = \int_{A_{\text{REV}}} da_{\Gamma \text{REV}}. \quad (5.136)$$

<sup>10</sup>The universal component  $\varphi^{FM}$  is chosen here, to keep the generality of the model. Hence, it can be used for different fluid matters by only adapting the respective material parameters. Later in this monograph, the universal component will be identified with  $\text{CO}_2$ ,  $\varphi^{FM} = \varphi^{\text{CO}_2}$ .

## Interfacial Area

Based on (5.135) and the work of *Niessner* and *Hassanizadeh* [124], the so-called interfacial area  $a_\Gamma$  is introduced as the density of the internal phase-change surfaces measured with respect to the unit volume of the REV:

$$a_\Gamma := \frac{da_\Gamma}{dv}. \quad (5.137)$$

The interfacial area  $a_\Gamma$  comprises all menisci separating the liquid and the gaseous phases in the pore space of the REV, cf. Figure 5.5. In turn, the menisci depend on the surface tensions of the involved phases and the pore structure, or in other words, on the capillary-pressure relation, which is given in (5.101) as a function of the effective saturation. This justifies that  $a_\Gamma$  can be assumed as  $a_\Gamma = a_\Gamma(s_{\text{eff}}^L)$  or as  $a_\Gamma = a_\Gamma(s^L)$ , respectively. Finally, it has to be mentioned that the influence of the common lines on the phase-change process, i. e., the influence of the contact lines of the interface with the solid material, is neglected in this study.

The first to incorporate interfacial areas into a macroscopic formulation of multiphase flow were *Hassanizadeh* and *Gray* [80, 81]. It is also claimed by *Niessner & Hassanizadeh* [125], *Joekar-Niasar et al.* [90] and *Pop et al.* [138] that the inclusion of the interfacial area into the capillary-pressure-saturation relation removes the hysteresis, which appears otherwise in the classical  $p^c$ - $s^L$ -relationship during alternating drainage and imbibition processes. However, the effect of hysteresis is not observed in this monograph, since either imbibition or drainage cases are regarded in the numerical examples and no alteration between these two effects is considered.

To calculate the interfacial area, different approaches exist. In [124], *Niessner* and *Hassanizadeh* present an empirical derivation of the interfacial area  $a_\Gamma$  based on data obtained by *Joekar-Niasar et al.* [90], using pore-network model tests introduced by, e. g., *Sahimi* [157]. *Nuske et al.* [130] extended this model by including the interfaces between the fluid phases and the solid phase. Another approach, which is also based on the work of *Niessner* and *Hassanizadeh*, but uses a lattice *Boltzmann* simulation to derive the material parameters, is given by *Ahrenholz et al.* [3]. In this monograph, use is made of an approximation by *Graf* [74], who described the interfacial area between the fluid phases as a function of the liquid saturation.

The basic idea of the latter contribution is to approximate the pore space by introducing a sphere with the pore-space equivalent volume  $V^F$ , which is composed of the fluid volumes  $V^L$  and  $V^G$  that are again given as a function of the filling heights  $h^L$  and  $h^G$ , cf. Figure 5.6 (left):

$$\begin{aligned} V^F &= V^L + V^G = \frac{4}{3} \pi (\tilde{r}^F)^3, \\ V^\beta &= \frac{1}{3} \pi (h^\beta)^2 (3\tilde{r}^F - h^\beta), \quad \beta = \{L, G\}. \end{aligned} \quad (5.138)$$

Furthermore, the surface area between the liquid and gaseous volumes reads

$$A^{GL} = \pi h^\beta (2\tilde{r}^F - h^\beta), \quad (5.139)$$

where in (5.138) and (5.139)  $\tilde{r}^F$  is the radius of the volume-equivalent sphere and  $h^\beta$  has to be taken as the larger value out of  $h^L$  and  $h^G$  such that  $h^\beta \geq \tilde{r}^F$ .

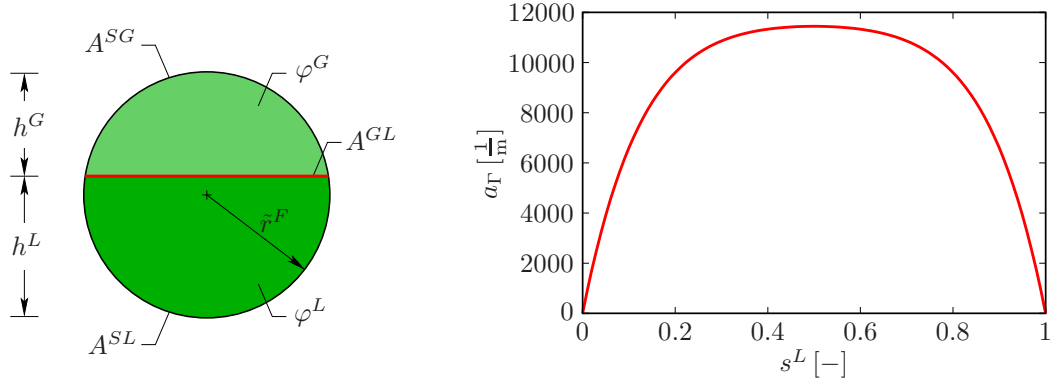


Figure 5.6: Volume-equivalent sphere of the pore space (left) and interfacial area  $a_\Gamma(s^L)$  presented for  $d_{50} = 0.06$  mm and  $n^S = 0.6$  (right).

Based on (3.4), the saturation  $s^\beta$  is defined by the local ratio of  $V^\beta$  over  $V^F$ . Thus,

$$s^\beta = \frac{n^\beta}{n^F} = \frac{V^\beta}{V^F} = \frac{(h^\beta)^2 (3\tilde{r}^F - h^\beta)}{4(\tilde{r}^F)^3}. \quad (5.140)$$

Proceeding from (5.140), the filling height  $h^\beta$  can be determined as a function of the saturation  $s^\beta$  and the equivalent pore-fluid radius  $\tilde{r}^F$ :

$$\begin{aligned} h^\beta &= \left[ \frac{36864}{8910} (s^\beta)^3 - \frac{18432}{2970} (s^\beta)^2 + \frac{12084}{2970} s^\beta \right] \tilde{r}^F \approx \\ &\approx [4.137 (s^\beta)^3 - 6.206 (s^\beta)^2 + 4.069 s^\beta] \tilde{r}^F. \end{aligned} \quad (5.141)$$

Since the distribution, sizes and forms of the solid particles, as well as the tortuosity and connectivity of the pores are unknown, it is not possible to calculate the exact pore volume  $V^F$ . Therefore, an appropriate approximation is needed. Comparing a spherical pore with radius  $\tilde{r}^F$  with a characteristic, spherical solid particle with radius  $\tilde{r}^S$  yields

$$\left. \begin{aligned} V^S &= n^S V \\ V^F &= n^F V \end{aligned} \right\} \text{ such that } \frac{n^F}{n^S} = \frac{V^F}{V^S} = \frac{(\tilde{r}^F)^3}{(\tilde{r}^S)^3} \text{ and, thus, } \tilde{r}^F = \left( \frac{n^F}{n^S} \right)^{1/3} \tilde{r}^S. \quad (5.142)$$

Proceeding from  $d_{50}$  as the medial grain diameter of a granular soil, one ends up with

$$\tilde{r}^F = \frac{1}{2} \left( \frac{n^F}{n^S} \right)^{1/3} d_{50}. \quad (5.143)$$

Given the above results, the interfacial area  $a_\Gamma$  can be specified. Based on (5.137), (5.138)<sub>1</sub> and (5.139) with  $A_\Gamma = A^{GL}$ ,  $a_\Gamma$  can be obtained as a function of  $s^\beta$  via

$$\begin{aligned} a_\Gamma(s^\beta) &= \frac{da_\Gamma}{dV} = \frac{A_\Gamma}{V} = n^F \frac{A^{GL}}{V^F} = \\ &= \frac{3 n^F h^\beta (2\tilde{r}^F - h^\beta)}{4(\tilde{r}^F)^3}. \end{aligned} \quad (5.144)$$



While  $\tilde{r}^F$ , at a certain state of the solid deformation, is a function of  $d_{50}$ ,  $h^\beta$  depends on  $s^L$ , which is given as a function of the capillary pressure  $p^c$ . As a result, the  $a_\Gamma$ - $s^L$  curve, cf. Figure 5.6 (right), is comparable to the curve found by *Joekar-Niasar et al.* [90], when their three-dimensional plane ( $a_\Gamma$ - $s^L$ - $p^c$ ) is cut at a certain value of  $p^c$ .

### Interfacial mass transfer

Given the equation of the interfacial area (5.137), the macroscopic density production  $\hat{\rho}^\beta$  and the interfacial mass-transfer  $\hat{\rho}_\Gamma^\beta$  are related to each other through

$$\hat{\rho}^G = a_\Gamma \hat{\rho}_\Gamma^L \quad \text{and} \quad \hat{\rho}^L = a_\Gamma \hat{\rho}_\Gamma^G. \quad (5.145)$$

After  $a_\Gamma$  has now been calculated from (5.144), it is still necessary to determine the interfacial mass transfer  $\hat{\rho}_\Gamma^\beta$  such that  $\hat{\rho}^\beta$  can be fixed, cf. (5.145). For this purpose, one proceeds from the energy jump across the singular surface  $\Gamma$ , cf. (3.65)<sub>2</sub>,

$$\left[ \left[ \rho^\alpha \left( \varepsilon^\alpha + \frac{1}{2} \dot{\mathbf{x}}_\alpha \cdot \dot{\mathbf{x}}_\alpha \right) \mathbf{w}_{\alpha\Gamma} - \mathbf{T}^\alpha \dot{\mathbf{x}}_\alpha + \mathbf{q}^\alpha \right] \cdot \mathbf{n}_\Gamma = 0, \right. \quad (5.146)$$

where  $\mathbf{T}^\alpha = (\mathbf{T}^\alpha)^T$  has been used according to (3.44). Applying (5.146) to the solid constituent  $\varphi^S$ , one obtains with the aid of (3.44):

$$\left[ \left[ \rho^S \left( \varepsilon^S + \frac{1}{2} \dot{\mathbf{x}}_S \cdot \dot{\mathbf{x}}_S \right) \mathbf{w}_{S\Gamma} - (\mathbf{T}_E^S - n^S p^{FR}) \dot{\mathbf{x}}_S + \mathbf{q}^S \right] \cdot \mathbf{n}_\Gamma = 0. \right. \quad (5.147)$$

Since the solid material is inert and not involved in the phase-transition process, all terms related to the solid material itself are considered continuous over the singular surface. Thus, it remains that

$$n^S \left[ \left[ p^{FR} \right] \dot{\mathbf{x}}_S \cdot \mathbf{n}_\Gamma = 0. \right. \quad (5.148)$$

However, since the solid velocity  $\dot{\mathbf{x}}_S$  is not necessarily perpendicular to the single-surface normal  $\mathbf{n}_\Gamma$ , it is obvious to require

$$\left[ \left[ p^{FR} \right] \right] = 0. \quad (5.149)$$

In the next step, (5.146) has to be applied to the fluid component  $\varphi^{FM}$ . Thus,

$$\left[ \left[ \left( \varepsilon^{FM} + \frac{1}{2} \dot{\mathbf{x}}_{FM} \cdot \dot{\mathbf{x}}_{FM} \right) \rho^{FM} \mathbf{w}_{FM\Gamma} - \mathbf{T}^{FM} \dot{\mathbf{x}}_{FM} + \mathbf{q}^{FM} \right] \cdot \mathbf{n}_\Gamma = 0. \right. \quad (5.150)$$

Following the same procedure as to obtain (5.132) from (5.131), with the gaseous phase of  $\varphi^{FM}$  only existent in  $\mathcal{B}^+$  and the liquid phase of  $\varphi^{FM}$  only in  $\mathcal{B}^-$ , the jump in the energy balance becomes

$$\begin{aligned} & (\varepsilon^G + \frac{1}{2} \dot{\mathbf{x}}_G \cdot \dot{\mathbf{x}}_G) \rho^G \mathbf{w}_{G\Gamma} \cdot \mathbf{n}_\Gamma - (\mathbf{T}^G \dot{\mathbf{x}}_G - \mathbf{q}^G) \cdot \mathbf{n}_\Gamma - \\ & - (\varepsilon^L + \frac{1}{2} \dot{\mathbf{x}}_L \cdot \dot{\mathbf{x}}_L) \rho^L \mathbf{w}_{L\Gamma} \cdot \mathbf{n}_\Gamma + (\mathbf{T}^L \dot{\mathbf{x}}_L - \mathbf{q}^L) \cdot \mathbf{n}_\Gamma = 0. \end{aligned} \quad (5.151)$$

Applying (5.134)<sub>1,2</sub> to (5.151) yields

$$\begin{aligned} & (\varepsilon^G + \frac{1}{2} \dot{\mathbf{x}}_G \cdot \dot{\mathbf{x}}_G) \hat{\varrho}_\Gamma^G - (\mathbf{T}^G \dot{\mathbf{x}}_G - \mathbf{q}^G) \cdot \mathbf{n}_\Gamma + \\ & + (\varepsilon^L + \frac{1}{2} \dot{\mathbf{x}}_L \cdot \dot{\mathbf{x}}_L) \hat{\varrho}_\Gamma^L + (\mathbf{T}^L \dot{\mathbf{x}}_L - \mathbf{q}^L) \cdot \mathbf{n}_\Gamma = 0. \end{aligned} \quad (5.152)$$

Finally, this equation can be solved with the help of (5.134)<sub>3</sub>, in the form  $\hat{\varrho}_\Gamma^G = -\hat{\varrho}_\Gamma^L$ , such that

$$\hat{\varrho}_\Gamma^L = \frac{(n^G p^{GR} \dot{\mathbf{x}}_G - n^L p^{LR} \dot{\mathbf{x}}_L + \mathbf{q}^G - \mathbf{q}^L) \cdot \mathbf{n}_\Gamma}{\varepsilon^G - \varepsilon^L + \frac{1}{2} \dot{\mathbf{x}}_G \cdot \dot{\mathbf{x}}_G - \frac{1}{2} \dot{\mathbf{x}}_L \cdot \dot{\mathbf{x}}_L}, \quad (5.153)$$

where (5.60)<sub>2,4</sub> together with (5.70) have been used to substitute the partial stresses  $\mathbf{T}^G$  and  $\mathbf{T}^L$ .

In (5.152), the difference  $\varepsilon^G - \varepsilon^L$  of internal energies can be substituted by the *Gibbs* energy (enthalpy) difference  $\zeta^G - \zeta^L$ , through a *Legendre* transformation, cf. (B.5), i. e.,

$$\zeta^\beta = \varepsilon^\beta + \frac{p^{\beta R}}{\rho^{\beta R}} \quad \rightarrow \quad \varepsilon^\beta = \zeta^\beta - \frac{p^{\beta R}}{\rho^{\beta R}}. \quad (5.154)$$

Furthermore, since the effective pore pressure  $p^{FR}$  has been found to be jump-free, cf. (5.149), one can conclude that

$$\llbracket p^{FR} \rrbracket = p^{FR+} - p^{FR-} = 0 \quad \text{with} \quad \begin{cases} p^{FR+} = s^G p^{GR} \\ p^{FR-} = s^L p^{LR} \end{cases}. \quad (5.155)$$

Following this, the partial pore pressures  $s^G p^{GR}$  and  $s^L p^{LR}$  and, as a result, the partial pressures  $n^G p^{GR}$  and  $n^L p^{LR}$  are equivalent, such that

$$n^G p^{GR} \dot{\mathbf{x}}_G - n^L p^{LR} \dot{\mathbf{x}}_L = n^L p^{LR} (\dot{\mathbf{x}}_G - \dot{\mathbf{x}}_L) = n^L p^{LR} (\mathbf{w}_G - \mathbf{w}_L). \quad (5.156)$$

Inserting (5.154) and (5.156) into (5.152) finally yields

$$\hat{\varrho}_\Gamma^L = \frac{[n^L p^{LR} (\mathbf{w}_G - \mathbf{w}_L) + \mathbf{q}^G - \mathbf{q}^L] \cdot \mathbf{n}_\Gamma}{\Delta\zeta_{\text{vap}} - \frac{p^{GR}}{\rho^{GR}} + \frac{p^{LR}}{\rho^{LR}} + \frac{1}{2} \dot{\mathbf{x}}_G \cdot \dot{\mathbf{x}}_G - \frac{1}{2} \dot{\mathbf{x}}_L \cdot \dot{\mathbf{x}}_L}, \quad (5.157)$$

where  $\Delta\zeta_{\text{vap}} := \zeta^G - \zeta^L$  is the latent heat or the enthalpy of evaporation, cf. Section 4.2.

Equation (5.157) is often simplified with the argument that differences in mass-specific pressures  $\frac{p^{LR}}{\rho^{LR}} - \frac{p^{GR}}{\rho^{GR}}$  and in mass-specific kinetic energies  $\frac{1}{2} \dot{\mathbf{x}}_G \cdot \dot{\mathbf{x}}_G - \frac{1}{2} \dot{\mathbf{x}}_L \cdot \dot{\mathbf{x}}_L$  are small in comparison with the latent heat  $\Delta\zeta_{\text{vap}}$ , cf. *Morland & Gray* [120]. Following this argumentation, (5.157) recasts to

$$\hat{\varrho}_\Gamma^L = \frac{[n^L p^{LR} (\mathbf{w}_G - \mathbf{w}_L) + \mathbf{q}^G - \mathbf{q}^L] \cdot \mathbf{n}_\Gamma}{\Delta\zeta_{\text{vap}}}. \quad (5.158)$$

Furthermore, if phase transitions are mainly induced by heat, the pressure-dependent term in the nominator of (5.158) is negligible compared to the heat conduction and (5.158) further reduces to

$$\hat{\varrho}_{\Gamma}^L = \frac{(\mathbf{q}^G - \mathbf{q}^L) \cdot \mathbf{n}_{\Gamma}}{\Delta\zeta_{\text{vap}}}. \quad (5.159)$$

Note that this equation, is well known from classical thermodynamics, e. g., *Silhavy* [165]. Finally, the interfacial normal  $\mathbf{n}_{\Gamma}$ , cf. Figure 3.3, has to be found. For this purpose, use is made of the fact that the interface is always oriented perpendicular to the gradient of the fluid densities  $\text{grad } \rho^{\beta R}$ . Thus, similar to the level-set method,  $\text{grad } \rho^{\beta R}$  is calculated and normalised, to provide a simple way for the determination of  $\mathbf{n}_{\Gamma}$ .

With (5.145) and (5.159) the constitutive relation for the mass production is provided by

$$\hat{\rho}^L = a_{\Gamma} \hat{\varrho}_{\Gamma}^G = -a_{\Gamma} \frac{(\mathbf{q}^G - \mathbf{q}^L) \cdot \mathbf{n}_{\Gamma}}{\Delta\zeta_{\text{vap}}}. \quad (5.160)$$

For the numerical implementation of the mass production between the fluid phases it is necessary to define a switching criterion, which controls if phase transition occurs or not.

### 5.4.3 Switching criterion for the mass transition

In analogy to models for plasticity, where a yield surface restricts the stress domain to the elastic region, cf., e. g., *Ehlers* [55], the surfaces in the phase diagram in Figure 4.1 divide the  $p^{\beta R}$ - $\theta$ - $\rho^{\beta R}$  regions of the different phases. Since in the present case only the liquid and gas regions are of interest, it suffices to look at the 2-d phase diagram in Figure 4.2 (a), where the pressure  $p^{\beta R}$  is depicted over the temperature  $\theta$ . Therein, the vaporisation curve can be calculated from the *Antoine* equation (4.19), which relates the vapour pressure  $p_{\text{vap}}^R$  to the temperature  $\theta$ . This vaporisation curve divides the liquid phase from the gaseous phase and stands in analogy to the yield surface of the theory of plasticity. By comparing the effective fluid pressure  $p^{\beta R}$  with the vapour pressure  $p_{\text{vap}}^R$ , it is possible to identify the current phase state, cf. Figure 5.3. Therewith, a switching criterion is defined that furthermore depends on the direction of the phase transition, i. e., evaporation or condensation.

In the evaporation case, initially only liquid exists,  $s^L = 1$ , and the switching criterion reads

$$\text{if } s^L \neq 0 \quad \begin{cases} p^{LR} > p_{\text{vap}}^R & \text{then } \hat{\rho}^L = 0, \\ p^{LR} \leq p_{\text{vap}}^R & \text{then } \hat{\rho}^L \neq 0. \end{cases} \quad (5.161)$$

When the transition occurs in the other direction, i. e., from gas to liquid, the switching criterion for condensation starting from  $s^G = 1$  is given by

$$\text{if } s^G \neq 0 \quad \begin{cases} p^{GR} < p_{\text{vap}}^R & \text{then } \hat{\rho}^G = 0, \\ p^{GR} \geq p_{\text{vap}}^R & \text{then } \hat{\rho}^G \neq 0. \end{cases} \quad (5.162)$$

Hence, the set of constitutive relations that belongs to the set of governing equations is completed. The relevant governing balance relations will be recapitulated and formulated in their strong form in the next section.

## 5.5 Governing balance relations in the strong form

With the constitutive relations derived in the previous section, the final form of the governing balance relations for the considered multiphasic system can be defined, in order to conclude the closure problem. In this regard, the governing balance relations must be identified from the materially independent mass, momentum and energy balances (5.3). Since the evaluation of the solid volume balance in Section 5.2.1 showed that this volume balance is already incorporated in the comprehensive formulations for the solid volume fraction  $n^S$  and the effective solid density  $\rho^{SR}$ , cf. (5.14), it must not be added as a separate governing balance relation. Consequently, the remaining equations (5.3)<sub>2,3,4</sub>, which are not used otherwise, are selected as the governing balance relations.

Proceeding from Section 5.2.2, the fluid mass-balance equations can be directly applied as they were presented in (5.16):

$$\begin{aligned} (\rho^L)'_S + \operatorname{div}(\rho^L \mathbf{w}_L) + \rho^L \operatorname{div}(\mathbf{u}_S)'_S &= \hat{\rho}^L, \\ (\rho^G)'_S + \operatorname{div}(\rho^G \mathbf{w}_G) + \rho^G \operatorname{div}(\mathbf{u}_S)'_S &= \hat{\rho}^G. \end{aligned} \quad (5.163)$$

In the mixture momentum balance (5.24) from Section 5.2.3 only slight changes concerning the overall *Cauchy* stress tensor are made by including (5.59), (5.60) and the definition of the total pore pressure  $p^{FR}$  (5.57), viz.:

$$\mathbf{0} = \operatorname{div} \mathbf{T}_{E \text{ mech.}}^S - \operatorname{grad} p^{FR} + \rho \mathbf{g} + \hat{\rho}^L (\mathbf{w}_G - \mathbf{w}_L). \quad (5.164)$$

Finally, the energy balance (5.27) is adapted to the derived constitutive relations. Analogous to the momentum balance, it also remains to process the *Cauchy* stress tensors with the help of (5.59), (5.60), (5.57) and  $\mathbf{L}_\alpha = \operatorname{grad} \mathbf{x}'_\alpha$ , where the specific procedure is presented in Appendix B.6, and which yields

$$\begin{aligned} \sum_\alpha \rho^\alpha (\varepsilon^\alpha)'_\alpha &= \mathbf{T}_{E \text{ mech.}}^S \cdot \operatorname{grad}(\mathbf{u}_S)'_S - p^{FR} \operatorname{div}(\mathbf{u}_S)'_S - n^L p^{LR} \operatorname{div} \mathbf{w}_L - \\ &\quad - n^G p^{GR} \operatorname{div} \mathbf{w}_G - \sum_\alpha \operatorname{div} \mathbf{q}^\alpha + \sum_\alpha \rho^\alpha r^\alpha - \hat{\mathbf{p}}^L \cdot \mathbf{w}_L - \hat{\mathbf{p}}^G \cdot \mathbf{w}_G + \\ &\quad + \hat{\rho}^L [\varepsilon^G - \varepsilon^L + \frac{1}{2}(\mathbf{w}_G \cdot \mathbf{w}_G - \mathbf{w}_L \cdot \mathbf{w}_L)]. \end{aligned} \quad (5.165)$$

Note in passing that the kinetic part of the phase-transition energy,  $\hat{\rho}^L [\frac{1}{2}(\mathbf{w}_G \cdot \mathbf{w}_G - \mathbf{w}_L \cdot \mathbf{w}_L)]$ , can be neglected under lingering-flow conditions. Furthermore, the assumption of negligible external heat supplies ( $\sum_\alpha \rho^\alpha r^\alpha = 0$ ), i. e., for example no radiation, is made. Thus, both terms are dropped in the subsequent weak form of the overall energy balance, cf. (6.10).

With the set of the governing balance relations and the corresponding set of constitutive relations at hand, phase transitions in deformable, porous media can be simulated after defining the respective initial and boundary values. Hence, the computation of initial-boundary-value problems (IBVP) is possible.



## Chapter 6: Numerical treatment

After the compilation of the model, the logical next step is to apply it to initial-boundary-value problems (IBVP) and solve these in numerical simulations. Therefore, an appropriate solution method for the treatment of partial differential equations (PDE) has to be chosen. A common discretisation method for IBVP within the field of solid mechanics is the finite-element method (FEM). This spatial discretisation scheme is then usually combined with a finite-difference method (FDM) in time to solve the PDE of the model. Although the problem of CO<sub>2</sub> sequestration is mainly governed by the physics of fluids, where commonly finite-volume methods (FVM) are applied to discretise the fluid mechanics, the model derived in this monograph still uses the FEM by embedding the solid and fluid mechanics into the framework of the TPM. This provides an elegant way to simulate deforming, porous solid materials with percolating fluids. For a deeper insight into the field of FEM, the interested reader is referred to, e.g., *Bathe* [12], *Braess* [29], *Schwarz* [162] and *Zienkiewicz & Taylor* [181].

The numerical implementation of the triphasic thermoelastic model is accomplished in the FE tool PANDAS<sup>1</sup>. This tool was developed at the Institute of Applied Mechanics (Chair of Continuum Mechanics) at the University of Stuttgart to solve porous-media problems concerning a wide field of applications in different materials, e.g., soils, foams, biological tissues or bones. In particular, *Ellsiepen* [64], *Eipper* [63] and *Ammann* [6] started this work and established the basis for further enhancements of PANDAS. To name a few of those enhancements, *Acartürk* [2] added real chemical mixtures together with electrically charged materials. In terms of the solid-deformation behaviour, the suite of tools was extended to visco-elastic materials at large strains by *Markert* [114] and *Karajan* [94] and to elasto-plastic materials by *Graf* [74] and *Avci* [8]. The latter two contributions also introduce threephase models including capillary-pressure-saturation relationships and, thus, together with the work on CO<sub>2</sub> sequestration by *Komarova* [98], build the basis for the numerical implementation in this monograph. The possibility of modelling discontinuities, e.g., fractures or cracks, was provided by *Rempler* [146], by upgrading the governing fields towards the so-called extended finite-element method (XFEM).

To solve larger problems with a large number of degrees of freedom (DOF), a parallelisation of the computation is inevitable. This can be achieved by a coupling interface provided by *Schenke* and *Ehlers* [158] that links PANDAS to the commercial finite-element package ABAQUS<sup>2</sup> using the user-defined element subroutine of ABAQUS. The latter is applied in the simulation of the numerical example on evaporation in Section 7.2.1.

Within this chapter, the choice of the set of primary variables is firstly discussed. Then, boundary conditions (BC), ansatz and test functions are introduced, and the weak for-

---

<sup>1</sup>Porous media Adaptive Nonlinear finite-element solver based on Differential Algebraic Systems, see <http://www.get-pandas.com>.

<sup>2</sup>FEM-based commercial simulation program, see <http://www.3ds.com/products-services/simulia/products/abaqus/>.

mulations of the governing balance relations are given as a necessity for the application of the FEM. Thereafter, the spatial and temporal solution procedures are outlined briefly. This provides all necessary means for the numerical treatment of the IBVP formulated in Chapter 7.

## 6.1 Finite-element method

### Selection of primary variables

At the end of Chapter 5, the final forms of the governing balance relations of the model were presented by the relations (5.163), (5.164) and (5.165). These balance equations are related to a corresponding set of primary variables. The choice of this latter set depends on the specifications of the IBVP, i. e., to avoid unwanted constraints implied by the applied BC, it might be necessary to switch from the effective fluid pressures  $p^{LR}$  and  $p^{GR}$  as primary variables to the liquid saturation  $s^L$  and the total pore pressure  $p^{FR}$ . In this regard, the first set of primary variables that is used within this monograph is collected in the vector  $\mathbf{u}_1$ . This set contains the solid displacement  $\mathbf{u}_S$ , the effective fluid pressures  $p^{LR}$  and  $p^{GR}$  and the temperature  $\theta$ :

$$\mathbf{u}_1 = [\mathbf{u}_S, p^{LR}, p^{GR}, \theta]^T . \quad (6.1)$$

Hereby, the solid displacement  $\mathbf{u}_S$  corresponds to the overall momentum balance (5.164), the effective fluid pressures  $p^{LR}$  and  $p^{GR}$  are related to the fluid volume balances (5.163) and the temperature  $\theta$  belongs to the overall energy balance (5.165).

In a second set  $\mathbf{u}_2$ , the constituent pressures are replaced by the overall pore pressure  $p^{FR}$  and the liquid saturation  $s^L$ , viz.:

$$\mathbf{u}_2 = [\mathbf{u}_S, p^{FR}, s^L, \theta]^T . \quad (6.2)$$

In this case, the governing balance relation corresponding to  $s^L$  is the liquid mass balance (5.163)<sub>1</sub>, whereas for  $p^{FR}$  the following overall mass balance has to be derived:

$$(\rho)'_S + \rho \operatorname{div}(\mathbf{u}_S)'_S + \operatorname{div}(\rho^L \mathbf{w}_L + \rho^G \mathbf{w}_G) = 0 . \quad (6.3)$$

A detailed derivation thereof is given in Appendix B.4. If  $\mathbf{u}_2$  is used as the set of primary variables, the effective pore pressures  $p^{LR}$  and  $p^{GR}$  are no longer intrinsically calculated and, thus, have to be derived with the aid of the capillary pressure (5.52) and Dalton's law (5.57) via

$$p^{LR} = p^{FR} - s^G p^c \quad \text{and} \quad p^{GR} = p^{FR} + s^L p^c . \quad (6.4)$$

Note that the numerical solution of the problem may yield values greater than one or smaller than zero for the liquid saturation  $s^L$ , when the latter is chosen as a primary variable. These physically unacceptable values also cause non-physical results for the effective fluid pressures, cf. (6.4). To overcome this problem, the implementation of the second set of primary variables  $\mathbf{u}_2$  should be associated with the introduction of appropriate "if-conditions" to remove non-physical values of  $s^L$ .

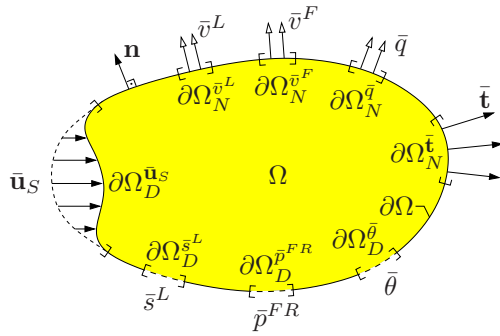


The change in primary variables can also help to improve the performance of the numerical computations. Specifically, this alludes to the capillary-pressure-saturation relation, which can cause numerical oscillations due to steep gradients in its formulations, cf. Figure 5.1. For more information and a detailed discussion of this problem, please refer to *Graf* [74] or *Helmig* [84].

Below, only the second set of primary variables  $\mathbf{u}_2$  will be used to illustrate the numerical treatment of the derived model, to avoid double formulations. Therefore, the index in the vector  $\mathbf{u}_{(\cdot)}$ , indicating the set of primary variables, will be omitted in the following.

## Boundary conditions

Next, the BC corresponding to the governing equations have to be investigated. In specific, these are *Dirichlet* (essential) boundaries  $\partial\Omega_D$ , which define exact values for the respective primary variables on the boundary, and *Neumann* (natural) boundaries  $\partial\Omega_N$  that formulate the flux corresponding to a primary variable over the boundary. Since these two kinds of BC cannot be defined simultaneously for one specific primary variable at a certain position, the surface  $\partial\Omega$  of the body has to be divided, cf. Figure 6.1. However, overlapping definitions between the primary variables are permitted.



Restrictions imposed on the BC:

$$\begin{aligned}
 \partial\Omega_{\mathbf{u}_S} &= \partial\Omega_D^{\bar{\mathbf{u}}_S} \cup \partial\Omega_N^{\bar{\mathbf{t}}}, & \emptyset &= \partial\Omega_D^{\bar{\mathbf{u}}_S} \cap \partial\Omega_N^{\bar{\mathbf{t}}}, \\
 \partial\Omega_{p^{FR}} &= \partial\Omega_D^{\bar{p}^{FR}} \cup \partial\Omega_N^{\bar{v}^F}, & \emptyset &= \partial\Omega_D^{\bar{p}^{FR}} \cap \partial\Omega_N^{\bar{v}^F}, \\
 \partial\Omega_{s^L} &= \partial\Omega_D^{\bar{s}^L} \cup \partial\Omega_N^{\bar{v}^L}, & \emptyset &= \partial\Omega_D^{\bar{s}^L} \cap \partial\Omega_N^{\bar{v}^L}, \\
 \partial\Omega_{\theta} &= \partial\Omega_D^{\bar{\theta}} \cup \partial\Omega_N^{\bar{q}}, & \emptyset &= \partial\Omega_D^{\bar{\theta}} \cap \partial\Omega_N^{\bar{q}}.
 \end{aligned} \tag{6.5}$$

Figure 6.1: The observed domain  $\Omega$  with the applied BC on the boundary  $\partial\Omega$  for the set of primary variables  $\mathbf{u}$ .

## Ansatz and test functions

For the numerical treatment of the IBVP, the ansatz (trial) and test functions corresponding to the set of primary variables (6.2) are chosen from the *Sobolev* space  $\mathcal{H}^1(\Omega)$  to be square integrable on  $\Omega$ . The ansatz functions  $\mathcal{A}^{(\cdot)}(t)$  with  $t \in [t_0, T]$  read:

$$\begin{aligned}
 \mathcal{A}^{\mathbf{u}_S}(t) &:= \{ \mathbf{u}_S \in \mathcal{H}^1(\Omega)^d : \mathbf{u}_S(\mathbf{x}, t) = \bar{\mathbf{u}}_S(\mathbf{x}, t) \text{ on } \partial\Omega_D^{\bar{\mathbf{u}}_S} \}, \\
 \mathcal{A}^{p^{FR}}(t) &:= \{ p^{FR} \in \mathcal{H}^1(\Omega) : p^{FR}(\mathbf{x}, t) = \bar{p}^{FR}(\mathbf{x}, t) \text{ on } \partial\Omega_D^{\bar{p}^{FR}} \}, \\
 \mathcal{A}^{s^L}(t) &:= \{ s^L \in \mathcal{H}^1(\Omega) : s^L(\mathbf{x}, t) = \bar{s}^L(\mathbf{x}, t) \text{ on } \partial\Omega_D^{\bar{s}^L} \}, \\
 \mathcal{A}^{\theta}(t) &:= \{ \theta \in \mathcal{H}^1(\Omega) : \theta(\mathbf{x}, t) = \bar{\theta}(\mathbf{x}, t) \text{ on } \partial\Omega_D^{\bar{\theta}} \}.
 \end{aligned} \tag{6.6}$$

The ansatz functions are defined such that they provide the values of the *Dirichlet* BC at the boundary  $\partial\Omega_D$ . The test (weighting) functions  $\mathcal{T}^{(\cdot)}(t)$  disappear at the *Dirichlet* boundaries  $\partial\Omega_D$ , and are given as

$$\begin{aligned}\mathcal{T}^{\mathbf{u}^S} &:= \{ \delta \mathbf{u}_S \in \mathcal{H}^1(\Omega)^d : \delta \mathbf{u}_S(\mathbf{x}) = \mathbf{0} \text{ on } \partial\Omega_D^{\mathbf{u}^S} \}, \\ \mathcal{T}^{p^{FR}} &:= \{ \delta p^{FR} \in \mathcal{H}^1(\Omega) : \delta p^{FR}(\mathbf{x}) = 0 \text{ on } \partial\Omega_D^{p^{FR}} \}, \\ \mathcal{T}^{s^L} &:= \{ \delta s^L \in \mathcal{H}^1(\Omega) : \delta s^L(\mathbf{x}) = 0 \text{ on } \partial\Omega_D^{s^L} \}, \\ \mathcal{T}^\theta &:= \{ \delta \theta \in \mathcal{H}^1(\Omega) : \delta \theta(\mathbf{x}) = 0 \text{ on } \partial\Omega_D^\theta \}.\end{aligned}\tag{6.7}$$

In (6.6)<sub>1</sub> and (6.7)<sub>1</sub>, the superscript  $d \in \{1, 2, 3\}$  denotes the spatial dimension of the physical problem.

### 6.1.1 Weak formulations of the governing equations

The governing balance relations (5.163), (5.164) and (5.165) are formulated locally in their strong form and are, thus, continuously fulfilled at each material point  $\mathcal{P}$  of the mixture body  $\mathcal{B}$ . This system of coupled PDE appears to be too complicated to be solved numerically. Therefore, it is necessary within the framework of the FEM to transform these balance relations into an energetic expression that is satisfied in a so-called weak sense, i. e., it fulfills the relations in an integral sense over the spatial domain  $\Omega$ . This transformation from the strong, local form into the weak, global form  $\mathcal{G}_{(\cdot)}$  is accomplished by multiplying the governing balance equations with the independent test functions  $\delta \mathbf{u}_S$ ,  $\delta p^{FR}$ ,  $\delta s^L$  and  $\delta \theta$  introduced in (6.7), to account for the error made by this approximation procedure. The integration of the governing balance relations is conducted using the *Gaußian* integral theorem. In this regard, the final weak form of the mixture mass-balance equation and the mass-balance equation of the constituent  $\varphi^L$  read

$$\begin{aligned}\mathcal{G}_{p^{FR}}(\mathbf{u}, \delta p^{FR}) &= \int_{\Omega} \{(\rho)'_S + \rho \operatorname{div}(\mathbf{u}_S)'_S\} \delta p^{FR} \, dv - \int_{\Omega} (\rho^L \mathbf{w}_L + \rho^G \mathbf{w}_G) \cdot \operatorname{grad} \delta p^{FR} \, dv + \\ &\quad + \int_{\partial\Omega_N^{\bar{v}^F}} \underbrace{(\rho^L \mathbf{w}_L + \rho^G \mathbf{w}_G) \cdot \mathbf{n}}_{\bar{v}^F} \delta p^{FR} \, da = 0, \\ \mathcal{G}_{s^L}(\mathbf{u}, \delta s^L) &= \int_{\Omega} \{(\rho^L)'_S + \rho^L \operatorname{div}(\mathbf{u}_S)'_S\} \delta s^L \, dv - \int_{\Omega} \rho^L \mathbf{w}_L \cdot \operatorname{grad} \delta s^L \, dv - \\ &\quad - \int_{\Omega} \hat{\rho}^L \delta s^L \, dv + \int_{\partial\Omega_N^{\bar{v}^L}} \underbrace{\rho^L \mathbf{w}_L \cdot \mathbf{n}}_{\bar{v}^L} \delta s^L \, da = 0.\end{aligned}\tag{6.8}$$

Therein, arguments of the boundary integrals over  $\partial\Omega_N^{\bar{v}^F}$  and  $\partial\Omega_N^{\bar{v}^L}$  denote the volumetric effluxes of the domain  $\Omega$ , once for both fluid phases,  $\bar{v}^F = (\rho^L \mathbf{w}_L + \rho^G \mathbf{w}_G) \cdot \mathbf{n}$ , and once

for the liquid phase solely,  $\bar{v}^L = \rho^L \mathbf{w}_L \cdot \mathbf{n}$  with  $\mathbf{n}$  being the outward-oriented unit normal vector, cf. Figure 6.1. These effluxes can be directly defined by *Neumann* BC.

Proceeding to the next balance equation, the weak form of the mixture momentum balance is given as

$$\begin{aligned} \mathcal{G}_{\mathbf{u}_S}(\mathbf{u}, \delta \mathbf{u}_S) &= \int_{\Omega} (\mathbf{T}_E^S - p^{FR} \mathbf{I}) \cdot \text{grad } \delta \mathbf{u}_S \, dv - \int_{\Omega} \rho \mathbf{g} \cdot \delta \mathbf{u}_S \, dv + \\ &+ \int_{\Omega} \hat{\rho}^L (\mathbf{w}_L - \mathbf{w}_G) \delta \mathbf{u}_S \, dv - \int_{\partial \Omega_N^{\bar{\mathbf{t}}}} \underbrace{(\mathbf{T}_E^S - p^{FR} \mathbf{I}) \mathbf{n}}_{\bar{\mathbf{t}}} \cdot \delta \mathbf{u}_S \, da = 0, \end{aligned} \quad (6.9)$$

where  $\bar{\mathbf{t}} = (\mathbf{T}_E^S - p^{FR} \mathbf{I}) \mathbf{n}$  is the external total stress vector on the *Neumann* boundary  $\partial \Omega_N^{\bar{\mathbf{t}}}$ . And finally, the weak form of the mixture energy balance is derived analogously, viz.:

$$\begin{aligned} \mathcal{G}_{\theta}(\mathbf{u}, \delta \theta) &= \int_{\Omega} \left\{ \rho^S (\varepsilon^S)'_S + \rho^L (\varepsilon^L)'_L + \rho^G (\varepsilon^G)'_G - \mathbf{T}_{E \text{ mech.}}^S \cdot \text{grad } (\mathbf{u}_S)'_S + \right. \\ &\quad \left. + n^S p^{FR} \text{div } (\mathbf{u}_S)'_S + \hat{\mathbf{p}}^L \cdot \mathbf{w}_L + \hat{\mathbf{p}}^G \cdot \mathbf{w}_G \right\} \delta \theta \, dv - \\ &- \int_{\Omega} \left( \sum_{\alpha} \mathbf{q}^{\alpha} + n^L p^{LR} \mathbf{w}_L + n^G p^{GR} \mathbf{w}_G \right) \cdot \text{grad } \delta \theta \, dv + \\ &+ \int_{\Omega} \hat{\rho}^L (\varepsilon^L - \varepsilon^G) \delta \theta \, dv + \\ &+ \int_{\partial \Omega_N^{\bar{q}}} \underbrace{\left( \sum_{\alpha} \mathbf{q}^{\alpha} + n^L p^{LR} \mathbf{w}_L + n^G p^{GR} \mathbf{w}_G \right) \cdot \mathbf{n}}_{\bar{q}} \delta \theta \, da = 0 \end{aligned} \quad (6.10)$$

with the *Neumann* BC on  $\partial \Omega_N^{\bar{q}}$  being governed by the heat efflux  $\bar{q} = \left( \sum_{\alpha} \mathbf{q}^{\alpha} + n^L p^{LR} \mathbf{w}_L + n^G p^{GR} \mathbf{w}_G \right) \cdot \mathbf{n}$ . Furthermore, the time derivatives of the internal energies with respect to the fluid motions, i. e.,  $(\varepsilon^L)'_L$  and  $(\varepsilon^G)'_G$  in (6.10), are transformed by (3.15) via

$$(\varepsilon^{\beta})'_{\beta} = (\varepsilon^{\beta})'_S + \text{grad } \varepsilon^{\beta} \cdot \mathbf{w}_{\beta}, \quad (6.11)$$

so that the mixture energy balance is given solely with respect to the motion of the solid constituent.

A compact formulation of the FE problem is obtained as follows (cf. *Ellsiepen* [64]):

$$\text{Find } \mathbf{u} \in \mathcal{A}^u(t) \text{ such that } \mathcal{G}_{\mathbf{u}}(\mathbf{u}, \delta \mathbf{u}) = \mathbf{0} \quad \forall \delta \mathbf{u} \in \partial \Omega_u, \quad t \in [t_0, T]. \quad (6.12)$$

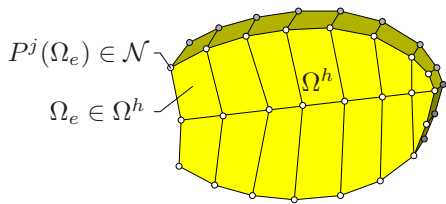
Therein,  $\mathcal{G}_{\mathbf{u}} = [\mathcal{G}_{\mathbf{u}_S}, \mathcal{G}_{p^{FR}}, \mathcal{G}_{s^L}, \mathcal{G}_{\theta}]^T$  is the system of the governing balance relations in the weak formulation.

For the sake of completeness, the weak forms of the effective fluid mass balances, corresponding to the fluid partial pressures  $p^{LR}$  and  $p^{GR}$  of the set of primary variables  $\mathbf{u}_1$ , are supplemented in Appendix B.5.

## 6.2 Discretisation procedures

### 6.2.1 Spatial discretisation

As the name already conveys, it is a major principle of the FEM to subdivide the continuous domain  $\Omega$  into  $E$  non-overlapping finite elements  $\Omega_e$ , as is shown in Figure 6.2. Each finite element is composed of  $N_e$  nodal points named as  $P^j$ . The total number of



$$\Omega \approx \Omega^h = \bigcup_{e=1}^E \Omega_e, \quad (6.13)$$

$$\mathcal{N} = \bigcup_{j=1}^N P^j(\Omega_e).$$

Figure 6.2: Example of the spatial discretisation of a spatial domain  $\Omega$ .

nodal points is denoted by  $N$ . The edges of the elements connecting the nodal points are straight lines. Furthermore, the nodal points and edges of each element are shared with the neighbouring elements, except for nodal points and edges belonging to a boundary. This yields a finite-element mesh that is composed of the set of nodes  $\mathcal{N}$ . Note that the continuous domain  $\Omega$  is only approximated by this spatial discretisation  $\Omega^h$ , because of the simple geometry of the finite elements. The resulting error is naturally reduced by increasing the number of elements.

This spatial discretisation also alters the ansatz and test spaces,  $\mathcal{A}^{(\cdot)}(t)$  and  $\mathcal{T}^{(\cdot)}(t)$ , in subdividing them into  $N$  discretised ansatz and test spaces,  $\mathcal{A}^{(\cdot)h}(t)$  and  $\mathcal{T}^{(\cdot)h}(t)$ . In detail, this yields for the primary variables  $\mathbf{u}$  the following discretised ansatz functions  $\mathbf{u}^h$ :

$$\begin{aligned} \mathbf{u}_S(\mathbf{x}, t) &\approx \mathbf{u}_S^h(\mathbf{x}, t) = \bar{\mathbf{u}}_S^h(\mathbf{x}, t) + \sum_{j=1}^N \phi_{\mathbf{u}_S}^j(\mathbf{x}) \mathbf{u}_S^j(t) \in \mathcal{A}^{\mathbf{u}_S^h}(t), \\ p^{FR}(\mathbf{x}, t) &\approx p^{FRh}(\mathbf{x}, t) = \bar{p}^{FRh}(\mathbf{x}, t) + \sum_{j=1}^N \phi_{p^{FR}}^j(\mathbf{x}) p^{FRj}(t) \in \mathcal{A}^{p^{FRh}}(t), \\ s^L(\mathbf{x}, t) &\approx s^{Lh}(\mathbf{x}, t) = \bar{s}^{Lh}(\mathbf{x}, t) + \sum_{j=1}^N \phi_{s^L}^j(\mathbf{x}) s^{Lj}(t) \in \mathcal{A}^{s^{Lh}}(t), \\ \theta(\mathbf{x}, t) &\approx \theta^h(\mathbf{x}, t) = \bar{\theta}^h(\mathbf{x}, t) + \sum_{j=1}^N \phi_{\theta}^j(\mathbf{x}) \theta^j(t) \in \mathcal{A}^{\theta^h}(t), \end{aligned} \quad (6.14)$$

where  $\{\bar{\mathbf{u}}_S^h, \bar{p}^{FRh}, \bar{s}^{Lh}, \bar{\theta}^h\}$  are determined by the *Dirichlet* BC and  $\{\mathbf{u}_S^j, p^{FRj}, s^{Lj}, \theta^j\}$  are the unknown nodal quantities, also called the degrees of freedom (DOF) of the system. Analogously, the discretised test functions  $\delta \mathbf{u}^h$  corresponding

to the primary variables  $\mathbf{u}^h$  read:

$$\begin{aligned}
\delta \mathbf{u}_S(\mathbf{x}) &\approx \delta \mathbf{u}_S^h(\mathbf{x}) = \sum_{j=1}^N \phi_{\mathbf{u}_S}^j(\mathbf{x}) \delta \mathbf{u}_S^j && \in \mathcal{T}^{\mathbf{u}_S^h}, \\
\delta p^{FR}(\mathbf{x}) &\approx \delta p^{FRh}(\mathbf{x}) = \sum_{j=1}^N \phi_{p^{FR}}^j(\mathbf{x}) \delta p^{FRj} && \in \mathcal{T}^{p^{FRh}}, \\
\delta s^L(\mathbf{x}) &\approx \delta s^{Lh}(\mathbf{x}) = \sum_{j=1}^N \phi_{s^L}^j(\mathbf{x}) \delta s^{Lj} && \in \mathcal{T}^{s^{Lh}}, \\
\delta \theta(\mathbf{x}) &\approx \delta \theta^h(\mathbf{x}) = \sum_{j=1}^N \phi_{\theta}^j(\mathbf{x}) \delta \theta^j && \in \mathcal{T}^{\theta^h}.
\end{aligned} \tag{6.15}$$

Therein, the same global basis functions  $\{\phi_{\mathbf{u}_S}^j, \phi_{p^{FR}}^j, \phi_{s^L}^j, \phi_{\theta}^j\}$  are chosen both for the ansatz and test functions, according to the well-known *Bubnov-Galerkin* method<sup>3</sup>. Please note in passing that the global basis function of the solid displacement has multiple entries corresponding to the dimension of the physical problem (in 3-d:  $\phi_{\mathbf{u}_S}^j = [\phi_{u_{S1}}^j, \phi_{u_{S2}}^j, \phi_{u_{S3}}^j]^T$ ). Hence, every scalar-valued DOF  $\{u_{S1}^j, \dots, u_{Sd}^j, p^{FRj}, s^{Lj}, \theta^j\}$  is assigned to a basis function  $\phi_{\text{DOF}}^j$  at each nodal point  $P^j$ . Furthermore, the DOF are only time dependent, whereas the basis functions are determined by the spatial position  $\mathbf{x}$ . Thus, the values of the DOF (representing the physical quantities) are mapped by the basis function  $\phi_{\text{DOF}}^j$  to any place within the finite elements  $E^*$  belonging to the respective node  $P^j$ . This can be mathematically formulated into, cf. *Rempler* [146]:

$$\phi_{\text{DOF}}^j(\mathbf{x}) = 0 \quad \text{if } \mathbf{x} \notin \bigcup_{e \in E^*} \Omega_e \quad \text{and} \quad \phi_{\text{DOF}}^j(\mathbf{x}_i) = \delta_i^j \quad \text{with} \quad \begin{cases} i = j & : \delta_i^j = 1, \\ i \neq j & : \delta_i^j = 0, \end{cases} \tag{6.16}$$

where the basis functions  $\phi_{\text{DOF}}^j$  are normalised by the *Kronecker* symbol  $\delta_i^j$  (for  $\{i, j\} = 1, \dots, N$ ), ensuring that at each nodal position  $\mathbf{x}_i$ , the nodal quantity corresponds to the approximated value of the DOF (except for *Dirichlet* boundary nodes). A further limitation is stipulated for the discretised test functions  $\{\delta \mathbf{u}_S^h, \delta p^{FRh}, \delta s^{Lh}, \delta \theta^h\}$ , which must fulfill the so-called *partition-of-unity principle*, i. e., the sum of the basis functions at each point  $\mathbf{x} \in \Omega^h$  must be equal to one. This yields a system of  $\text{DOF} \times N$  linearly independent equations for each DOF.

The gradient of the primary variables  $\text{grad } \mathbf{u}$  appearing in the weak forms of the balance equations (6.8), (6.9) and (6.10) are calculated by the partial derivative of the ansatz and

---

<sup>3</sup>This is also known as the *Galerkin* method. Contrary to this, the *Petrov-Galerkin* method is characterised by selecting different global basis functions for the ansatz and test functions. For more information in this regard and a comparison between the two methods, please refer to, e. g., *Ehlers et al.* [58] or *Helmig* [84].

test functions, via:

$$\begin{aligned} \text{grad } \mathbf{u}^h(\mathbf{x}, t) &= \sum_{i=1}^{N_u} \text{grad } \phi_u^i(\mathbf{x}) \mathbf{u}^i(t), \\ \text{grad } \delta \mathbf{u}^h(\mathbf{x}, t) &= \sum_{i=1}^{N_u} \text{grad } \phi_u^i(\mathbf{x}) \delta \mathbf{u}^i(t). \end{aligned} \quad (6.17)$$

The strongly coupled problem arising from the multiphasic model is solved here in a monolithic way<sup>4</sup>. That means, all independent linear equations corresponding to the primary variables (DOF) are calculated simultaneously. In principle, different ansatz functions for the primary variables  $\mathbf{u}^h$  can be chosen. However, this choice influences the stability of the numerical solutions, i. e., a poor choice could cause oscillations. *Acartürk* [2] and *Graf* [74] explicate that the reason for this performance is found in the governing overall momentum balance (5.164), specifically in the overall stress. Assuming negligible fluid extra stresses, the overall stress is composed of the mechanical extra-stress tensor of the solid matrix, given by (5.80)<sub>1</sub>, and the effective pore pressure, presented in (5.119). By means of the definitions of the linearised solid strain (5.7) and the solid deformation gradient (5.5), the solid extra-stress tensor depends on the gradient of the solid displacement vector  $\mathbf{u}_S$ . In this regard, a mixed finite-element formulation consisting of quadratic ansatz functions for the solid displacement  $\mathbf{u}_S$  and linear ansatz functions for the remaining primary variables, i. e., pore pressure  $p^{FR}$ , liquid saturation  $s^L$  and temperature  $\theta$ , leads to an approximation of equal polynomial order with respect to the primary variables. These elements are also called extended *Taylor-Hood* elements, cf. Figure 6.3, where a 2-d triangular element (6 nodes) and a 3-d hexahedral element (20 nodes) are exemplary depicted.

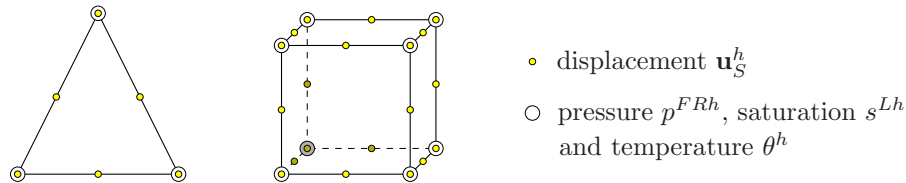


Figure 6.3: Extended triangular (2-d) and hexahedral (3-d) *Taylor-Hood* elements.

Mathematically, the mixed finite elements must fulfill the *Ladyzhenskaya-Babuška-Brezzi* (or inf-sub) condition. More information in this direction can be found in, e. g., *Braess* [29], *Brezzi & Fortin* [30] and *Hughes* [88].

The final feature of the spatial discretisation is the integration of the weak balance equations locally at a reference element that is positioned at the local coordinates  $\boldsymbol{\xi} = (\xi_1, \dots, \xi_d)$ , where usually  $\xi_{(\cdot)} \in [0, 1]$  or  $\xi_{(\cdot)} \in [-1, 1]$ . The results of this integration are mapped to the global coordinates  $\mathbf{x}$ . The advantage of this approach is the conduction of complicated integrations on a simple local geometry, where after the results have to be

<sup>4</sup>It is also possible to solve this model in a decoupled way. Therefore, special methods such as the operator-splitting method would be required, which are presented, e. g., in *Markert et al.* [116] or *Zinatbakhsh* [182].

transformed to the original, complex physical geometry. The transformation between the local and global coordinates is given by

$$\mathbf{x}(\boldsymbol{\xi}) = \sum_{j=1}^{N_e} \phi_{\text{geo}}^j(\boldsymbol{\xi}) \mathbf{x}_j = \sum_{j=1}^{N_e} \phi^j(\boldsymbol{\xi}) \mathbf{x}_j, \quad (6.18)$$

where  $\mathbf{x}(\boldsymbol{\xi})$  defines the position of an arbitrary point in the element and is calculated by utilising the mapping basis function  $\phi_{\text{geo}}^j(\boldsymbol{\xi})$  on the nodal point in the global coordinate system of the finite element  $\Omega_e$ , see Figure 6.4. This is accomplished for all nodes  $N_e$  of

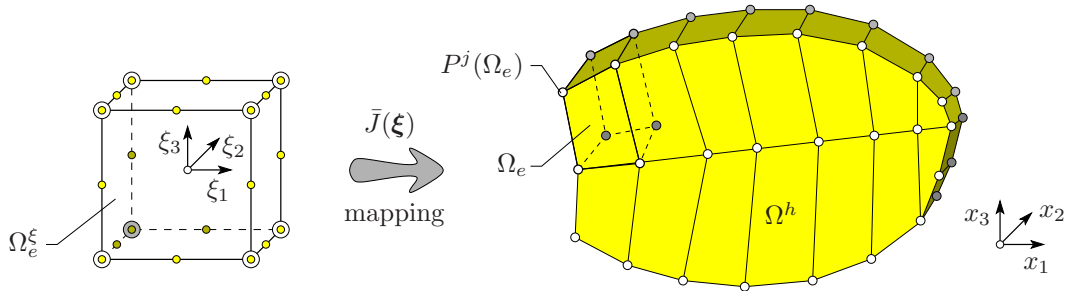


Figure 6.4: Illustration of the mapping procedure between the hexahedral reference element  $\Omega_e^\xi$  and the actual element  $\Omega_e$ , i. e., from the coordinates  $\boldsymbol{\xi}$  to  $\mathbf{x}$ .

the element  $\Omega_e$ . In this work, an isoparametric geometry transformation is applied, i. e.,  $\phi_{\text{geo}}^j(\boldsymbol{\xi}) = \phi^j(\boldsymbol{\xi})$ . This leads to the transformation of the differential line element  $d\mathbf{x}$  to  $d\boldsymbol{\xi}$  by the *Jacobian determinant*  $\bar{J}$ , given as

$$\bar{J}(\boldsymbol{\xi}) = \det \left( \frac{d\mathbf{x}(\boldsymbol{\xi})}{d\boldsymbol{\xi}} \right). \quad (6.19)$$

Therewith, the integration of a function  $f(\mathbf{x})$  over the finite element  $\Omega_e$  can be reformulated within the local coordinates of the reference element domain  $\Omega_e^\xi$  via

$$\int_{\Omega_e} f(\mathbf{x}) dv = \int_{\Omega_e^\xi} f(\mathbf{x}(\boldsymbol{\xi})) \bar{J}(\boldsymbol{\xi}) dv_\xi \quad (6.20)$$

with the incremental volume of the reference element  $dv_\xi$ . By applying the *Gaussian quadrature* scheme to the integral expression in the local element coordinates in (6.20), the final numerical integration reads

$$\int_{\Omega_e} f(\mathbf{x}) dv = \sum_{k=1}^{K_G} f(\mathbf{x}(\boldsymbol{\xi}_k)) \bar{J}(\boldsymbol{\xi}_k) w_k. \quad (6.21)$$

Therein, the function  $f(\mathbf{x}(\boldsymbol{\xi}_k))$  is evaluated by the integration at the *Gauß points*  $K_G$ , which are located in the reference element at  $\boldsymbol{\xi}_k$ , furthermore weighted with the quadrature weighting factors  $w_k$  and summed over all *Gauß points* of the element  $\Omega_e$ . The weighting factors are hereby chosen according to the number of *Gauß points* and their position, where, in turn, the number of *Gauß points* must be derived according to the integration order, to get an accurate FEM solution, cf. *Wieners et al.* [179] for more details.

## 6.2.2 Temporal discretisation

Before the temporal discretisation of the governing equations are discussed, it is convenient to reformulate the semi-discrete initial-value problem, which is spatially discretised but still continuous in time, in an abstract manner. This is achieved by collecting all nodal DOF in a vector  $\mathbf{y}$ , viz.:

$$\mathbf{y} = [(\mathbf{u}_S^1, p^{FR,1}, s^{L,1}, \theta^1), \dots, (\mathbf{u}_S^N, p^{FR,N}, s^{L,N}, \theta^N)]^T. \quad (6.22)$$

Please be aware that the solid displacement velocity  $\mathbf{u}_S$  contains multiple entries depending on the regarded spatial dimension  $d$  of the IBVP. Since in the weak formulations of the governing balance relations (6.8), (6.9) and (6.10), the time derivatives are only given with respect to the solid motion, in the following  $(\cdot)'_S$  will be denoted as  $(\cdot)'$ . Therewith, the abstract formulation of the semi-discrete IBVP reads

$$\mathcal{F}(t, \mathbf{y}, \mathbf{y}') = [\mathbf{M}\mathbf{y}'(t) + \mathbf{k}(\mathbf{y}(t)) - \mathbf{f}(t)] \stackrel{!}{=} \mathbf{0}. \quad (6.23)$$

Herein, the generalised mass matrix is expressed by  $\mathbf{M}$ , the generalised stiffness vector is presented by  $\mathbf{k}(\mathbf{y})$ , and  $\mathbf{f}$  is the generalised vector of external forces, composed of the *Neumann* BC.

Proceeding to the temporal discretisation of (6.23), the implicit (or backward) *Euler* time-integration method is chosen, which belongs to the general class of *Runge-Kutta* methods. In case of 1<sup>st</sup>-order systems with quasi-static behaviour, large time-steps are desirable for the simulation. However, this requires an unconditional stability of the time-integration method, which is guaranteed, for example, by the implicit *Euler* method, but not by explicit schemes. Furthermore, this implicit or backward *Euler* method is a so-called single-step method, where the unknown values of the next time-step are determined only from one previous solution. A deeper discussion of the single-step *Runge-Kutta* methods and their numerical relevance can be found, e. g., in *Rempler* [146].

The implicit *Euler* scheme proceeds from a backward *Taylor*-series expansion of the temporal discretisation of the vector of unknowns  $\mathbf{y}$  around time  $t_{n+1}$ ,

$$\mathbf{y}_n = \mathbf{y}_{n+1} - \Delta t \mathbf{y}'_{n+1} \quad \rightarrow \quad \mathbf{y}'_{n+1} = \frac{1}{\Delta t} (\mathbf{y}_{n+1} - \mathbf{y}_n), \quad n = 0, 1, \dots, \quad (6.24)$$

where the time  $t_n$  refers to the previous time-step and, consequently, time  $t_{n+1}$  denotes the current time. Furthermore, the actual time-step size  $\Delta t = t_{n+1} - t_n > 0$  splits the total simulation time  $[t_0, T]$  into a number of subintervals  $[t_n, t_{n+1}]$ . Hereby, only the first expansion term of the *Taylor* series is kept, while the higher-order terms are neglected.

Next, the time-integration scheme (6.24) is substituted into the previously derived problem formulation (6.23). It yields

$$\mathcal{F}_{n+1}(t_{n+1}, \mathbf{y}_{n+1}, \mathbf{y}'_{n+1}(\mathbf{y}_{n+1})) = [\mathbf{M}(\mathbf{y}_{n+1}) \mathbf{y}'_{n+1} + \mathbf{k}(\mathbf{y}_{n+1}) - \mathbf{f}_{n+1}] \stackrel{!}{=} \mathbf{0}. \quad (6.25)$$

This nonlinear set of differential algebraic equations is solved in this monograph by the well-known *Newton-Raphson* iteration method. Therefore, the required global or residual



tangent  $D\mathcal{F}_{n+1}^k$  is numerically calculated according to *Acartürk* [2], and it reads

$$D\mathcal{F}_{n+1}^k := \frac{d\mathcal{F}_{n+1}^k}{d\mathbf{y}_{n+1}^k} = \frac{\partial\mathcal{F}_{n+1}^k}{\partial\mathbf{y}_{n+1}^k} + \frac{1}{\Delta t} \frac{\partial\mathcal{F}_{n+1}^k}{\partial(\mathbf{y}')_{n+1}^k}. \quad (6.26)$$

The numerical calculation of the residual tangent has the advantage of a simple numerical implementation, but is numerically costly and leads in some cases to instability of the numerical solution, which can be avoided by inserting the analytical tangent, cf. *Wagner* [176] for more details. With the global tangent of (6.26), a linear system of equations

$$D\mathcal{F}_{n+1}^k \Delta\mathbf{y}_{n+1}^k = -\mathcal{F}_{n+1}^k \quad (6.27)$$

has to be solved for the stage increment vector  $\Delta\mathbf{y}_{n+1}^k$  at the current *Newton* step  $k$ . Therefore, both direct and iterative solvers can be used, where an overview of these solvers is presented, e. g., in *Ellsiepen* [64]. In a last step, the stage increment is added to the solution vector and the next *Newton* step  $k + 1$  is calculated:

$$\mathbf{y}_{n+1}^{k+1} = \mathbf{y}_{n+1}^k + \Delta\mathbf{y}_{n+1}^k. \quad (6.28)$$

This iteration procedure is repeated until the norm of the residuum falls below a pre-defined tolerance  $\epsilon_{\text{tol}}$ ,

$$\|\mathcal{F}_{n+1}^{k+1}\| < \epsilon_{\text{tol}}. \quad (6.29)$$

Admittedly, this was a rather brief description of the temporal discretisation and the solution procedure. For more information, the interested reader is referred to the works of, e. g., *Ammann* [6], *Ellsiepen* [64] and *Rempler* [146].

Thereby, the numerical model is completed and can now be utilised to simulate different IBVP concerning the sequestration of  $\text{CO}_2$ , as is presented in the next chapter.



# Chapter 7: Numerical examples

In this chapter, the previously developed theoretical model is applied to simulate CO<sub>2</sub> sequestration and to investigate the problem of phase transition. This is achieved in conjunction with the numerical implementation introduced in Chapter 6. Furthermore, the material-parameter set is chosen such that it represents CO<sub>2</sub> and water percolating a porous rock matrix. Therefore, the relations derived in Chapter 4 are drawn on for the thermodynamical behaviour of the CO<sub>2</sub>, whereas for the parameters describing flow and deformation, it is resorted to the works of *Graf* [74], *Class* [36, 37] and *Rutqvist* [154, 155], which also address either CO<sub>2</sub> sequestration directly or related fields, e. g., remediation of contaminated porous media.

After discretisation, the strongly coupled system of partial differential equations given by (6.9)-(6.10) is solved monolithically with an unconditionally stable, implicit time-integration scheme using the finite-element solver PANDAS. For the example presented in Section 7.2.1 a parallel solution technique is applied, where PANDAS is included into the commercial FEM-program ABAQUS, cf. *Schenke & Ehlers* [158].

To gain an impression of what happens during CO<sub>2</sub> injection into a deep aquifer, at first, a numerical example of a fictitious aquifer is simulated to demonstrate the dependence between the pressure and temperature conditions, the phase behaviour of CO<sub>2</sub> and the solid deformations of the porous rock. Thereafter, the phase-transition process in consequence of changing temperature conditions is examined further, both in the evaporation and in the condensation case. Hereby, use is made of the derived constitutive relation for the mass production, cf. Section 5.4, in order to get an understanding of the influence of the mass transfer between the two fluid phases on the phase-transition process.

## 7.1 CO<sub>2</sub> sequestration into a deep aquifer

The reasons and requirements for injecting CO<sub>2</sub> into deep saline aquifers have been discussed at length in Chapter 2. Therein, it was pointed out why numerical simulations can help in understanding the physical and thermodynamical processes during CO<sub>2</sub> injection and, thereupon, being able to make risk assessments by estimating the safety of the storage site.

In CO<sub>2</sub> sequestration, the CO<sub>2</sub> is injected with a high pressure into depths greater than 800 m to displace the reservoir water and to ensure the supercritical state of the CO<sub>2</sub>. Before the injected CO<sub>2</sub> dissolves into the reservoir water, it rises until it reaches the bottom of the cap-rock layer, due to its lower density compared to that of the water in place. Hence, a disturbance of the cap-rock layer, e. g., fracture, fault or inclination, leads to situations where the undissolved CO<sub>2</sub> might leak to the surface or ends up at surrounding physical conditions that lead to the phase change from supercritical to gas. The latter is accompanied by an expansion of the CO<sub>2</sub>, which can intensify the stress on the cap-rock layer, and thus, is an unwanted incident. This phase-change process is

simulated in the following model.

### 7.1.1 Injection into a reservoir with an inclined cap-rock layer

For the simulation of CO<sub>2</sub> injection into a water-filled reservoir, a three-phasic model (solid  $S$ , water  $L$ , CO<sub>2</sub>  $G$ ) is considered, where the first set of primary variables  $\mathbf{u}_1$  from (6.1) is chosen, consisting of the solid displacement  $\mathbf{u}_S$ , the effective water pressure  $p^{LR}$  and the effective CO<sub>2</sub> pressure  $p^{GR}$ . The temperature is omitted here as a degree of freedom since a constant temperature distribution is assumed, which is governed by the geothermal gradient  $\Delta_g\theta = 25.0$  K/km. The water is regarded as incompressible, whereas the CO<sub>2</sub> is modelled as compressible by calculating the effective CO<sub>2</sub> density  $\rho^{GR}$  by one single EOS. In this first simulation example, the mass transfer between the liquid and gaseous CO<sub>2</sub> phases is omitted, i. e.,  $\hat{\rho}^\alpha = 0$ . Since both CO<sub>2</sub> phases are modelled by one EOS alone, the phase change only becomes visible in the density jump.

To simulate phase-change occurrence during CO<sub>2</sub> injection into a deep aquifer, the simulation setup is made up of a section of the subsurface with the dimensions of 500 m width and a height that reaches from the surface to a depth of  $-850$  m. The model consists of two permeable reservoir layers, whereas the lower layer is enclosed between the impermeable cap- and base-rock layers. The cap-rock layer has an inclination that shifts its bottom boundary from  $-700$  m up to  $-500$  m, cf. Figure 7.1 (left). By modelling the whole reservoir body from surface to bottom also the weight of the water-filled overlying rock is considered in the simulation. The model is confined in horizontal direction and the vertical displacement is blocked at the bottom boundary. The temperature is assumed to be constant throughout the whole simulation and has a vertical gradient of  $\Delta_g\theta = 25.0$  K/km, starting with ambient temperature  $\theta = 283.15$  K at the surface boundary. Initially, a hydrostatic pressure distribution across the whole model is applied by defining hydrostatic pressure distributions at the right and left boundaries. The CO<sub>2</sub> is injected at the left boundary of the lower reservoir layer over a height of 10 m and 5 m above the top of the base-rock layer, cf. blue arrows in Figure 7.1 (left). The CO<sub>2</sub> is injected over a time period from  $t = 0$  min to  $t = 33.3$  min by setting a *Dirichlet* BC that increases the pressure of the CO<sub>2</sub> constituent up to  $p^{GR} = 7.85$  MPa. After the injection is stopped, the movement of the CO<sub>2</sub> is only triggered by buoyancy forces.

The material parameters used in this simulation were chosen on the basis of *Rutqvist & Tsang* [155], as well as of *Graf* [74] and are displayed in the table in Figure 7.1. Please note here that the initial intrinsic permeabilities  $K_{0S}^S$  and the *Lamé* parameters  $\lambda^S$  and  $\mu^S$  of the reservoir layers differ from that of the cap- and base-rock layers.

Concerning the mesh, initially a rather coarse elementation is applied, obeying the large dimensions of the model setup, cf. Figure 7.1 (left). To account for the moving front of the CO<sub>2</sub> plume as well as for the jump in density at phase change, a spatial mesh-adaptivity depending on the change in saturation  $s^G$  and effective CO<sub>2</sub> density  $\rho^{GR}$  is exerted, which significantly improves the numerical performance in these cases.

The results of the simulation are presented in Figure 7.2, where the partial pore density  $\rho_F^{CO_2} = s^G \rho^{GR}$  of the CO<sub>2</sub> phase is plotted for six characteristic times 30.57 min, 33.0 min,

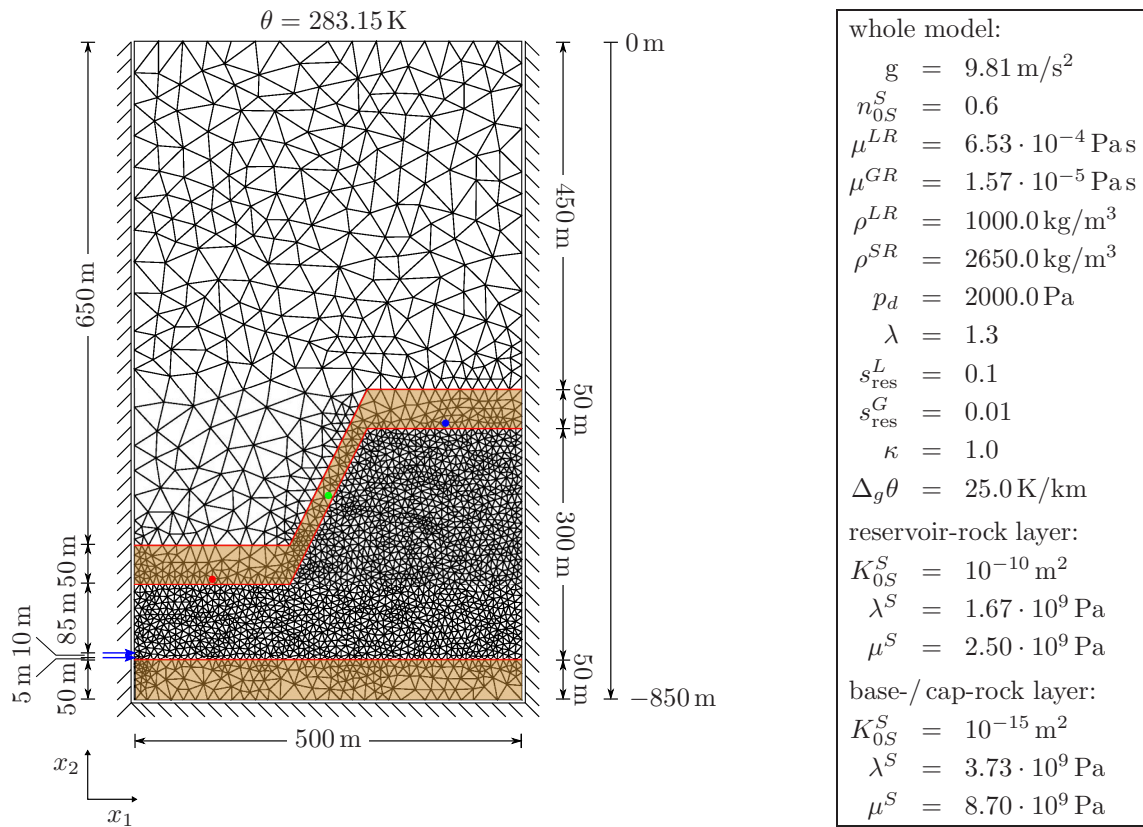


Figure 7.1: Geometry of the model to simulate CO<sub>2</sub> injection into a water-filled reservoir with an inclined cap-rock layer and a base-rock layer (light brown). The red, green and blue dots mark the places where the vertical displacement is measured for Figure 7.3. The table shows the applied material parameters with different intrinsic permeabilities and *Lamé* parameters for the reservoir-, base- and cap-rock layers.

34.80 min, 39.80 min, 42.22 min and 66.25 min. In chronological order, these show the entry of CO<sub>2</sub>, the spreading due to the injection pressure, further migration due to buoyancy forces along the bottom of the cap-rock layer after the injection is stopped, phase change from supercritical to gaseous CO<sub>2</sub> when the plume moves up along the inclination, the arrival at the upper part of the cap-rock layer, and the final stage when almost all CO<sub>2</sub> in its gaseous state is collected under the highest point of the reservoir layer. The point of phase change between the supercritical and the gaseous phase is clearly indicated by the sudden decrease in density from 600 kg/m<sup>3</sup> to around 150 kg/m<sup>3</sup> at a depth of roughly -675 m. It can also be noticed that the plume widens after the phase change, owed to the increase in specific volume of the gaseous CO<sub>2</sub>. Additionally, Figure 7.2 displays the seepage velocity of the CO<sub>2</sub> by black vectors. These show that the flow is highest when pressure or buoyancy forces are strong.

To investigate the solid deformation during the injection process, the vertical displacement  $u_{S2}$  in the cap-rock layer was monitored at three different positions, cf. red, green and blue points in Figure 7.1 (left), and plotted over time in Figure 7.3. Admittedly, the displacements are not large, which is due to the confining overburden pressure, but it

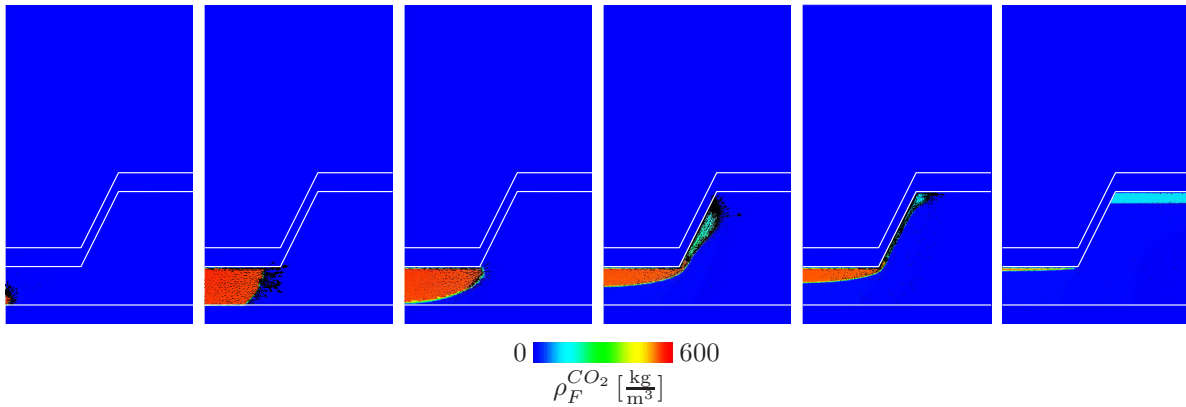


Figure 7.2: Result of the CO<sub>2</sub>-injection simulation at times 30.57 min, 33.65 min, 34.80 min, 39.80 min, 42.22 min and 66.25 min. The contour plot shows the partial pore density  $\rho_F^{CO_2} = s^G \rho^{GR}$  of the CO<sub>2</sub> phase and the black arrows indicate the partial seepage velocity of the CO<sub>2</sub> plume,  $\mathbf{w}_{CO_2 F} = s^G \mathbf{w}_G$ .

is still possible to find a connection between the migrating CO<sub>2</sub> plume and the solid deformations. For a better comparison, the dotted black lines in Figure 7.3 refer to the six time shots used in Figure 7.2. The first kink in the red curve can be attributed to the first appearance of CO<sub>2</sub> in the reservoir layer. The next apparent event is the shut-down of the injection at  $t = 33.3$  min. Hereby, a short delay between shutting down the injection and the change in the tangent of the vertical displacement is observed in Figure 7.3. The green line, which belongs to the second measuring point at the inclination of the cap-rock layer, shows that as soon as the plume has passed this point the displacement recedes back to zero. When a steady state is reached and the gaseous CO<sub>2</sub> is collected under the upper part of the cap-rock, the displacement remains constant for  $t > 60$  min, cf. blue line in Figure 7.3.

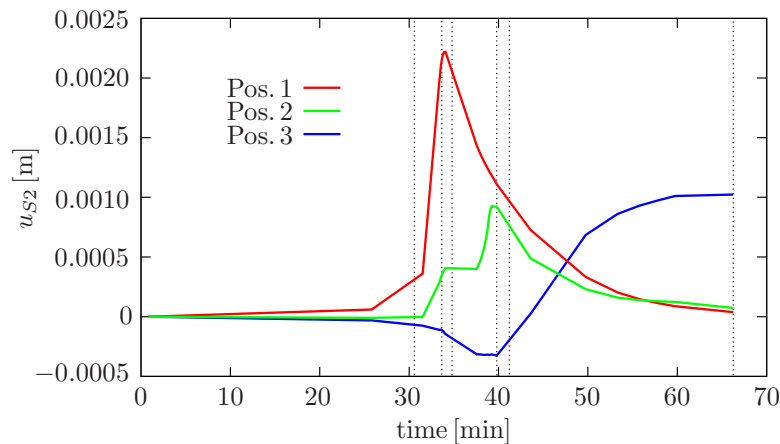


Figure 7.3: Evolution of the vertical displacement  $u_{S2}$  at three discrete positions just above the lower boundary of the cap-rock layer, cf. Figure 7.1. The dotted, vertical lines indicate the times used in Figure 7.2.

It becomes obvious that the phase-change process has a significant influence on CO<sub>2</sub>

sequestration and it is worth to investigate this in more detail. Since the  $\text{CO}_2$  is represented by just one mass balance in this current model, the phase transition is only visible in the change of  $\text{CO}_2$  density. Thus, this model is not capable of monitoring, for example, how much mass is transferred between the two phases and the influence of temperature changes on the phase-transition process. Consequently, in the upcoming section, the model is changed in a way that both fluid mass balances are used for the two  $\text{CO}_2$  phases, while omitting the water phase. These mass balances are coupled by the derived constitutive relation for the mass transfer. Furthermore, the energy balance is added to account for the change in temperature.

## 7.2 Phase transition and mass transfer during evaporation and condensation

This section presents the potential of the derived model of mass transfer during the phase transition of  $\text{CO}_2$  in a porous rock by conducting the simulation of evaporation and condensation in two academic examples. The somewhat constructed idea of the examples consists of a 2-d model of a  $\text{CO}_2$ -filled reservoir, where the  $\text{CO}_2$  has completely displaced the water. This reservoir is intersected by a well containing either high or low temperature fluids that heat or cool the reservoir, which in turn leads to the evaporation or condensation of the  $\text{CO}_2$ .

Please note here that in real  $\text{CO}_2$ -sequestration processes also the dissolution of  $\text{CO}_2$  in the saline water is of great importance. But since the focus lies here on single-substance phase transitions between pure phases, this effect is omitted.

The academic character of the example emanates from the fact that it does only demonstrate a fraction of the model's capabilities, since, e. g., the thermal induced deformations of sandstone are admittedly rather small. Furthermore, the example is composed of a simplified geometry with idealised BC. However, the material parameters and the thermodynamical conditions represent a realistic system. For the numerical implementation of the two examples, the second set of primary variables  $\mathbf{u}_2$ , cf. (6.2), is selected, which consists of the solid displacement  $\mathbf{u}_S$ , the total pore pressure  $p^{FR}$ , the liquid saturation  $s^L$  and the temperature  $\theta$ .

### 7.2.1 Evaporation around a hot pipe

This example of a hot pipe, or well intersecting a reservoir that is fully saturated with liquid  $\text{CO}_2$  tends to show the evaporation process due to heating. The simulation domain of 10 m x 10 m is composed of a thermoelastic porous solid filled initially with liquid  $\text{CO}_2$ ,  $s_0^L = 0.99$ . The liquid phase-state is guaranteed by the initial pore pressure of  $p_0^{FR} = 4.5$  MPa and the initial temperature of  $\theta_0 = 270$  K. To simulate a connection of the outer boundaries to a surrounding environment that also contains liquid  $\text{CO}_2$ , *Dirichlet* BC are applied at these boundaries for the pore pressure and the liquid saturation in the form of  $p^{FR} = 4.5$  MPa and  $s^L = 0.99$ , respectively. The simulation domain is chosen as a

quarter of the original setup, by taking advantage of the double symmetry. In this regard, the domain is confined in normal direction at the mirror boundaries and in horizontal and vertical direction at the curved boundary of the heating pipe with a radius 2 m, cf. Figure 7.4. At this heating pipe, indicated by the red-coloured part, a *Dirichlet* BC is applied, where the temperature is increased from  $\theta = 270$  K to  $\theta = 295$  K over 450 s and held constant thereafter. Furthermore, gravitational forces are omitted in this example.

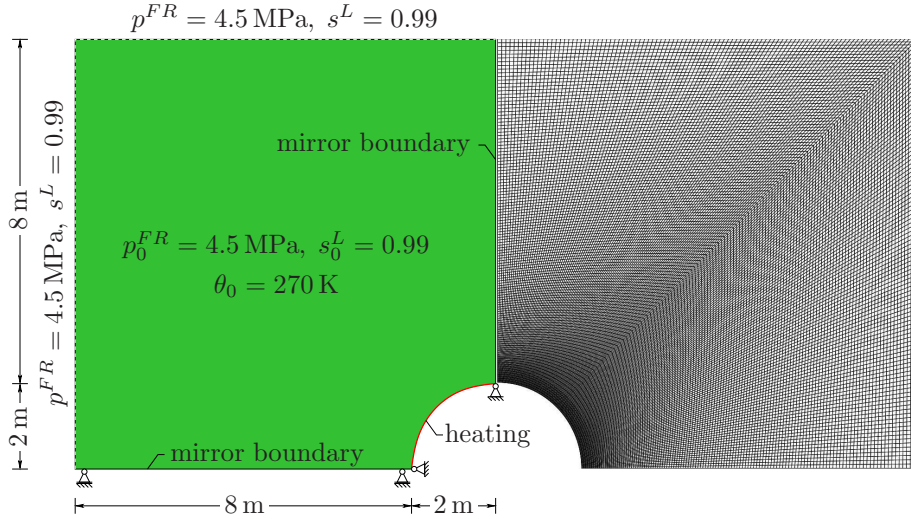


Figure 7.4: Simulation setup of a quarter of the double-symmetric domain (left) and the applied mesh (right).

The parameters used in this example are plotted in Table 7.1. The solid-material parameters resemble that of sandstone and were taken from *Graf* [74] and *Rutqvist et al.* [156]. For the fluid phases, i. e.,  $\text{CO}_2$ , the thermodynamic parameters stem from *Abbott & Ness* [1], whereas the relations derived in Chapter 4 are applied for the specific heat capacities  $c_V^{\beta R}$ , the vaporisation enthalpy  $\Delta\zeta_{\text{vap}}$ , the thermal conductivities  $H^{\beta R}$  and the shear viscosities  $\mu^{\beta R}$ .

Concerning the numerical implementation, a parallel solution technique is utilised, where PANDAS is included into the commercial FEM-program ABAQUS, cf. *Schenke & Ehlers* [158].

The results of the simulation are depicted in Figures 7.5 and 7.6 and visualise the evaporation of liquid  $\text{CO}_2$  due to heating. For each parameter, five snapshots are presented, taken during the simulation at times 3.3 min, 37.3 h, 91.6 h, 155.7 h and 255.7 h. By utilising the symmetry of the example, four parameters are concentrated into one picture, which also allows for a good understanding of the coupled effects between the respective parameters. The first set of pictures in Figure 7.5 shows in the upper left the changes in temperature  $\theta$  due to the applied cooling condition, the resulting gaseous mass production  $\hat{\rho}^G$  in the upper right, the gas saturation  $s^G$  in the lower left and the partial gas pore-density  $\rho_F^G := s^G \rho^{GR}$  in the lower right. When the evaporation temperature is reached, phase transition commences, the gas saturation increases and from the sudden changes in the partial pore-density of the gas  $\rho_F^G$  the proliferation of the gas front becomes obvious. Comparing the plots of the gas saturation  $s^G$  and the gas mass production  $\hat{\rho}^G$ , it can be clearly



Table 7.1: Parameters used for the 2-d simulation of evaporation in a porous sandstone.

initial solid volume fraction	$n_{0S}^S = 0.83$
effective densities	$\rho_{0S}^{SR} = 2650 \text{ kg/m}^3$
intrinsic permeability, permeability parameter	$K_{0S}^S = 1.3 \cdot 10^{-10} \text{ m}^2, \kappa = 1$
<i>Lamé</i> parameters	$\mu^S = 2.5 \cdot 10^9 \text{ Pa}, \lambda^S = 1.67 \cdot 10^9 \text{ Pa}$
thermal expansion coefficient	$\alpha^S = 1.2 \cdot 10^{-5} \text{ 1/K}$
medial grain diameter	$d_{50} = 6 \cdot 10^{-5} \text{ m}$
initial temperature	$\theta_0 = 270 \text{ K}$
<i>Brooks &amp; Corey</i> parameters	$p_d = 4000 \text{ Pa}, \lambda = 2.6$
residual saturations	$s_{\text{res}}^L = 0.01, s_{\text{res}}^G = 0.01$
thermodynamic parameters for CO <sub>2</sub>	$R^{\text{CO}_2} = 188.91 \text{ mJ/K}, \theta_{\text{crit}}^{\text{CO}_2} = 304.21 \text{ K}$ $p_{\text{crit}}^{\text{CO}_2\text{R}} = 7.38 \cdot 10^6 \text{ Pa}$
<i>Antoine</i> parameters for CO <sub>2</sub>	$A_A = 7.8101, B_A = 987.44, C_A = 290.9$
specific solid heat capacity	$c_V^S = 700 \text{ J/kgK}$
solid thermal conductivity	$H^S = 2000 \text{ W/mK}$

observed that the mass transfer only appears in the transition zone where both phases coexist, i. e., for intermediate saturations. Consequently, after complete evaporation and  $s^G = 1$ , the mass production stops.

The second set of pictures in Figure 7.6 contains the liquid saturation  $s^L$ , the liquid partial pore-density  $\rho_F^L$ , the interfacial area  $a_\Gamma$  and the pore pressure  $p^{FR}$ , from left to right and top to bottom. As expected, these show the decrease in liquid saturation and a change in liquid density from  $950 \text{ kg/m}^3$  to  $0 \text{ kg/m}^3$ . According to the saturation dependence of the interfacial area  $a_\Gamma$ , depicted in Figure 5.6 (right), the plot of  $a_\Gamma$  in Figure 7.6 indicates high values for intermediate saturations, which reflects the increase and decrease of the interfacial area during the phase-transition process. The increase in pore pressure  $p^{FR}$  is caused by the decrease in density, i. e., from a high liquid density of  $950 \text{ kg/m}^3$  to a low

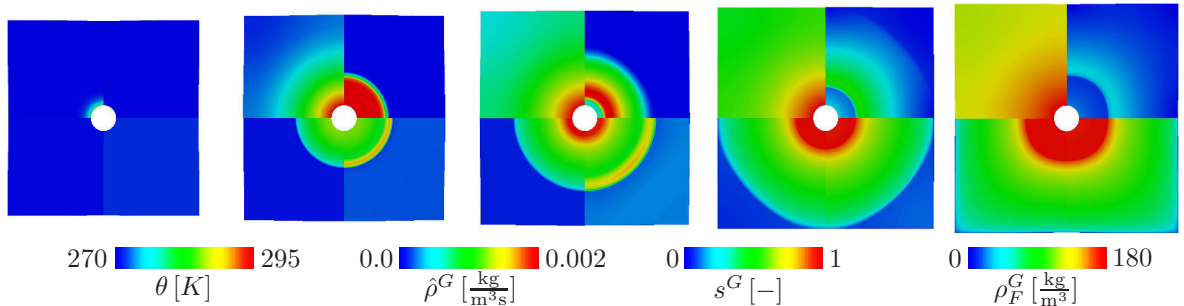


Figure 7.5: Results of the evaporation simulation at times 3.3 min, 37.3 h, 91.6 h, 155.7 h, 255.7 h. The depicted quantities are: upper-left: temperature  $\theta$ , upper-right: gaseous mass production  $\hat{\rho}^G$ , lower-left: gas saturation  $s^G$ , lower-right: gaseous partial pore-density  $\rho_F^G = s^G \rho^{GR}$ .

gas density of  $180 \text{ kg/m}^3$ , which is furthermore accompanied by an increase in volume. Last, a comparison between the different time shots reveals a dilatation of the overall system, which is also due to the increase in pore pressure.

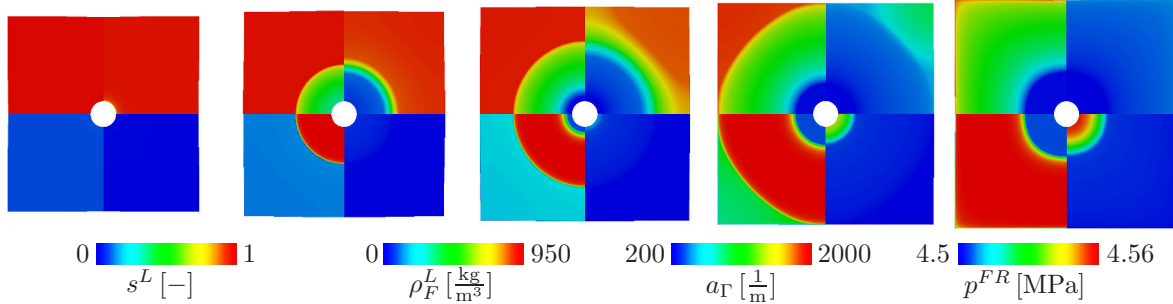


Figure 7.6: Results of the evaporation simulation at times 3.3 min, 37.3 h, 91.6 h, 155.7 h, 255.7 h. The depicted quantities are: upper-left: liquid saturation  $s^L$ , upper-right: liquid partial pore density  $\rho_F^L = s^L \rho^{LR}$ , lower-left: interfacial area  $a_\Gamma$ , lower-right: pore pressure  $p^{FR}$ .

## 7.2.2 Condensation

For the example of condensation of  $\text{CO}_2$  due to cooling, a pipe containing cool liquids crossing a reservoir is considered. As a representation thereof, a 2-d simulation domain of  $10 \text{ m} \times 10 \text{ m}$  is chosen that is composed of a thermoelastic porous solid and filled completely with gaseous  $\text{CO}_2$ ,  $s_0^L = 0.01$ , cf. Figure 7.7 (left). This example refers to the work of *Ehlers* and *Häberle* [61]. The gaseous state of the  $\text{CO}_2$  is guaranteed by an initial pore pressure of  $p_0^{FR} = 4.0 \text{ MPa}$  and an initial temperature of  $\theta_0 = 320 \text{ K}$ . The same pressure is applied as *Dirichlet* BC at the upper boundary in order to simulate an open boundary with a connection to a surrounding environment that also contains gaseous  $\text{CO}_2$ . Note in passing that the implied BC of  $s^L = 0.01$  at the upper boundary yields  $p^{FR} \approx p^{GR}$ . The domain is horizontally confined at the left and right boundaries and vertically confined at the bottom. Moreover, to induce the condensation process at the cool pipe, the blue-coloured part at the bottom and a width of  $2 \text{ m}$  is subjected to a temperature decrease from  $\theta = 320 \text{ K}$  to  $\theta = 200 \text{ K}$  over  $500 \text{ s}$  and held constant thereafter, as can be seen in Figure 7.7 (right). For a realistic simulation, the solid parameters resemble that of sandstone and are recorded in Table 7.2. The thermodynamic parameters of  $\text{CO}_2$  in Table 7.2 have been taken from *Abbott & Ness* [1], and fluid and solid parameters from *Graf* [74] and *Rutqvist et al.* [156]. The effective fluid shear viscosities are determined as a function of temperature and effective density given by *Fenghour et al.* [66], cf. Section 4.4.

The results of the simulation are depicted in Figures 7.8-7.12, which visualise the condensation of the gaseous  $\text{CO}_2$  in consequence of cooling. For each parameter, four snapshots are presented, taken during the simulation at times  $0 \text{ h}$ ,  $17.5 \text{ h}$ ,  $47.0 \text{ h}$  and  $82.8 \text{ h}$ . The change in temperature due to the applied cooling condition was already depicted in Figure 7.7 (right). Figure 7.8 shows the liquid mass production  $\hat{\rho}^L$  indicating the mass fraction that is transferred from the gaseous  $\text{CO}_2$  to the liquid  $\text{CO}_2$ . It can be clearly observed that the mass transfer only appears in the transition zone where both phases coexist. Note

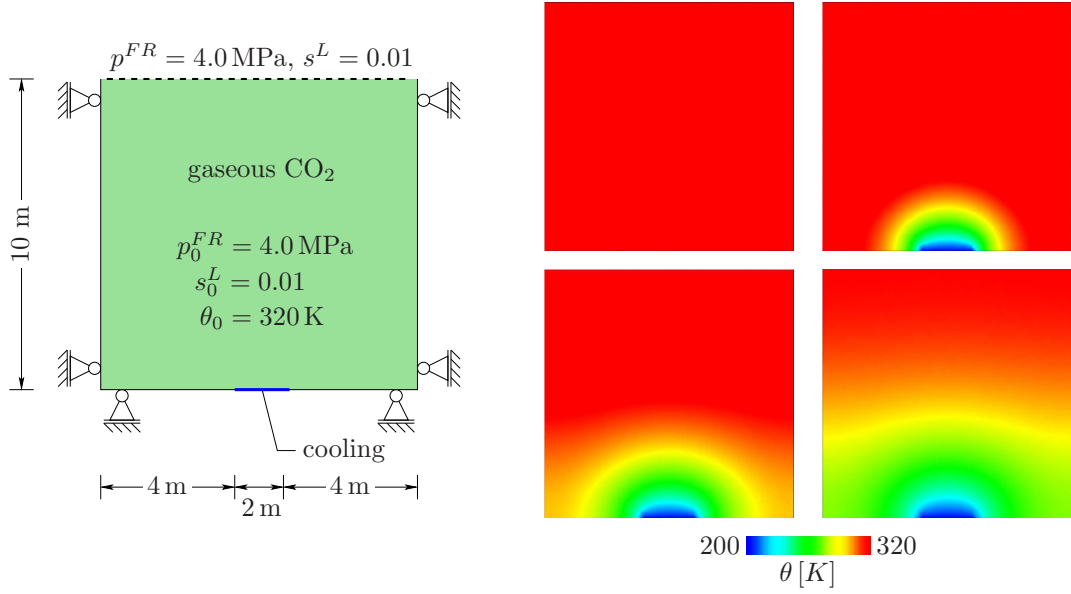


Figure 7.7: Simulation setup of the condensation example (left) and the temperature distribution  $\theta$  at times 0 h, 17.5 h, 47.0 h and 82.8 h (right).

Table 7.2: Parameters used for the 2-d simulation of CO<sub>2</sub> condensation in a porous sandstone.

initial solid volume fraction	$n_{0S}^S = 0.9$
effective densities	$\rho_{0S}^{SR} = 2650 \text{ kg/m}^3$
intrinsic permeability, permeability parameter	$K_{0S}^S = 1.3 \cdot 10^{-10} \text{ m}^2, \kappa = 1$
<i>Lamé</i> parameters	$\mu^S = 2.5 \cdot 10^9 \text{ Pa}, \lambda^S = 1.67 \cdot 10^9 \text{ Pa}$
thermal expansion coefficient	$\alpha^S = 1.2 \cdot 10^{-5} \text{ 1/K}$
medial grain diameter	$d_{50} = 6.0 \cdot 10^{-5} \text{ m}$
initial temperature	$\theta_0 = 320 \text{ K}$
<i>Brooks &amp; Corey</i> parameters	$p_d = 2000 \text{ Pa}, \lambda = 1.3$
residual saturations	$s_{\text{res}}^L = 0.01, s_{\text{res}}^G = 0.01$
thermodynamic parameters for CO <sub>2</sub>	$R^{\text{CO}_2} = 188.91 \text{ mJ/K}, \theta_{\text{crit}}^{\text{CO}_2} = 304.21 \text{ K}$
	$p_{\text{crit}}^{\text{CO}_2\text{R}} = 7.38 \cdot 10^6 \text{ Pa}$
<i>Antoine</i> parameters for CO <sub>2</sub>	$A_A = 7.8101, B_A = 987.44, C_A = 290.9$
specific heat capacities	$c_V^S = 700 \text{ J/(kg K)}, c_V^{LR} = 933.6 \text{ J/(kg K)}$
	$c_V^{GR} = 790.65 \text{ J/(kg K)}$
thermal conductivity of solid	$H^S = 2000 \text{ W/(m K)}$
thermal conductivity of CO <sub>2</sub>	$H^{\text{CO}_2\text{R}} = 0.26 \text{ W/(m K)}$

that this zone is indicated by the intermediate gas saturations  $s^G$  and  $s^L$ , depicted in Figures 7.10 and 7.11. Thus, after complete transition of the gaseous CO<sub>2</sub> to liquid CO<sub>2</sub>, the mass production vanishes. The saturation plots in Figures 7.10 and 7.11 also contain the

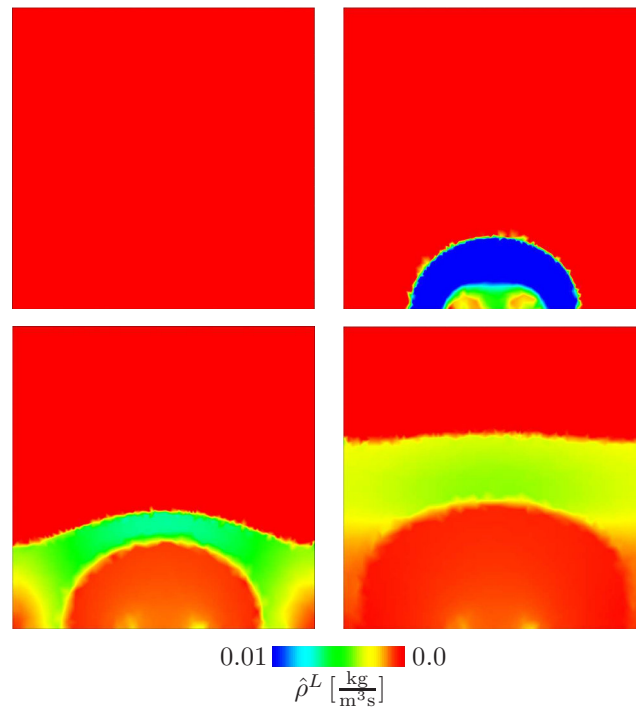


Figure 7.8: Liquid mass production  $\hat{\rho}^L$  at times 0 h, 17.5 h, 47.0 h and 82.8 h.

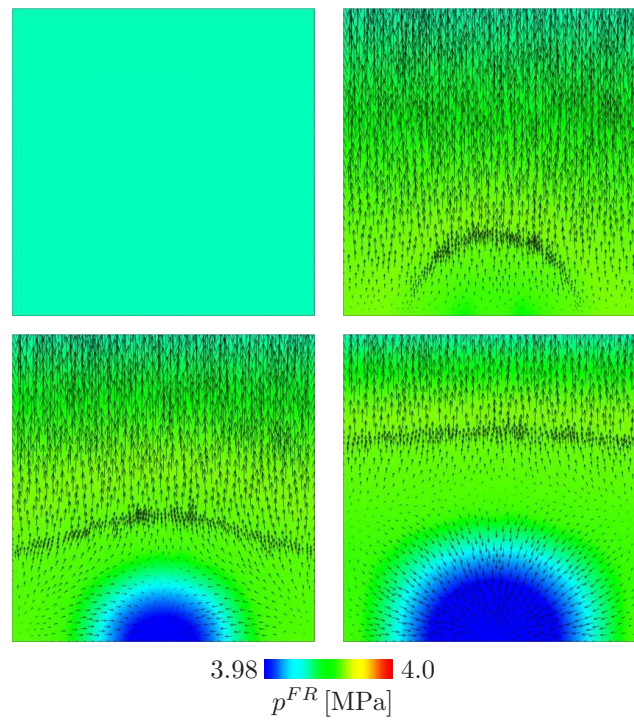


Figure 7.9: Pore pressure  $p^{FR}$  together with the solid displacement vector  $\mathbf{u}_S$  (black arrows) at times 0 h, 17.5 h, 47.0 h and 82.8 h.

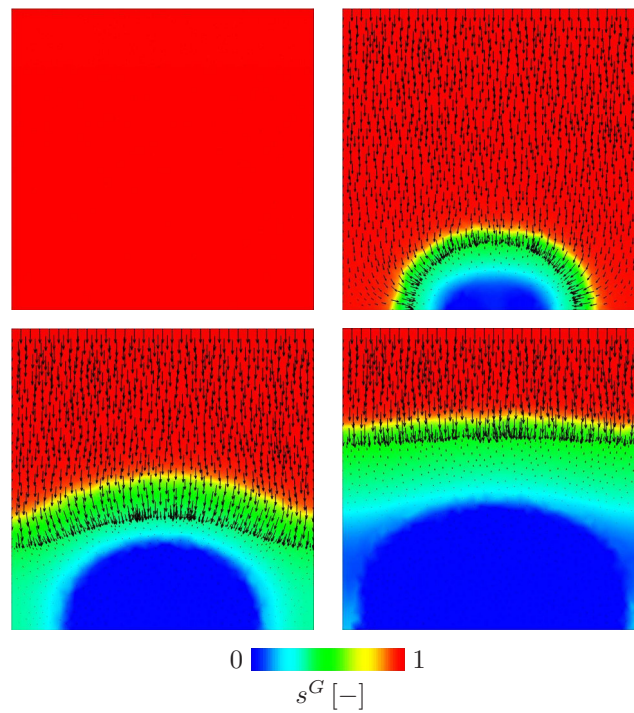


Figure 7.10: Gas saturation  $s^G$  and gaseous seepage-velocity vectors  $\mathbf{w}_G$  (black arrows) at times 0 h, 17.5 h, 47.0 h and 82.8 h.

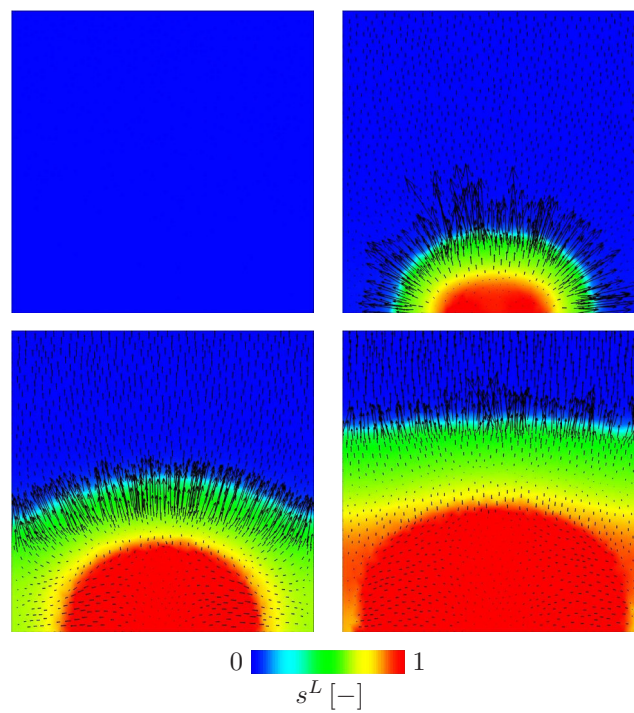


Figure 7.11: Liquid saturation  $s^L$  and liquid seepage-velocity vectors  $\mathbf{w}_L$  (black arrows) at times 0 h, 17.5 h, 47.0 h and 82.8 h.

gaseous and liquid seepage-velocity vectors,  $\mathbf{w}_G$  and  $\mathbf{w}_L$ , respectively. It can be seen that gaseous  $\text{CO}_2$  is replenished from the open boundary and liquid  $\text{CO}_2$  is fanning-out along the transition zone. Finally, Figure 7.12 shows the partial pore densities  $\rho_F^\beta := s^\beta \rho^{\beta R}$  of the two fluid phases. The figure illustrates the transition from gaseous  $\text{CO}_2$ , with a density of about  $110 \text{ kg/m}^3$ , to liquid  $\text{CO}_2$ , with a maximum density of  $1200 \text{ kg/m}^3$ . Consequently, this increase in density causes a drop in pore pressure  $p^{FR}$  that again affects the field of the solid-displacement vectors, represented by the black arrows in Figure 7.9. As anticipated, the plot exhibits a settlement zone around the cooling region.

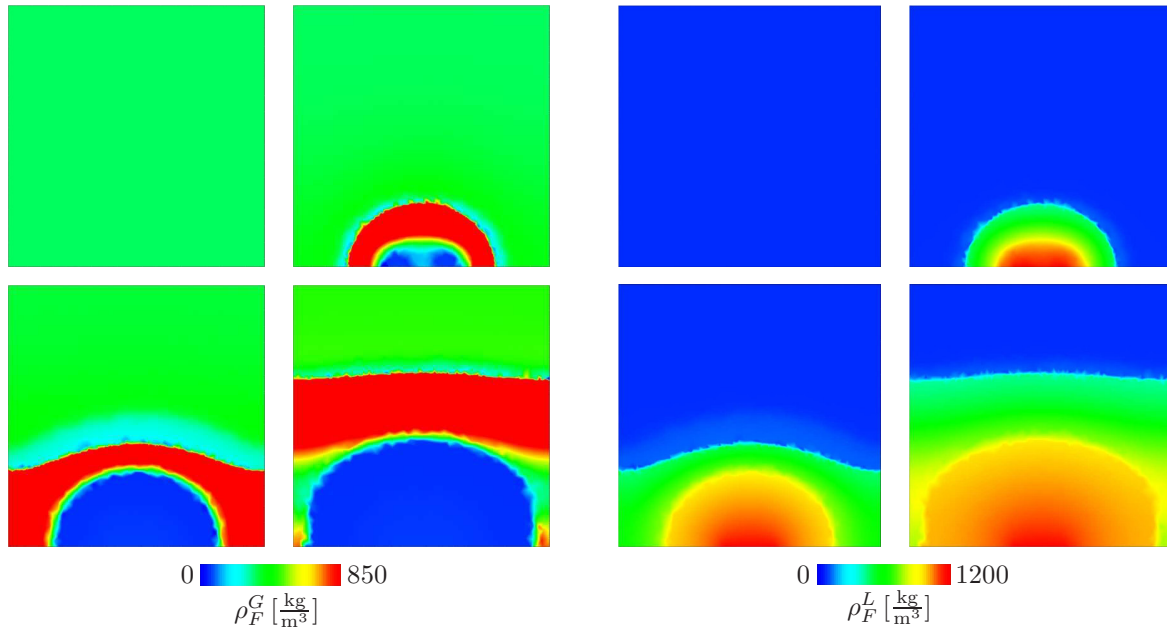


Figure 7.12: Partial pore density of the gaseous phase  $\rho_F^G = s^G \rho^{GR}$  (left) and partial pore density of the liquid phase  $\rho_F^L = s^L \rho^{LR}$  (right), each at times 0 h, 17.5 h, 47.0 h and 82.8 h.

# Chapter 8: Summary and Outlook

## 8.1 Summary

For the realisation of CO<sub>2</sub> sequestration into deep aquifers, it is essential to guarantee the safety and economic viability of the storage site. From the multitude of issues that concern the safety of the reservoir, the problems related to the thermodynamical behaviour of the CO<sub>2</sub> and the deformation of the porous rock were further investigated in this monograph. Numerical simulations have proven to be a helpful tool to predict the processes within the reservoir during CO<sub>2</sub> injection. In this regard, a reasonable model had to be developed including all physical and thermodynamical effects that govern the sequestration process. Therefore, an abundant continuum-mechanical model environment was found within the TPM, which enables the derivation of a multiphasic and multiphysics approach.

To illustrate the effects that the phase transition exerts on the solid deformation and the flow processes, a triphasic model was considered, consisting of the thermoelastic solid phase and two compressible fluid phases. The model was formulated such that the two fluid phases can either represent the immiscible phases of two different substances, e. g., water and CO<sub>2</sub>, or that the two fluid phases correspond to one single fluid matter, for instance CO<sub>2</sub>, and describe different phase states, e. g., gas and liquid.

Based on the exploitation of the entropy inequality, a thermodynamically consistent set of constitutive relations was derived, which specifies the physics of the CO<sub>2</sub> sequestration problem. Concerning the thermoelastic porous-rock matrix, a multiplicative split of the deformation tensor was applied and the resulting mechanical and thermal parts were described by a linear elastic (*Hookean*) law and by a thermal expansion relation, respectively. The fluid constituents percolating the porous solid were thermodynamically governed by an EOS to account for the compressible nature of the fluid phases, where the *van-der-Waals* equation was chosen. Furthermore, suitable definitions for the specific heat capacity, the thermal conductivity and the shear viscosity were included for a correct representation of the thermal behaviour of the fluid phases.

Special attention was paid to the phase-transition process between the gaseous and liquid phases of the fluid substance. In this regard, a microstructural description of the interface between the two fluid phases was based on the introduction of an immaterial, smooth singular surface. Thereby, additional jump conditions appeared in the balance relations of the fluid constituents that account for the jump over the interface. The evaluation of these jump conditions resulted in a constitutive relation of the mass transfer on the microstructure, depending on the heat flux and the latent heat of evaporation. The upscaling to the continuum-mechanical macroscale was then achieved by considering the interfacial area, i. e., the volume-specific area of the interface surface as a mapping function.

The strongly coupled partial differential equations were spatially discretised by mixed finite elements and an implicit *Euler* time-integration scheme governed the temporal dis-

cretisation. The monolithic solution of the partial differential equations was achieved by implementation into the in-house FE-program PANDAS. In some of the presented IBVP, it was also required to use an adaptive mesh refinement in order to account for the jump in density at the interface between the two fluid phases as well as for the moving CO<sub>2</sub> front. The coupling of PANDAS to the commercial FE-program ABAQUS that enables parallel computation, proved useful in the simulation of large-scale problems.

By the simulation of a CO<sub>2</sub> injection into a water-filled deep aquifer with realistic boundary conditions and parameters, it was possible to visualise the solid deformations of the cap-rock layer induced by the high injection pressure. Additionally, an inclination in the cap-rock layer showed the effects of buoyancy and the change between the supercritical and gaseous phases due to varying temperature and pressure conditions. Moreover, this also exhibited an influence on the solid deformations. In two further numerical examples, the phase-transition process caused by alternating temperature conditions was examined in more detail, both for evaporation and condensation. Hereby, the derived constitutive relation for the mass transfer, stemming from the assumption of a singular surface at the phase interface, was applied. Hence, a quantitative measure for the exchanged amount of mass between the fluid phases was established.

## 8.2 Outlook

At this state, the developed model is capable to describe a triphasic, thermoelastic porous-material model, e. g., for the simulation of CO<sub>2</sub> injection into a sandstone reservoir, including an elaborate description of the thermodynamics of the involved fluids, especially the phase transition. However, since in the model with explicit consideration of the mass transfer both fluid phases are already occupied by the gaseous and liquid phases of a single fluid matter, an extension to a four-phasic model, for instance, by adding water as an additional constituent, would allow for a wider field of applications. In this context, a further improvement in the sense of a realistic description of a CO<sub>2</sub> reservoir could be achieved by including dissolution effects between the various fluid matters. Within this mindset of a maximal accurate model for the physical conditions, also a formulation that accounts for separate temperatures of each constituents, instead of a single temperature, should be discussed. Of course, this would increase the set of governing equations by the respective energy balances and additional constitutive relations for the coupling between the latter. Furthermore, the so far thermoelastic behaviour of the solid material might be insufficient for a correct description of the solid displacements and, thus, could be expanded towards an elasto-plastic description, e. g., *Avci* [8]. While talking about solid deformation, the fracturing of the cap-rock layer poses a great threat to the safety of a CO<sub>2</sub> storage site. For the formulation of a model, which explicitly describes the crack propagation, one could either resort to extended finite elements (XFEM), cf. e. g., *Rempier* [146] and *Häberle & Ehlers* [77], or to phase-field models, for example *Luo & Ehlers* [111], as well as *Ehlers & Luo* [62].

Since the model, and especially the thermodynamical part, was formulated mostly independent of a specific fluid substance (except for the shear viscosity and thermal conduc-



tivity), it would be a simple task to apply the model to problems that concern different fluid matters. This could be achieved by changing the respective material parameters that govern, for example, the EOS or the capillary-pressure-saturation relation.

Furthermore, questions remain in the proposed model, for example in the definition of the interfacial area. To this extent, a rather simple approach was applied, but could be easily substituted by other definitions, e.g., *Nuske et al.* [130] and *Niessner & Hassanizadeh* [125]. The previously mentioned inclusion of dissolution processes would also affect the phase transition formulation, since in that case, no longer mass transfer between phases of a single substance is regarded, but the transfer between mixtures. The constitutive relation can then be directly derived from the entropy inequality, yielding a formulation similar to the two-film principle, as it was already briefly mentioned in Section 5.4.1.

Moreover, the exploitation of the entropy inequality revealed a problematic relationship between the thermodynamical consistent formulation of a model and the phenomenological relations needed therein, for example, in the derivation of the capillary-pressure-saturation relation or in the choice of an appropriate EOS. From the existing phenomenological relations, only few have a mathematical form that is compatible with the constitutive modelling procedure, i.e., the *Brooks & Corey*  $p^c$ - $s^L$ -relation and the *van-der-Waals* EOS. However, especially the latter relation has drawbacks in the correct description of the physical behaviour of the fluid. Thus, it would be necessary to find constitutive phenomenological relations that satisfy both the thermodynamical consistency and the descriptive accuracy.

Another issue represents the validation and verification of the developed model. Obviously, it is almost impossible to survey phase transitions of the  $\text{CO}_2$  in the deep aquifer, which makes the comparison of the model with real in situ data unfeasible. However, pore-scale experiments do exist and can also be observed by advanced imaging devices. In the context of this monograph, the contributions of *Shahraeeni* and *Or* [163, 164] should be mentioned here, which monitor the phase-transition process within a porous medium by synchrotron x-ray tomography. This might present a possibility to validate the developed model, which, in a further step, could be compared to benchmark problems, for example, by *Class et al.* [37].



# Appendix A: Selected relations of tensor calculus

An excerpt of important vector and tensor operations is collected within this appendix. The chosen collection is strongly restricted to relations which are particularly required in the presented monograph. In general, the relations are extracted from the comprehensive work of *Ehlers* [51], which is partly based on the fundamental textbook of *de Boer* [18].

## A.1 Tensor algebra

For the following considerations arbitrary **placeholders** are introduced, viz.:

$$\begin{aligned}
 \{\alpha, \beta\} &\in \mathbb{R} && : \text{scalars (zero-order tensors) as rational quantities,} \\
 \{\mathbf{a}, \mathbf{b}, \mathbf{c}\} &\in \mathcal{V}^3 && : \text{vectors (first-order tensors) of the proper} \\
 &&& \text{Euklidian 3-d vector space } \mathcal{V}^3, \\
 \{\mathbf{A}, \mathbf{B}, \mathbf{C}\} &\in \mathcal{V}^3 \otimes \mathcal{V}^3 && : \text{tensors (of second order) of the corresponding} \\
 &&& \text{dyadic product space } \mathcal{V}^3 \otimes \mathcal{V}^3.
 \end{aligned}$$

Collected rules for **products** of second-order tensors with scalars or vectors:

$$\begin{aligned}
 \alpha(\beta \mathbf{A}) &= (\alpha \beta) \mathbf{A} && : \text{associative law} \\
 \mathbf{A}(\alpha \mathbf{a}) &= \alpha(\mathbf{A} \mathbf{a}) = (\alpha \mathbf{A}) \mathbf{a} && : \text{associative law} \\
 (\alpha + \beta) \mathbf{A} &= \alpha \mathbf{A} + \beta \mathbf{A} && : \text{distributive law} \\
 \alpha(\mathbf{A} + \mathbf{B}) &= \alpha \mathbf{A} + \alpha \mathbf{B} && : \text{distributive law} \\
 \mathbf{A}(\mathbf{a} + \mathbf{b}) &= \mathbf{A} \mathbf{a} + \mathbf{A} \mathbf{b} && : \text{distributive law} \\
 (\mathbf{A} + \mathbf{B}) \mathbf{a} &= \mathbf{A} \mathbf{a} + \mathbf{B} \mathbf{a} && : \text{distributive law} \\
 \alpha \mathbf{A} &= \mathbf{A} \alpha && : \text{commutative law} \\
 \mathbf{a} &= \mathbf{A} \mathbf{b} && : \text{linear mapping} \\
 \mathbf{I} \mathbf{a} &= \mathbf{a} && : \mathbf{I} : \text{identical element (linear mapping)} \\
 \mathbf{0} \mathbf{a} &= \mathbf{0} && : \mathbf{0} : \text{zero element (linear mapping)}
 \end{aligned} \tag{A.1}$$

Collected rules for **scalar (inner) products** of tensors:

$$\begin{aligned}
(\alpha \mathbf{A}) \cdot \mathbf{B} &= \mathbf{A} \cdot (\alpha \mathbf{B}) = \alpha (\mathbf{A} \cdot \mathbf{B}) && : \text{associative law} \\
\mathbf{A} \cdot (\mathbf{B} + \mathbf{C}) &= \mathbf{A} \cdot \mathbf{B} + \mathbf{A} \cdot \mathbf{C} && : \text{distributive law} \\
\mathbf{A} \cdot \mathbf{B} &= \mathbf{B} \cdot \mathbf{A} && : \text{commutative law} \\
\mathbf{A} \cdot \mathbf{B} &= 0 \quad \forall \mathbf{A}, \text{ if } \mathbf{B} \equiv \mathbf{0} \\
\mathbf{A} \cdot \mathbf{A} &> 0 \quad \forall \mathbf{A} \neq \mathbf{0}
\end{aligned} \tag{A.2}$$

Collected rules for **tensor products** of second-order tensors:

$$\begin{aligned}
\alpha (\mathbf{A} \mathbf{B}) &= (\alpha \mathbf{A}) \mathbf{B} = \mathbf{A} (\alpha \mathbf{B}) && : \text{associate law} \\
(\mathbf{A} \mathbf{B}) \mathbf{a} &= \mathbf{A} (\mathbf{B} \mathbf{a}) && : \text{associate law} \\
(\mathbf{A} \mathbf{B}) \mathbf{C} &= \mathbf{A} (\mathbf{B} \mathbf{C}) && : \text{associate law} \\
\mathbf{A} (\mathbf{B} + \mathbf{C}) &= \mathbf{A} \mathbf{B} + \mathbf{A} \mathbf{C} && : \text{distributive law} \\
(\mathbf{A} + \mathbf{B}) \mathbf{C} &= \mathbf{A} \mathbf{C} + \mathbf{B} \mathbf{C} && : \text{distributive law} \\
\mathbf{A} \mathbf{B} &\neq \mathbf{B} \mathbf{A} && : \text{no commutative law} \\
\mathbf{I} \mathbf{A} &= \mathbf{A} \mathbf{I} = \mathbf{A} && : \mathbf{I} : \text{identical element (linear mapping)} \\
\mathbf{0} \mathbf{A} &= \mathbf{A} \mathbf{0} = \mathbf{0} && : \mathbf{0} : \text{zero element (linear mapping)}
\end{aligned} \tag{A.3}$$

Collected rules for **transposed** and **inverse** second-order tensors:

$$\begin{aligned}
(\mathbf{a} \otimes \mathbf{b})^T &= (\mathbf{b} \otimes \mathbf{a}) && \mathbf{A}^{-1} = (\det \mathbf{A})^{-1} (\text{cof } \mathbf{A})^T \\
(\alpha \mathbf{A})^T &= \alpha \mathbf{A}^T && \rightarrow \mathbf{A}^{-1} \text{ exists if } \det \mathbf{A} \neq 0 \\
(\mathbf{A} \mathbf{B})^T &= \mathbf{B}^T \mathbf{A}^T \\
\mathbf{a} \cdot (\mathbf{B} \mathbf{b}) &= (\mathbf{B}^T \mathbf{a}) \cdot \mathbf{b} && \mathbf{A} \mathbf{A}^{-1} = \mathbf{A}^{-1} \mathbf{A} = \mathbf{I} \\
\mathbf{A} \cdot (\mathbf{B} \mathbf{C}) &= (\mathbf{B}^T \mathbf{A}) \cdot \mathbf{C} && (\mathbf{A}^{-1})^T = (\mathbf{A}^T)^{-1} =: \mathbf{A}^{T-1} \\
(\mathbf{A} + \mathbf{B})^T &= \mathbf{A}^T + \mathbf{B}^T && (\mathbf{A} \mathbf{B})^{-1} = \mathbf{B}^{-1} \mathbf{A}^{-1}
\end{aligned} \tag{A.4}$$

The computation rules of the **determinant** and the **cofactor** are given via

$$\begin{aligned}
\det \mathbf{A} &= \frac{1}{6} (\mathbf{A} \ast \mathbf{A}) \cdot \mathbf{A} = \frac{1}{6} (\text{tr } \mathbf{A})^3 - \frac{1}{2} (\text{tr } \mathbf{A}) (\mathbf{A}^T \cdot \mathbf{A}) + \frac{1}{3} (\mathbf{A} \mathbf{A})^T \cdot \mathbf{A} \\
\text{cof } \mathbf{A} &= \frac{1}{2} \mathbf{A} \ast \mathbf{A}, \quad \text{where } \text{cof } \mathbf{A} = \frac{1}{2} (a_{ik} a_{no} e_{inj} e_{kop}) (\mathbf{e}_j \otimes \mathbf{e}_p) =: \overset{+}{a}_{jp} (\mathbf{e}_j \otimes \mathbf{e}_p)
\end{aligned}$$

can be evaluated using (A.8) and index notation. Thus, the coefficient matrix  $\overset{+}{a}_{jp}$  contains at each position  $(\cdot)_{jp}$  the corresponding subdeterminant, e. g.,  $\overset{+}{a}_{11} = a_{22} a_{33} - a_{23} a_{32}$ .

Collected rules for the **determinant** and the **inverse** of second-order tensors:

$$\begin{aligned}
 (\operatorname{cof} \mathbf{A})^T &= \operatorname{cof} \mathbf{A}^T & \det(\operatorname{cof} \mathbf{A}) &= (\det \mathbf{A})^2 \\
 \det \mathbf{A}^T &= \det \mathbf{A} & \det \mathbf{A}^{-1} &= (\det \mathbf{A})^{-1} \\
 \det(\mathbf{A} \mathbf{B}) &= \det \mathbf{A} \det \mathbf{B} & \det(\mathbf{A} + \mathbf{B}) &= \det \mathbf{A} + \operatorname{cof} \mathbf{A} \cdot \mathbf{B} + \\
 \det(\alpha \mathbf{A}) &= \alpha^3 \det \mathbf{A} & &+ \mathbf{A} \cdot \operatorname{cof} \mathbf{B} + \det \mathbf{B} \\
 \det \mathbf{I} &= 1 & &
 \end{aligned} \tag{A.5}$$

Collected rules for the **trace** operator of second-order tensors:

$$\begin{aligned}
 \operatorname{tr} \mathbf{A} &= \mathbf{A} \cdot \mathbf{I} & \operatorname{tr}(\alpha \mathbf{A}) &= \alpha \operatorname{tr} \mathbf{A} \\
 \operatorname{tr}(\mathbf{a} \otimes \mathbf{b}) &= \mathbf{a} \cdot \mathbf{b} & \operatorname{tr} \mathbf{A}^T &= \operatorname{tr} \mathbf{A} \\
 \operatorname{tr}(\mathbf{A} \mathbf{B}) &= \operatorname{tr}(\mathbf{B} \mathbf{A}) & \operatorname{tr}(\mathbf{A} \mathbf{B} \mathbf{C}) &= \operatorname{tr}(\mathbf{B} \mathbf{C} \mathbf{A}) \\
 &= \mathbf{A} \cdot \mathbf{B}^T = \mathbf{A}^T \cdot \mathbf{B} & &= \operatorname{tr}(\mathbf{C} \mathbf{A} \mathbf{B})
 \end{aligned} \tag{A.6}$$

The third-order **fundamental (Ricci) tensor** and the **axial vector**:

$$\begin{aligned}
 \mathbf{a} \times \mathbf{b} &= \overset{3}{\mathbf{E}}(\mathbf{a} \otimes \mathbf{b}) \quad : \text{ where } \overset{3}{\mathbf{E}} \text{ is the permutation tensor, cf. (A.8)} \\
 \mathbf{A} \times \mathbf{B} &= \overset{3}{\mathbf{E}}(\mathbf{A} \mathbf{B}^T) \quad : \text{ with the specific case } \mathbf{I} \times \mathbf{C} = \overset{3}{\mathbf{E}} \mathbf{C}^T = 2 \overset{A}{\mathbf{c}} \\
 \overset{A}{\mathbf{c}} &= \frac{1}{2} \overset{3}{\mathbf{E}} \mathbf{C}^T \quad : \text{ where } \overset{A}{\mathbf{c}} \text{ is the axial vector of } \mathbf{C}
 \end{aligned} \tag{A.7}$$

In index notation, the properties of the permutation tensor are given, viz.:

$$\begin{aligned}
 \overset{3}{\mathbf{E}} &= e_{ijk} (\mathbf{e}_i \otimes \mathbf{e}_j \otimes \mathbf{e}_k) \quad \text{with the "permutation symbol" } e_{ijk} \\
 e_{ijk} &= \begin{cases} 1 & : \text{ even permutation} \\ -1 & : \text{ odd permutation} \\ 0 & : \text{ double indexing} \end{cases} \longrightarrow \begin{cases} e_{123} = e_{231} = e_{312} = 1 \\ e_{321} = e_{213} = e_{132} = -1 \\ \text{all remaining } e_{ijk} \text{ vanish} \end{cases}
 \end{aligned} \tag{A.8}$$

## A.2 Tensor analysis

The **product rule** of derivatives of products of functions:

$$(\mathbf{a} \otimes \mathbf{b})' = \mathbf{a}' \otimes \mathbf{b} + \mathbf{a} \otimes \mathbf{b}' \quad \text{and} \quad (\mathbf{A} \mathbf{B})' = \mathbf{A}' \mathbf{B} + \mathbf{A} \mathbf{B}' \tag{A.9}$$

Collected **derivatives** of tensors and their invariants:

$$\begin{aligned}
\frac{\partial \mathbf{A}}{\partial \mathbf{A}} &= (\mathbf{I} \otimes \mathbf{I})^{\underline{23}} = \overset{4}{\mathbf{I}} & \frac{\partial \operatorname{tr} \mathbf{A}}{\partial \mathbf{A}} &= \mathbf{I} \\
\frac{\partial \mathbf{A}^T}{\partial \mathbf{A}} &= (\mathbf{I} \otimes \mathbf{I})^{\underline{24}} & \frac{\partial \det \mathbf{A}}{\partial \mathbf{A}} &= \operatorname{cof} \mathbf{A} = (\det \mathbf{A}) \mathbf{A}^{T-1} \\
\frac{\partial \mathbf{A}^{-1}}{\partial \mathbf{A}} &= -(\mathbf{A}^{-1} \otimes \mathbf{A}^{T-1})^{\underline{23}} & \frac{\partial \operatorname{cof} \mathbf{A}}{\partial \mathbf{A}} &= \det \mathbf{A} [(\mathbf{A}^{T-1} \otimes \mathbf{A}^{T-1}) - \\
& & & - (\mathbf{A}^{T-1} \otimes \mathbf{A}^{T-1})^{\underline{24}}]
\end{aligned} \tag{A.10}$$

Selected computation rules for the **gradient** and the **divergence** operators:

$$\begin{aligned}
\operatorname{grad}(\alpha \beta) &= \alpha \operatorname{grad} \beta + \beta \operatorname{grad} \alpha & \operatorname{div}(\mathbf{a} \otimes \mathbf{b}) &= \mathbf{a} \operatorname{div} \mathbf{b} + (\operatorname{grad} \mathbf{a}) \mathbf{b} \\
\operatorname{grad}(\alpha \mathbf{b}) &= \mathbf{b} \otimes \operatorname{grad} \alpha + \alpha \operatorname{grad} \mathbf{b} & \operatorname{div}(\alpha \mathbf{B}) &= \mathbf{B} \operatorname{grad} \alpha + \alpha \operatorname{div} \mathbf{B} \\
\operatorname{grad}(\alpha \mathbf{B}) &= \mathbf{B} \otimes \operatorname{grad} \alpha + \alpha \operatorname{grad} \mathbf{B} & \operatorname{div}(\mathbf{A} \mathbf{b}) &= (\operatorname{div} \mathbf{A}^T) \cdot \mathbf{b} + \mathbf{A}^T \cdot \operatorname{grad} \mathbf{b} \\
\operatorname{div}(\alpha \mathbf{b}) &= \mathbf{b} \cdot \operatorname{grad} \alpha + \alpha \operatorname{div} \mathbf{b} & \operatorname{div} \left( \frac{\mathbf{b}}{\alpha} \right) &= \frac{1}{\alpha} \operatorname{div} \mathbf{b} - \frac{1}{\alpha^2} \mathbf{b} \cdot \operatorname{grad} \alpha
\end{aligned} \tag{A.11}$$

# Appendix B: Thermodynamical supplements and specific evaluations

## B.1 Thermodynamic potentials and *Legendre* transformation

The fundamental thermodynamic potentials, namely the internal energy  $\varepsilon$ , the internal enthalpy  $\zeta$ , the *Helmholtz* free energy  $\psi$  and the *Gibbs* free enthalpy  $\xi$ , can be formulated by different variables, depending on the observed process. In solid mechanics usually the energetically conjugated variable pairs tension and strain  $\{\frac{1}{\rho_0} \mathbf{S}, \mathbf{E}\}$  and temperature and entropy  $\{\theta, \eta\}$  are used, while for the description of fluids the first pair is replaced by pressure and specific volume  $\{p, v\}$ . Therewith, the potentials read for the two kinds of observation:

$$\begin{aligned} \varepsilon(\mathbf{E}, \eta) &\rightarrow \varepsilon(v, \eta), \\ \zeta(\frac{1}{\rho_0} \mathbf{S}, \eta) &\rightarrow \zeta(p, \eta), \\ \psi(\mathbf{E}, \theta) &\rightarrow \psi(v, \theta), \\ \xi(\frac{1}{\rho_0} \mathbf{S}, \theta) &\rightarrow \xi(p, \theta). \end{aligned} \tag{B.1}$$

Please note that superscripts indicating a certain constituent were omitted here.

The *Legendre* transformations between the conjugated variables allows for a switch between the thermodynamic potentials. Exemplary, this is presented here for the transformation between  $\theta$  and  $\eta_{E \text{ mech.}}^S$ , which yields the definition of the *Helmholtz* free energy  $\psi^S$  based on the internal energy  $\varepsilon^S$ :

$$\begin{aligned} \dot{\varepsilon}^S(\mathbf{E}_S, \eta_{E \text{ mech.}}^S) &= \frac{\partial \varepsilon^S}{\partial \mathbf{E}_S} \cdot \dot{\mathbf{E}}_S + \frac{\partial \varepsilon^S}{\partial \eta_{E \text{ mech.}}^S} \dot{\eta}_{E \text{ mech.}}^S, \\ &= \frac{1}{\rho_0^S} \mathbf{S}^S \cdot \dot{\mathbf{E}}_S + \theta \dot{\eta}_{E \text{ mech.}}^S, \end{aligned} \tag{B.2}$$

where

$$\frac{1}{\rho_0^S} \mathbf{S}^S = \frac{\partial \varepsilon}{\partial \mathbf{E}_S} \quad \text{and} \quad \theta = \frac{\partial \varepsilon}{\partial \eta_{E \text{ mech.}}^S} \tag{B.3}$$

were applied. With

$$\theta \dot{\eta}_{E \text{ mech.}}^S = (\theta \eta_{E \text{ mech.}}^S) \cdot - \eta_{E \text{ mech.}}^S \dot{\theta} \tag{B.4}$$

it follows

$$\begin{aligned} \underbrace{(\varepsilon^S - \theta \eta_{E \text{ mech.}}^S)}_{=: \psi} \cdot &= \frac{1}{\rho_0} \mathbf{S}^S \cdot \dot{\mathbf{E}}_S - \eta_{E \text{ mech.}}^S \dot{\theta}, \\ \rightarrow \psi^S(\mathbf{E}_S, \theta) &= \varepsilon^S(\mathbf{E}_S, \eta_{E \text{ mech.}}^S) - \eta_{E \text{ mech.}}^S \theta. \end{aligned} \tag{B.5}$$

For a detailed discussion of the thermodynamical potentials and a summary of the various *Legendre* transformations the interested reader is referred to, e. g., *Ehlers* [48].

## B.2 *Maxwell* relations and fundamental relations

A list of thermodynamic formulas that are a consequence of the relations presented in B.1 and, which are important for the alternation between different energy expressions is presented, based on *Lewis & Randall* [105]:

<i>Maxwell</i> relations	energy-function derivatives
$\left(\frac{\partial\theta}{\partial v}\right)_\eta = -\left(\frac{\partial p}{\partial\eta}\right)_v$	$\left(\frac{\partial\varepsilon}{\partial\eta}\right)_v = \left(\frac{\partial\zeta}{\partial\eta}\right)_p = \theta$
$\left(\frac{\partial\theta}{\partial p}\right)_\eta = \left(\frac{\partial v}{\partial\eta}\right)_p$	$\left(\frac{\partial\varepsilon}{\partial v}\right)_\eta = \left(\frac{\partial\psi}{\partial v}\right)_\theta = -p$
$\left(\frac{\partial\eta}{\partial v}\right)_\theta = \left(\frac{\partial p}{\partial\theta}\right)_v$	$\left(\frac{\partial\zeta}{\partial p}\right)_\eta = \left(\frac{\partial\xi}{\partial p}\right)_\theta = v$
$\left(\frac{\partial\eta}{\partial p}\right)_\theta = -\left(\frac{\partial v}{\partial\theta}\right)_p$	$\left(\frac{\partial\xi}{\partial\theta}\right)_p = \left(\frac{\partial\psi}{\partial\theta}\right)_v = -\eta$

Since these relations are needed for the description of the thermodynamical behaviour of liquids and gases in Chapter 4, the formulations were written with respect to fluids. However, analogous formulas for solid constituents can be derived from the relations in B.1. Superscripts indicating a certain constituent were omitted.

## B.3 Derivation of the *Maxwell* criterion

The *Maxwell* criterion, briefly introduced in Section 4.1, is derived here based on *Baehr* [11]. The coexistence of both phases in the two-phase region requires the local phase equilibrium between the liquid and gas phase, i. e., the equilibrium of the respective chemical potentials:

$$\mu^L = \mu^G . \quad (\text{B.6})$$

With  $\mu^\beta = \psi^\beta + p^{\beta R} v^{\beta R}$  and  $\psi^\beta = \varepsilon^\beta - \theta^\beta \eta^\beta$ , it follows from (B.6)

$$\varepsilon^L - \theta^L \eta^L + p^{LR} v^{LR} = \varepsilon^G - \theta^G \eta^G + p^{GR} v^{GR} . \quad (\text{B.7})$$

Furthermore, Figure 4.6 shows that the two phases coexist at the constant vapour pressure  $p_{\text{vap}}^R$  for a given constant temperature  $\theta$ , cf. *Antoine* equation (4.19). This yields for (B.7):

$$\varepsilon^L - \theta \eta^L + p_{\text{vap}}^R v^{LR} = \varepsilon^G - \theta \eta^G + p_{\text{vap}}^R v^{GR} . \quad (\text{B.8})$$

Thus, it can be written after sorting and applying the *Legendre* transformation (3.49):

$$p_{\text{vap}}^R (v^{GR} - v^{LR}) = (\varepsilon^L - \theta \eta^L) - (\varepsilon^G - \theta \eta^G) = \psi^L - \psi^G . \quad (\text{B.9})$$



The differential of the *Helmholtz* free energy

$$d\psi^\beta = -p^{\beta R} dv - \eta^\beta d\theta , \quad (\text{B.10})$$

becomes for constant temperature  $\theta$

$$d\psi^\beta = -p^{\beta R}(\theta, v^{\beta R}) dv . \quad (\text{B.11})$$

The integration of (B.11) between  $v^{LR}$  and  $v^{GR}$  together with (B.9) finally delivers

$$p_{\text{vap}}^R (v^{GR} - v^{LR}) = \int_{v^{LR}}^{v^{GR}} p^{\beta R} dv . \quad (\text{B.12})$$

Geometrically, equation (B.12) formulates the determination of the vapour pressure  $p_{\text{vap}}^R(\theta)$  such that the grey indicated regions in Figure 4.6 have the same area.

## B.4 Derivation of overall mass balance

The overall mass balance is derived by adding up all constituent mass balances for  $\varphi^\alpha$ ,  $\alpha = \{S, L, G\}$ . This summation follows the constraints presented in Section 3.3. Starting from the specific balance equations of the constituents

$$\begin{aligned} (\rho^S)'_S + \rho^S \operatorname{div} \dot{\mathbf{x}}_S &= 0 , \\ (\rho^L)'_L + \rho^L \operatorname{div} \dot{\mathbf{x}}_L &= \hat{\rho}^L , \\ (\rho^G)'_G + \rho^G \operatorname{div} \dot{\mathbf{x}}_G &= \hat{\rho}^G , \end{aligned} \quad (\text{B.13})$$

the dependencies of the time derivatives of the fluid densities,  $(\rho^L)'_L$  and  $(\rho^G)'_G$ , are switched from the respective fluid constituents  $\varphi^\beta$  to the solid constituent  $\varphi^S$  using (3.15) and the fluid velocities,  $\dot{\mathbf{x}}_L$  and  $\dot{\mathbf{x}}_G$ , are treated by (3.14), which yields in total

$$\begin{aligned} (\rho^S)'_S + \rho^S \operatorname{div} (\mathbf{u}_S)'_S &= 0 , \\ (\rho^L)'_S + (\operatorname{grad} \rho^L) \cdot \mathbf{w}_L + \rho^L \operatorname{div} \mathbf{w}_L + \rho^L \operatorname{div} (\mathbf{u}_S)'_S &= \hat{\rho}^L , \\ (\rho^G)'_S + (\operatorname{grad} \rho^G) \cdot \mathbf{w}_G + \rho^G \operatorname{div} \mathbf{w}_G + \rho^G \operatorname{div} (\mathbf{u}_S)'_S &= \hat{\rho}^G , \end{aligned} \quad (\text{B.14})$$

where in addition  $\dot{\mathbf{x}}_S = (\mathbf{u}_S)'_S$  was used. In the next step, these three equations are added up under the conditions of  $\sum_\alpha \hat{\rho}^\alpha = 0$ ,  $\sum_\alpha \rho^\alpha = \rho$  and the rule for the divergence operator, cf. Appendix A, viz.:

$$(\rho)'_S + \operatorname{div} (\rho^L \mathbf{w}_L) + \operatorname{div} (\rho^G \mathbf{w}_G) + \rho \operatorname{div} (\mathbf{u}_S)'_S = 0 , \quad (\text{B.15})$$

which can be further summarised to

$$(\rho)'_S + \operatorname{div} (\rho^L \mathbf{w}_L + \rho^G \mathbf{w}_G) + \rho \operatorname{div} (\mathbf{u}_S)'_S = 0 . \quad (\text{B.16})$$

## B.5 Weak forms of the effective fluid mass-balance relations

For the first set of primary variables  $\mathbf{u}_1$  (6.1), the corresponding weak forms of the effective fluid mass balance relations read

$$\begin{aligned} \mathcal{G}_{p^{LR}}(\mathbf{u}_1, \delta p^{LR}) &= \int_{\Omega} \{(\rho^L)'_S + \rho^L \operatorname{div}(\mathbf{u}_S)'_S\} \delta p^{LR} \, dv - \int_{\Omega} \rho^L \mathbf{w}_L \cdot \operatorname{grad} \delta p^{LR} \, dv - \\ &\quad - \int_{\Omega} \hat{\rho}^L \delta p^{LR} \, dv + \int_{\Gamma_N^{\bar{v}^L}} \rho^L \mathbf{w}_L \cdot \mathbf{n} \delta p^{LR} \, da = 0, \\ \mathcal{G}_{p^{GR}}(\mathbf{u}_1, \delta p^{GR}) &= \int_{\Omega} \{(\rho^G)'_S + \rho^G \operatorname{div}(\mathbf{u}_S)'_S\} \delta p^{GR} \, dv - \int_{\Omega} \rho^G \mathbf{w}_G \cdot \operatorname{grad} \delta p^{GR} \, dv + \\ &\quad - \int_{\Omega} \hat{\rho}^G \delta p^{GR} \, dv + \int_{\Gamma_N^{\bar{v}^G}} \rho^G \mathbf{w}_G \cdot \mathbf{n} \delta p^{GR} \, da = 0. \end{aligned} \tag{B.17}$$

## B.6 Treatment of the stress terms of the overall energy balance

For the final formulation of the overall energy balance in (5.165) it is necessary to adapt the terms containing the *Cauchy* stress tensors in (5.27), i. e.,

$$\mathbf{T}^S \cdot \mathbf{L}_S + \mathbf{T}^L \cdot \mathbf{L}_L + \mathbf{T}^G \cdot \mathbf{L}_G. \tag{B.18}$$

Incorporating the definitions of the extra stresses (5.59) and (5.60), as well as  $\mathbf{L}_\alpha = \operatorname{grad} \dot{\mathbf{x}}_\alpha$ , yields

$$(\mathbf{T}_{E \text{ mech.}}^S - n^S p^{FR} \mathbf{I}) \cdot \operatorname{grad}(\mathbf{u}_S)'_S + (\mathbf{T}_{E \text{ dis.}}^L - n^L p^{LR} \mathbf{I}) \cdot \operatorname{grad} \dot{\mathbf{x}}_L + (\mathbf{T}_E^G - n^G p^{GR} \mathbf{I}) \cdot \operatorname{grad} \dot{\mathbf{x}}_G. \tag{B.19}$$

The extra stress terms of the fluid constituents can be neglected, cf. (5.70), and with  $\mathbf{I} \cdot \operatorname{grad}(\cdot) = \operatorname{div}(\cdot)$  one finds

$$\mathbf{T}_{E \text{ mech.}}^S \cdot \operatorname{grad}(\mathbf{u}_S)'_S - n^S p^{FR} \operatorname{div}(\mathbf{u}_S)'_S - n^L p^{LR} \operatorname{div} \dot{\mathbf{x}}_L - n^G p^{GR} \operatorname{div} \dot{\mathbf{x}}_G. \tag{B.20}$$

Next, with the relations between the volume fractions and saturations (3.4) and *Dalton's* law for the total pore pressure (5.57), the last three terms in (B.20) are reformulated to

$$\begin{aligned} &- (1 - n^F) p^{FR} \operatorname{div}(\mathbf{u}_S)'_S - n^L p^{LR} \operatorname{div} \dot{\mathbf{x}}_L - n^G p^{GR} \operatorname{div} \dot{\mathbf{x}}_G = \\ &= - p^{FR} \operatorname{div}(\mathbf{u}_S)'_S + (n^L p^{LR} + n^G p^{GR}) \operatorname{div} \dot{\mathbf{x}}_S - n^L p^{LR} \operatorname{div} \dot{\mathbf{x}}_L - n^G p^{GR} \operatorname{div} \dot{\mathbf{x}}_G = \\ &= - p^{FR} \operatorname{div}(\mathbf{u}_S)'_S - n^L p^{LR} \operatorname{div} \mathbf{w}_L - n^G p^{GR} \operatorname{div} \mathbf{w}_G, \end{aligned} \tag{B.21}$$

where in addition, the relation for the seepage velocities (3.14) was applied. Hence, the final formulation of the *Cauchy* stress tensor terms for the insertion into (5.165), reads

$$\mathbf{T}_{E\text{mech.}}^S \cdot \text{grad}(\mathbf{u}_S)'_S - p^{FR} \text{div}(\mathbf{u}_S)'_S - n^L p^{LR} \text{div} \mathbf{w}_L - n^G p^{GR} \text{div} \mathbf{w}_G. \quad (\text{B.22})$$

## B.7 Simplification of the direct momentum and mass production terms in the energy balance of the overall aggregate

It is convenient to combine the direct momentum and mass production terms in the energy balance of the overall aggregate (5.26):

$$\begin{aligned} \dots - \hat{\mathbf{p}}^S \cdot \dot{\mathbf{x}}_S - \hat{\mathbf{p}}^L \cdot \dot{\mathbf{x}}_L - \hat{\mathbf{p}}^G \cdot \dot{\mathbf{x}}_G - \\ - \hat{\rho}^S (\varepsilon^S + \frac{1}{2} \dot{\mathbf{x}}_S \cdot \dot{\mathbf{x}}_S) - \hat{\rho}^L (\varepsilon^L + \frac{1}{2} \dot{\mathbf{x}}_L \cdot \dot{\mathbf{x}}_L) - \hat{\rho}^G (\varepsilon^G + \frac{1}{2} \dot{\mathbf{x}}_G \cdot \dot{\mathbf{x}}_G). \end{aligned} \quad (\text{B.23})$$

Writing (3.36)<sub>1</sub> for the three constituents  $\varphi^S$ ,  $\varphi^L$  and  $\varphi^G$  while using (3.35)<sub>2</sub> yields

$$\hat{\mathbf{p}}^S + \hat{\mathbf{p}}^L + \hat{\mathbf{p}}^G + \hat{\rho}^S \dot{\mathbf{x}}_S + \hat{\rho}^L \dot{\mathbf{x}}_L + \hat{\rho}^G \dot{\mathbf{x}}_G = \mathbf{0}. \quad (\text{B.24})$$

After scalar multiplication of (B.24) by  $\dot{\mathbf{x}}_S$  it is added to (B.23), where also the definition of the seepage velocities (3.14) is exploited:

$$\begin{aligned} \dots - \hat{\mathbf{p}}^L \cdot \mathbf{w}_L - \hat{\mathbf{p}}^G \cdot \mathbf{w}_G + \hat{\rho}^S \dot{\mathbf{x}}_S \cdot \dot{\mathbf{x}}_S + \hat{\rho}^L \dot{\mathbf{x}}_L \cdot \dot{\mathbf{x}}_S + \hat{\rho}^G \dot{\mathbf{x}}_G \cdot \dot{\mathbf{x}}_S - \\ - \hat{\rho}^S (\varepsilon^S + \frac{1}{2} \dot{\mathbf{x}}_S \cdot \dot{\mathbf{x}}_S) - \hat{\rho}^L (\varepsilon^L + \frac{1}{2} \dot{\mathbf{x}}_L \cdot \dot{\mathbf{x}}_L) - \hat{\rho}^G (\varepsilon^G + \frac{1}{2} \dot{\mathbf{x}}_G \cdot \dot{\mathbf{x}}_G). \end{aligned} \quad (\text{B.25})$$

With the relation  $\sum_\alpha \hat{\rho}^\alpha = 0$  the third term in (B.25) becomes:

$$\hat{\rho}^S \dot{\mathbf{x}}_S \cdot \dot{\mathbf{x}}_S = -\hat{\rho}^L \dot{\mathbf{x}}_S \cdot \dot{\mathbf{x}}_S - \hat{\rho}^G \dot{\mathbf{x}}_S \cdot \dot{\mathbf{x}}_S. \quad (\text{B.26})$$

Next, the binomial formula is applied for the kinematical terms containing either  $\hat{\rho}^L$  or  $\hat{\rho}^G$ :

$$\begin{aligned} -\hat{\rho}^L \dot{\mathbf{x}}_S \cdot \dot{\mathbf{x}}_S + \hat{\rho}^L \dot{\mathbf{x}}_L \cdot \dot{\mathbf{x}}_S - \hat{\rho}^L \frac{1}{2} \dot{\mathbf{x}}_L \cdot \dot{\mathbf{x}}_L = -\hat{\rho}^L \frac{1}{2} \mathbf{w}_L \cdot \mathbf{w}_L - \hat{\rho}^L \frac{1}{2} \dot{\mathbf{x}}_S \cdot \dot{\mathbf{x}}_S, \\ -\hat{\rho}^G \dot{\mathbf{x}}_S \cdot \dot{\mathbf{x}}_S + \hat{\rho}^G \dot{\mathbf{x}}_G \cdot \dot{\mathbf{x}}_S - \hat{\rho}^G \frac{1}{2} \dot{\mathbf{x}}_G \cdot \dot{\mathbf{x}}_G = -\hat{\rho}^G \frac{1}{2} \mathbf{w}_G \cdot \mathbf{w}_G - \hat{\rho}^G \frac{1}{2} \dot{\mathbf{x}}_S \cdot \dot{\mathbf{x}}_S, \end{aligned} \quad (\text{B.27})$$

where again (3.14) was used. Under the consideration of  $\hat{\rho}^S \equiv 0$  and  $\hat{\rho}^L = -\hat{\rho}^G$  the two equations in (B.27) add up to  $\hat{\rho}^L (\frac{1}{2} \mathbf{w}_G \cdot \mathbf{w}_G - \frac{1}{2} \mathbf{w}_L \cdot \mathbf{w}_L)$ . Thus, the simplified form of (B.23) reads:

$$\dots - \hat{\mathbf{p}}^L \cdot \mathbf{w}_L - \hat{\mathbf{p}}^G \cdot \mathbf{w}_G + \hat{\rho}^L [\varepsilon^G - \varepsilon^L + \frac{1}{2} (\mathbf{w}_G \cdot \mathbf{w}_G - \mathbf{w}_L \cdot \mathbf{w}_L)]. \quad (\text{B.28})$$

## B.8 Calculation of different versions of the liquid momentum production

The result of the liquid momentum production (5.62), i. e., the two right-most terms, can be varied by the relations of the volume fractions (3.3)<sub>2</sub>, saturations (3.4) and capillary pressure (5.52), via:

$$\begin{aligned}
\hat{\mathbf{p}}^L &= \hat{\mathbf{p}}_{E \text{ dis.}}^L + \mathcal{P} \text{grad } n^L - \frac{s^L}{n^F} \rho^L \frac{\partial \psi^L}{\partial s^L} \text{grad } n^S \\
\rightarrow \hat{\mathbf{p}}^L &= \hat{\mathbf{p}}_{E \text{ dis.}}^L + p^{GR} \text{grad } n^L + p^c s^L \text{grad } n^S, \\
\rightarrow \hat{\mathbf{p}}^L &= \hat{\mathbf{p}}_{E \text{ dis.}}^L + p^{LR} \text{grad } n^L + p^c (s^G \text{grad } n^L - s^L \text{grad } n^G), \\
\rightarrow \hat{\mathbf{p}}^L &= \hat{\mathbf{p}}_{E \text{ dis.}}^L + p^{LR} \text{grad } n^L + p^c n^F \text{grad } s^L.
\end{aligned} \tag{B.29}$$

## B.9 Justifying the assumption of an overall temperature for all constituents

Here, the duration for the assimilation between the temperatures of two constituents (with different initial temperatures) is examined in order to justify the assumption of the usage of only one single overall temperature for all constituents. Since the numerical examples in this work consider mostly (except for the CO<sub>2</sub> injection into a water filled reservoir example, cf. Section 7.1) conditions, where only one single fluid phase exists inside the porous solid structure, it is chosen here to investigate the temperature assimilation between a solid phase  $\varphi^S$  (sandstone) and a fluid phase  $\varphi^F$  (CO<sub>2</sub>).

The starting point for the justification procedure are the constituent energy balances of the two constituents  $\varphi^S$  and  $\varphi^F$ , cf. (3.45):

$$\begin{aligned}
\rho^S (\varepsilon^S)'_S - \mathbf{T}^S \cdot \mathbf{L}_S + \text{div } \mathbf{q}^S - \rho^S r^S - \hat{\varepsilon}^S &= 0, \\
\rho^F (\varepsilon^F)'_F - \mathbf{T}^F \cdot \mathbf{L}_F + \text{div } \mathbf{q}^F - \rho^F r^F - \hat{\varepsilon}^F &= 0.
\end{aligned} \tag{B.30}$$

Since this examination is only concerned about the assimilation of the two temperatures  $\theta^S$  and  $\theta^F$ , a non deformable ( $\mathbf{L}_\alpha = \mathbf{0}$ ), flow-free ( $\dot{\mathbf{x}}_\alpha = \mathbf{0}$ ), heat-flux-free ( $\mathbf{q}^\alpha = \mathbf{0}$ ), radiance-free ( $r^\alpha = 0$ ) system with incompressible constituents ( $\rho^{\alpha R} = \text{const.}$ ) is considered, which simplifies (B.30) towards:

$$\begin{aligned}
\rho^S (\varepsilon^S)' - \hat{\varepsilon}^S &= 0, \\
\rho^F (\varepsilon^F)' - \hat{\varepsilon}^F &= 0,
\end{aligned} \tag{B.31}$$

where also the subscripts for the indication of the observer of the time derivative can be omitted, due to the negligence of solid deformations. Regarding the first terms in (B.31), while considering  $\varepsilon^\alpha = \psi^\alpha + \theta^\alpha \eta^\alpha$  and the relation between the entropy and the *Helmholtz*

free energy

$$\eta^\alpha = -\frac{\partial\psi^\alpha}{\partial\theta^\alpha}, \quad (\text{B.32})$$

yields:

$$\begin{aligned} \rho^\alpha (\varepsilon^\alpha)' &= \rho^\alpha (\psi^\alpha + \theta^\alpha \eta^\alpha)' = \rho^\alpha (\psi^\alpha)' + \rho^\alpha (\theta^\alpha)' \eta^\alpha + \rho^\alpha \theta^\alpha (\eta^\alpha)' = \\ &= -\rho^\alpha \frac{\partial\psi^\alpha}{\partial\theta^\alpha} (\theta^\alpha)' + \rho^\alpha (\theta^\alpha)' \eta^\alpha + \rho^\alpha \theta^\alpha (\eta^\alpha)' = \\ &= -\rho^\alpha \eta^\alpha (\theta^\alpha)' + \rho^\alpha (\theta^\alpha)' \eta^\alpha + \rho^\alpha \theta^\alpha (\eta^\alpha)' = \\ &= \rho^\alpha \theta^\alpha (\eta^\alpha)' = \rho^\alpha \theta^\alpha \frac{\partial\eta^\alpha}{\partial\theta^\alpha} (\theta^\alpha)' = \rho^\alpha c_V^{\alpha R} (\theta^\alpha)', \end{aligned} \quad (\text{B.33})$$

where in the last step the relation for the specific heat was used:

$$c_V^{\alpha R} = \theta^\alpha \frac{\partial\eta^\alpha}{\partial\theta^\alpha}. \quad (\text{B.34})$$

The second terms in (B.31) symbolise the direct energy productions  $\hat{\varepsilon}^\alpha$  that describe the caloric interactions between the two constituents, governed by the temperature difference between them. Thus, following the result for the direct energy production gained by *Ghadiani* [71] and *Graf* [74] by exploiting the dissipation inequality, furthermore using (3.35)<sub>4</sub> and (3.36)<sub>3</sub> and neglecting the terms with  $\dot{\mathbf{x}}_\alpha$  and  $\hat{\rho}^\alpha$  for a flow-free and non-reacting system, the constitutive relations for  $\hat{\varepsilon}^S$  and  $\hat{\varepsilon}^F$  read:

$$\hat{\varepsilon}^S = -\hat{\varepsilon}^F = -a_{SF} k_{SF}^\varepsilon (\theta^S - \theta^F), \quad (\text{B.35})$$

wherein,  $a_{SF}$  is the interfacial area between the solid and the fluid and  $k_{SF}^\varepsilon$  represents the surface-specific heat-exchange coefficient.

Merging (B.33) and (B.35) together in (B.31) and using  $\rho^\alpha = n^\alpha \rho^{\alpha R}$ , yields:

$$\begin{aligned} n^S \rho^{SR} c_V^S (\theta^S)' + a_{SF} k_{SF}^\varepsilon (\theta^F - \theta^F) &= 0, \\ n^F \rho^{FR} c_V^{FR} (\theta^F)' - a_{SF} k_{SF}^\varepsilon (\theta^S - \theta^F) &= 0. \end{aligned} \quad (\text{B.36})$$

After sorting the constant parts and replacing them by

$$A^\varepsilon = -\frac{a_{SF} k_{SF}^\varepsilon}{n^S \rho^{SR} c_V^S} \quad \text{and} \quad B^\varepsilon = \frac{a_{SF} k_{SF}^\varepsilon}{n^F \rho^{FR} c_V^{FR}}, \quad (\text{B.37})$$

it follows:

$$\begin{aligned} (\theta^S)' &= A^\varepsilon (\theta^S - \theta^F), \\ (\theta^F)' &= B^\varepsilon (\theta^S - \theta^F). \end{aligned} \quad (\text{B.38})$$

The decrease of the temperature difference  $\Delta\theta_{SF} = \theta^S - \theta^F$  over time indicates the duration of the temperature assimilation. Therewith, the two equations in (B.38) can be combined to

$$(\Delta\theta_{SF})' = (\theta^S)' - (\theta^F)' = (A^\varepsilon - B^\varepsilon) (\theta^S - \theta^F). \quad (\text{B.39})$$

This is a differential equation of the form  $(\dot{\cdot}) = y(\cdot)$ , for which an analytic solution can be found with the ansatz  $(\cdot) = (\cdot)_0 e^{\lambda t}$ . Applying this approach to (B.39) provides:

$$\Delta\theta_{SF} = (\Delta\theta_{SF})_0 \exp\left\{ [A^\varepsilon - B^\varepsilon] t \right\} = (\Delta\theta_{SF})_0 \exp\left\{ \left[ -\frac{a_{SF} k_{SF}^\varepsilon}{n^S \rho^{SR} c_V^S} - \frac{a_{SF} k_{SF}^\varepsilon}{n^F \rho^{FR} c_V^{FR}} \right] t \right\}. \quad (\text{B.40})$$

Therein,  $(\Delta\theta_{SF})_0$  is the initial temperature difference between the two constituents, which should decrease over a short time, in order to justify the assumption of a single overall temperature. The interfacial area  $a_{SF}$  is calculated based on the procedure and assumptions presented in Section 5.4.2, where the important relations read:

$$a_{SF} = n^F \frac{A^F}{V^F} = n^F \frac{4\pi (\tilde{r}^F)^2}{\frac{4}{3}\pi (\tilde{r}^F)^3} = \frac{3n^F}{\tilde{r}^F} \quad \text{and} \quad \tilde{r}^F = \frac{1}{2} \left( \frac{n^F}{n^S} \right)^{1/3} d_{50}. \quad (\text{B.41})$$

The remaining coefficients are taken as:  $n^S = 0.6$ ,  $n^F = 0.4$ ;  $d_{50} = 0.00006$ ,  $k_{SF}^\varepsilon = 10.0 \text{ W}/(\text{m}^2 \text{ K})$ ,  $\rho^{SR} = 2650.0 \text{ kg}/\text{m}^3$ ,  $\rho^{FR} = 900.0 \text{ kg}/\text{m}^3$ ,  $c_V^S = 700.0 \text{ J}/(\text{kg K})$  and  $c_V^{FR} = 950.0 \text{ J}/(\text{kg K})$ , representing sandstone and  $\text{CO}_2$ .

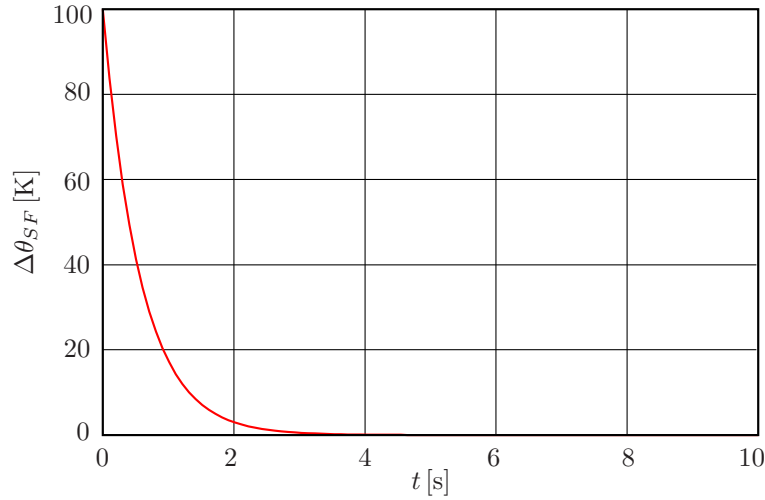


Figure B.1: Temperature assimilation of  $\text{CO}_2$  and sandstone over time, with initial temperature difference of 100 K.

Therewith, (B.40) is plotted over time, for an initial temperature difference of  $(\Delta\theta_{SF})_0 = 100 \text{ K}$ . Figure B.1 shows that after less than 4s both constituents have reached equal temperatures. This short assimilation time clearly justifies the assumption of a single overall temperature  $\theta = \theta^\alpha$  for all constituents for the purposes of this monograph.

## B.10 Real solutions of a cubic equation in case of the *van-der-Waals* EOS

The vdW-EOS introduced in Chapter 4 is a cubic EOS that reads:

$$p^{\beta R} = \frac{R^\beta \theta \rho^{\beta R}}{1 - b \rho^{\beta R}} - a (\rho^{\beta R})^2, \quad (\text{B.42})$$

where  $R^\beta$  is the specific gas constant and  $a$  and  $b$  are material parameters depending on the critical pressure and temperature of the respective substance (e.g.,  $\text{CO}_2$ ), cf. Chapter 4. The vdW-EOS is used in this monograph to calculate the effective density  $\rho^{\beta R}$  from the effective pressure  $p^{\beta R}$  and the temperature  $\theta$ . Hence, it is necessary to find the real solutions for  $\rho^{\beta R}$  by solving the cubic equation (B.42). Here, this is accomplished based on the procedure presented in *Numerical Recipes* by *Press et al.* [140].

In a first step, (B.42) is written with respect to the density as follows

$$\underbrace{ab}_{A_c} (\rho^{\beta R})^3 - \underbrace{a}_{B_c} (\rho^{\beta R})^2 + \underbrace{(R^\beta \theta + b p^{\beta R})}_{C_c} \rho^{\beta R} - \underbrace{p^{\beta R}}_{D_c} = 0, \quad (\text{B.43})$$

where  $A_c$ ,  $B_c$ ,  $C_c$  and  $D_c$  are the coefficients of the cubic equation:

$$A_c = ab, \quad B_c = -a, \quad C_c = R^\beta \theta + b p^{\beta R}, \quad D_c = -p^{\beta R}. \quad (\text{B.44})$$

For convenience, two auxiliary variables are defined via:

$$Q_c = \frac{1}{9} \left[ \frac{B_c^2}{A_c^2} - 3 \frac{C_c}{A_c} \right], \quad \text{and} \quad R_c = \frac{1}{54} \left[ 2 \frac{B_c^3}{A_c^3} - 9 \frac{B_c C_c}{A_c^2} + 27 \frac{D_c}{A_c} \right]. \quad (\text{B.45})$$

Therewith, it is possible to distinguish, if the vdW-EOS has three or only one real solution for the given  $p^{\beta R}$  and  $\theta$ , by checking

$$R_c^2 < Q_c^3 \begin{cases} \text{true} & \rightarrow \text{three real solutions,} \\ \text{false} & \rightarrow \text{one real solution.} \end{cases} \quad (\text{B.46})$$

Therein, the first case corresponds to pressure-temperature conditions within the two-phase region, where phase transition between gas and liquid occurs, and the second case relates to all conditions outside this region, with a distinct relationship between  $p^{\beta R}$ - $\theta$ - $\rho^{\beta R}$ , cf. Figure 4.2(b).

The three real solution in the first case are determined by

$$\begin{aligned} \rho_1^{\beta R} &= -2\sqrt{Q_c} \cos\left(\frac{S_c}{3}\right) - \frac{B_c}{3A_c}, \\ \rho_2^{\beta R} &= -2\sqrt{Q_c} \cos\left(\frac{S_c + 2\pi}{3}\right) - \frac{B_c}{3A_c}, \\ \rho_3^{\beta R} &= -2\sqrt{Q_c} \cos\left(\frac{S_c - 2\pi}{3}\right) - \frac{B_c}{3A_c}, \end{aligned} \quad (\text{B.47})$$

where  $\cos(\cdot)$  is the cosine operator and  $S_c$  is another auxiliary term

$$S_c = \arccos\left(\frac{R_c}{\sqrt{Q_c^3}}\right), \quad (\text{B.48})$$

with  $\arccos(\cdot)$  symbolising the inverse trigonometric function of the cosine. From these three solutions only the two with the lowest,  $\min\{\rho_1^{\beta R}, \rho_2^{\beta R}, \rho_3^{\beta R}\}$ , and highest value

$\max\{\rho_1^{\beta R}, \rho_2^{\beta R}, \rho_3^{\beta R}\}$ , have a physical meaning, i. e., they represent the gas and liquid densities on the border of the two-phase region, cf. Figure 4.2(b). From these two remaining solutions, the required density corresponding to the actual conditions is found with the help of the *Antoine* equation and the vapour pressure  $p_{\text{vap}}^R$ , according to the procedure described in Chapter 4.

Proceeding with the second case, the one real solution of the vdW-EOS is determined after introducing another auxiliary term:

$$T_c = \text{sgn}(R_c) \left[ |R_c| + \sqrt{R_c^2 - Q_c^3} \right]^{1/3}, \quad (\text{B.49})$$

where the operator  $\text{sgn}(\cdot)$  stands for the signum function and is defined as follows

$$\text{sgn}(\cdot) := \begin{cases} -1 & \text{if } (\cdot) < 0, \\ 0 & \text{if } (\cdot) = 0, \\ 1 & \text{if } (\cdot) > 0. \end{cases} \quad (\text{B.50})$$

In this regard, the one real solution is given by

$$\rho^{\beta R} = T_c + \frac{Q_c}{T_c} - \frac{B_c}{3A_c}, \quad (\text{B.51})$$

This density corresponds to thermodynamical states outside of the two-phase region. In particular,  $\rho^{\beta R}$  can represent in this case gas, liquid or supercritical phases.



# Bibliography

- [1] ABBOTT, M. M. & VAN NESS, H. C.: *Thermodynamics with Chemical Applications*. McGraw-Hill 1989.
- [2] ACARTÜRK, A.: *Simulation of Charged Hydrated Porous Materials*. Dissertation, Report No. II-18 of the Institute of Applied Mechanics (CE), University of Stuttgart 2009.
- [3] AHRENHOLZ, B.; NIESSNER, J.; HELMIG, R. & KRAFCZYK, M.: Pore-scale determination of parameters for macroscale modeling of evaporation processes in porous media. *Water Resources Research* **47** (2011), W07543.
- [4] ALTENBACH, H.: *Kontinuumsmechanik: Einführung in die materialunabhängigen und materialabhängigen Gleichungen*. Springer-Verlag, Berlin 2012.
- [5] ALTS, T. & HUTTER, K.: Continuum description of the dynamics and thermodynamics of phase boundaries between ice and water. Part I: Surface balance laws and their interpretation in terms of three-dimensional balance laws averaged over the phase change boundary layer. *Journal of Non-Equilibrium Thermodynamics* **13** (1988), 221–257.
- [6] AMMANN, M.: *Parallel Finite Element Simulations of Localization Phenomena in Porous Media*. Dissertation, Report No. II-11 of the Institute of Applied Mechanics (CE), University of Stuttgart 2005.
- [7] ANTOINE, C.: Tensions des vapeurs: nouvelle relation entre les tensions et les températures. *Comptes Rendus des Séances de l'Académie des Sciences* **107** (1888), 681–684.
- [8] AVCI, O.: *Coupled Deformation and Flow Processes of Partially Saturated Soil: Experiments, Model Validation and Numerical Investigations*. Dissertation, Report No. II-26 of the Institute of Applied Mechanics (CE), University of Stuttgart 2013.
- [9] AVOGADRO, L. R. A. C.: Essai d'une manière de déterminer les masses relatives des molécules élémentaires des corps, et les proportions selon lesquelles elles entrent dans les combinaisons. *Journal de physique, de chimie, d'histoire naturelle et des arts* **73** (1811), 58–76.
- [10] BACHU, S.: CO<sub>2</sub> storage in geological media: Role, means, status and barriers to deployment. *Progress in Energy and Combustion Science* **34** (2008), 254–273.
- [11] BAEHR, H. D.: *Thermodynamik: Eine Einführung in die Grundlagen und ihre technischen Anwendungen*. Springer-Verlag, Berlin, Heidelberg, New York 1996.
- [12] BATHE, K. J.: *Finite-Elemente-Methoden*, 2nd edn. Springer-Verlag, Berlin 2002.

- [13] BEAR, J.: *Hydraulics of Groundwater*. Water Resources and Environmental Engineering, McGraw-Hill, New York 1979.
- [14] BEDEAUX, D. & KJELSTRUP, S.: Transfer coefficients for evaporation. *Physica A* **270** (1999), 413–426.
- [15] BIELINSKI, A.: *Numerical Simulation of CO<sub>2</sub> Sequestration in Geological Formations*. Dissertation, Institute for Modelling Hydraulic and Environmental Systems, University of Stuttgart 2007.
- [16] BIOT, M. A.: General theory of three dimensional consolidation. *Journal of Applied Physics* **12** (1941), 155–164.
- [17] BLUHM, J.; BLOSSFELD, W. M. & RICKEN, T.: Energetic effects during phase transition under freezing-thawing load in porous media – a continuum multi-phase description and FE-simulation. *Zeitschrift für Angewandte Mathematik und Mechanik* **94** (2014), 586–608.
- [18] DE BOER, R.: *Vektor- und Tensorrechnung für Ingenieure*. Springer-Verlag, Berlin 1982.
- [19] DE BOER, R.: Thermodynamics of phase transitions in porous media. *Applied Mechanics Reviews* **48** (1995), 613–622.
- [20] DE BOER, R.: *Theory of Porous Media*. Springer-Verlag, Berlin 2000.
- [21] DE BOER, R. & BLUHM, J.: Phase transitions in gas- and liquid-saturated porous solids. *Transport in Porous Media* **34** (1999), 249–267.
- [22] DE BOER, R. & EHLERS, W.: *Theorie der Mehrkomponentenkontinua mit Anwendungen auf bodenmechanische Probleme*. Forschungsberichte aus dem Fachbereich Bauwesen, Heft 40, Universität-GH-Essen 1986.
- [23] DE BOER, R. & KOWALSKI, S. J.: Thermodynamics of fluid-saturated porous media with a phase change. *Acta Mechanica* **109** (1995), 167–189.
- [24] BOWEN, R. M.: Toward a thermodynamics and mechanics of mixtures. *Archive For Rational Mechanics And Analysis* **24** (1967), 370–403.
- [25] BOWEN, R. M.: Theory of mixtures. In Eringen, A. C. (ed.): *Continuum Physics*, Vol. III, Academic Press, New York 1976, pp. 1–127.
- [26] BOWEN, R. M.: Incompressible porous media models by use of the theory of mixtures. *International Journal of Engineering Science* **18** (1980), 1129–1148.
- [27] BOWEN, R. M.: Compressible porous media models by use of the theory of mixtures. *International Journal of Engineering Sciences* **20** (1982), 697–735.

- [28] BRADSHAW, J.; BACHU, S.; BONIJOLY, D.; BURRUSS, R.; HOLLOWAY, S.; CHRISTENSEN, N. P. & MATHIASSEN, O. M.: CO<sub>2</sub> storage capacity estimation: Issues and development of standards. *International Journal of Greenhouse Gas Control* **1** (2007), 62–68.
- [29] BRAESS, D.: *Finite Elemente*. Springer Verlag, Berlin 1997.
- [30] BREZZI, F. & FORTIN, M.: *Mixed and Hybrid Finite Element Methods*. Springer-Verlag, New York 1991.
- [31] BROOKS, R. H. & COREY, A. T.: *Hydraulic Properties of Porous Media*, Vol. 3. Hydrology Papers, Colorado State University 1964.
- [32] BRUCKNER, T.; BASHMAKOV, I. A.; MULUGETTA, Y.; CHUM, H.; DE LA VEGA NAVARRO, A.; EDMONDS, J.; FAAIJ, A.; FUNGTAMMASAN, B.; GARG, A.; HERTWICH, E.; HONNERY, D.; INFELD, D.; KAINUMA, M.; KHENNAS, S.; KIM, S.; NIMIR, H. B.; RIAHI, K.; STRACHAN, N.; WISER, R. & ZHANG, X.: *Climate Change 2014: Mitigation of Climate Change. Contribution of Working Group III to the Fifth Assessment Report of the Intergovernmental Panel on Climate Change*, Chap. Energy Systems, Cambridge University Press, Cambridge, United Kingdom and New York, NY, USA 2014. pp. 511–597.
- [33] BRUNNER, G. & BUDICH, M.: *Supercritical Fluids as Solvents and Reaction Media*, Chap. Separation of organic compounds from aqueous solutions by means of supercritical carbon dioxide, Elsevier Science Publishers B.V., Amsterdam 2004. pp. 489–522.
- [34] CELIA, M. A.; BACHU, S.; NORDBOTTON, J. M.; GASDA, S. E. & DAHLE, H. K.: Quantitative estimation of CO<sub>2</sub> leakage from geological storage: analytical models, numerical models, and data needs. *Proceedings of 7th International Conference on Greenhouse Gas Control Technologies* **1** (2005), 663–671.
- [35] CHAMMARI, A.; NAON, B.; CHERBLANC, F. & BÉNET, J.-C.: Water transport in soil with phase change. *Mechanical Modelling and Computational Issues in Civil Engineering* **23** (2005), 135–142.
- [36] CLASS, H.: *Theorie und numerische Modellierung nichtisothermer Mehrphasenprozesse in NAPL kontaminierten porösen Medien*. Dissertation, Institute for Modelling Hydraulic and Environmental Systems, University of Stuttgart 2001.
- [37] CLASS, H.; EBIGBO, A.; HELMIG, R.; DAHLE, H.; NORDBOTTEN, J. M.; CELIA, M. A.; AUDIGANE, P.; DARCIS, M.; ENNIS-KING, J.; Y-FAN; FLEMISCH, B.; GASDA, S. E.; KRUG, S.; LABREGERE, D.; MIN, J.; SBAI, A.; THOMAS, S. G. & TRENTY, L.: A benchmark study on problems related to CO<sub>2</sub> storage in geologic formations. *Special Issue of Computational Geosciences* **13** (2009), 409–434.
- [38] COATS, K. H.; NIELSEN, R. L. & WEBER, A. G.: Simulation of three-dimensional, two-phase flow in oil and gas reservoirs. *Society of Petroleum Engineers Journal* **7** (1967), 377–388.

- [39] COLEMAN, B. D. & NOLL, W.: The thermodynamics of elastic materials with heat conduction and viscosity. *Archive of Rational Mechanics and Analysis* **13** (1963), 167–178.
- [40] COURT, B.; BANDILLA, K. W.; CELIA, M. A.; JANZEN, A.; DOBOSSY, M. E. & NORDBOTTEN, J. M.: Applicability of vertical-equilibrium and sharp-interface assumptions in CO<sub>2</sub> sequestration modeling. *International Journal of Greenhouse Gas Control* **10** (2012), 134–147.
- [41] DALLA, E.; HILPERT, M. & MILLER, C. T.: Computation of the interfacial area for two-fluid porous medium systems. *Journal of Contaminant Hydrology* **56** (2002), 25–48.
- [42] DARCY, H.: *Les fontaines publiques de la ville de Dijon*. Dalmont, Paris 1856.
- [43] DAS GUPTA, N. N. & GHOSH, S. K.: A report on the Wilson cloud chamber and its application in physics. *Review of Modern Physics* **18** (1946)(2), 225–365.
- [44] DIEBELS, S.: A micropolar theory of porous media: Constitutive modelling. *Transport in Porous Media* **34** (1999), 193–208.
- [45] DIEBELS, S.: A macroscopic description of the quasi-static behavior of granular materials based on the theory of porous media. *Granular Matter* **2** (2000), 143–152.
- [46] DOUGHTY, C. & PRUESS, K.: Modeling supercritical carbon dioxide injection in heterogeneous porous media. *Vadose Zone Journal* **3** (2004), 1–22.
- [47] EBIGBO, A.: *Modelling of Biofilm Growth and its Influence on CO<sub>2</sub> and Water (Two-Phase) Flow in Porous Media*. Dissertation, Institute for Modelling Hydraulic and Environmental Systems, University of Stuttgart 2009.
- [48] EHLERS, W.: Elemente der nichtlinearen Kontinuumsthermodynamik. Lecture Notes, Institute of Applied Mechanics, Chair of Continuum Mechanics, University of Stuttgart 1996.
- [49] EHLERS, W.: On thermodynamics of elasto-plastic porous media. *Archives of Mechanics* **41** (1989), 73–93.
- [50] EHLERS, W.: Toward finite theories of liquid-saturated elasto-plastic porous media. *International Journal of Plasticity* **7** (1991), 443–475.
- [51] EHLERS, W.: Vector and Tensor Calculus: An Introduction. Lecture notes, Institute of Applied Mechanics, Chair of Continuum Mechanics, University of Stuttgart 1995–2004, <http://www.mechbau.uni-stuttgart.de/lis2/Downloads/Downloads.html>.
- [52] EHLERS, W.: Grundlegende Konzepte in der Theorie Poröser Medien. *Technische Mechanik* **16** (1996), 63–76.

- [53] EHLERS, W.: *IUTAM Symposium on Mechanics of Granular and Porous Media*, Chap. Shear band localization in fluid-saturated granular elasto-plastic porous media, Kluwer, Dordrecht 1997. pp. 377–388.
- [54] EHLERS, W.: Foundations of multiphasic and porous materials. In Ehlers, W. & Bluhm, J. (eds.): *Porous Media: Theory, Experiments and Numerical Applications*, Springer-Verlag, Berlin 2002, pp. 3–86.
- [55] EHLERS, W.: Challenges of porous media models in geo- and biomechanical engineering including electro-chemically active polymers and gels. *International Journal of Advances in Engineering Sciences and Applied Mathematics* **1** (2009), 1–24.
- [56] EHLERS, W.: *Poröse Medien – ein Kontinuummechanisches Modell auf Basis der Mischungstheorie*. Institute of Applied Mechanics (Civil Engineering), University of Stuttgart 2012, Nachdruck der Habilitationsschrift aus dem Jahre 1989 (Forschungsbericht aus dem Fachbereich Bauwesen der Universität-GH-Essen, 47, Essen 1989).
- [57] EHLERS, W.; DIEBELS, S. & VOLK, W.: Deformation and compatibility for elasto-plastic micropolar materials with applications to geomechanical problems. *Journal de Physique IV* **8** (1998), 127–134.
- [58] EHLERS, W.; ELLSIEPEN, P.; BLOME, P.; MAHNKOPF, D. & MARKERT, B.: *Theoretische und numerische Studien zur Lösung von Rand- und Anfangswertproblemen in der Theorie Poröser Medien*. Forschungsbericht zum DFG-Projekt Eh 107/6-2, Universität Stuttgart 1999.
- [59] EHLERS, W. & GRAF, T.: Saturated elasto-plastic porous media under consideration of gaseous and liquid phase transitions. In Schanz, T. (ed.): *Theoretical and Numerical Unsaturated Soil Mechanics*, Vol. 113, Springer Proceedings in Physics, Springer-Verlag, Berlin 2007, pp. 111–118.
- [60] EHLERS, W.; GRAF, T. & AMMANN, M.: Deformation and localization analysis of partially saturated soil. *Computer Methods in Applied Mechanics and Engineering* **193** (2004), 2885–2910.
- [61] EHLERS, W. & HÄBERLE, K.: Interfacial mass transfer during gas-liquid phase change in deformable porous media with heat transfer. *Transport in Porous Media* **114** (2016), 525–556.
- [62] EHLERS, W. & LUO, C.: A phase-field approach embedded in the theory of porous media for the description of dynamic hydraulic fracturing. *Computer Methods in Applied Mechanics and Engineering* **315** (2017), 348–368.
- [63] EIPPER, G.: *Theorie und Numerik finiter elastischer Deformationen in flüdigesättigten porösen Festkörpern*. Dissertation, Report No. II-01 of the Institute of Applied Mechanics (CE), University of Stuttgart 1998.

- [64] ELLSIEPEN, P.: *Zeit- und ortsadaptive Verfahren angewandt auf Mehrphasenprobleme poröser Medien*. Dissertation, Report No. II-03 of the Institute of Applied Mechanics (CE), University of Stuttgart 1999.
- [65] ENNIS-KING, J. P. & PATERSON, L.: Role of convective mixing in the long-term storage of carbon dioxide in deep saline formations. *SPE Journal* **10** (2005), SPE-84344.
- [66] FENGHOUR, A.; WAKEHAM, W. A. & VESOVIC, V.: The viscosity of carbon dioxide. *Journal of Physical and Chemical Reference Data* **27** (1998), 31–44.
- [67] FOLK, R. L.: Practical petrographic classification of limestone. *Bulletin of the American Associations of Petroleum Geologists* **43** (1959), 1–38.
- [68] FREDLUND, D. G. & RAHARDJO, H.: *Soil mechanics for unsaturated soil*. John Wiley & Sons Inc., New York 1993.
- [69] FREDLUND, M. D.; WILSON, G. W. & FREDLUND, D. G.: Use of the grain-size distribution for estimation of the soil-water characteristic curve. *Canadian Geotechnical Journal* **39** (2002), 1103–1117.
- [70] GASDA, S. E.; NORDBOTTEN, J. M. & CELIA, M. A.: Vertically-averaged approaches to CO<sub>2</sub> injection with solubility trapping. *Water Resources Research* **47** (2011), W05528.
- [71] GHADIANI, S. R.: *A Multiphase Continuum Mechanical Model for Design Investigations of an Effusion-Cooled Rocket Thrust Chamber*. Dissertation, Report No. II-13 of the Institute of Applied Mechanics (CE), University of Stuttgart 2005.
- [72] GLADKIKH, M. & BRYANT, S.: Prediction of interfacial areas during imbibition in simple porous media. *Advances in Water Resources* **26** (2003), 609–622.
- [73] GLOBAL CCS INSTITUTE: *The Global Status of CCS: 2012*. Canberra, Australia 2012.
- [74] GRAF, T.: *Multiphase Flow Processes in Deformable Porous Media under Consideration of Fluid Phase Transitions*. Dissertation, Report No. II-17 of the Institute of Applied Mechanics (CE), University of Stuttgart 2008.
- [75] GRAY, W. G.: General conservation equations for multi-phase systems: 4. Constitutive theory including phase change. *Advances in Water Resources* **6** (1983), 130–140.
- [76] GRAY, W. G. & MILLER, C. T.: Thermodynamically constrained averaging theory approach for modeling flow and transport phenomena in porous medium systems: 8. Interface and common curve dynamics. *Advances in Water Resources* **33** (2010), 1427–1443.

- [77] HÄBERLE, K. & EHLERS, W.: Carbon-dioxide storage and phase transitions: towards an understanding of crack development in the cap-rock layer. *Proceedings in Applied Mathematics and Mechanics* **12** (2012), 377–378.
- [78] HADAMARD, J.: *Leçons sur la propagation des ondes et les équations de l'hydrodynamique*. Herman, Paris 1903, reprinted by Chelsea Publishing Company, New York 1949.
- [79] HASSANIZADEH, S. M. & GRAY, W. G.: General conservation equations for multiphase systems: 1. Averaging procedure. *Advances in Water Resources* **2** (1979), 25–40.
- [80] HASSANIZADEH, S. M. & GRAY, W. G.: Boundary and interface conditions in porous media. *Water Resources Research* **25** (1989), 1705–1715.
- [81] HASSANIZADEH, S. M. & GRAY, W. G.: Mechanics and thermodynamics of multiphase flow in porous media including interphase boundaries. *Advances in Water Resources* **13** (1990), 169–186.
- [82] HAUPT, P.: Foundation of continuum mechanics. In Hutter, K. (ed.): *Continuum Mechanics in Environmental Sciences and Geophysics*, CISM Courses and Lectures No. 337, Springer-Verlag, Wien 1993, pp. 1–77.
- [83] HELD, R. J. & CELIA, M. A.: Modeling support of functional relationships between capillary pressure, saturation, interfacial area and common lines. *Advances in Water Resources* **24** (2001), 325–343.
- [84] HELMIG, R.: *Multiphase Flow and Transport Processes in the Subsurface*. Springer, Berlin 1997.
- [85] HERZOG, H. J.: Scaling up carbon dioxide capture and storage: From megatons to gigatons. *Energy Economics* **33** (2011), 597–604.
- [86] HOMS Y, G. M.: Viscous fingering in porous media. *Annual Review of Fluid Mechanics* **19** (1987), 271–311.
- [87] HUANG, H.; LIN, P. & ZHOU, W.: Moisture transport and diffusive instability during bread baking. *SIAM Journal on Applied Mathematics* **68** (2006), 222–238.
- [88] HUGHES, T. J. R.: *The Finite Element Method: Linear Static and Dynamic Finite Element Analysis*. Dover Publications, New York 2012.
- [89] JAMET, D.: Diffuse interface models in fluid mechanics. GdR CNRS documentation 2014, <http://pmc.polytechnique.fr/mp/GDR/docu/Jamet.pdf>.
- [90] JOEKAR-NIASAR, V.; HASSANIZADEH, S. M. & LEIJNSE, A.: Insights into the relationships among capillary pressure, saturation, interfacial area and relative permeability using pore-network modelling. *Transport in Porous Media* **74** (2008), 201–219.

- [91] JUANES, R.; SPITERI, E. J.; ORR JR., F. M. & BLUNT, M. J.: Impact of relative permeability hysteresis on geological CO<sub>2</sub> storage. *Water Resources Research* **52** (2006), W12418.
- [92] JURIC, D. & TRYGGVASON, G.: Computations of boiling flows. *International Journal of Multiphase Flow* **24** (1998), 387–410.
- [93] KANG, M.; NORDBOTTEN, J. M.; DOSTER, F. & CELIA, M. A.: Analytical solutions for two-phase subsurface flow to a leaky fault considering vertical flow effects and fault properties. *American Geophysical Union* **50** (2014), 3536–3552.
- [94] KARAJAN, N.: *An Extended Biphasic Description of the Inhomogeneous and Anisotropic Intervertebral Disc*. Dissertation, Report No. II-17 of the Institute of Applied Mechanics (CE), University of Stuttgart 2009.
- [95] KARAJAN, N.; EHLERS, W. & MARKERT, B.: An anisotropic porous media model of the intervertebral disc. *PAMM* **3** (2003), 180–181.
- [96] KEELING, C. D.: The concentration and isotopic abundances of carbon dioxide in the atmosphere. *Tellus* **12** (1960)(2), 200–203.
- [97] KELLY, P. D.: A reacting continuum. *International Journal of Engineering Science* **2** (1964), 129–153.
- [98] KOMAROVA, I.: *Carbon-Dioxide Storage in the Subsurface: A Fully Coupled Analysis of Transport Phenomena and Solid Deformation*. Dissertation, Report No. II-24 of the Institute of Applied Mechanics (CE), University of Stuttgart 2012.
- [99] KOPP, A.; CLASS, H. & HELMIG, R.: Investigations on CO<sub>2</sub> storage capacity in saline aquifers - Part 2: Estimation of storage capacity coefficients. *International Journal of Greenhouse Gas Control* **3** (2009), 277–287.
- [100] KOSINSKI, W.: *Field singularities and wave analysis in continuum mechanics*. Ellis Harwood, Chichester 1986.
- [101] KOWALSKI, S. J.: Toward a thermodynamics and mechanics of drying processes. *Chemical Engineering Science* **55** (2000), 1289–1304.
- [102] KRUSCHWITZ, J. & BLUHM, J.: Modeling of ice formation in porous solids with regard to the description of frost damage. *Computational Materials Science* **32** (2005), 407–417.
- [103] KUMAR, A.; NOH, M.; POPE, G. A.; SEPEHRNOORI, K.; BRYANT, S. & LAKE, L. W.: Reservoir simulation of CO<sub>2</sub> storage in deep saline aquifers. *SPE Journal* **10** (2005), SPE 89343.
- [104] LEMMON, E. W.; MCLINDEN, M. O. & FRIEND, D. G.: Thermophysical properties of fluid systems 2015, <http://webbook.nist.gov>.



- [105] LEWIS, G. N. & RANDALL, M.: *Thermodynamics*, 2nd edn. McGraw-Hill, New York, Toronto, London 1961.
- [106] LEWIS, W. K. & WHITMAN, W. G.: Principle of gas absorption. *Industrial & Engineering Chemistry* **16** (1924), 1215–1220.
- [107] LIU, I.-S.: Method of Lagrange multipliers for exploitation of the entropy principle. *Archive for Rational Mechanics and Analysis* **46** (1972), 131–148.
- [108] LOZANO, A.-L.; CHERBLANC, F. & BÉNET, J.-C.: Water evaporation versus condensation in a hygroscopic soil. *Transport in Porous Media* **80** (2009), 209–222.
- [109] LOZANO, A.-L.; CHERBLANC, F.; COUSIN, B. & BÉNET, J.-C.: Experimental study and modelling of water phase change kinetics in soils. *European Journal of Soil Science* **59** (2008), 939–949.
- [110] LU, S. & PISTER, K.: Decomposition of deformation and representation of the free energy function for isotropic thermoelastic solids. *International Journal of Solids and Structures* **11** (1975), 927–934.
- [111] LUO, C. & EHLERS, W.: Hydraulic fracturing based on the Theory of Porous Media. *Proceedings in Applied Mathematics and Mechanics* **15** (2015), 401–402.
- [112] LYKOV, A. V.: On systems of differential equations for heat and mass transfer in capillary porous bodies. *Journal of Engineering Physics* **26** (1974), 11–17.
- [113] MAHNKOPF, D.: *Lokalisierung fluidgesättigter poröser Festkörper bei finiten elasto-plastischen Deformationen*. Dissertation, Report No. II-05 of the Institute of Applied Mechanics (CE), University of Stuttgart 2000.
- [114] MARKERT, B.: *Porous Media Viscoelasticity with Application to Polymeric Foams*. Dissertation, Report No. II-12 of the Institute of Applied Mechanics (CE), University of Stuttgart 2005.
- [115] MARKERT, B.: A constitutive approach to 3-d nonlinear fluid flow through finite deformable porous continua, with application to a high-porosity polyurethane foam. *Transport in Porous Media* **70** (2007), 427–450.
- [116] MARKERT, B.; HEIDER, Y. & EHLERS, W.: Comparison of monolithic and splitting solution schemes for dynamic porous media problems. *International Journal for Numerical Methods in Engineering* **82** (2010), 1341–1383.
- [117] MARKERT, B.; MONASTYRSKY, B. & EHLERS, W.: Fluid penetration effects in porous media contact. *Continuum Mechanics and Thermodynamics* **20** (2008), 303–315.
- [118] MCHUGH, M. A. & KRUKONIS, V. J.: *Supercritical fluid extraction: principles and practice*. Butterworth Heinemann, London 1986.

- [119] METZ, B.; DAVIDSON, O.; DE CONINCK, H. C.; LOOS, M. & MEYER, L. A. (eds.): *IPCC Special Report on Carbon Dioxide Capture and Storage*. Cambridge University Press, Cambridge and New York 2005.
- [120] MORLAND, L. W. & GRAY, J. M. N. T.: Phase change interactions and singular fronts. *Continuum Mechanics and Thermodynamics* **7** (1995), 387–414.
- [121] MORLAND, L. W. & SELLERS, S.: Multiphase mixtures and singular surfaces. *International Journal of Non-Linear Mechanics* **36** (2001), 131–146.
- [122] MORROW, N. R.: Physics and thermodynamics of capillary action in porous media. *Industrial & Engineering Chemistry* **62** (1970), 32–56.
- [123] MYHRE, G.; SHINDELL, D.; BRÉON, F.-M.; COLLINS, W.; FUGLESTVEDT, J.; HUANG, J.; KOCH, D.; LAMARQUE, J.-F.; LEE, D.; MENDOZA, B.; NAKAJIMA, T.; ROBOCK, A.; STEPHENS, G.; TAKEMURA, T. & ZHANG, H.: *Climate Change 2013: The Physical Science Basis. Contribution of Working Group I to the Fifth Assessment Report of the Intergovernmental Panel on Climate Change*, Chap. Anthropogenic and Natural Radiative Forcing, Cambridge University Press, Cambridge and New York 2013. pp. 659–740.
- [124] NIESSNER, J. & HASSANIZADEH, S. M.: A model for two-phase flow in porous media including fluid-fluid interfacial area. *Water Resources Research* **44** (2008), 1–10.
- [125] NIESSNER, J. & HASSANIZADEH, S. M.: Modeling kinetic interphase mass transfer for two-phase flow in porous media including fluid-fluid interfacial area. *Transport in Porous Media* **80** (2009), 329–344.
- [126] NIESSNER, J. & HASSANIZADEH, S. M.: Non-equilibrium interphase heat and mass transfer during two-phase flow in porous media – theoretical considerations and modeling. *Advances in Water Resources* **32** (2009), 1756–1766.
- [127] NORDBOTTEN, J. M. & CELIA, M. A.: *Geological Storage of CO<sub>2</sub>: Modeling Approaches for Large-Scale Simulation*. John Wiley & Sons Inc., Hoboken, New Jersey 2011.
- [128] NORDBOTTEN, J. M.; FLEMISCH, B.; GASDA, S. E.; NILSEN, H. M.; FAN, Y.; PICKUP, G. E.; WIESE, B.; CELIA, M. A.; DAHLE, H. K.; EIGESTAD, G. T. & PRUESS, K.: Uncertainties in practical simulation of CO<sub>2</sub> storage. *International Journal of Greenhouse Gas Control* **9** (2012), 234–242.
- [129] NORDBOTTEN, J. M.; KAVETSKI, D.; CELIA, M. A. & BACHU, S.: A semi-analytical model estimating leakage associated with CO<sub>2</sub> storage in large-scale multi-layered geological systems with multiple leaky wells. *Environmental Science and Technology* **43** (2009), 743–749.

- [130] NUSKE, P.; JOEKAR-NIASAR, V. & HELMIG, R.: Non-equilibrium in multiphase multicomponent flow in porous media: An evaporation example. *International Journal of Heat and Mass Transfer* **74** (2014), 128–142.
- [131] OGDEN, R. W.: *Nonlinear Elastic Deformations*. Ellis Harwood, Chichester 1984.
- [132] OOSTROM, M.; WHITE, M. D. & BRUSSEAU, M. L.: Theoretical estimation of free and entrapped nonwetting-wetting fluid interfacial areas in porous media. *Advances in Water Resources* **24** (2001), 887–898.
- [133] OTT, H.; PENTLAND, C. H. & OEDAI, S.: CO<sub>2</sub>-brine displacement in heterogeneous carbonates. *International Journal of Greenhouse Gas Control* **33** (2015), 135–144.
- [134] OTT, J. B. & BOERIO-GOATES, J.: *Chemical Thermodynamics: Principles and Applications*. Elsevier, San Diego, London 2000.
- [135] PITZER, K. S.; LIPPMANN, D. Z.; JR., R. F. C.; HUGGINS, C. M. & PETERSEN, D. E.: The volumetric and thermodynamic properties of fluids II: Compressibility factor, vapor pressure and entropy of vaporization. *Journal of the American Chemical Society* **77** (1955), 3433–3440.
- [136] PLUG, W.-J. & BRUINING, J.: Capillary pressure for the sand-CO<sub>2</sub>-water system under various pressure conditions. Application to CO<sub>2</sub> sequestration. *Advances in Water Resources* **30** (2007), 2339–2353.
- [137] POLING, B. E.; PRAUSNITZ, J. M. & O’CONNELL, J. P.: *The Properties of Gases and Liquids*, 5th edn. McGraw-Hill, New York 2001.
- [138] POP, I. S.; VAN DUIJN, C. J.; NIESSNER, J. & HASSANIZADEH, S. M.: Horizontal redistribution of fluids in a porous medium: The role of interfacial area in modeling hysteresis. *Advances in Water Resources* **32** (2009), 383–390.
- [139] POTTER, M. C. & SOMERTON, C. W.: *Thermodynamics for Engineers*. McGraw-Hill, New York 1995.
- [140] PRESS, W. H.; TEUKOLSKY, S. A.; VETTERLING, W. T. & FLANNERY, B. P.: *Numerical Recipes in C: The Art of Scientific Computing*, 2nd edn. Cambridge University Press, Cambridge 1992.
- [141] PRUESS, K. & GARCÍA, J.: Multiphase flow dynamics during CO<sub>2</sub> disposal into saline aquifers. *Environmental Geology* **42** (2002), 282–295.
- [142] PRUESS, K.; GARCÍA, J.; KOVSCEK, T.; OLDENBURG, C.; RUTQVIST, J.; STEEFEL, C. & XU, T.: Code intercomparison builds confidence in numerical simulation models for geological disposal of CO<sub>2</sub>. *Energy* **29** (2004), 1431–1444.
- [143] PRUESS, K. & NORDBOTTEN, J. M.: Numerical simulation studies of the long-term evolution of a CO<sub>2</sub> plume in a saline aquifer with a sloping caprock. *Transport in Porous Media* **90** (2011), 135–151.

- [144] PRUESS, K.; OLDENBURG, C. & MORIDIS, G.: *TOUGH2 User's Guide, Version 2.0*. Earth Sciences Division, Lawrence Berkeley National Laboratory, University of California at Berkeley, California, USA.
- [145] REEVES, P. C. & CELIA, M. A.: A functional relationship between capillary pressure, saturation, and interfacial area as revealed by a pore-scale network model. *Water Resources Research* **32** (1996), 2345–2358.
- [146] REMPLER, H.-U.: *Damage in Multi-Phasic Materials Computed with the Extended Finite-Element Method*. Dissertation, Report No. II-23 of the Institute of Applied Mechanics (CE), University of Stuttgart 2011.
- [147] RICKEN, T. & BLUHM, J.: Remodeling and growth of living tissue: a multiphase theory. In *Proceedings of the 2nd GAMM Seminar on Continuum Biomechanics*, W. Ehlers and B. Markert 2007.
- [148] RICKEN, T. & BLUHM, J.: Modeling fluid saturated porous media under frost attack. *GAMM-Mitteilungen* **33** (2010), 40–56.
- [149] RICKEN, T. & BLUHM, J.: Modeling of liquid and gas saturated porous solids under freezing and thawing cycles. In Schanz, T. & Hettler, A. (eds.): *Aktuelle Forschung in der Bodenmechanik 2013*, Springer Berlin Heidelberg 2014, pp. 23–42.
- [150] RICKEN, T.; SCHWARZ, A. & BLUHM, J.: A triphasic model of transversely isotropic biological tissue with applications to stress and biologically induced growth. *Computational Materials Science* **39** (2007), 124–136.
- [151] RICKEN, T.; SINDERN, A.; BLUHM, J.; WIDMANN, R.; DENECKE, M.; GEHRKE, T. & SCHMIDT, T. C.: Concentration driven phase transitions in multiphase porous media with application to methane oxidation in landfill cover layers. *Zeitschrift für Angewandte Mathematik und Mechanik* **94** (2014), 609–622.
- [152] RICKEN, T. & USTOHALOVA, V.: Modeling of thermal mass transfer in porous media with applications to the organic phase transition in landfills. *Computational Materials Science* **32** (2005), 498–508.
- [153] RUIZ, T. & BÉNET, J.-C.: Phase change in a heterogeneous medium: comparison between the vaporisation of water and heptane in an unsaturated soil at two temperatures. *Transport in Porous Media* **44** (2001), 337–353.
- [154] RUTQVIST, J.; BIRKHOLZER, J. T. & TSANG, C.-F.: Coupled reservoir-geomechanical analysis of the potential for tensile and shear failure associated with CO<sub>2</sub> injection in multilayered reservoir-caprock systems. *International Journal of Rock Mechanics & Mining Sciences* **45** (2008), 132–143.
- [155] RUTQVIST, J. & TSANG, C.-F.: A study of caprock hydromechanical changes associated with CO<sub>2</sub>-injection into a brine formation. *Environmental Geology* **42** (2002), 296–305.

- [156] RUTQVIST, J.; VASCO, D. W. & MYER, L.: Coupled reservoir-geomechanical analysis of CO<sub>2</sub> injection and ground deformations at In Salah, Algeria. *International Journal of Greenhouse Gas Control* **4** (2010), 225–230.
- [157] SAHIMI, M.: *Flow and Transport in Porous Media and Fractured Rock: From Classical Methods to Modern Approaches*. Second, Revised and Enlarged Edition, Wiley-VCH, Weinheim 2011.
- [158] SCHENKE, M. & EHLERS, W.: Parallel solution of volume-coupled multi-field problems using an Abaqus-PANDAS software interface. *Proceedings in Applied Mathematics and Mechanics* **15** (2015), 419–420.
- [159] SCHOLZ, B.: *Application of a Micropolar Model to the Localization Phenomena in Granular Materials: General Model, Sensitivity Analysis and Parameter Optimization*. Dissertation, Report No. II-15 of the Institute of Applied Mechanics (CE), University of Stuttgart 2007.
- [160] SCHREFLER, B. A. & SCOTTA, R.: A fully coupled model for two-phase flow in deformable porous media. *Computer Methods in Applied Mechanics and Engineering* **190** (2001), 3223–3246.
- [161] SCHREFLER, B. A. & ZHAN, X.: A fully coupled model for water flow and air flow in deformable porous media. *Water Resources Research* **29** (1993), 155–167.
- [162] SCHWARZ, H. R.: *Methode der finiten Elemente*. Teubner, Stuttgart 1991.
- [163] SHAHRAEENI, E. & OR, D.: Pore-scale analysis of evaporation and condensation dynamics in porous media. *Langmuir* **26** (2010), 13924–13936.
- [164] SHAHRAEENI, E. & OR, D.: Pore-scale evaporation-condensation dynamics resolved by synchrotron x-ray tomography. *Physical Review E* **85** (2012), 1–8.
- [165] SILHAVY, M.: *The Mechanics and Thermodynamics of Continuous Media*. Theoretical and Mathematical Physics, Springer-Verlag Berlin Heidelberg 1997.
- [166] SOAVE, G.: Equilibrium constants from a modified Redlich-Kwong equation of state. *Chemical Engineering Science* **27** (1972), 1197–1203.
- [167] SPAN, R. & WAGNER, W.: A new equation of state for carbon dioxide covering the fluid region from the triple-point temperature to 1100 K at pressures up to 800 MPa. *Journal of Physical and Chemical Reference Data* **25** (1996), 1509–1596.
- [168] STEEB, H. & DIEBELS, S.: A thermodynamic-consistent model describing growth and remodeling phenomena. *Computational Materials Science* **28** (2003), 597–607.
- [169] SU, G.-J.: Modified law of corresponding states for real gases. *Industrial & Engineering Chemistry* **38** (1946), 803–806.
- [170] TANGUY, S.; MÉNARD, T. & BERLEMONT, A.: A level set method for vaporizing two-phase flow. *Journal of Computational Physics* **221** (2007), 837–853.

- [171] TRUESDELL, C.: *Rational Thermodynamics*, 2nd edn. Springer-Verlag, New York 1984.
- [172] TRUESDELL, C. & NOLL, W.: The nonlinear field theories of mechanics. In Flügge, S. (ed.): *Handbuch der Physik*, Vol. III/3, Springer-Verlag, Berlin 1965.
- [173] TRUESDELL, C. & TOUPIN, R. A.: The classical field theories. In Flügge, S. (ed.): *Handbuch der Physik*, Vol. III/1, Springer-Verlag, Berlin 1960, pp. 226–902.
- [174] VAN GENUCHTEN, M. T.: A closed-form equation for predicting the hydraulic conductivity of unsaturated soils. *Soil Science Society of America Journal* **44** (1980), 892–898.
- [175] VESOVIC, V.; WAKEHAM, W. A.; OLCHOWY, G. A.; SENEGERS, J. V.; WATSON, J. T. R. & MILLAT, J.: The transport properties of carbon dioxide. *Journal of Physical and Chemical Reference Data* **19** (1990), 763–808.
- [176] WAGNER, A.: *Extended Modelling of the Multiphasic Human Brain Tissue with Application to Drug-Infusion Processes*. Dissertation, Report No. II-27 of the Institute of Applied Mechanics (CE), University of Stuttgart 2014.
- [177] WANG, Y. & OBERLACK, M.: A thermodynamic model of multiphase flows with moving interfaces and contact line. *Continuum Mechanics and Thermodynamics* **23** (2011), 409–433.
- [178] WHITAKER, S.: Simultaneous heat, mass, and momentum transfer in porous media: A theory of drying. *Advances in Heat Transfer* **13** (1977), 119–203.
- [179] WIENERS, C.; AMMANN, M.; DIEBELS, S. & EHLERS, W.: Parallel 3-d simulations for porous media models in soil mechanics. *Computational Mechanics* **29** (2002), 75–87.
- [180] WIENERS, C.; EHLERS, W.; AMMANN, M.; KARAJAN, N. & MARKERT, B.: Parallel solution methods for porous media models in biomechanics. *Proceedings in Applied Mathematics and Mechanics* **5** (2005), 35–38.
- [181] ZIENKIEWICZ, O. C. & TAYLOR, R. L.: *The Finite Element Method*, 5th edn., Vol. 1. Butterworth-Heinemann, Oxford 2000.
- [182] ZINATBAKHS, S.: *Coupled Problems in the Mechanics of Multi-Physics and Multi-Phase Materials*. Dissertation, Report No. II-27 of the Institute of Applied Mechanics (CE), University of Stuttgart 2015.

# Curriculum Vitae

## Personal Data:

Name: Kai Klaus Häberle  
Date of birth: 9<sup>th</sup> July, 1982  
Place of birth: Langenau, Germany  
Nationality: German  
Parents: Klaus and Klara Häberle  
Siblings: Thomas Häberle  
Marital status: married to Cornelia Häberle  
Children: Carlotta Häberle

## Education:

09/1989 – 07/1993 elementary school “Verbandsgrundschule Heusteig”,  
Asselfingen, Germany  
09/1993 – 07/2002 secondary school “Robert-Bosch-Gymnasium”,  
Langenau, Germany  
07/2002 degree: “Allgemeine Hochschulreife” (high school diploma)  
10/2003 – 01/2010 studies in environmental engineering at the  
University of Stuttgart, Germany  
01/2010 degree: “Diplom-Ingenieur (Dipl.-Ing.) Umweltschutztechnik”

## Civilian Service:

08/2002 – 05/2003 civilian service, “Kreiskrankenhaus” Langenau, Germany

## Education in Foreign Countries:

08/2006 – 06/2007 ERASMUS, Norwegian University of Science and Technology,  
Trondheim, Norway  
research project, University Centre Svalbard,  
Longyearbyen, Spitzbergen, Norway

## Internships:

07/2003 – 09/2003 ARGE Donaumoos, Riedheim, Germany  
10/2008 – 03/2009 Heidelberger Druckmaschinen AG, Heidelberg, Germany

## Professional Occupation:

04/2010 – 03/2016 assistant lecturer and research associate at the  
Institute of Applied Mechanics (Civil Engineering) at the  
University of Stuttgart, Germany  
09/2016 CFD-engineer at Alfred Kärcher GmbH & Co. KG, Winnenden, Germany



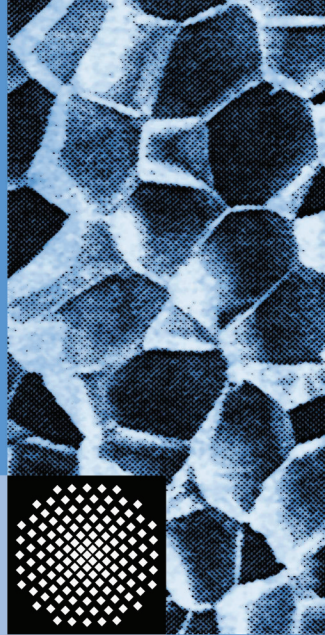


## Released Report Series

- II-1 GERNOT EIPPER: *Theorie und Numerik finiter elastischer Deformationen in fluidgesättigten porösen Festkörpern*, June 1998.
- II-2 WOLFRAM VOLK: *Untersuchung des Lokalisierungsverhaltens mikropolarer poröser Medien mit Hilfe der Cosserat-Theorie*, May 1999.
- II-3 PETER ELLSIEPEN: *Zeit- und ortsadaptive Verfahren angewandt auf Mehrphasenprobleme poröser Medien*, July 1999.
- II-4 STEFAN DIEBELS: *Mikropolare Zweiphasenmodelle: Formulierung auf der Basis der Theorie Poröser Medien*, March 2000.
- II-5 DIRK MAHNKOPF: *Lokalisierung fluidgesättigter poröser Festkörper bei finiten elastoplastischen Deformationen*, March 2000.
- II-6 HEINER MÜLLERSCHÖN: *Spannungs-Verformungsverhalten granularer Materialien am Beispiel von Berliner Sand*, August 2000.
- II-7 STEFAN DIEBELS (Ed.): *Zur Beschreibung komplexen Materialverhaltens: Beiträge anlässlich des 50. Geburtstages von Herrn Prof. Dr.-Ing. Wolfgang Ehlers*, August 2001.
- II-8 JACK WIDJAJAKUSUMA: *Quantitative Prediction of Effective Material Parameters of Heterogeneous Materials*, June 2002.
- II-9 ALEXANDER DROSTE: *Beschreibung und Anwendung eines elastisch-plastischen Materialmodells mit Schädigung für hochporöse Metallschäume*, October 2002.
- II-10 PETER BLOME: *Ein Mehrphasen-Stoffmodell für Böden mit Übergang auf Interface-Gesetze*, October 2003.
- II-11 MARTIN AMMANN: *Parallel Finite Element Simulations of Localization Phenomena in Porous Media*, April 2005.
- II-12 BERND MARKERT: *Porous Media Viscoelasticity with Application to Polymeric Foams*, July 2005.
- II-13 SAEED REZA GHADIANI: *A Multiphase Continuum Mechanical Model for Design Investigations of an Effusion-Cooled Rocket Thrust Chamber*, September 2005.
- II-14 WOLFGANG EHLERS & BERND MARKERT (Eds.): *Proceedings of the 1st GAMM Seminar on Continuum Biomechanics*, September 2005.
- II-15 BERND SCHOLZ: *Application of a Micropolar Model to the Localization Phenomena in Granular Materials: General Model, Sensitivity Analysis and Parameter Optimization*, November 2007.

- II-16 WOLFGANG EHLERS & NILS KARAJAN (Eds.): *Proceedings of the 2nd GAMM Seminar on Continuum Biomechanics*, December 2007.
- II-17 TOBIAS GRAF: *Multiphasic Flow Processes in Deformable Porous Media under Consideration of Fluid Phase Transitions*, 2008.
- II-18 AYHAN ACARTÜRK: *Simulation of Charged Hydrated Porous Materials*, 2009.
- II-19 NILS KARAJAN: *An Extended Biphasic Description of the Inhomogeneous and Anisotropic Intervertebral Disc*, 2009.
- II-20 BERND MARKERT: *Weak or Strong – On Coupled Problems In Continuum Mechanics*, 2010.
- II-21 WOLFGANG EHLERS & BERND MARKERT (Eds.): *Proceedings of the 3rd GAMM Seminar on Continuum Biomechanics*, 2012.
- II-22 WOLFGANG EHLERS: *Poröse Medien – ein kontinuumsmechanisches Modell auf der Basis der Mischungstheorie*, 2012.
- II-23 HANS-UWE REMPLER: *Damage in multi-phasic Materials Computed with the Extended Finite-Element Method*, 2012.
- II-24 IRINA KOMAROVA: *Carbon-Dioxide Storage in the Subsurface: A Fully Coupled Analysis of Transport Phenomena and Solid Deformation*, 2012.
- II-25 YOUSEF HEIDER: *Saturated Porous Media Dynamics with Application to Earthquake Engineering*, 2012.
- II-26 OKAN AVCI: *Coupled Deformation and Flow Processes of Partial Saturated Soil: Experiments, Model Validation and Numerical Investigations*, 2013.
- II-27 ARNDT WAGNER: *Extended Modelling of the Multiphasic Human Brain Tissue with Application to Drug-Infusion Processes*, 2014.
- II-28 JOFFREY MABUMA: *Multi-Field Modelling and Simulation of the Human Hip Joint*, 2014.
- II-29 ROBERT KRAUSE: *Growth, Modelling and Remodelling of Biological Tissue*, 2014.
- II-30 SEYEDMOHAMMAD ZINATBAKHS: *Coupled Problems in the Mechanics of Multi-Physics and Multi-Phase Materials*, 2015.
- II-31 DAVID KOCH: *Thermomechanical Modelling of Non-isothermal Porous Materials with Application to Enhanced Geothermal Systems*, 2016.
- II-32 MAIK SCHENKE: *Parallel Simulation of Volume-coupled Multi-field Problems with Special Application to Soil Dynamics*, 2017.
- II-33 STEFFEN MAUTHE: *Variational Multiphysics Modeling of Diffusion in Elastic Solids and Hydraulic Fracturing in Porous Media*, 2017.





ISBN 978-3-937399-34-8  
(D 93 – Dissertation, Universität Stuttgart)